ANL-7705

ANL-7705

Argonne National Laboratory

REACTOR DEVELOPMENT PROGRAM PROGRESS REPORT

June 1970

The facilities of Argonne National Laboratory are owned by the United States Government. Under the terms of a contract (W-31-109-Eng-38) between the U. S. Atomic Energy Commission, Argonne Universities Association and The University of Chicago, the University employs the staff and operates the Laboratory in accordance with policies and programs formulated, approved and reviewed by the Association.

MEMBERS OF ARGONNE UNIVERSITIES ASSOCIATION

The University of Arizona
Carnegie-Mellon University
Case Western Reserve University
The University of Chicago
University of Cincinnati
Illinois Institute of Technology
University of Illinois
Indiana University
Iowa State University
The University of Iowa
Kansas State University
The University of Kansas
Loyola University
Marquette University
Michigan State University
The University of Michigan
University of Minnesota
University of Missouri
Northwestern University
University of Notre Dame
The Ohio State University
Ohio University
The Pennsylvania State University
Purdue University
Saint Louis University
Southern Illinois University
University of Texas
Washington University
Wayne State University
The University of Wisconsin

LEGAL NOTICE

This report was prepared as an account of Government sponsored work. Neither the United States, nor the Commission, nor any person acting on behalf of the Commission:

A. Makes any warranty or representation, expressed or implied, with respect to the accuracy, completeness, or usefulness of the information contained in this report, or that the use of any information, apparatus, method, or process disclosed in this report may not infringe privately owned rights; or

B. Assumes any liabilities with respect to the use of, or for damages resulting from the use of any information, apparatus, method, or process disclosed in this report.

As used in the above, "person acting on behalf of the Commission" includes any employee or contractor of the Commission, or employee of such contractor, to the extent that such employee or contractor of the Commission, or employee of such contractor prepares, disseminates, or provides access to, any information pursuant to his employment or contract with the Commission, or his employment with such contractor.

Printed in the United States of America
Available from
Clearinghouse for Federal Scientific and Technical Information
National Bureau of Standards, U. S. Department of Commerce
Springfield, Virginia 22151
Price: Printed Copy $3.00; Microfiche $0.65

ANL-7705
Reactor Technology

ARGONNE NATIONAL LABORATORY
9700 South Cass Avenue
Argonne, Illinois 60439

REACTOR DEVELOPMENT PROGRAM PROGRESS REPORT

June 1970

Robert B. Duffield, Laboratory Director
Robert V. Laney, Associate Laboratory Director

Division	Director
Applied Physics	R. Avery
Center for Environmental Studies	L. E. Link
Chemical Engineering	R. C. Vogel
EBR-II Project	M. Levenson
Engineering and Technology	S. A. Davis
Materials Science	P. G. Shewmon
Reactor Analysis and Safety	W. R. Simmons

Report coordinated by
M. Weber and V. G. Trice, Jr.

Issued July 31, 1970

FOREWORD

The Reactor Development Program Progress Report, issued monthly, is intended to be a means of reporting those items of significant technical progress which have occurred in both the specific reactor projects and the general engineering research and development programs. The report is organized in accordance with budget activities in a way which, it is hoped, gives the clearest, most logical overall view of progress. Since the intent is to report only items of significant progress, not all activities are reported each month. In order to issue this report as soon as possible after the end of the month editorial work must necessarily be limited. Also, since this is an informal progress report, the results and data presented should be understood to be preliminary and subject to change unless otherwise stated.

The issuance of these reports is not intended to constitute publication in any sense of the word. Final results either will be submitted for publication in regular professional journals or will be published in the form of ANL topical reports.

The last six reports issued
in this series are:

November 1969	ANL-7640
December 1969	ANL-7655
January 1970	ANL-7661
February 1970	ANL-7669
March 1970	ANL-7679
April-May 1970	ANL-7688

REACTOR DEVELOPMENT PROGRAM

Highlights of Project Activities for June 1970

EBR-II

Run 42, completed May 18, was the longest period that EBR-II has ever operated without interruption. During the almost 23 days of the run, 1,139 MWd were accumulated. The cumulative operational total for EBR-II is now 35,136 MWd.

An in-core prooftest has demonstrated the feasibility of the xenon-tag technique for identifying and locating defective, gas-bonded, ceramic fuel elements. Tag released from capsules in the upper triflute reflector of a driver subassembly was recovered from the reactor cover gas and identified.

Destructive and nondestructive examinations of Mark-II elements irradiated to a burnup of 2.2 at. % in EBR-II show the elements to be performing as predicted. The destructive examination revealed no fuel-cladding interaction or unusual microstructural features.

ZPR-3

ZPR-3 Assembly 61, a second critical assembly in support of EBR-II, has been adjusted to have a volume close to that of EBR-II. This assembly, with a nickel-rich reflector, was characterized by axial and radial uranium, plutonium, and boron reaction-rate traverses and by measurement of central fission ratios. Neutron spectra at core center, interface, and reflector regions were determined, and gamma dosimetry was carried out at various core locations.

Assembly 62, changed from the earlier assembly only in that the nickel-rich reflector will be replaced by a stainless steel-rich reflector, is now being constructed.

ZPR-6

As an initial step, approximately 400 kg of plutonium has been loaded into Assembly 7. This assembly will be a uniform 3,500-liter mixed plutonium-uranium oxide reactor, and its predicted critical mass is 1,245 kg of plutonium.

ZPR-9

Using the Doppler oscillator and autorod systems, the Doppler effect of 1-kg samples of UO_2 and PuO_2 was measured in Assembly 26, the FTR-3 critical assembly. Central reactivity worths of a number of materials were determined, and radial distributions of reactivity worths of ^{239}Pu, ^{235}U, and ^{10}B were made near the core midplane.

ZPPR

Fast-neutron spectrum measurements were made at two locations in ZPPR Assembly 2, the demonstration-reactor benchmark assembly, and compared with fundamental-mode calculations using the MC^2 code. Polarity-correlation measurements done in this two-zoned system display the long-standing discrepancy between calculated and measured values of β/ℓ. Radial fission-rate traverses have been made, and small-sample central perturbation worths of a number of materials have been evaluated by calculation and by experimental measurement.

TABLE OF CONTENTS

	Page
I. LIQUID METAL FAST BREEDER REACTORS--CIVILIAN	1
A. Physics Development	1
1. Theoretical Reactor Physics	1
2. Experimental Reactor Physics	13
3. ZPR-6 and -9 Operations and Analysis	25
4. ZPR-3 and ZPPR Operations and Analysis	29
B. Component Development	39
1. Instrumentation and Control	39
2. Fuel Handling, Vessels, and Internals	45
C. Sodium Technology	47
1. On-line Impurity Monitors	47
2. Analytical Program	50
3. Fission Product and Cover Gas Technology	52
4. Materials-Coolant Compatibility	54
5. Purification of Sodium	56
6. Sodium Chemistry	58
D. EBR-II--Research and Development	60
1. New Subassemblies and Experimental Support	60
2. Instrumented Subassemblies	65
3. Experimental Irradiation and Testing	66
4. Materials-Coolant Compatibility	69
5. Leak Detection and Location--Xenon Method	72
6. Reactor Analysis, Testing and Methods Development	79
7. Driver Fuel Development	102
8. Operation with Failed Fuel	110
9. Hot Fuel Examination Facilities	111
10. Physics Mock-up Studies	113
E. EBR-II--Fuel Fabrication	115
1. Cold Line Operations	115
F. EBR-II--Operations	116
1. Reactor Plant	116
2. Fuel Cycle Facility	117
PUBLICATIONS	125

TABLE OF CONTENTS

	Page
II. OTHER FAST REACTORS--OTHER FAST BREEDER REACTORS--FUEL DEVELOPMENT	130
A. Irradiation Effects, Mechanical Properties and Fabrication	130
1. Irradiation Effects on Creep of FFTF-specified Type 316 Stainless Steel	130
2. Mechanical Properties of Austenitic Stainless Steel	131
PUBLICATION	131
III. GENERAL REACTOR TECHNOLOGY	132
A. Applied and Reactor Physics Development	132
1. Theoretical Reactor Physics--Research and Development	132
2. Nuclear Data--Research and Development	138
B. Reactor Fuels and Materials Development	142
1. Fuels and Cladding--Research and Development	142
2. Radiation Damage on Structural Materials--Research and Development	144
3. Techniques of Fabrication and Testing--Research and Development	146
4. Engineering Properties of Reactor Materials--Research and Development	150
C. Engineering Development--Research and Development	152
1. Instrumentation and Control	152
2. Heat Transfer and Fluid Flow	156
3. Engineering Mechanics	159
D. Chemistry and Chemical Separations	161
1. Fuel Cycle Technology--Research and Development	161
2. General Chemistry and Chemical Engineering--Research and Development	165
PUBLICATIONS	169

TABLE OF CONTENTS

	Page
IV. NUCLEAR SAFETY RESEARCH AND DEVELOPMENT	171
A. LMFBR Safety--Research and Development	171
1. Accident Analysis and Safety Evaluation	171
2. Reactor Control and Stability	173
3. Coolant Dynamics	173
4. Fuel Element Failure Propagation	177
5. Fuel Meltdown Studies with TREAT	178
6. Materials Behavior and Energy Transfer	181
7. Fast Reactor Safety Test Facility Study	182
8. Violent Boiling	185
9. Post-accident Heat Removal	189
B. Effluent Control--Environmental Studies--Research and Development	192
1. Mass-Energy Balance	192
PUBLICATIONS	194
PUBLICATION--General	196

I. LIQUID METAL FAST BREEDER REACTORS--CIVILIAN

A. Physics Development

1. Theoretical Reactor Physics

a. General Reactor Physics

(i) Dynamics

Last Reported: ANL-7669, pp. 11-13 (Feb 1970).

(a) QX1--FTR Rod Ejection Case (D. A. Meneley and E. L. Fuller)

This study is one in a continuing series designed to show the importance of space-time effects to LMFBR transient analysis. Emphasis was placed on comparing the QX1 solution with that obtained by so-called adiabatic methods. The transient that was analyzed was initiated by control-rod ejection from an FFTF-type core, similar to that loaded in ZPR-9. This core is a two-enrichment-zone oxide, with a total core volume of ~1000 liters. It is surrounded by a boron carbide control ring, which is in turn surrounded by a nickel reflector. The radial dimensions are given in Table I.A.1. These resulted from a dimension search in the core to achieve k_{eff} = 1.0. All steady-state and shape function calculations used a 29-group diffusion-theory model.

TABLE I.A 1. Radial Dimensions of FTR-3

Region	Radius, cm	Region	Radius, cm
Inner core	40.9431	Reflector	90.5068
Outer core	65.5483	Shield	102.4779
Control	67.5234		
Extrapolated core height = 134.75565 cm			

The transient was initiated by time-linear removal of the control over an interval of 1 sec. The vacancy was occupied by a nickel follower. For comparison, three types of calculation were made, corresponding to three degrees of sophistication. The least sophisticated was a point-kinetics calculation. Next came an "adiabatic" calculation in which the true inserted reactivity was used. The reactivity was determined by performing static calculations at two intermediate boron carbide concentrations, and fitting the result to a quadratic function over the interval of interest. The net reactivity was reduced by negative Doppler feedback

based on a simple fuel-temperature model. For the adiabatic model, it was assumed that the Doppler coefficient, T dk/dT, was constant. For the adiabatic calculation, T dk/dT = -0.00459, a value found from a static calculation for a fuel temperature of 3000°K (melting point). This seemed to be a reasonable choice, a priori. (All initial steady-state fuel temperatures were taken to be 1300°K.) The third, and most sophisticated, calculation was a full space-time solution of the problem, using the code QX1.

The amplitude functions found from the three calculations are shown in Fig. I.A.1 (the adiabatic calculation described above is denoted by Adiabatic 1). Both the adiabatic and point-kinetics results are surprisingly poor, considering that the core radius is relatively small. The most important error in the point-kinetics model was due to the underestimate of the reactivity effect of the boron-rod removal. The Doppler feedback effect becomes important long before the fuel melts. Therefore, a static calculation was done for a fuel temperature of 1600°K, yielding T dk/dT = -0.00480. The adiabatic calculation was then rerun, resulting in the amplitude function denoted by Adiabatic 2 in Fig. I.A.1. The differences between the plots for these two adiabatic cases indicate the magnitude of the effect of the constant Doppler coefficient assumed over this range. The discrepancy relative to the true solution around t = 0.13 sec was due to the use of an incorrect effective temperature in calculating the Doppler coefficient for these cases. This was proven by recomputing the coefficient from the temperature distributions given in the QX1 run at t = 0.127 sec. The value of -0.00555 was obtained for T dk/dT by this method. The adiabatic result with the corrected coefficient is labeled Adiabatic 3 in Fig. I.A.1. The amplitude function diverges from the correct value for t > 0.14 sec; this is due to the fact that the effective Doppler coefficient changes rapidly as the fuel-temperature distribution changes from a constant value to a shape approximating the power distribution.

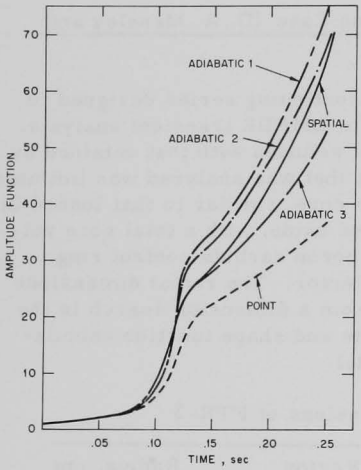

Fig. I.A.1. Amplitude Functions for FTR-3 Rod Ejection Transient

These calculations indicate that, for this case, the most important improvement that should be made in the adiabatic model is inclusion of a region-dependent reactivity table to reduce the effective temperature error. Secondly, the temperature dependence of the Doppler coefficient should be computed as $T\gamma$ dk/dT (or some higher approximation), using three or more fuel temperatures.

The total cost of each adiabatic run made in the above study was approximately half that of the QX1 run. Generation of reactivity tables and/or more accurate feedback coefficients could result in a higher cost for the adiabatic model. In more complicated cases (for example space-dependent coolant voiding), the feedback coefficients can be interdependent, in which case an accurate adiabatic-model calculation could involve a prohibitive manpower cost compared to the direct QX1 calculation.

(ii) Analysis of Neutronic Characteristics of Reactors and Fuel Cycles (J. T. Madell and D. A. Meneley)

Last Reported: ANL-7669, pp. 9-11 (Feb 1970).

(a) Effect of Subassembly Clearance on Reactor Performance Characteristics. In a fast breeder reactor, the subassembly gap may be designed to allow for steel swelling of the cladding and subassembly wrapper during irradiation. The influence of increasing the subassembly allowances to accommodate steel swellings on the neutronic characteristics and the fuel costs of 1000-MWe LMFBR is being investigated.

Three reactor designs with cladding OD's of 0.22, 0.26, and 0.30 in. were considered in the study. Fuel-cycle and fuel-cost calculations were performed for each reactor design with a 50- and 300-mil clearance between subassemblies. Many parameters were held constant for the three designs to limit the scope of the study to the effects of subassembly clearance.

Table I.A.2 shows the parameters that were held constant in the three reactor designs. The reactor design with 0.30-in. cladding OD is similar to the final AI Reference Design. Thermal-hydraulic calculations were performed to select the core height and coolant velocity so that the fuel (4420°F) and cladding (~1300°F) temperatures and pressure drop (~100 psi) would be within design limitations for the three reactor types.

TABLE I.A.2. Constant Parameters for 1000-MWe Reactors

Reactor power	2400 MWt	Pin-to-pin spacing	0.050 in.
Average linear power	10 kW/ft	Outer/inner core enrichment	1.5
Inlet temperature	780°F	Average core burnup (two stages)	6.7 at. %
Temperature rise	360°F	Number of control subassemblies	15 (tantalum)
Fuel material	Mixed oxide	Axial blanket height	1.13 ft
Fuel density	85% TD	Gas plenum height	3.17 ft
Fuel pins/subassembly	271	Cladding thickness	(0.05 x cladding OD) in.

Equilibrium fuel-cycle calculations were performed with the SYNBURN* code, which used a modified cross-section set** generated for the study by an MC^2 calculation with the ENDF/B library data. The two-dimensional equilibrium fuel-cycle calculations were performed for the six cases, and the results of the calculations were used by CYCOST code† to obtain the fuel costs. Key assumptions in the fuel-cost calculations were a fissile plutonium value of $10/g and a total annual charge of 12.53%. CYCOST determines the fabrication costs from the design specifications of the fuel element, and the calculated rates for the core of the three designs ranged between $1.65/g and $2.60/g. Table I.A.3 briefly describes the six reactor systems and their calculated performance features. Increasing the subassembly clearance decreases the fuel volume fraction by ~8%, increases the core diameter by ~5%, decreases the breeding ratio by ~4%, and increases the plutonium fissile inventory by ~5%. All these changes increased fuel cost by ~5%.

TABLE I.A.3. Description and Performance Characteristics for the Three Reactor Designs with Two Subassembly Clearance Specifications

	Reactor Design No. 1 Cladding OD = 0.22 in.		Reactor Design No. 2 Cladding OD = 0.26 in.		Reactor Design No. 3 Cladding OD = 30 in.	
Subassembly gap, in.	0.05	0.30	0.05	0.30	0.05	0.30
Core height, ft	2.75	2.75	3.0	3.0	3.58	3.58
Core diameter, ft	7.40	7.77	8.03	8.39	8.28	8.62
Core volume, liters	3340	3690	4300	4700	5470	5920
Breeding ratio	1.22	1.17	1.27	1.23	1.30	1.25
Burn time, days	149	148	212	212	271	269
Pu fissile loading, kg	1753	1833	2175	2260	2612	2680
Fuel cost, mils/kW-hr	1.131	1.205	0.973	1.036	0.883	0.952

Increasing the subassembly clearance to accommodate steel swelling may permit a longer residence time for the subassembly and, in turn, a higher fuel burnup. To investigate the incentive for higher burnup, additional fuel-cycle calculations were performed for the three reactor designs with 300-mil clearances at 4- and 10-at. % burnup; the results are presented in Table I.A.4. The other design specifications for the reactor remained identical to the cases with 6.7 at. %. The results indicate that the small economic penalty for increasing the subassembly clearance may be offset if an additional amount (~1 at. %) of burnup can be achieved. Other quantities affected by increased burnup are the need for more shim control

*Private communication with P. A. Pizzica and D. A. Meneley (Feb 1969).

**Reactor Development Program Progress Report, November 1969, ANL-7640.

†Private communication with T. D. Wolsko (Aug 1969).

(as indicated by a larger unpoisoned k_{eff} at startup), a longer burn time (which influences the production schedules of the utility), and the breeding ratio (which influences the doubling time).

TABLE I.A.4. Results of Equilibrium Fuel-cycle Calculations for 4-, 6.7-, and 10-at. % Burnup

Design No.	Burnup, at. %	Unpoisoned K	Burn Time, days	Breeding Ratio	Fuel Cost, mils/kW-hr
1	4.0	1.009	87	1.23	1.873
	6.7	1.033	148	1.17	1.205
	10.0	1.054	227	1.12	0.905
2	4.0	1.006	124	1.28	1.595
	6.7	1.020	212	1.23	1.036
	10.0	1.034	324	1.18	0.795
3	4.0	1.004	157	1.29	1.438
	6.7	1.009	269	1.25	0.952
	10.0	1.021	410	1.20	0.761

(b) Parametric Study of Neutronic Characteristics of LMFBR Types of Systems. A parametric study was conducted to compare the neutronic characteristics of various types of fast reactors. Four fuel types and two core sizes were selected for the study. For each fuel type and core volume, calculations were performed for the range of core compositions given in Table I.A.5. The fuel compositions represented the compositions expected at midcycle of 100,000-MWd/MT exposure. The core was composed of two regions, the outer region having a 50% greater enrichment than the inner region. Tantalum was placed in the outer region for control purposes. The blanket consisted of 55% depleted uranium fuel, 15% steel, and 30% sodium. In a preliminary study, the blanket thickness

TABLE I.A.5. Description of Systems for Parametric Study

		Oxide, Carbide, Nitride (85%)			U, Pu-10 wt % Zr (70%)		
Fuel Type, % TD	Base Case	Fuel	Sodium	Steel	Fuel	Sodium	Steel
Core Volume = 3500 liters with 20-cm-thick Blanket							
Core Volume Fractions	1	30	47.5	22.5	25	50	25
	2	35	45	20	30	47.5	22.5
	3	40	42.5	17.5	35	45	20
Core Volume = 5500 liters with 25-cm-thick Blanket							
Core Volume Fractions	4	35	42.5	22.5	30	50	20
	5	40	40	20	35	47.5	17.5
	6	45	37.5	17.5	40	45	15

was varied until the breeding ratio agreed with that obtained from a two-dimensional calculation of a reactor with a similar core composition and volume. A reflector of 80% steel and 20% sodium resides in the outermost region of the reactors.

The neutronic quantities were obtained by one-dimensional (spherical) diffusion-theory calculations using the 26-group set developed for the core-design study. The critical enrichment was determined for each case, and the reaction summaries were obtained for the critical systems. The reactivity coefficients were obtained from perturbation calculations.

Figures I.A.2 and I.A.3 show the relationship between the volume fraction of the four types of fuel and the breeding ratios for the 3500- and 5500-liter cores, respectively. The breeding ratio is a strong function of the fuel volume fraction or atom density. It also depends upon the amount of light elements in the fuel. The highest breeding ratio is achieved by the metal (U, Pu-10 wt % Zr) fuel, and the lowest by the oxide (U, Pu, O_2) fuel. Comparison of the two figures also shows that the breeding ratio is greater for the larger core; this effect is, in part, due to the higher concentration of fertile material (or lower enrichment) in the larger core. The breeding ratio of the nitride-fueled system is substantially lower than that of the carbide-fueled system, even though the atom densities of the heavy and light isotopes in the fuel were identical. The difference in breeding ratio is principally caused by the parasitic (n,p) reaction in nitrogen. In addition to lowering the breeding ratio, the reaction produces hydrogen in the nitride fuel, which may unfavorably affect its burnup capabilities.

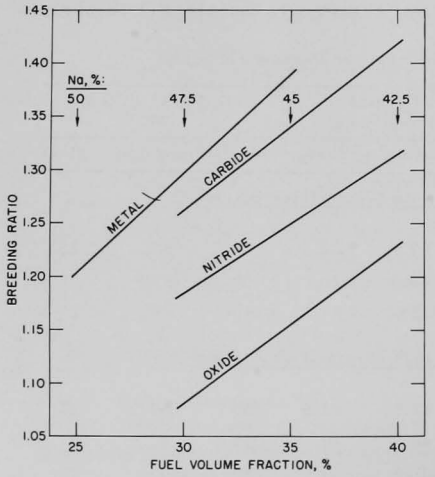

Fig. I.A.2. Relationship of Volume Fraction to Breeding Ratio for 3500-liter Core

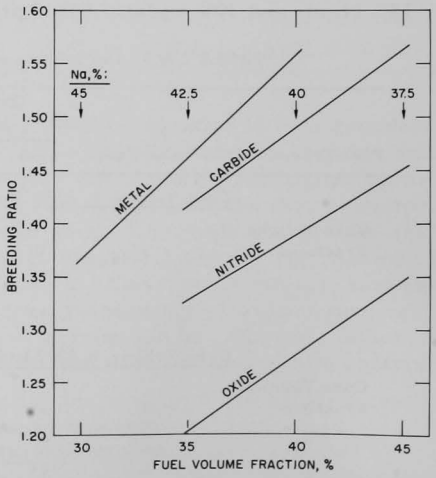

Fig. I.A.3. Relationship of Volume Fraction to Breeding Ratio for 5500-liter Core

For each of the three fuel volume fractions considered in the study, three combinations of steel and sodium volume fractions were investigated. The breeding ratios for the oxide-fueled systems of 5500 liters are plotted for the set of nine core compositions in Fig. I.A.4. These results are typical for all the fuel types and core volumes investigated. For a given fuel volume fraction, the breeding ratio can be improved by increasing the sodium content in favor of the steel content. A replacement of 5% volume fraction of steel with sodium produces ~4% increase in the breeding ratio.

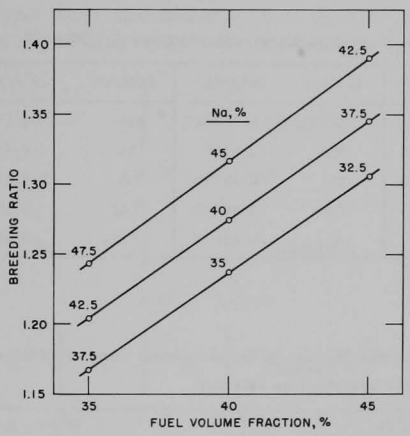

Fig. I.A.4

Breeding Ratios vs Fuel Volume Fraction for Various Core Compositions in an Oxide-fueled 5500-liter Core

b. Fast Critical Experiments--Theoretical Support--Idaho

(i) Supplementary Analytical Interpretation of Integral Data

Last Reported: ANL-7669, pp. 13-14 (Feb 1970).

(a) Predicted Perturbation Sample Worths in ZPPR Assembly 2 (R. G. Palmer and A. P. Olson)

Perturbation calculations in two-dimensional (r,z) geometry have been made using the ARC System diffusion-perturbation modules to predict small sample central perturbation worths in the equal core volume loading of ZPPR Assembly 2. Real and adjoint fluxes were obtained using neutron cross sections from MC^2. The isotopes ^{239}Pu, ^{240}Pu, ^{241}Pu, molybdenum, and ^{238}U were heterogeneously self-shielded, while the remaining isotopes were homogeneously self-shielded. Cross sections for the two core regions were spatially flux-volume-weighted by the CALHET-2 Code to account for the fine structure of the flux in the unit cells. Blanket and reflector regions used homogeneously self-shielded cross sections from MC^2.

Perturbation sample cross sections were homogeneously self-shielded, and not flux-volume-weighted. This type of cross sections best represents a small perturbation sample, whereas a flux-volume-weighted, heterogeneously self-shielded cross section best represents the reactivity worth of an individual plate within the unit cell.

Table I.A.6 lists central perturbation worths for small samples. Using a conversion factor of 1027 Ih/% ρ (from MACH 1) leads to perturbation sample worths presented in Table I.A.7. Corrections for finite sample-size effects have not yet been applied.

TABLE I.A.6. Central Perturbation Worths in Equal-volume Core of ZPPR-2

Isotope	$10^4\rho/kg^a$	Isotope	$10^4\rho/kg^a$	Isotope	$10^4\rho/kg^a$	Isotope	$10^4\rho/kg^a$
^{239}Pu	14.089	^{235}U	11.888	O	-0.70902	Mn	-1.1593
^{240}Pu	1.0742	^{236}U	-1.8689	Mo	-2.6450	^{9}Be	-0.75403
^{241}Pu	22.514	^{238}U	-0.97722	Fe	-0.38775	^{10}B	-267.17
^{233}U	19.721	Na	-0.40185	Cr	-0.54379	^{27}Al	-0.55448
^{234}U	-0.57000	C	-1.0344	Ni	-0.42872	^{181}Ta	-5.4825

[a] $\rho = \Delta k/k$; Ih/% ρ = 1027.

TABLE I.A.7. Central Perturbation Sample Worths in Equal-volume Core of ZPPR-2

(Uncorrected for sample-size effects)

Capsule ID No.	Isotope	Worth, Ih (for Ih/% ρ = 1027) Sample	Capsule ID No.	Isotope	Worth, Ih (for Ih/% ρ = 1027) Sample
B-1	92.85 wt % ^{10}B	-10.68	Nb-2	Nb	-
B-2	92.85 wt % ^{10}B	-1.918	Nb-3	Nb	-
B-3	92.85 wt % ^{10}B	-0.667	Nb-4	Nb	-
B-4	92.85 wt % ^{10}B	-0.188	W-1	W	-
B-5	92.85 wt % ^{10}B	-4.680	W-2	W	-
B-6	92.85 wt % ^{10}B	-2.436	W-3	W	-
B-7	92.85 wt % ^{10}B	-1.266	W-4	W	-
B-8	19.89 wt % ^{10}B	-1.280	Ni-1	Ni	-0.167
B-9	19.89 wt % ^{10}B	-0.264	Mn-1	Mn	-0.214
B-10	19.89 wt % ^{10}B	-0.097	Cr-3	Cr	-0.151
SS-1	304 SS[a]	-0.150	V-1	V	-
Fe-1	Fe	-0.133	C-1	C	-0.085
Fe_2O_3-2	Fe, O	-0.026	Ti-1	Ti	-
Ta-1	99.988 at. % ^{181}Ta	-3.969	Poly-1	C, H	-
Ta-2	99.988 at. % ^{181}Ta	-1.050	Poly-2	C, H	-
Ta-3	99.988 at. % ^{181}Ta	-0.264	Poly-3	C, H	-
Ta-4	99.988 at. % ^{181}Ta	-0.780	Al-1	Al	-0.065
Ta-5	99.988 at. % ^{181}Ta	-0.332	Al_2O_3-1	Al, O	-0.020
Mo-1	Mo	-1.179	Al_2O_3-3	Al, O	-0.097
Mo-2	Mo	-0.309	Zr-1	Zr	-
Mo-3	Mo	-0.205	Na-4	Na	-0.053
Mo-4	Mo	-0.101	D-45	-	-
Nb-1	Nb	-			

[a] 304 SS ≈ 69.05 wt % iron, 18.7 wt % chromium, 10.5 wt % nickel, 1.75 wt % manganese.

(ii) ZPR Heterogeneity Method Development (R. G. Palmer)

Last Reported: ANL-7669, pp. 14-15 (Feb 1970).

(a) GEDANKEN Studies (J. P. Plummer)

The GEDANKEN investigation (see Progress Report for August 1969, ANL-7606, pp. 8-10; and Progress Report for February 1970, ANL-7669, pp. 14-15) has been nearly concluded and most of the results are now available. The four GEDANKEN's on which extensive work was done are numbered 2, 5, 6, and 7. The unit cell for each, with mirror boundary conditions at each end, is shown in Fig. I.A.5. Each GEDANKEN contains 22 such unit cells (actually 11 as depicted arranged alternately with 11 mirror-image cells) in a semiinfinite slab core 38.5 cm thick, with a 20-cm ^{238}U blanket at each end. Each GEDANKEN is a different combination of four materials: ^{239}Pu, ^{238}U, ^{23}Na, and ^{12}C.

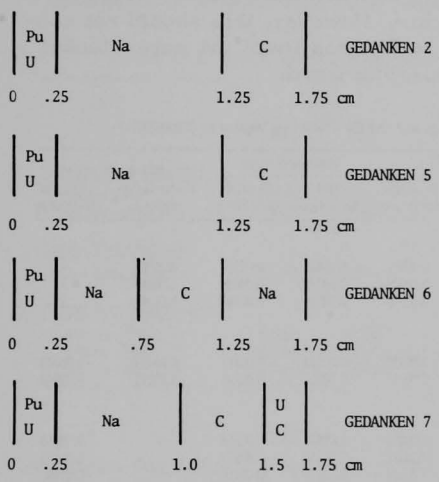

Fig. I.A.5. GEDANKEN Cells

GEDANKEN 2, formerly called GEDANKEN 1, has been analyzed most completely, including both the full and half sodium-voided cores. The ^{238}U-to-^{239}Pu ratio in the fuel plates is 3.67:1. GEDANKEN 5 is a two-zone core in which the outer-zone fuel plates have a 50% greater Pu/(U + Pu) ratio than the inner-zone plates. GEDANKEN 6 has the same homogeneous concentrations as GEDANKEN 2 and differs only in a restructuring of the sodium and carbon plate configurations. GEDANKEN 7 features a uranium-carbide plate halfway between consecutive fuel plates. The fuel plates have a uranium-to-plutonium ratio of 3.16:1. For simplicity, claddings, matrices, and drawers are omitted from all the GEDANKEN's.

Since prescriptions for cell homogenization of cross sections are invariant to positioning of the cells in the core relative to the center plane of the reactor and to the core-blanket interfaces, two exact transport-theory (TESS or 1-D transport in ARC) calculations were done for each GEDANKEN, as well as for their associated sodium-voided cores and cores with central reactivity samples inserted. In one case, the left-hand face of the cell as shown in Fig. I.A.5 would lie on the center plane of

the reactor, whereas the core-blanket interface would be a right-hand face. In the other case, the situation would be reversed. The first case, with a fuel plate at the center of the reactor, is the most reactive orientation of the cells in the core whereas the second case is the least reactive. (The former is designated High and the latter Low in Tables I.A.8-I.A.11.) Thus all the results obtained for heterogeneity factors, sodium-void effects, and central sample worths by the various spatial homogenization procedures must be compared to a range of "exact" values rather than to one number. This is a kind of natural limit in the resolving power of the GEDANKEN "experiments" as an instrument to measure the accuracy of the various spatial homogenization methods. The situation is not quite so clear-cut as this, because either one or the other orientation of the cells in the core results in the core containing two half-fuel plates, which have a direct effect on the heterogeneity factor. However, this should not confuse the issue too much since the half-fuel plates lie at the core-blanket interfaces and hence have the lowest possible worth.

TABLE I.A.8. Results of Various Weighting Procedures and Leakage Treatments Applied to GEDANKEN 2

	"Exact"		Pseudo Σ_a		Modified Source		CALHET-2	
	Low	High	Real Weighting	Bivariate Weighting	Real Weighting	Bivariate Weighting	Perturbation Theory	Volume Weighting
Heterogeneity Factor, $\Delta k/k$								
Normal core	0.00519	0.00638	0.00618	0.00557	0.00485	0.00589	0.00563	-
Half sodium-voided core	0.00416	0.00521	0.00502	0.00444	0.00382	0.00476	0.00447	-
Fully sodium-voided core	0.00302	0.00393	0.00370	0.00335	0.00268	0.00348	0.00341	-
Sodium-void Effect, Δk								
Half sodium void	-0.00145	-0.00159	-0.00158	-0.00155	-0.00141	-0.00151	-0.00157	-0.00042
Full sodium void	-0.00209	-0.00236	-0.00239	-0.00214	-0.00204	-0.00229	-0.00213	0.00008
Central Sample Worth, Δk								
0.02 cm ^{239}Pu	0.00549	0.00567	0.00570	0.00556	0.00575	0.00566	-	0.00563
0.20 cm ^{238}U	-0.00665	-0.00665	-0.00679	-0.00657	-0.00668	-0.00657	-	-0.00654
0.50 cm ^{12}C	-0.00149	-0.00183	-0.00182	-0.00159	-0.00173	-0.00158	-	-0.00161

TABLE I.A.9. Results of Various Weighting Procedures and Leakage Treatments Applied to GEDANKEN 5 (Two-zone Core)

	"Exact"		Pseudo Σ_a		Modified Source		
	Low	High	Real Weighting	Bivariate Weighting	Real Weighting	Bivariate Weighting	Volume Weighting
Heterogeneity Factor, $\Delta k/k$							
Normal core	0.00516	0.00653	0.00608	0.00545	0.00462	0.00602	-
Inner-zone sodium void	0.00423	0.00538	0.00509	0.00458	0.00377	0.00498	-
Outer-zone sodium void	0.00391	0.00501	0.00459	0.00430	0.00339	0.00452	-
Total sodium void	0.00296	0.00383	0.00363	0.00340	0.00250	0.00354	-
Sodium-void Effect, Δk							
Inner-zone void	0.01008	0.00988	0.01003	0.01015	0.01015	0.00998	0.01096
Outer-zone void	-0.00847	-0.00874	-0.00871	-0.00837	-0.00845	-0.00872	-0.00720
Total void	0.00218	0.00169	0.00193	0.00233	0.00225	0.00190	0.00435
Central Sample Worth, Δk							
0.02 cm ^{239}Pu	0.00534	0.00546	0.00549	0.00538	0.00548	0.00541	0.00545
0.20 cm ^{238}U	-0.00656	-0.00651	-0.00665	-0.00650	-0.00664	-0.00655	-0.00645
0.50 cm ^{12}C	-0.00157	-0.00183	-0.00184	-0.00168	-0.00184	-0.00171	-0.00166

TABLE I.A.10. Results of Various Weighting Procedures and Leakage Treatments Applied to GEDANKEN 6

	"Exact"		Pseudo Σ_a		Modified Source		
	Low	High	Real Weighting	Bivariate Weighting	Real Weighting	Bivariate Weighting	Volume Weighting
Heterogeneity Factor, $\Delta k/k$							
Normal core	0.00508	0.00637	0.00624	0.00564	0.00470	0.00582	-
Sodium-voided core	0.00299	0.00387	0.00365	0.00334	0.00263	0.00343	-
Sodium-void Effect, Δk							
Full sodium void	-0.00197	-0.00238	-0.00247	-0.00217	-0.00195	-0.00226	0.00012
Central Sample Worth, Δk							
0.02 cm ^{239}Pu	0.00549	0.00565	0.00569	0.00554	0.00569	0.00559	0.00562
0.20 cm ^{238}U	-0.00661	-0.00667	-0.00680	-0.00659	-0.00679	-0.00666	-0.00655
0.50 cm ^{12}C	-0.00149	-0.00184	-0.00185	-0.00163	-0.00183	-0.00169	-0.00161

TABLE I.A.11. Results of Various Weighting Procedures and Leakage Treatments Applied to GEDANKEN 7

	"Exact"		Pseudo Σ_a		Modified Source		
	Low	High	Real Weighting	Bivariate Weighting	Real Weighting	Bivariate Weighting	Volume Weighting
Heterogeneity Factor, $\Delta k/k$							
Normal core	0.00501	0.00686	0.00624	0.00599	0.00538	0.00616	-
Sodium-voided core	0.00402	0.00562	0.00512	0.00507	0.00420	0.00498	-
Sodium Void Effect, Δk							
Full sodium void	0.00279	0.00255	0.00266	0.00286	0.00261	0.00260	0.00376
Central Sample Worth, Δk							
0.02 cm ^{239}Pu	0.00509	0.00524	0.00523	0.00513	0.00523	0.00515	0.00520
0.20 cm ^{238}U	-0.00587	-0.00600	-0.00602	-0.00589	-0.00600	-0.00591	-0.00589
0.50 cm ^{12}C	-0.00230	-0.00259	-0.00255	-0.00236	-0.00254	-0.00238	-0.00235

Tables I.A.8-I.A.11 present the results currently available for GEDANKEN's 2, 5, 6, and 7, respectively. Both the real flux and bivariate (flux and adjoint) weighting schemes are based on the treatment by Nicholson.* They are programmed into the double S_n transport-theory code TESS. Also in TESS are two different options for providing for the leakage of the finite system when doing a cell calculation. One is the standard method of treating DB^2 as a pseudoabsorption cross section. The other multiplies the source term in each group by the factor $\Sigma_t/(\Sigma_t + DB^2)$ for that group and is identical to the leakage treatment modification made in the CALHET Code as reported in the Progress Report for August 1969, ANL-7606. This is called the modified source leakage treatment.

Table I.A.12 shows that inclusion of anisotropic scattering does not alter the conclusions one reaches based on isotropic scattering only, even when the number of energy groups is increased to 22.

*Nicholson, R. B., "Cross Section Averaging Schemes for Group Collapsing and Cell Homogenization in Neutron Transport Calculations for Critical Assemblies," in Reactor Physics Division Annual Report: July 1, 1968 to June 30, 1969, pp. 488-498 (January 1970).

TABLE I.A.12. Anisotropy and Group Structure Effects

Exact system: GEDANKEN 2 with a fuel plate at the center of the reactor

	Percent Heterogeneity Factor, $\frac{k_{exact} - k_{hom}}{k_{hom}}$	
Groups	Isotropic	First-order Anisotropic
12	0.00638	0.00664
22	0.00689	0.00684

Conclusions from Tables I.A.8-I.A.11 are, first, that both cross-section homogenization schemes and both leakage treatments are good. Bilinear weighting seems to be slightly better than real flux weighting in predicting the heterogeneity effect.

For calculating the sodium-void effect or central sample worths, bilinear weighting coupled with the modified source leakage treatment is most consistently accurate. Simple volume weighting does quite well for the worth of small central samples.

A CALHET analysis has been undertaken at present on GEDANKEN 2 only. The perturbation result from CALHET is sensitive to the type of leakage treatment employed.* Good results are obtained with the modified source method, now incorporated in CALHET-2. These are the values reported in Table I.A.8. Also incorporated in CALHET-2 is a prescription to flux-weight the cross sections. This flux-weighting scheme corresponds to the original flux-weighting scheme in TESS involving only the scalar fluxes, as mentioned in ANL-7606, rather than the prescription involving $|\mu|$-weighting now also in TESS, which has proved slightly better for a slab-geometry system. Nevertheless, the weighted cross sections from CALHET-2 will be used for the core composition in TESS calculations for all the GEDANKEN systems as soon as time permits.

*For example, the pseudo Σ_a leakage treatment in CALHET gives a perturbation result for GEDANKEN 2 of $\Delta k/k = 0.00851$.

2. Experimental Reactor Physics

a. Fast Critical Experiments--Experimental Support--Idaho (S. G. Carpenter)

(i) Neutron Spectrum Measurements (G. G. Simons)

Last Reported: ANL-7669, pp. 16-17 (Feb 1970).

Three fast-neutron spectrum measurements were made over the energy range of 0.9 keV to 1.8 MeV at two locations in ZPPR Assembly 2. A hydrogen and a methane cylindrical proportional counter positioned with their centers of active volumes 5 in. from the reactor interface were used in partially voided drawers in matrix positions 137-37 and 127-47. Figure I.A.6 shows these drawer configurations containing the two counters, preamplifiers, and core materials used for matrix positions 137-37 and 127-47.

An auxiliary experiment was run in location 137-37, using the detector configurations shown in Fig. I.A.7, to ascertain the effect of encasing the detectors in 1/2 in. of lead. Calculations were made which showed that neutron scattering in a lead sleeve would not appreciably change the neutron spectrum from 1 keV to 1 MeV. (See Spectrum Shift Effect of Lead Shielding for Proton Recoil Spectrometer Measurements in ZPPR Assembly 2, by Arne P. Olson and Nam Chin Paik, memorandum of April 3, 1970.) The results of this experiment were required to determine if the lead would modify the neutron angular distribution such that the heterogeneity effect of the drawer loadings around the detectors would be decreased.

The central measurement configuration, made at approximately 2% $\Delta k/k$ subcritical, consisted of replacing the core drawer in position 137-37 with the counter drawer and withdrawing all control and poison rods. For the outer-core measurement, poison rods No. 5, 7, 10, and 18 and all control rods were withdrawn. The reactor was 1.4% $\Delta k/k$ subcritical. The core loading diagram was shown in Fig. I.A.6 of the Progress Report for March 1970, ANL-7679.

The spectrometer system used for these three measurements consisted of improved high-count-rate electronics including pulse pileup rejection circuitry which was operated in both single- and dual-parameter modes with a Data Machines 622 on-line, 18-bit, 8K computer. The in-core neutron flux levels resulting from the loadings described above were selected relative to predetermined high count rates compatible with correct operation of the new electronics. Proper operation of the spectrometer at count rates exceeding 30,000 cps for the methane counter and

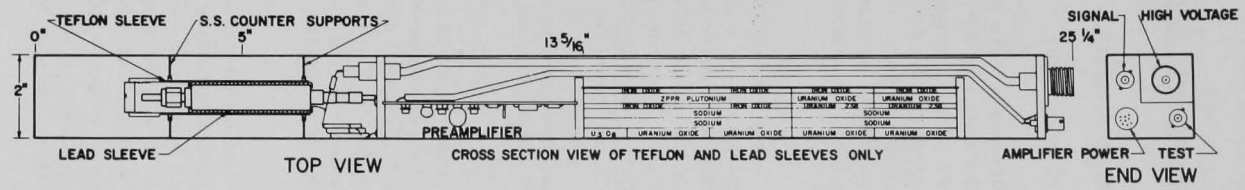

METHANE GAS FILLED PROTON RECOIL PROPORTIONAL COUNTER LOADED IN A MATRIX DRAWER

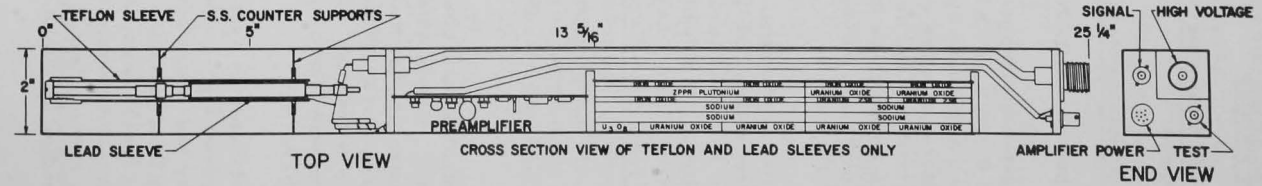

HYDROGEN GAS FILLED PROTON RECOIL PROPORTIONAL COUNTER LOADED IN A MATRIX DRAWER

Fig. I.A.6. Proportional-counter Configurations Used in ZPPR Assembly 2

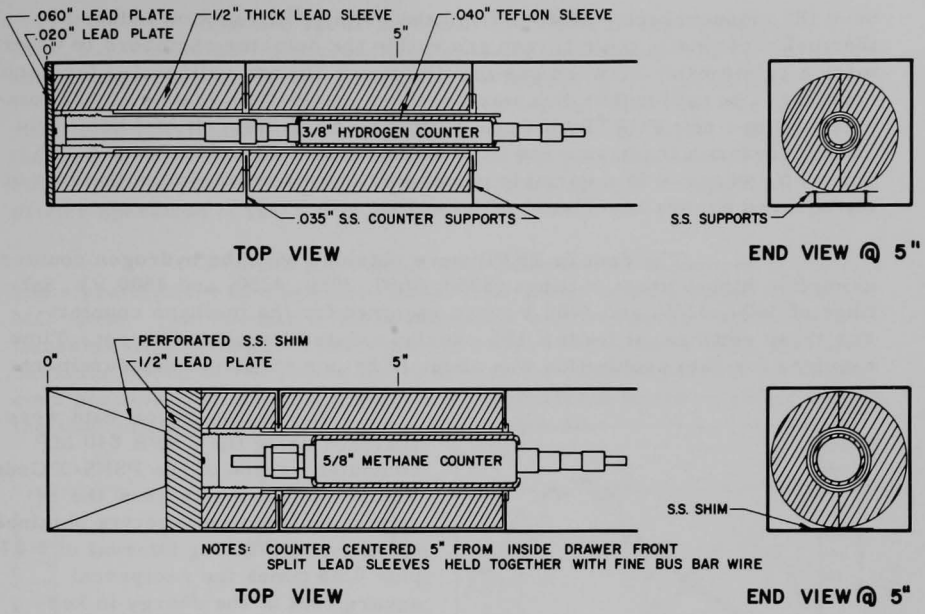

Fig. I.A.7. Proton-recoil Proportional Counters Encased in Lead for ZPPR Assembly 2

10,000 cps for the hydrogen counter was verified in the Argonne Fast Source Reactor (AFSR). The maximum possible count rate limit has not been determined for this system. This upper limit will be set by the saturation-inducing events in the hydrogen counter. Since a new, smaller, less efficient hydrogen counter is presently being used, count-rate limitations are much less severe than those existing when the larger counter was used.

Two new cylindrical detectors were used for these measurements. A nominal 3/8-in.-dia hydrogen counter, containing 10 atm of predominantly hydrogen gas, was used for neutron energies below 130 keV. A nominal 5/8-in.-dia methane counter, filled with 8.2 atm of predominantly methane gas, was used for neutron energies above 100 keV. The 30-keV overlap was required to verify the counter normalizations. Both counters had a 0.70-mil anode and a sensitive length two diameters long. These two detectors replaced the larger more sensitive counters previously used at ZPPR and ZPR-3. Thus it was possible to complete the present central spectrum measurement with ZPPR less than 2% $\Delta k/k$ subcritical without exceeding the count-rate limitations imposed upon the associated electronics.

Both the hydrogen and the methane counters were calibrated in the AFSR thermal column just prior to the Assembly 2 fast-neutron spectrometer measurement. This was a standard calibration procedure, which

used the monoenergetic protons from the $^{14}N(n,p)^{14}C$ reaction induced by thermal neutrons in the nitrogen gas within the detector chambers to determine a relationship between gas multiplication (A) and voltage (V) for each counter. The calibration data were reduced on the Data Machines 622 computer using a new FORTRAN Code written by E. F. Bennett of ANL. This code performs a least-squares fit to the straight-line relation $(\ln A)/V^x$ versus V, where x is a variable parameter chosen to minimize the sum of the squared errors associated with the fit.

The data in ZPPR were obtained with the hydrogen counter using five high-voltage settings (3350, 3650, 3950, 4250, and 4500 V). Settings of 3400, 3250, and 3000 V were required for the methane counter. For these settings, at least a 15% overlap existed for each data set. Time required for data acquisition was about 10 hr per spectrum measurement.

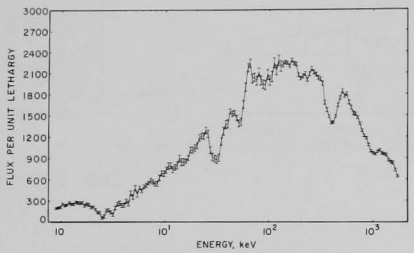

Fig. I.A.8. Neutron Spectrum in Location 137-37 from Lead-covered Proton-recoil Proportional Counters

The proton-recoil data were analyzed using the ZPPR 840 MP computer verson of the PSNS-X Code. Figures I.A.8-I.A.10 show the resultant fast-neutron spectra obtained using a slope-taking interval of 0.07 plus 0.08 times the reciprocal square root of the energy in keV. These raw proton data were corrected for distortions induced by nonuniform electric fields at the ends of the counter and for carbon recoils. Also, the energy-dependent variation in W, energy loss per ion pair, for the low-energy hydrogen counter data was included in the analysis according to a prescription suggested by E. F. Bennett (ZPR-C Memo No. 32, Feb. 16, 1970).

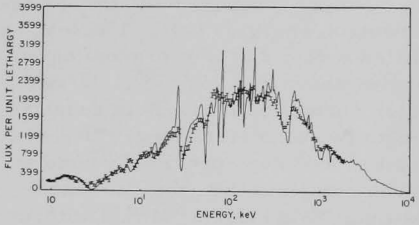

Fig. I.A.9. Neutron Spectrum in Location 137-37 from Proton-recoil Proportional Counters and Ultrafine MC^2 Calculation

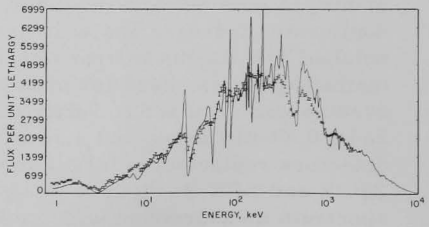

Fig. I.A.10. Neutron Spectrum in Location 127-47 from Proton-recoil Proportional Counters and Ultrafine MC^2 Calculation

The two spectra measured at 137-37 are shown in Figs. I.A.8 and I.A.9. Superposition of these data showed that no measureable change resulted from encasing the detectors in 1/2 in. of lead. Thus the presence of lead did not aid in overcoming the heterogeneity of the plate-type environment in which the measurement was made. However, the lead sleeves could be used to decrease the gamma-ray background in environments where the gamma-ray flux is too severe for otherwise proper operation of these detectors.

Figures I.A.9 and I.A.10 compare the measured spectra and a preliminary fundamental-mode, 1980-group calculation using the MC^2 Code. The calculated fluxes smoothed with an energy-dependent Gaussian window function are shown in Figs. I.A.11 and I.A.12. This fundamental-mode model should be valid near the core center. In the outer-core position (147-27), the actual neutron spectrum would be softer than the theoretical spectrum, as shown in Fig. I.A.12.

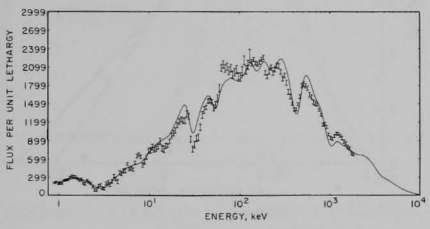

Fig. I.A.11. Experimental and Smoothed MC^2 Calculated Spectra--Location 137-37

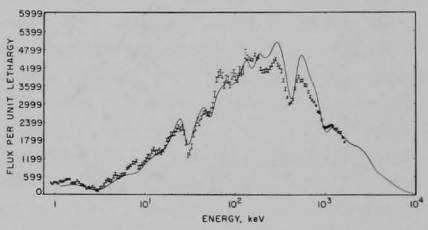

Fig. I.A.12. Experimental and Smoothed MC^2 Calculated Spectra--Location 127-47

(ii) Pulsed, Cross-correlation and Noise Measurements
(W. K. Lehto)

Last Reported: ANL-7679, pp. 1-2 (March 1970).

Polarity-correlation experiments have been done in ZPPR Assembly 2 using the correlator described in ANL-7679. The instantaneous sign of the analog signal from each of two detectors (plastic scintillators viewed by phototubes) was sampled by trigger circuits and used as input to the ZPPR computer for subsequent calculation of the cross-correlation function. Data were taken with the reactor critical and at several degrees of subcriticality. The decay constants were obtained from a least-squares fit of the function

$$C_{12}(\tau) = A_1 + A_2 e^{-\alpha t}$$

to the data.

Figure I.A.13 shows the correlation functions for the various degrees of subcriticality; Fig. I.A.14 shows the decay constants

plotted against dollars subcritical. These results point out the long-standing discrepancy between the calculated and measured value of β/ℓ, the ratio being α_c/α_m = 1.059. This is consistent with the findings in other laboratories.

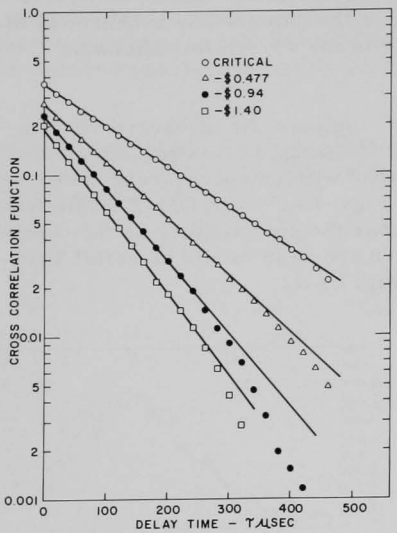

Fig. I.A.13. Polarity-correlation Functions for ZPPR Assembly 2

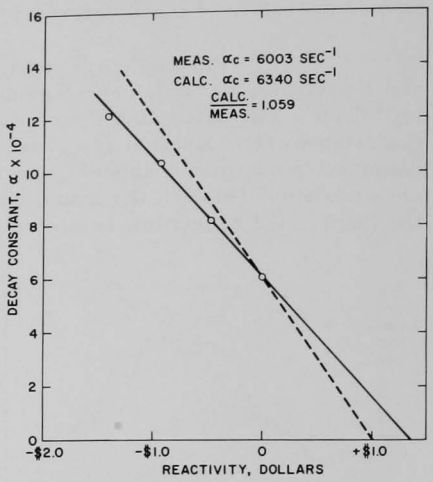

Fig. I.A.14. Decay Constant vs Reactivity for ZPPR Assembly 2

Another frequently observed discrepancy is obvious from inspection of Fig. I.A.14, in that, these data extrapolate to $\rho > \$1$ at $\alpha = 0$. In this case, the extrapolated value is $1.33.

b. Fast Critical Experiments--Experimental Support--Illinois

(i) Neutron Spectrum Measurement

Last Reported: ANL-7688, pp. 13-14 (April-May 1970).

(a) Response Function Effects in Proton-Recoil Neutron Spectroscopy (E. F. Bennett and T. J. Yule)

Neutron spectra in fast reactors have been measured routinely with proton-recoil proportional counters. If neutron spectra are to be accurately determined by this method, the measured proton-recoil energy distribution must be corrected for distortions introduced by

the finite size of the detector. Distortions arise from the truncation of proton-recoil tracks by the counter walls or by the extension of tracks into the end region, where there is little or no multiplication. These distortions may be termed geometrical. Distortions are also introduced by the behavior of the electric field near the ends of the counter. Near the end of the counter there is a transition in field strength which induces a nonuniform gas multiplication.* The effect of this transition is to produce a low amplitude "tail" upon the response function and unless this "tail" is accounted for in the analysis of the measurement a substantial systematic error will result.

The significance of this correction may be best seen in measurements of very hard spectra where only a small residual neutron flux remains at energies in the kilovolt region. Figure I.A.15 shows a spectrum of this type, with and without response function corrections. The measurement is of the neutron flux in a depleted-uranium slab with the detector placed a short distance from a fission converter. Few neutrons exist below about 8 keV, and essentially all the amplitude there is due to response-function effects acting coherently with a slow variation in W (the energy loss per ion pair for protons in hydrogen gas).

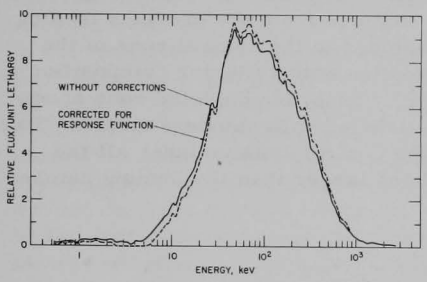

Fig. I.A.15. An Example of the Extent of the Corrections for Finite-size Effects in Proton-recoil Spectrometers. The neutron spectrum was measured in the interior of a depleted-uranium block.

The response correction is clearly significant everywhere, but the results at low energies are much more seriously affected when referred to the ratio of correction to flux level. If substantial neutrons exist at low energies, their amplitude will be essentially unchanged. The correction will remain at about the same absolute level and so will diminish correspondingly on a fractional basis.

c. Planning and Evaluation of FFTF Critical Assembly Experiments (A. Travelli)

Last Reported: ANL-7688, pp. 16-17 (April-May 1970).

(i) Evaluation of Fissile Depletion and Boron Removal Experiments in ZPPR/FTR-2. The FTR-2 experiments in which the B_4C ring was gradually removed from the periphery of the core while a central region was depleted of fissile material have been analyzed in a preliminary fashion in previous monthly reports. The two types of perturbation were

*Reactor Development Program Progress Report, December 1969, ANL-7655.

considered separately; the calculations of the boron worths were reported on p. 5 of ANL-7632;* the calculations of the depletion worths were reported on p. 18 of ANL-7640.** Comparison of these calculations with the experimental data was satisfactory, but the analysis involved several approximations which included (a) the use of an approximate five-group cross-section set for the calculation of the boron worths, (b) the assumption that the transverse buckling would not change appreciably with either type of perturbation, (c) a very simple geometrical model, and (d) the assumption that the two types of perturbation do not interfere with each other. A more accurate evaluation of the experiments is reported here, in which these approximations have been at least partially removed.

Figure I.A.16 shows the assembly configurations built on ZPPR in the main steps of the experiments. Every region in the figure is labeled with the number of the loading obtained from the previous loading by depleting that region (if the region belongs to the central zone of the core) or by replacing its control composition with reflector composition (if the region belongs to the control ring). Thus, the depleted zone of any loading includes all the central regions labeled with numbers smaller than or equal to the loading number, while the control zone includes all the control-ring regions labeled with numbers larger than the loading number.

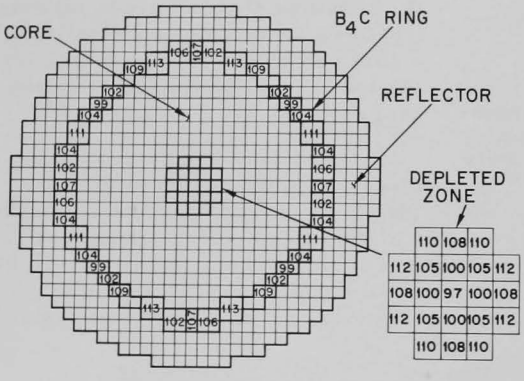

Fig. I.A.16

Various Assembly Configurations of ZPPR Corresponding to Core Loadings of Fissile and Boron-removal Experiments in ZPPR/FTR-2.

In general, the progressive removal of boron from the ring corresponded to removing ring sectors with areas equal to the area of four matrix drawers from a control ring which was virtually complete at the beginning but empty of boron at the end. Thus, the ring looked like a complete ring with two-drawer gaps at the beginning of the experiments and like an empty ring with two-drawer fillings at the end. The computational model was chosen according to these considerations and is depicted

*Reactor Development Program Progress Report, October 1969, ANL-7632.
**Reactor Development Program Progress Report, November 1969, ANL-7640.

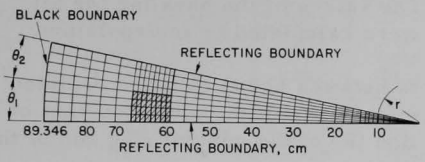

Fig. I.A.17. Model Used in Computations

in Fig. I.A.17. The symbols R and D are defined, respectively, as the fraction of the initial complete ring and of the final depleted zone present in any loading. The reactor is represented in (R,θ) geometry, the outer radii of the core and of the reflector being chosen so that their areas correspond to the effective midplane areas of the experimental assembly. The central depleted zone is represented by a circle of radius r, whose area also corresponds to the effective experimental value. The intermittent control ring is represented by a series of sectors (half of one sector is shown shaded in Fig. I.A.17) whose thickness equals the effective thickness of the complete experimental ring. When less than half the ring is present ($R < 0.5$), the half-thickness of each control section (θ_1) is chosen so that the area of the sector is equal to the area of four matrix drawers; the half-thickness of the reflector sector that separates two control sectors (θ_2) is chosen so that the total ring area occupied by control regions equals the experimental value. When more than half the ring is present, θ_2 is chosen so that the area of each reflector sector between control sectors is equal to the area of four matrix drawers, while θ_1 is chosen so that the desired amount of boron is represented in the reactor. Obviously, both methods yield the same values for both angles when half the ring is present ($R = 0.5$). For the number of control sectors present in the ring, this approach yields a value close to the number actually used in all the loadings build during the experiments in question. The computational model described does not take into account the jagged outlines of the core and of the control regions. Only a two-dimensional (x-y) calculation could do this adequately. However, the fact that only a small fraction of the core volume needs to be considered in the (R,θ) geometry makes it possible to use a large number of energy groups and a large number of mesh points. Since the change of the energy spectrum of the neutron flux in the reflector and in the boron regions is important in establishing the worth of the boron region, and since a large number of energy groups and of mesh points was deemed more important than a rigorous geometric representation in achieving the correct spectrum, the (R,θ) geometry was chosen over the (x,y) geometry.

The cross sections used in the calculations were taken from the 29-group Argonne cross-section set (29004). The calculation was run in diffusion theory by means of the DIFF2D code.

The value of the axial buckling was assumed to be independent of radius, energy, and azimuthal angle, and calculated in four cases

(no ring, no depletion; no ring, full depletion; full ring, no depletion; full ring, full depletion) so that it would yield the same value of the effective multiplication constant in a one-dimensional (R) calculation as obtained in a two-dimensional (R-Z) calculation. The values of the buckling for all other intermediate values of R and D were calculated by interpolation.

The interference effects between boron ring and depleted zone were calculated by expanding the effective multiplication constant of the reactor in power series of the fraction (R) of the control ring and of the fraction (D) of the depleted zone:

$$k(R,D) = \sum_{m=0}^{\infty} \sum_{n=0}^{\infty} \left[\frac{\partial^{m+n}k}{\partial R^m \partial D^n}\right]_{\substack{R=0\\D=0}} \frac{R^m D^n}{m!n!}$$

$$= \sum_{m=0}^{\infty} \left[\frac{\partial^m k}{\partial R^m}\right]_{\substack{R=0\\D=0}} \frac{R^m}{m!} + \sum_{n=0}^{\infty} \left[\frac{\partial^n k}{\partial D^n}\right]_{\substack{R=0\\D=0}} \frac{D^n}{n!} - k(0,0)$$

$$+ \sum_{m=1}^{\infty} \sum_{n=1}^{\infty} \left[\frac{\partial^{m+n}k}{\partial R^m \partial D^n}\right]_{\substack{R=0\\D=0}} \frac{R^m D^n}{m!n!}$$

$$= k(R,0) + k(0,D) - k(0,0) + RD \cdot C(R,D); \qquad (1)$$

$$C(R,D) = \sum_{m=0}^{\infty} \sum_{n=0}^{\infty} \left[\frac{\partial^{m+n+2}k}{\partial R^{m+1} \partial D^{n+1}}\right] \frac{R^m D^n}{(m+1)!(n+1)!} . \qquad (2)$$

As shown in Eq. 1, the function C(R,D) makes it possible to infer exactly any value of the effective multiplication constant of any loading from the knowledge of the effective multiplication constants of two loadings which have the same ring and no depleted zone or the same depleted zone and no ring. The C(R,D) function corresponds to the interference effects between the ring and the depletion.

Table I.A.13 shows the results obtained from a series of calculations for five different values of R and D. In particular, the values obtained for C(R,D) show that the function generally has a small value (i.e., the interference effects between ring and depletion are small), smoothly varying, and separable in the two variables. The values of C shown in Table I.A.13 were then used to obtain by interpolation the values of C for any other (R,D) combination.

TABLE I.A.13. Values of Axial Buckling, Effective Multiplication Constant, and Interference Function as Calculated for Various Values of R and D

D	R = 0.0	R = 0.25	R = 0.50	R = 0.75	R = 1.0	
1.0	5.920	5.946	5.972	5.998	6.024	$B_z^2 \times 10^4$, cm^{-2}
	0.987	0.959	0.937	0.925	0.914	k
	-	-0.018	-0.017	-0.014	-0.012	C
0.75	5.922	5.949	5.976	6.002	6.028	$B_z^2 \times 10^4$, cm^{-2}
	1.001	0.974	0.953	0.941	0.930	k
	-	-0.019	-0.017	-0.014	-0.013	C
0.50	5.924	5.952	5.980	6.006	6.033	$B_z^2 \times 10^4$, cm^{-2}
	1.015	0.990	0.969	0.958	0.948	k
	-	-0.020	-0.018	-0.015	-0.013	C
0.25	5.926	5.955	5.984	6.010	6.037	$B_z^2 \times 10^4$, cm^{-2}
	1.031	1.007	0.987	0.976	0.967	k
	-	-0.021	-0.019	-0.016	-0.014	C
0.0	5.928	5.958	5.988	6.014	6.042	$B_z^2 \times 10^4$, cm^{-2}
	1.048	1.025	1.007	0.997	0.988	k
	-	-	-	-	-	C

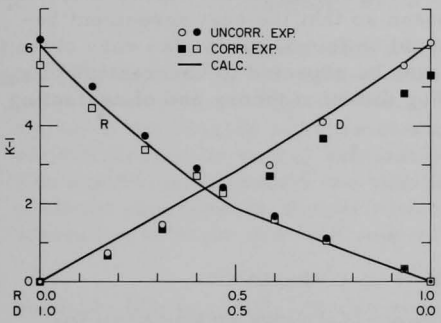

Fig. I.A.18. Comparison of Calculations with Experimental Values (corrected and uncorrected) of Effective Multiplication Constant of a Reactor with No Depletion and a Fraction (R) of the Control Ring and of a Reactor with No Control Ring and a Fraction (D) of the Depleted Zone

Figure I.A.18 shows the values of (k_{eff} - 1) as function of R for every configuration having no depleted zone and a fraction R of the control ring, and the values of (k_{eff} - 1) as function of D for every configuration having no ring and a fraction D of the depleted zone. The uncorrected experimental points are obtained by adding up all the measured reactivity changes corresponding, respectively, to ring (or depleted zone) changes in a series of experiments leading to the reactor in question from a reactor with full ring (or full depletion). However, the experiments were usually performed with both depletion and ring present in the reactor; the corrected experimental points were obtained from the uncorrected points by using the calculated values of C to correct for this difference. Every reactivity change observed in the experiments was modified so that it would correspond to what would have been found had there been no depletion (or ring) in the reactor. The solid curves show the results of direct calculations.

The comparison shown in Fig. I.A.18 indicates that experiments and calculations are in good qualitative agreement with each other. The ^{10}B and ^{239}Pu worths are overestimated in the calculations by approximately 8 and 12%, in this order; these values are almost exactly the same

found in previous comparisons between experimental worths of ^{10}B and ^{239}Pu in FTR-1 and calculations using the same cross-section set. The correction of the experimental data is always rather small, and never exceeds 12% of their value. Even though the correction is based exclusively on calculations, the fact that it is small and little dependent on the reactor details makes it possible to place reasonable confidence on the values of the corrected experimental data plotted in Fig. I.A.18. The data indicate that the total worth of the control ring in FTR-2 is close to 5.5% of the effective multiplication constant.

Reducing the measured reactivity changes to the corresponding values that would be obtained in the absence of different types of perturbations (as in Fig. I.A.18) offers the advantages of a clear physical meaning and of a more regular behavior of the curves. However, it is interesting to investigate also how accurately the calculations could match the results of the experiments actually performed. This procedure does not offer a clear physical interpretation, but it removes the uncertainty inherent in the application of a calculated correction to the experimental data.

The results of this comparison are shown in Fig. I.A.19 and Table I.A.14. The curve calculated for k_{eff} in Fig. I.A.19 has been shifted upwards by 0.017. This value was chosen so that the best agreement between calculations and experiments could be found, but is also very close to the amount by which the calculations may be expected to underestimate k_{eff} because of the combined effects of using diffusion theory and of neglecting high-energy heterogeneity effects.

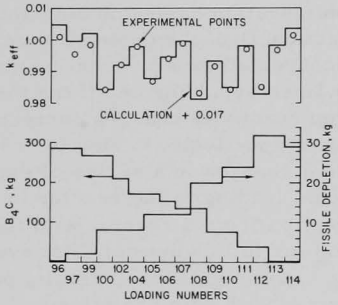

Fig. I.A.19

Comparison of Calculations with Experimental Values of k_{eff} as Measured for Various Loadings

TABLE I.A.14. Description of Main Properties of Various Loadings and Comparison of Calculations with Experiments

Loading Number	Fissile Mass, kg	No. of B_4C Drawers	k(E)	k(C)	k(E) - k(C), %	Fissile Exchanges %Δk(E)	Fissile Exchanges %Δk(C)	Fissile Exchanges C/E	Control Exchanges %Δk(E)	Control Exchanges %Δk(C)	Control Exchanges C/E
96	527.041	240	1.00086	0.98776	1.310						
						-0.564	-0.521	0.924			
97	525.043	240	0.99522	0.98255	1.267						
									0.319	0.238	0.747
99	525.043	224	0.99841	0.98493	1.348						
						-1.433	-1.766	1.233			
100	519.050	224	0.98408	0.96727	1.681						
									0.798	0.786	0.985
102	519.050	176	0.99206	0.97513	1.693						
									0.568	0.549	0.966
104	519.050	144	0.99774	0.98062	1.712						
						-1.116	-1.010	0.905			
105	515.054	144	0.98658	0.97052	1.606						
									0.739	0.691	0.935
106	515.054	112	0.99397	0.97743	1.654						
									0.483	0.511	1.058
107	515.054	96	0.99880	0.98254	1.626						
						-1.542	-1.821	1.181			
108	507.064	96	0.98338	0.96433	1.905						
									0.820	1.182	1.442
109	507.064	64	0.99158	0.97615	1.543						
						-0.733	-0.835	1.140			
110	503.068	64	0.98425	0.96780	1.645						
									1.275	1.354	1.062
111	503.068	32	0.99700	0.98134	1.566						
						-1.197	-1.536	1.284			
112	495.077	32	0.98503	0.96597	1.906						
									1.192	1.556	1.306
113	495.077	0	0.99695	0.98154	1.541						
						+0.472	+0.544	1.152			
114	498.073	0	1.00167	0.98697	1.470						

Table I.A.14 shows in condensed form the main properties of the various loadings and the calculated and experimental values of k_{eff}. In addition, the table lists both for fissile and for control exchanges the experimental k-changes, the calculated k-changes, and their ratios. The results are consistent with those shown graphically in Fig. I.A.18 and previously discussed.

3. ZPR-6 and -9 Operations and Analysis

a. Clean Critical Experiments (L.G. LeSage)

Last Reported: ANL-7688, pp. 17-18 (April-May 1970).

(i) ZPR-6 Assembly 7. Loading of plutonium into Assembly 7 has begun, and the initial loading step of about 400 kg of ^{239}Pu + ^{241}Pu is complete. The predicted critical mass of Assembly 7 is 1,245 kg of ^{239}Pu + ^{241}Pu.

b. Doppler Experiments

Last Reported: ANL-7679, p. 11 (March 1970).

(i) Doppler Experiments in ZPR-9 Assembly 26, FTR-3 (J. Daughtry and R. B. Pond)

Measurements were done to determine the Doppler effect for ^{238}U and for ^{239}Pu in ZPR-9 Assembly 26 as part of the FTR-3 Phase B program of critical experiments. The measurements were made at the center of the reactor and consisted of a determination of the change in reactivity caused by heating samples of the materials weighing about 1 kg. The experimental method has been used at Argonne National Laboratory in previous experiments, mainly with uranium-fueled cores, and has been described in detail in previous reports.*

Table I.A.15 gives the results obtained with the freely expandable UO_2 and PuO_2 Doppler samples. The reactivities listed are the changes in reactivity due to heating the sample from the reference temperature to the temperatures listed in the table. For the uranium sample, the

TABLE I.A.15. Measured Reactivity Changes for Freely Expandable Doppler Samples

		% of Autorod Worth		Inhours		Inhours/Kilogram	
Sample	Temperature, °C	Reactivity Change	σ	Reactivity Change	σ	Reactivity Change	σ
N-1	20.0	0.000	0.215	0.0000	0.0111	0.0000	0.0099
	508.5	-19.276	0.071	-1.1209	0.0048	-1.0042	0.0043
	509.1	-19.188	0.125	-1.1158	0.0077	-0.9996	0.0069
	796.2	-26.277	0.041	-1.5280	0.0042	-1.3689	0.0038
INC-5	30.0	0.000	0.148	0.0000	0.0085	0.0000	0.0092
	521.8	-8.543	0.068	-0.4899	0.0041	-0.5305	0.0044
	796.2	-13.565	0.106	-0.7778	0.0064	-0.8423	0.0069

*Reactor Physics Division Annual Report, July 1, 1965 to June 30, 1966, ANL-7210, pp. 129-137.

reference temperature was 20°C; for the plutonium sample, the reference was 30°C due to the self-heating of the sample. The reactivities have been tabulated in percent of autorod worth, inhours, and inhours per kilogram. To obtain the values listed in inhours per kilogram, the values listed in inhours were divided by the total weight of uranium or plutonium, not by the weight of any one isotope.

Various aspects of the Doppler experiments are still under investigation. The most important of these is the reactivity effect due to expansion of the plutonium sample. In addition, the calibration of the autorod and the method of sample temperature averaging are being studied.

c. Mockup Experiments

Last Reported: ANL-7688, pp. 18-19 (April-May 1970).

(i) Small Sample Reactivity Worth Measurements in ZPR-9 Assembly 26, FTR-3 (R. M. Fleischman and J. W. Daughtry)

Step No. 4 of the FTR-3 Phase B Critical Experiments Program calls for measuring the reactivity worths of an assortment of small samples near the center of the core. Step No. 5 of the program calls for measuring the radial distributions of the reactivity worths of small samples of ^{239}Pu, ^{238}U, and ^{10}B near the core midplane. These two steps of the program were done concurrently using the ZPR-9 radial sample changer and autorod system.

The measurements reported here were made by monitoring the position of the calibrated autorod while pneumatically oscillating the sample in and out of the core. Two boron ion chambers, connected in parallel and located above the stationary half of the reactor, continuously monitored the neutron population at that location, and the servo control system positioned the autorod to maintain a constant current from these chambers.

The samples used in these measurements are described in Table I.A.16. All samples were contained in stainless steel capsules. The reactivity worths of empty capsules were measured in order to make the necessary stainless steel subtractions. Sample B-7 had a capsule similar to D-29. Samples MB-20, -21, -23, -24 and -25 had capsules similar to MB-19. All other samples had capsules similar to D-1.

The integral worth of the autorod was determined by two calibration methods. Both methods used computer acquisition of reactor-flux data from an ion chamber located on top of the ZPR-9 matrix. The first method was a computer code based on the Hurliman-Schmid* period evaluation. This method gave a value of 5.83 ± 0.12 Ih for the total autorod worth. The second method used inverse kinetics and gave a result of

*Hurliman, T., and Schmid, P., Nucleonik 5, pp. 236-239 (1963).

5.848 ± 0.009 Ih for the worth. The results obtained by the two methods were in agreement within the accuracy of the measurements. The second result was used in analyzing the data since it was more accurate and because the inverse-kinetics method was considered more reliable for the conditions of these calibrations.

TABLE I.A.16. Perturbation Sample Descriptions

Sample Identification	Material Element or Isotope	State	Geometry	Dimensions, in. OD	Thickness	Length	Sample Weight, g
Ta-4	Tantalum	Solid	Annulus	0.378	0.021	2.174	13.859
Ta-5	Tantalum	Solid	Annulus	0.378	0.011	2.175	5.893
Fe-1	Iron	Solid	Cylinder	0.389	-	2.172	33.277
Fe_2O_3-2	Iron Oxide	Powder	Cylinder	0.401	-	2.169	5.265
Al-1	Aluminum	Solid	Cylinder	0.390	-	2.173	11.437
Al_2O_3-3	Aluminum Oxide	Solid	Cylinder	0.376	-	2.174	15.061
B-7[a]	^{10}B	Powder	Annulus	0.4002	0.0094	2.1733	0.4968
Poly-1	Polyethylene	Solid	Cylinder	0.390	-	2.173	4.024
Pu-7	Plutonium	Solid	Annulus	0.390	0.005	2.175	2.7059
Pu-9	Plutonium	Solid	Annulus	0.3900	0.015	2.173	8.8533
Pu-11	Plutonium	Solid	Annulus	0.390	0.025	2.173	15.1219
Pu-13	Plutonium	Solid	Annulus	0.390	0.005	2.172	3.0306
Pu-15	Plutonium	Solid	Annulus	0.390	0.015	2.173	8.5102
Pu-17	Plutonium	Solid	Annulus	0.390	0.025	2.1725	13.9392
Pu-19	Plutonium	Solid	Annulus	0.390	0.005	2.173	3.4424
Pu-21	Plutonium	Solid	Annulus	0.390	0.015	2.173	8.5079
Pu-23	Plutonium	Solid	Annulus	0.390	0.025	2.172	13.9231
MB-20	^{235}U	Solid	Annulus	0.835	0.005	1.6875	5.23061
MB-21	^{235}U	Solid	Annulus	0.835	0.015	1.6875	15.77801
MB-23	^{238}U	Solid	Annulus	0.835	0.005	1.6875	6.31491
MB-24	^{238}U	Solid	Annulus	0.835	0.015	1.6875	19.07423
MB-25	^{238}U	Solid	Annulus	0.835	0.030	1.6875	38.16314
D-1	304 SS	Dummy					
D-29	304 SS	Dummy					
D-33	304 SS	Dummy					
D-37	304 SS	Dummy					
MB-19	304 SS	Dummy					

[a]90-95 wt % ^{10}B. A detailed sample analysis is not available, but will be reported later.

The traverse data are displayed in Figs. I.A.20-I.A.23. Other results obtained by the autorod measurement method is tabulated in

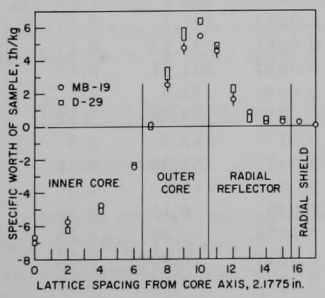

Fig. I.A.20

Stainless Steel Worth Traverse for ZPR-9 Assembly 26, FTR-3

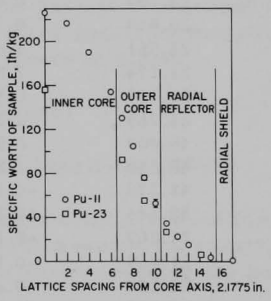

Fig. I.A.21

Plutonium Worth Traverse for ZPR-9 Assembly 26, FTR-3

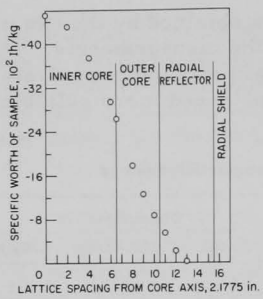

Fig. I.A.22

Boron Worth Traverse for ZPR-9 Assembly 26, FTR-3

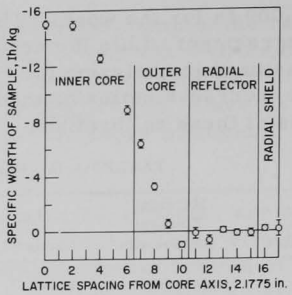

Fig. I.A.23

^{238}U Worth Traverse for ZPR-9 Assembly 26, FTR-3

Table I.A.17. Three boron samples and one enriched uranium sample, too large (in reactivity worth) to be measured with the autorod, were measured using the period code mentioned earlier. These data are still under analysis.

TABLE I.A.17. Results of Small-sample Reactivity-worth Measurements

		Ih		Ih/kg		
Sample ID	Stainless Steel Weight, g	Sample Worth	σ	Specific Worth	σ	Radius, in.
Ta-4	20.579	-1.1604	0.0032	-83.73	0.23	0.00
Ta-4	21.187	-0.735	0.012	-53.06	0.86	13.86
Ta-4	21.187	-0.2778	0.0095	-20.04	0.69	19.85
Ta-4	21.187	-0.0919	0.0054	-6.63	0.39	24.20
Ta-5	20.3021	-0.5617	0.0045	-95.33	0.78	0.00
Fe-1	20.740	-0.1809	0.0044	-5.44	0.13	0.00
Fe_2O_3-2	20.878	-0.0302	0.0061	-5.7	1.1	0.00
Al-1	20.668	-0.0925	0.0089	-8.09	0.78	0.00
Al_2O_3-3	20.391	-0.1354	0.0089	-8.99	0.59	0.00
Poly-1	20.824	1.7746	0.0042	441.0	1.0	0.00
Pu-7	21.107	0.600	0.010	221.7	3.7	0.00
Pu-13	20.814	0.5915	0.0072	195.2	2.4	0.00
Pu-15	21.561	1.6845	0.0065	197.93	0.77	0.00
Pu-17	21.174	2.8145	0.0057	201.91	0.42	0.00
Pu-19	21.159	0.5226	0.0050	151.8	1.5	0.00
Pu-21	21.069	1.3149	0.0058	154.56	0.69	0.00
MB-20	48.404	0.955	0.017	182.5	3.2	0.00
MB-21	48.240	2.876	0.011	182.30	0.71	0.00
MB-23	48.370	-0.1112	0.0095	-17.6	1.5	0.00
MB-24	48.345	-0.307	0.010	-16.11	0.52	0.00
D-1	21.069	-0.1433	0.0052	-6.80	0.25	0.00
D-1	21.069	-0.1433	0.0017	-6.800	0.083	0.00
D-33	28.258	-0.2035	0.0046	-7.20	0.16	0.00
D-37	27.522	-0.1842	0.0070	-6.69	0.26	0.00

4. ZPR-3 and ZPPR Operations and Analysis

a. Clean Critical Experiments (P. I. Amundson)

Last Reported: ANL-7688, pp. 20-27 (April-May 1970).

(i) ZPPR Assembly 2 (R. E. Kaiser)

Fission-rate traverses have been performed with ^{239}Pu, ^{238}U, and ^{235}U counters in a radial traverse tube located 3 in. back from the interface. Counts were taken at intervals of 2.173 in. (the matrix-tube width) throughout the two core zones, the blanket, and the reflector, including one point just outside the reflector. The results of these traverses, normalized to 1.0 at core center, are presented in Figs. I.A.24-I.A.26. The zone boundaries noted on these figures correspond to the changes in drawer loadings along the matrix tube, and not to the cylindrical reactor dimensions.

Central perturbation measurements included a large number of plutonium samples, plus two each of tantalum, ^{10}B, and ^{238}U, and one iron sample. The last seven samples were inserted in the last few days before the shutdown to give a variety of materials for comparison before and after the loading change and as a checkpoint for the preanalysis calculations. The worth of each sample, based on total sample weight in each case, is given in Table I.A.18. The sizes and compositions of the plutonium samples are given in Table I.A.19. As yet, the data have not been corrected for isotopic content, although this work is in progress. Both radial reaction rate traverses and central perturbation measurements were performed in a traverse tube located 3 in. back from the interface.

Measurements of the neutron energy spectrum using proton-recoil proportional counter techniques have been made in the inner and outer core zones. The results of these measurements, including a discussion of revisions in the data-analysis procedures, are presented in this report under ZPPR Experimental Support. Within experimental uncertainties, the addition of a lead sleeve around the counter to reduce gamma background had no noticeable effect on the neutron spectrum. Future spectrum measurements on ZPPR will therefore be done with the lead sleeve in place.

b. Doppler Experiments (R. E. Kaiser)

Last Reported: ANL-7688, p. 27 (April-May 1970).

Basic cross-section libraries have been prepared for use in the analysis of ZPR-3 Assembly 53 and ZPPR Assembly 2 reactivity Doppler experiments. Further calculations are proceeding for both problems.

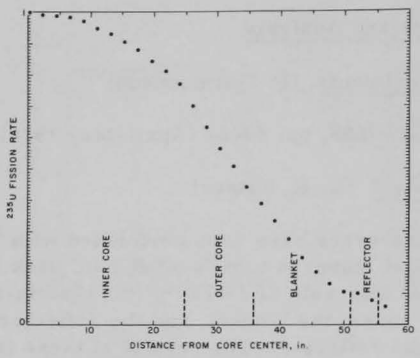

Fig. I.A.24
Radial ^{235}U Fission Traverse in ZPPR Assembly 2

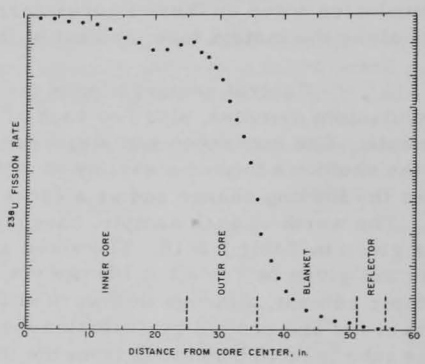

Fig. I.A.25
Radial ^{238}U Fission Traverse in ZPPR Assembly 2

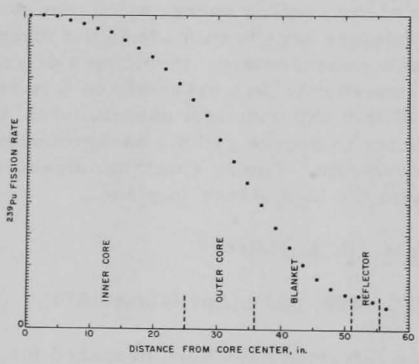

Fig. I.A.26
Radial ^{239}Pu Fission Traverse in ZPPR Assembly 2

TABLE I.A.18. Central Reactivity Measurements in ZPPR Assembly 2

Sample	Composition	Sample Weight, g	Worth, Ih/kg[a]	Sample	Composition	Sample Weight, g	Worth, Ih/kg[a]
Pu-26	<1% ^{240}Pu	4.4518	119.26 ± 0.96	Pu-42	22% ^{240}Pu	38.1472	98.80 ± 0.13
Pu-28	<1% ^{240}Pu	16.8639	117.18 ± 0.37	Pu-20	45% ^{240}Pu	3.5115	72.73 ± 2.48
Pu-30	<1% ^{240}Pu	38.0907	119.82 ± 0.33	Pu-22	45% ^{240}Pu	8.3384	73.06 ± 0.86
Pu-8	11.5% ^{240}Pu	3.0347	102.48 ± 3.49	Pu-24	45% ^{240}Pu	13.2560	72.40 ± 0.42
Pu-10	11.5% ^{240}Pu	8.8478	106.41 ± 0.76	U-238[b]	99.79 wt % ^{238}U	19.63	6.07 ± 0.41
Pu-12	11.5% ^{240}Pu	14.2288	107.90 ± 0.58	U-238[c]	99.79 wt % ^{238}U	85.76	5.79 ± 0.07
Pu-32	11.5% ^{240}Pu	3.9173	106.94 ± 1.32	B-5[d]	92.85 wt % ^{10}B	1.837	1717.6 ± 2.6
Pu-36	11.5% ^{240}Pu	38.6469	110.79 ± 0.20	B-7[e]	92.85 wt % ^{10}B	0.497	1919.9 ± 6.4
Pu-14	22% ^{240}Pu	3.0217	91.74 ± 2.08	Ta-1[f]	99.988 at. % ^{181}Ta	70.504	27.57 ± 0.09
Pu-16	22% ^{240}Pu	8.2391	95.57 ± 1.20	Ta-2[g]	99.988 at. % ^{181}Ta	18.647	31.42 ± 0.17
Pu-18	22% ^{240}Pu	13.7749	95.84 ± 0.49	Fe-1[f]	Fe	33.287	3.56 ± 0.28
Pu-38	22% ^{240}Pu	4.2427	96.90 ± 1.11				

[a]Per kg sample weight.
[b]Cylinder, 2.004 in. long, 0.2 in. diameter.
[c]Cylinder, 2.002 in. long, 0.42 in. diameter.
[d]Annular, powder, 2.173 in. long, 0.40 in. thick.
[e]Annular, powder, 2.173 in. long, 0.0094 in. thick.
[f]Cylinder, 2.173 in. long, 0.389 in. diameter.
[g]Cylinder, 2.173 in. long, 0.200 in. diameter.

TABLE I.A.19. Size and Composition Specifications for Plutonium Perturbation Samples in ZPPR Assembly 2

Sample No.	Type	OD,[a] in.	Wall Thickness, in.	Sample Mass, g	Composition, wt %				
					^{239}Pu	^{240}Pu	^{241}Pu	^{242}Pu	^{241}Am
8	Annular	0.390	0.005	3.0347	85.376	11.342	2.062	0.176	0.134
10	Annular	0.390	0.015	8.8478	85.376	11.342	2.062	0.176	0.134
12	Annular	0.390	0.025	14.2288	85.376	11.342	2.062	0.176	0.134
14	Annular	0.390	0.005	3.0217	72.319	21.678	3.779	0.615	0.264
16	Annular	0.390	0.015	8.2391	72.319	21.678	3.779	0.615	0.264
18	Annular	0.390	0.025	13.7749	72.319	21.678	3.779	0.615	0.264
20	Annular	0.390	0.005	3.5115	40.009	41.273	11.808	4.579	0.946
22	Annular	0.390	0.015	8.3384	40.009	41.273	11.808	4.579	0.946
24	Annular	0.390	0.025	13.2560	40.009	41.273	11.808	4.579	0.946
26	Cylinder	0.100	-	4.4518	97.205	1.005	0.048	0.002	-
28	Cylinder	0.200	-	16.8639	97.205	1.005	0.048	0.002	-
30	Cylinder	0.300	-	38.0907	97.205	1.005	0.048	0.002	-
32	Cylinder	0.100	-	3.9173	85.376	11.342	2.062	0.176	0.134
34	Cylinder	0.200	-	17.0474	85.376	11.342	2.062	0.176	0.134
36	Cylinder	0.300	-	38.6469	85.376	11.342	2.062	0.176	0.134
38	Cylinder	0.100	-	4.2427	72.319	21.678	3.779	0.615	0.264
40	Cylinder	0.200	-	16.9529	72.319	21.678	3.779	0.615	0.264
42	Cylinder	0.300	-	38.1472	72.319	21.678	3.779	0.615	0.264
44	Cylinder	0.100	-	4.4337	40.009	41.273	11.808	4.579	0.946
46	Cylinder	0.200	-	17.0297					
48	Cylinder	0.300	-	38.4081					

[a]All samples are 2.173 in. long.

c. Mockup Critical Experiments (W. P. Keeney and R. O. Vosburgh)

Last Reported: ANL-7688, pp. 32-54 (April-May 1970).

(i) Experimental Status. Assembly 61, the second critical assembly in support of the EBR-II Project, has been completed. The final transition step in Assembly 61 was reduction of ^{235}U in the core region so that the resulting critical volume would be closer to that of EBR-II. The experiments reported below were measured in this reduced fuel density with four rows of nickel-rich reflector.

Assembly 62, the third critical assembly in support of the EBR-II Project, is identical to Assembly 61 with the nickel-rich reflector replaced by a stainless steel-rich reflector of equal thickness. This transition step from Assembly 61 to Assembly 62 is now in progress.

(ii) Drawer Loading Descriptions, Assemblies 60 and 61. The core loading for Assembly 60 for Half 1 is shown in Fig. I.A.27. Assembly 61, Final Transition Step, with the reduced ^{235}U concentration core loading, is identical to these shown, except that the 1/32-in.-thick fuel column marked on the figure has been replaced by a 1/32-in.-thick natural-uranium column.

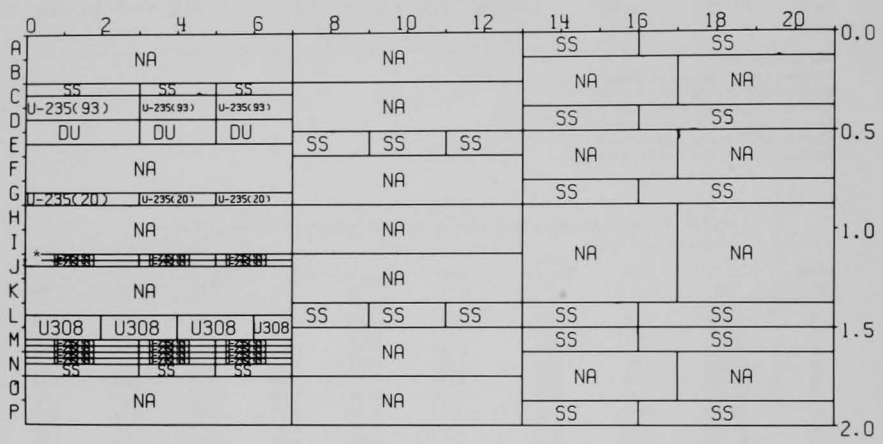

Fig. I.A.27. Assembly 60, Top View of Typical Core Region Drawer in Half 1

(iii) Critical Loadings, Assembly 61, Final Transition Step. With four rows of nickel-rich reflector, the concentration of ^{235}U in the core region was reduced by replacing a 1/32-in.-thick column of 93% enriched uranium with a 1/32-in.-thick column of natural uranium. The reference loading (final transition step) for this configuration is shown in Fig. I.A.28. The reference critical loading was 208.58 kg of ^{235}U. There was an excess reactivity (due to control rod being withdrawn) of +0.110% $\Delta k/k$.

The β values used for the kinetics code used to calibrate the control rods are listed in Table I.A.20. These β values were supplied by the EBR-II Project and derived from spherical MACH-1 calculations.

TABLE I.A.20. Assembly 61, Delayed-neutron Fractions, ^{235}U Density Reduced

Isotope	Group-effective Delayed-neutron Fractions, units x 10^{-3}						
	1	2	3	4	5	6	Total
^{235}U	0.2290	1.2834	1.1327	2.4523	0.7712	0.1566	6.0252
^{238}U	0.0120	0.1260	0.1490	0.3570	0.2070	0.0690	0.9200
Sum	0.2410	1.4094	1.2817	2.8093	0.9782	0.2256	6.9452

ℓ = 4.47 x 10^{-7} sec; 1h/% = 433.5.

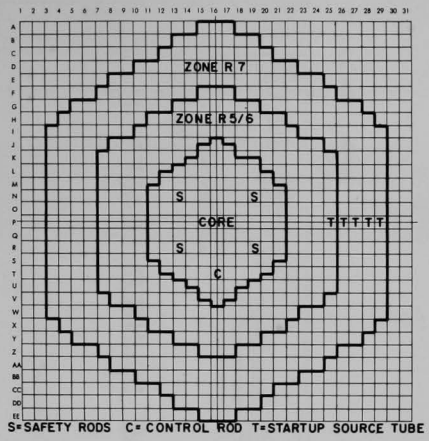

Fig. I.A.28

Assembly 61, Final Transition Step

(iv) Experimental Results, Assembly 61 (Final Transition Step)

(a) Proton-recoil Measurement of the Neutron Spectrum (G. G. Simons)

Three fast-neutron spectrum measurements were made in the ZPR-3 Assembly 61 loading shown in Fig. I.A.28. A 3/8-in.-dia hydrogen and a 5/8-in.-dia methane cylindrical proportional counter, positioned with their centers of active volumes 1 in. from the core centerline, were used in partially voided drawers in matrix positions 1-P-16, 1-P-11, and 1-P-9. Figure I.A.29 shows these drawers containing the two counters, preamplifiers, and core materials. Figure I.A.30 shows the material loadings for the different drawers.

The counters, calibration, and data analyses are discussed in Sect. I.A.2.a(i) of this report.

The three spectra are shown in Figs. I.A.31-I.A.33. The relatively hard spectrum combined with the high residual gamma-ray background present at the core center (1-P-16) made it impossible to measure the neutron spectrum below 2.2 keV.

(b) Radial Reaction-rate Traverses. The radial reaction rates were measured through the core axial center, which lies ~1/2 in. from the reactor interface, in the 1-P row. Counters traversed were $^{235}U(n,f)$, $^{238}U(n,f)$, $^{240}Pu(n,f)$, $^{239}Pu(n,f)$, and $^{10}B(n,\alpha)$.

(c) Axial Reaction-rate Traverses. Axial reaction rates were measured along core center in 1-P-16 and 2-P-16 matrix position. Reaction-rate measurements were also taken in a core drawer at the core-reflector interface (1-P-11 and 2-P-11). The drawer loading is the same

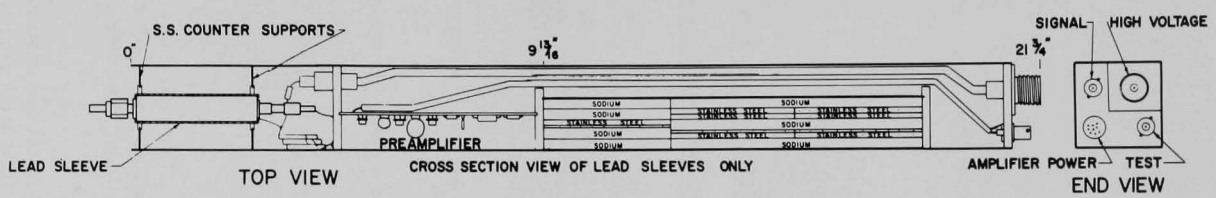

METHANE GAS FILLED PROTON RECOIL PROPORTIONAL COUNTER LOADED IN A MATRIX DRAWER

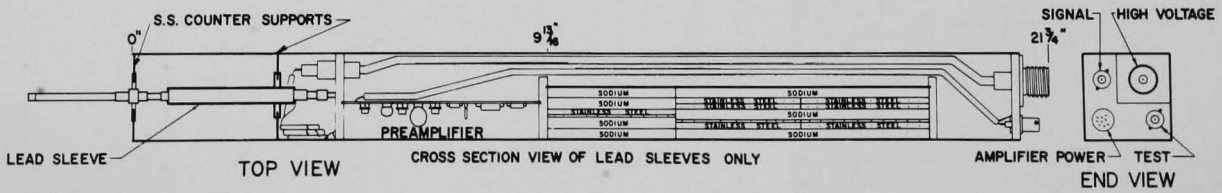

HYDROGEN GAS FILLED PROTON RECOIL PROPORTIONAL COUNTER LOADED IN A MATRIX DRAWER

Fig. I.A.29. Proportional-counter Configurations Used in ZPR-3 Assembly 61

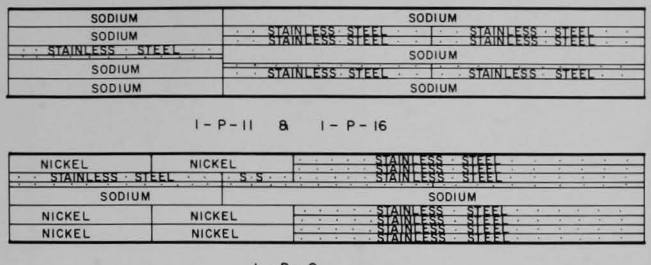

Fig. I.A.30. Proportional-counter Drawer Loadings for ZPR-3 Assembly 61

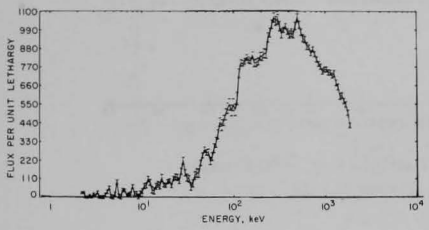

Fig. I.A.31. ZPR-3 Assembly 61 Neutron Spectrum Measured in Location 1-P-16 (core center) with the Proton-recoil Proportional Counters

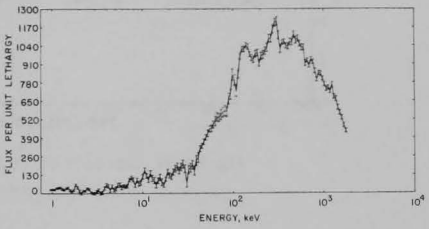

Fig. I.A.32. ZPR-3 Assembly 61 Neutron Spectrum Measured in Location 1-P-11 (core-reflector interface) with the Proton-recoil Proportional Counters

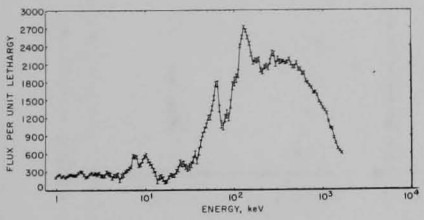

Fig. I.A.33

ZPR-3 Assembly 61 Neutron Spectrum Measured in Location 1-P-9 (reflector) with the Proton-recoil Proportional Counters

as shown in Fig. I.A.14 of the April-May Monthly Progress Report, ANL-7688, except that the natural-uranium column that replaced the 93% enriched-uranium column in the final transition step is next to the traverse slot shown. Counters traversed in both axial positions were $^{235}U(n,f)$, $^{238}U(n,f)$, $^{240}Pu(n,f)$, $^{239}Pu(n,f)$, and $^{10}B(n,\alpha)$. The results for the central core traverse are shown graphically in Figs. I.A.34-I.A.38.

(d) Irradiations. A series of foils and thermoluminescence dosimeters was irradiated at various parts of the assembly. The data are being analyzed.

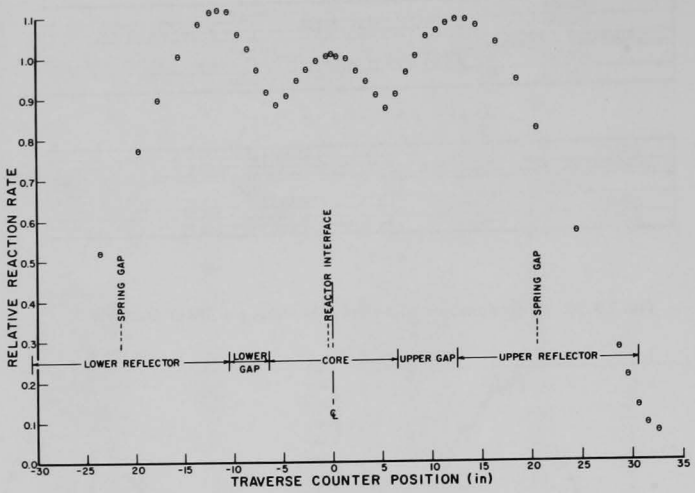

Fig. I.A.34. Assembly 61, Final Transition Step, ^{235}U Central Axial Reaction-rate Traverse in P-16

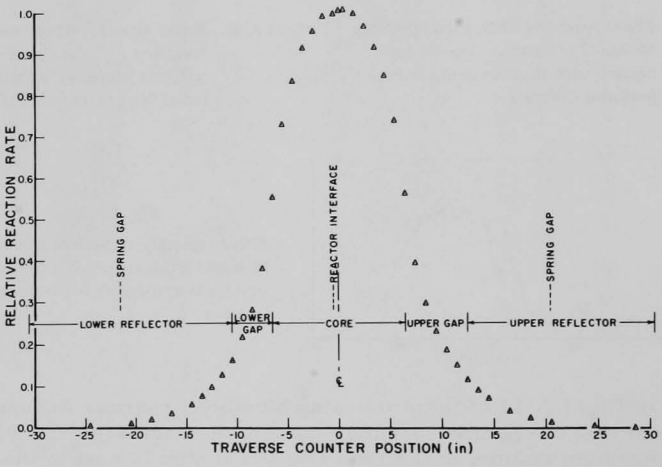

Fig. I.A.35. Assembly 61, Final Transition Step, ^{238}U Central Axial Reaction-rate Traverse in P-16

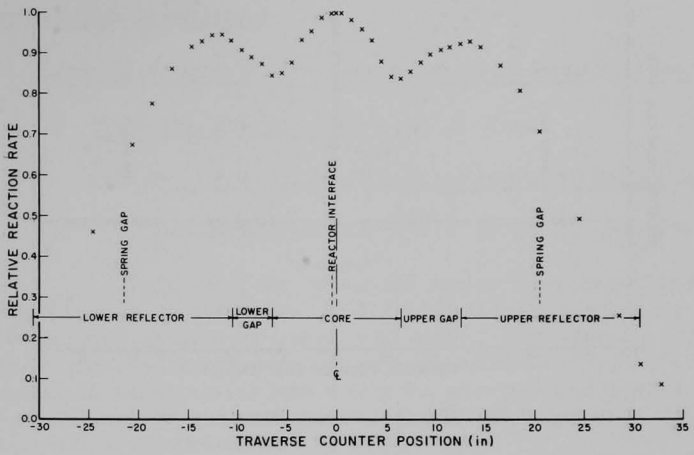

Fig. I.A.36. Assembly 61, Final Transition Step, ^{239}Pu Central Axial Reaction-rate Traverse in P-16

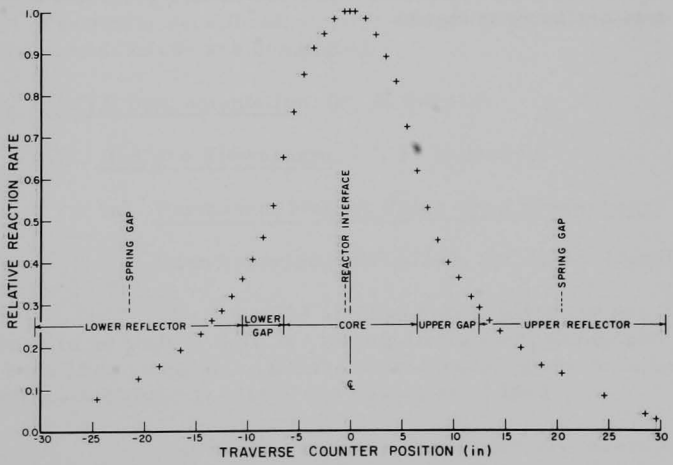

Fig. I.A.37. Assembly 61, Final Transition Step, ^{240}Pu Central Axial Reaction-rate Traverse in P-16

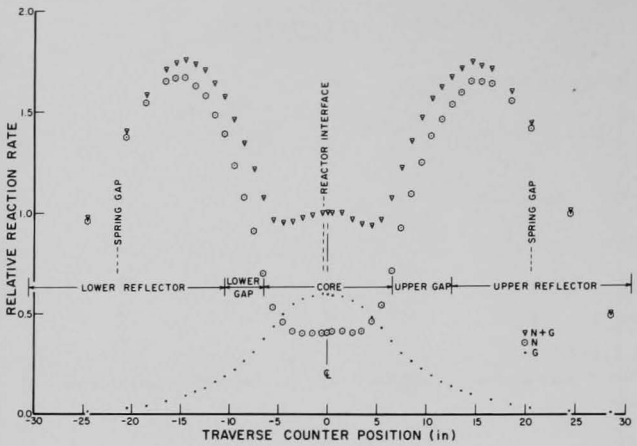

Fig. I.A.38. Assembly 61, Final Transition Step, ^{10}B Central Axial Reaction-rate Traverse in P-16

(e) Central Fission Ratios. Fission ratios were measured at the core center using the spherical back-to-back chambers. Fission rates of ^{233}U, ^{234}U, ^{236}U, ^{238}U, ^{235}U, ^{240}Pu, and ^{239}Pu were measured, and the data are being analyzed.

B. Component Development

1. Instrumentation and Control

a. Instrumentation Development for Instrumented Subassembly

(i) Fuel-Pin Thermocouples (A. E. Knox)

(a) In-pile Tests in EBR-II Instrumented Subassembly

Last Reported: ANL-7679, pp. 26-27 (Mar 1970).

Three of the seven fuel center thermocouples (FCTC 2, FCTC 3, and FCTC 17) in the Test XX01* EBR-II Instrumented Subassembly have failed because of open-circuited lead wires. Time-domain reflectometer measurements of the thermocouples indicate that the failures occurred in the drywell of the extension tube where the sheathed and flexible lead wires are joined. Two coolant thermocouples (OTC 6 and PSTC 16) appear to have failed in a similar manner.

Current evidence indicates that the four fuel center thermocouples (FCTC 1, FCTC 7, FCTC 10, and FCTC 15) positioned in the high-temperature regions of the subassembly are still operable. However, the extent of possible decalibrations will not be fully evaluated until post-irradiation examinations are completed.

b. FFTF Instrumentation (R. A. Jaross)

(i) In-Core Flowsensor (T. P. Mulcahey)

(a) Permanent Magnet Probe-type Flowsensors (F. Verber)

Last Reported: ANL-7688, pp. 66-68 (April-May 1970).

The Type 304 stainless steel parts for two Type A $4\frac{1}{4}$ flowsensors to be built at ANL for testing in the Core Component Test Loop (CCTL) have been completed, and the permanent magnets have been temperature-stabilized at 1300°F for operation at 1150° F.

A detailed assembly and testing procedure has been prepared, and assembly of the first flowsensor has started.

---

*Erroneously reported as Test XX02 in ANL-7679, p. 26.

(b) Eddy-current Probe-type Flowsensors (J. Brewer)

Last Reported: ANL-7688, p. 69 (April-May 1970).

Eddy-current Probe No. 10 was fabricated, and subjected to oscillating-rig tests at room temperature. It was then installed in the CAMEL for flowtests and tests related to failed fuel monitoring.

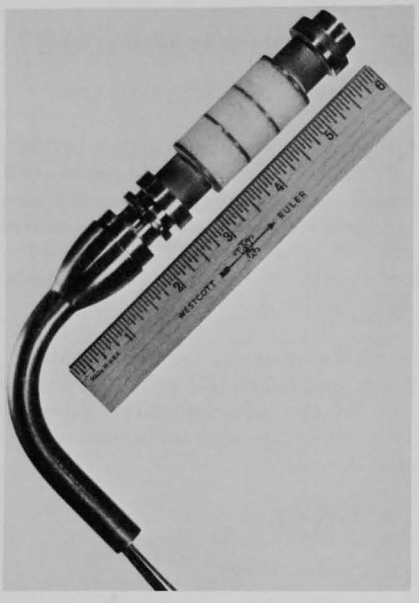

Fig. I.B.1. Eddy-current Probe No. 10, without Type 304 Protective Cover

With reference to Fig. I.B.1, Probe No. 10 features three coils wound around, and spaced 0.0625 in. apart on an Inconel 625 bobbin that was plasma-sprayed with an 0.002- to 0.004-in.-thick coat of alumina insulation. Each coil measures 0.695 in. ID, 0.890 in. OD, 0.500 in. wide, and consists of 169 turns, in six layers, of 0.015-in.-dia gold wire with Secon "D" ceramic insulation. The coils were wet-wound with Ceramabond 503 cement, with 200 g of tension applied to the wire.

An aluminum oxide-insulated, two-conductor, twisted cable (0.090 in. OD), with Type 304 stainless steel conductors and sheath material, is used for secondary signal leads. A similar cable (0.125 in. OD) is used for driver or primary leads. Each cable is 45 in. long. A Chromel-Alumel thermocouple is welded to the bobbin rear support.

In an oscillating-rig test with a drive current of 300 mA rms and 500 Hz, Probe No. 10 exhibited a sensitivity of 0.405 mV rms/ft-sec.

Preliminary tests in the CAMEL indicate that the flow sensitivity of Probe No. 10 will be in the range of 0.5-0.6 mV rms/ft-sec under the following conditions: drive current of 500 mA rms and 1000 Hz; sodium velocity from 1 to 10.5 ft/sec; and sodium temperature from 310 to 1000°F. The temperature range probably will extend to 1400°F. Figure I.B.2 shows the probe output signal versus sodium velocity. Reproducibility is good.

(c) Radiation Tests of Permanent Magnets (G. E. Yingling)

Last Reported: ANL-7688, p. 70 (April-May 1970).

Equipment for decanning and performing measurements on Alnico V, VI, and VIII magnets irradiated in EBR-II was removed from

the hot-cell mockup, reassembled in the hot cell, and checked out with a set of six standard magnets (2 x 4 in., L/D--8). There was good agreement between measurements made in the mockup and the hot cell.

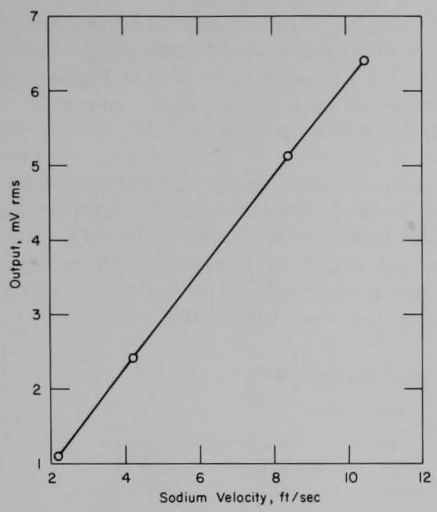

Fig. I.B.2. Signal Output of Eddy-current Probe No. 10 vs Sodium Velocity at 810°F. Probe drive current = 500 mA and 1000 Hz.

Next, the encapsulated magnets were transferred from their shielded container to the hot cell. This transfer was performed in a carefully controlled manner to ensure against capsule mixup. Later, it was found that all but one capsule number were distinguishable through the hot-cell periscope.

The magnets were decanned with a specially designed cutoff machine constructed of brass aluminum to prevent damage to the magnets. Immediately upon being removed from their respective capsules, each magnet was placed in its proper storage location in the hot cell.

Thus far, two sets of room-temperature moment measurements have been completed on all magnets with excellent repeatability. Disturbances of the ambient magnetic field due to movement of large metal objects in the cell have been minimal. Comparisons between pre- and postirradiation moments (with reference to the preirradiation moment) for each magnet yielded the following results:

Alnico	L/D	Change, %	Spread	
VIII	8	3.9	4.2	2.8
VI	8	-2.3	-4.0	-0.8
V	8	-0.6	-1.4	0.8
VIII	4	3.8	4.2	2.6
VI	4	-0.06	-2.1	1.7
V	4	1.0	-1.3	2.7
VIII	2	4.3	6.3	1.6
VI	2	2.8	-3.5	8.6
V	2	1.2	-7.1	6.3
VIII	1	5.5	7.3	3.4
VI	1	6.3	12.7	0.57
V	1	3.3	-3.4	11.8

(d) Flowsensor Tests for Failed Fuel Monitoring (J. Brewer)

Not previously reported.

Tests have been conducted in the CAMEL to determine the response of both eddy-current and permanent-magnet probe-type flowsensors to small injections of argon gas. This work is in direct support of the FFTF program to detect and locate failed fuel assemblies. Argon is used to simulate fission-gas release from a fuel assembly.

Table I.B.1 lists some early results of tests with the eddy-current (E-C) Probe No. 10 and a Type A-4 permanent-magnet (P-M) flowsensor. Signals from the E-C probe were fed through an HP 3400 A True rms meter ac-to-dc converter to one pen of an Electronik 19 two-pin strip-chart recorder. The converter has a response time of 1 sec. Signals from the P-M probe were fed directly to the other pen of the recorder.

TABLE I.B.1. Flowsensor Response to Gas Injections in the CAMEL

Sodium temp.: 800°F
Sodium velocity: 4 ft/sec in flowsensor annulus
Sodium flow rate: ~135 gpm

Output, mV, rms		Gas Injection		Time between Injections, min	Signal Deviation, mV rms		Increase in Response after Injection, %	
E-C No. 10	Type A-4 P-M	Rate, cc/sec	Duration, sec		E-C	P-M	E-C	P-M
2.25	1.93	75	2	20	0.25	0.03	11.1	1.55
2.27	1.93	75	4	20	0.26	0.05	11.45	2.59
2.40	1.95	75	6	150	0.32	0.12	13.3	6.16
2.40	2.05	100	2	20	0.40	0.1	16.65	4.88
2.43	2.10	100	4	12	0.37	0.04	15.2	1.91
2.43	2.12	100	6	12	0.37	0.05	15.2	2.36
2.45	2.08	33.3	2	20	a	0.1	-	4.81
2.45	2.13	33.3	2	12	a	0.04	-	1.88
2.45	2.13	33.3	4	12	0.30	0.05	12.25	2.35
2.50	2.15	33.3	3.25	8	0.28	0.03	11.2	1.39
2.60	2.14	33.3	3	12	0.30	0.06	11.5	2.80
2.58	2.12	33.3	2	10	0.20	0.05	7.75	2.36
2.55	2.13	33.3	2	7	0.20	0.02	7.84	0.94
2.55	2.12	50	2	12	0.30	0.05	11.75	2.36

[a]Indicates a slight negative deviation.

The results are not yet fully understood. The E-C probe appears to exhibit a threshold limit of detection and, above this, a saturation limit. Response time to gas injection appears to be 1 or 2 sec. It is expected that use of better electronic detection will yield improved results, especially with the E-C probe. Tests will continue.

c. Neutron-Detection Channel Development
(T. P. Mulcahey/G. F. Popper)

(i) Wide-range Circuits and Systems (G. F. Popper)

Last Reported: ANL-7595, pp. 37-39 (July 1969).

Test data taken at the EBR-II to compare the Gulf General Atomic (GGA) Wide-range Neutron Monitoring System with the EBR-II Linear Channel No. 7 compensated ion chamber (CIC) have been analyzed.

The test was performed because: (1) the EBR-II had been in a shutdown condition for approximately 60 days, and the gamma-flux level in the J-type thimble had decayed to less than 20 R/hr; (2) the GGA system had been returned to the manufacturer for correction of certain circuit defects found by ANL in September 1969; and (3) the GE NA-04 fission counter for the GGA system had been relocated from the J-2 to the J-1 thimble.

Figure I.B.3 compares the respective system responses during initial startup on December 16, 1969. Note that both the CIC (GE NA-09) and the Wide-range Channel Lams (Log Average Magnitude Squared) Campbelling signals give about two decades of overlap between the log count rate (LCR) signal and the Intermediate Range Channel in question. Also, observe the low CIC current ($<10^{-11}$ A) and the ~10^{-4}% power LAMS signal.

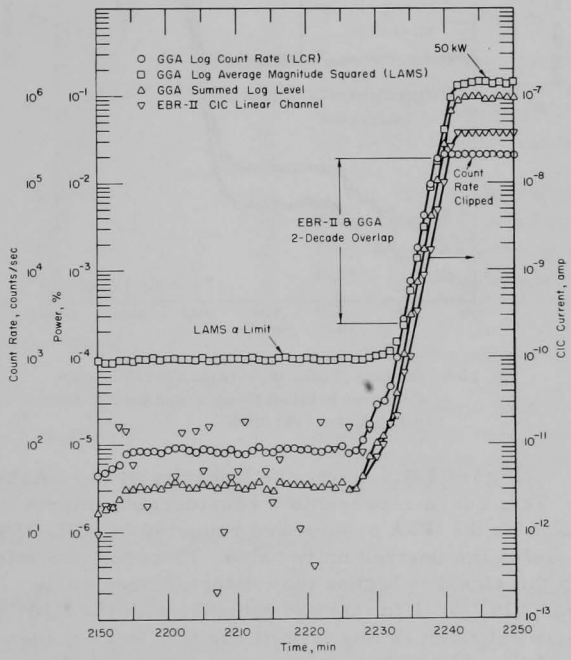

Fig. I.B.3. Response of GGA Wide-range Neutron Monitor Compared to EBR-II Compensated Ion Chamber during "Clean" Startup (20 R/hr)

Figure I.B.4 shows a similar comparison during a startup on December 20, 1969, after an unexpected shutdown. The reactor had been taken to power slowly (5 MW/hr) beginning on December 17, 1969; therefore the gamma level represents less than two days of full-power operation. Note the apparent gamma component in both the CIC and LAMS signals.

However, on comparison with Fig. I.B.3, the CIC lower limit shows an increase of over a decade and a half with almost no overlap, while the LAMS signal gives essentially the same overlap.

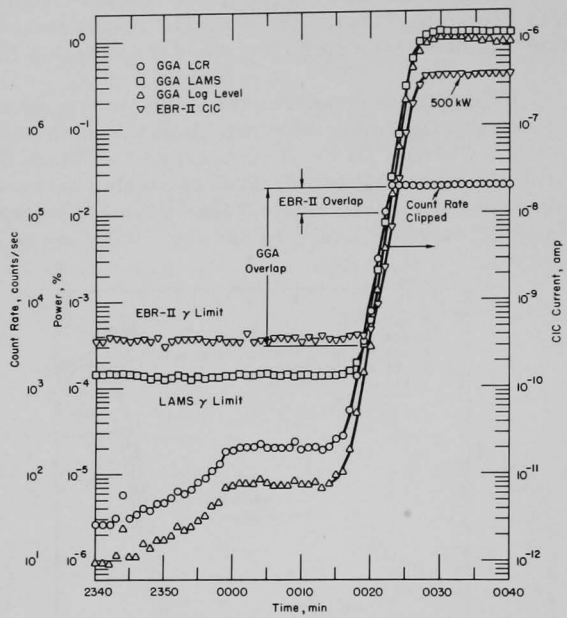

Fig. I.B.4. Response of GGA Wide-range Neutron Monitor Compared to EBR-II Compensated Ion Chamber during Restart (10^4 R/hr)

Figure I.B.5 shows the linearity of the LAMS signal with neutron flux. This curve represents a considerable improvement over previous data taken on the GGA system and reported in ANL-7595. The slope of the curve yields the desired unity value. However, the minimum base noise level in the signal is higher than detected previously. The current power reading ($<10^{-4}$%) is in marked contrast with the $<10^{-5}$% reading obtained in July 1969 before any circuit changes were made. Further investigation of the shift in base noise level will be made.

The Milletron Wide-range Neutron Monitor was installed at the EBR-II in April 1970. However, obvious electrical noise conditions in the counting range must be investigated and corrected before adequate system performance can be assured.

(ii) Out-of-Core Detectors, Cables, and Circuits

(a) Evaluation of Status. Failures at Westinghouse, first of detectors in June 1969, and then cables in November 1969 and April 1970, have delayed testing of acceptable high-temperature detectors.

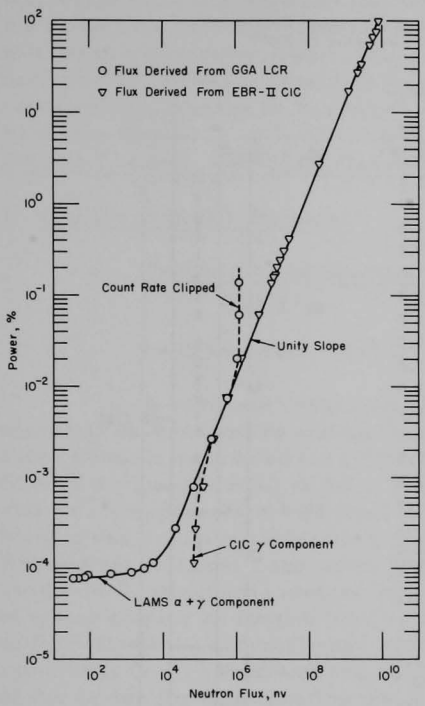

Fig. I.B.5. Characteristics of GGA LAMS Signal

Westinghouse is currently rebuilding and testing the CIC's and LASL detectors. The rebuilt LASL detectors failed in early May 1970 because of cable breakdown. Both types of detectors show promise.

Work on the Westinghouse 725°F fission counters has been deferred pending test results on the LASL fission counters.

The Reuter-Stokes (R-S) LASL detectors delivered to ANL in May 1970 do not appear to meet specifications; low insulation resistance is the primary consideration. Gamma testing of the R-S LASL detectors is essentially complete.

Reuter-Stokes has started high-temperature tests of the 725 and 1200°F fission counters; they are also rebuilding the CIC's.

2. Fuel Handling, Vessels, and Internals

a. Core Component Test Loop (CCTL) (R. A. Jaross)

Last Reported: ANL-7688, pp. 72-73 (April-May 1970).

(i) Operation of Loop to Test Second FFTF Fuel Assembly. Table I.B.2 lists the initial set of Mark-II fuel-assembly flow rate and pressure-drop data taken on May 22.

The temperature of the CCTL was then increased slowly from 400°F on May 22, to 750°F on May 26. At that time, a second sodium sample was taken for chemical analysis; results indicated carbon concentrations of 52, 28, and 58 ppm. Since the allowable limit is 20 ppm,

a third sodium sample was taken for check analysis on June 3, with the system operating at 800°F. This analysis indicated 13 ppm carbon. The difference in carbon content between the second and third samplings has been attributed to deficiencies in the analytical equipment and techniques.

TABLE I.B.2. Sodium Flow Rate-Pressure Relationship for FFTF Mark-II Fuel Assembly at 400°F

SODIUM FLOW RATE, gpm	PRESSURE, psig* TAP NO. 1	TAP NO. 2	TAP NO. 3	TAP NO. 4
76	2.2	2.0	1.5	1.2
100	4.0	3.3	2.0	1.4
136	6.1	5.0	2.5	1.5
178	8.1	6.2	2.3	0.8
214	11.5	8.7	3.3	1.0
257	15.8	11.8	4.4	1.4
288	19.5	14.5	5.3	1.7
334	25.2	18.6	6.9	2.2
373	31.6	23.4	8.6	2.8
410	38.0	28.1	10.3	3.4
455	46.5	34.0	12.5	4.1
447	46.4	33.9	12.4	4.0
379	32.8	24.1	8.6	2.8
352	28.4	20.9	7.4	2.3
311	22.6	16.7	5.9	1.8
284	18.9	13.9	4.8	1.3
246	14.2	10.6	3.6	1.0
205	10.0	7.4	2.5	0.6
131	4.2	3.2	1.0	0.2
72	2.0	1.7	1.4	1.2
119	5.1	4.2	2.2	1.4
142	9.0	6.7	2.4	0.7
248	15.2	11.3	4.1	1.2
311	23.2	17.1	6.2	1.9
332	32.8	23.8	8.6	2.7
434	43.7	31.9	11.6	3.7
465	49.6	36.3	13.2	4.3
404	38.5	28.2	10.2	3.2
338	27.8	20.5	7.3	2.3
281	19.2	14.2	4.1	2.1
220	12.0	9.0	3.2	1.1
155	6.5	4.8	1.7	0.5
97	2.6	2.0	0.6	0.2

*CORRECTED TO 0 psig AT NO FLOW

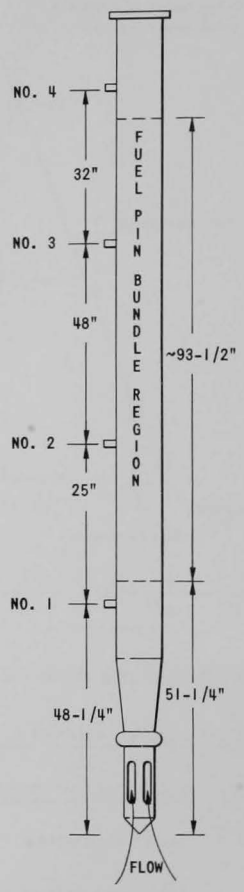

Operation of the CCTL has since been increased to a system temperature of 1050°F and sodium flow rate of 525 gpm. Some minor difficulties have been encountered. For example, on June 5, a small sodium leak occurred at a drain valve; it was quickly repaired. Also, the vapor traps on the inert-gas system showed evidence of plugging; they were cleaned.

C. Sodium Technology

Beginning with this issue, the work usually reported under Sodium Technology will be reported only once every three months. This report will summarize the work carried on during a three-month period. At about the same time that this report is issued, the Sodium Technology Program will issue a quarterly report, which may be referred to for the same material but for more detail, description, and discussion. The quarterly report corresponding to this month's Reactor Development Program Progress Report is ANL/ST-2, Sodium Technology Program Quarterly Report, January, February, March 1970.

1. On-line Impurity Monitors

a. Evaluation and Improvement of Oxygen-Activity Meter (J. T. Holmes)

Last Reported: ANL-7679, pp. 31-32 (March 1970).

A complete oxygen-monitoring station, including four electrochemical oxygen meters and methods for testing the meter response and calibration, is scheduled for installation on the Radioactive Sodium Chemistry Loop (RSCL) at EBR-II by mid-FY 1971. Prooftesting of the station's components in radioactive sodium will follow. The oxygen meter being given prime consideration in this program is being developed by Brookhaven National Laboratory (BNL) and ANL. However, commercially available Westinghouse meters will also be tested. The cells in both types of meter employ an oxygen (air) reference electrode. On-line calibration at EBR-II will be accomplished by equilibration of refractory-metal specimens (e.g., vanadium) and analysis of their oxygen content. Design of the device for equilibrating metal specimens in the RSCL is being reviewed by EBR-II. A response test being considered involves the periodic changing of oxygen activity in the reference electrode.

Apparatus is being readied at ANL-Illinois to test and precalibrate both the BNL-ANL and Westinghouse electrochemical meters by on-line distillation analysis, and by equilibration and analysis of refractory-metal specimens.

b. Evaluation and Improvement of the Carbon-Activity Meter (J. T. Holmes, C. Luner, and N. Chellew)

Last Reported: ANL-7669, pp. 48-49 (Feb 1970).

A carbon-monitoring station and methods for testing the meter response and calibration are scheduled for field testing in the RSCL at EBR-II. The carbon meter being given prime consideration is the

United Nuclear Corporation (UNC) diffusion meter, although other meters (emf) will be considered. The components of the carbon-monitoring station are being tested at ANL-Illinois before installation at EBR-II.

The response of the UNC iron diffusion probe to NaCN or Na_2C_2 added to sodium stirred in a copper pot was investigated at 630°C. Trace amounts (< 1 ppm carbon in sodium) of each reagent considerably increased the carbon flux through the iron membrane. For NaCN, the carbon flux reached a maximum of 0.078 $\mu g/(cm^2)$ (min) at 10-20 ppm carbon, and further incremental additions did not change the flux. For Na_2C_2, the situation was somewhat more complicated, in that at the conclusion of the experiment some of the carbide had decomposed. As a result of the decomposition, only about 25-30 ppm carbon as Na_2C_2 could be found in the sodium. At this concentration, the flux was 0.12 $\mu g/(cm^2)$ (min), almost twice that obtained for 25-30 ppm carbon as NaCN.

The response of the UNC carbon probe to the presence of different potential construction materials was also tested at 630°C in the stirred pot of sodium. Type 304 stainless steel decreased the carbon flux, whereas a nickel or ferritic (1020) steel rod increased it. Molybdenum and molybdenum-30 wt % tungsten caused no change in the flux. Since a decrease in the flux is interpreted as being due to a lowering of the carbon driving force from the sodium, the stainless steel housing of the UNC carbon meter will probably change the carbon concentration of the sodium that contacts the probe. Accordingly, molybdenum will be tested as a linear material for an ANL-designed housing to be used with a UNC carbon probe.

Prooftesting of the UNC carbon meter in a small, pumped-sodium apparatus, the Test and Evaluation Apparatus (TEA), has recently begun. A number of parameters expected to affect the carbon flux are being investigated. An increase from 0.8 to 2.4% in the water-vapor content of the decarburizing gas (10% H_2-90% Ar) increased the flux fivefold at both 625 and 750°C. Increasing the flow of sodium past the probe from 0.08 to 0.17 gal/min increased the flux about 10%. No significant effect of temperature over the range 625-750°C was observed.

c. Evaluation and Improvement of the Hydrogen-Activity Meter (J. T. Holmes and D. R. Vissers)

Last Reported: ANL-7661, pp. 29-31 (Jan 1970).

(i) Hydrogen-Monitoring Station. The principal objective of this work is to develop a hydrogen-monitoring station for measuring hydrogen dissolved in primary and secondary sodium of LMFBR's. Research has been directed toward the design and construction of a hydrogen-activity meter. The meter consists of a nickel membrane, a pressure-readout unit,

and a vacuum pump for periodic pumpdown. The nickel membrane and the pressure-readout system are allowed to equilibrate with the hydrogen in the sodium. The equilibrium hydrogen partial pressure is then measured directly by the pressure-readout unit on the vacuum side of the membrane. The main requirement of this monitor is accuracy.

A prototype ANL hydrogen-activity meter has been built and installed on a gas-flow apparatus where it is being evaluated with standard hydrogen-argon gas mixtures. Preliminary studies with the meter indicate that the basic concepts of the meter are sound and that there are suitable pressure-readout devices available for this application. Equilibrium hydrogen pressures equivalent to a dissolved hydrogen content in sodium of 0.5-4 ppm have been measured with a Varian Millitorr gauge.

(ii) Detection of Leaks in Steam Generators. A monitoring system is under development for detecting leaks in LMFBR steam generators by the detection of the hydrogen produced in the sodium-water reaction. The principal requirements of this detection system are rapid response, sensitivity, and, to avoid unnecessary shutdowns, reliability.

Water leaking at 0.01 lb/sec in an LMFBR steam-generator module may cause rapid wastage of metal from tubes adjacent to the leak. To avoid propagation of damage, it would be necessary to shut down the steam-generator module within a few seconds to more than 1 hr after onset of the leak, depending on the leak rate, tube material and thickness, and other factors. It would be desirable to be able to detect water leaks as small as 10^{-4} lb/sec, which is safely below the leak rate at which significant wastage occurs. To do this for the largest LMFBR steam-generator modules, it would be necessary to measure an increase of about 0.004 ppm hydrogen in the sodium. At a level of 0.1 ppm hydrogen in sodium, this amounts to a 4% increase in hydrogen concentration.

The monitoring system under development appears to meet the above requirements. It is based on the detection of change in hydrogen concentration in sodium by the change in the rate of hydrogen diffusion through a nickel membrane immersed in the sodium. A vacuum of 10^{-6} to 10^{-8} Torr is drawn on the membrane at a steady rate by an ion pump. The partial pressure of hydrogen on the vacuum side, a measure of the hydrogen flux and the hydrogen activity in the sodium, is determined by a mass spectrometer or by measuring the current to the ion pump. In the present work, the sensitivity and reliability of these detectors are being improved, and a complete leak-detection and alarm system is being developed.

The response time of the monitor depends chiefly on the rate of hydrogen diffusion through the nickel membrane. A transient-diffusion calculation indicated that 10 sec after a sudden change in the

hydrogen concentration in the sodium, the change in the hydrogen flux from the membrane would be 70% of the eventual total change in flux for a 10-mil-thick nickel membrane at 500°C. Thus, high-speed response is attainable with this detection system.

A monitor of the above description has been operated for over 1,000 hr in a pumped-sodium loop. A 10-liter/sec ion pump was used to draw the vacuum on the nickel membrane, and the current to the pump was monitored as an indication of the hydrogen flux. The activation energy for permeation of hydrogen through the membrane was found to be -12.9 kcal/mol, as compared to a published value of -13.16 kcal/mol. This close agreement indicates that the gas entering the pump was primarily hydrogen. With a stable high-voltage power supply to the ion pump, the noise on the recorded signal was about 0.15% for a hydrogen concentration in sodium of about 0.5 ppm, which indicates that this detection system has adequate sensitivity and a high signal-to-noise ratio.

2. Analytical Program

a. Analytical Standards Program (F. Cafasso, R. Meyer, M. Barsky, and S. Skladzien)

Not previously reported.

The objective of the analytical standards program is to formulate a set of standard methods that meet the analytical requirements of the national sodium-technology program. ANL has the responsibility of coordinating this program, as well as participating in it.

Drafts of two program plans have been completed: a Reactor Standards Program Plan and a National Standards Program Plan. In both plans, existing methods (interim methods) will be certified to meet immediate analytical needs; at the same time, new methods will be developed to meet long-term needs.

Full participation by ANL in development and testing of methods requires that our analytical capabilities be increased. Accordingly, recent effort has been directed toward the procurement and construction of various equipment items that are needed.

b. Development of Reference Analytical Methods for Oxygen, Carbon, and Nitrogen (R. Meyer, M. Roche, and L. E. Ross)

Last Reported: ANL-7661, pp. 27-29 (Jan 1970).

The sodium analytical group is conducting experiments to determine the suitability of proton activation analysis as a reference method for determining total oxygen, carbon, and nitrogen in sodium.

A thin-window nickel cell, used for bypass sampling and subsequent irradiation of sodium, and a counting vessel for the activated sodium are being fabricated. Equipment is being assembled and tested for heating and inductively stirring the sodium during bombardment.

A series of bombardments, using NaF pellets spiked with Al_2O_3, C, AlN, or B, has been completed. These were done to determine the sensitivities of the analyses, to investigate interfering reactions, and to find ways of minimizing activation of sodium. Oxygen interferes with the carbon analysis, and boron with the nitrogen analysis. Means have been found for correcting for these interferences when O/C ratios are less than 10 and B/N ratios are no greater than one. The background activity from ^{24}Na, produced by reaction of sodium with deuteron and neutron contaminants in the proton beam, has been reduced. Deuterons were eliminated by means of a stripper foil and magnet; neutron production, from reaction of the beam with the beam tube, was minimized by beam focusing. Projected sensitivities with this low ^{24}Na background are 50 ± 25 ppb O, 20 ± 10 ppb C, and 2 ± 1 ppb N.

The next step in this investigation, namely, the determination of oxygen, carbon, and nitrogen in metallic sodium, will proceed when fabrication, assembly, and testing of the necessary equipment is finished.

c. Analysis of Nonmetallic Impurities in Sodium by Equilibration of Refractory-metal Wires

Last Reported: ANL-7632, pp. 44-45 (Oct 1969).

Investigation of the equilibration method for measuring the activity of oxygen at low concentrations in liquid sodium is continuing. The equilibrium distribution of oxygen between vanadium and sodium has been reported in a manuscript entitled "Investigation of the Thermodynamics of V-O Solid Solutions by Distribution Coefficient Measurements in the V-O-Na System," which will be submitted for publication in Metallurgical Transactions. A manuscript describing the experimental technique will be submitted for publication in Nuclear Applications.

(i) Development as a Standard Analytical Method (R. J. Meyer and L. E. Ross)

In this procedure, a refractory-metal wire is exposed to sodium until the equilibrium for oxygen between the wire and the sodium has been attained. The oxygen concentration of the wire is measured, and the oxygen concentration of the sodium is inferred from previous calibrations. Vanadium wires are most useful at temperatures above 600°C. Thus, reactor application will require a side loop operating above this temperature. Calculations and preliminary experimental results indicate that niobium and tantalum wires may extend the useful range and/or lower the equilibration temperature required.

(ii) Oxygen in EBR-II Primary Sodium (T. Kassner and D. L. Smith)

A series of refractory-metal wires (V, V-10 wt % Cr, V-20 wt % Cr, and Nb) was immersed in the primary sodium of EBR-II at ~510°C for 9 days. Analysis of the wires for oxygen showed that the oxygen concentration in the sodium was >0.8 ppm, which is the maximum concentration measurable at 510°C.

d. Analytical Methods for Metallic and Halide Impurities in Sodium (R. J. Meyer, H. Edwards, and L. E. Ross)

Last Reported: ANL-7679, pp. 30-31 (Mar 1970).

There is need for a rapid survey method that simultaneously determines several metallic impurities in reactor sodium. Our current effort includes a search for and evaluation of methods to analyze flowing molten sodium directly, methods for examining aqueous solutions of a sample, and methods that use a preconcentration step such as distillation.

The only direct method under consideration is ultrasonic nebulization of liquid sodium to produce a metal-dust aerosol. This is then passed through an induction-coupled plasma, and the resultant spectrum is analyzed by emission spectroscopy. The combination of ultrasonic agitation and total consumption of the sample should counteract sampling inaccuracies due to segregation of impurities. An experimental evaluation of the method is planned.

Vacuum distillation is being tested as a means of preconcentrating metallic impurities. This would be followed by emission-spectroscopic or X-ray fluorescence analysis of the residue.

3. Fission Product and Cover Gas Technology

a. Definition of Radioisotope Problem Areas (W. E. Miller and W. Mecham)

Not previously reported.

During reactor operation, the primary coolant system of an LMFBR becomes highly radioactive from sodium activation products (^{24}Na and ^{22}Na), from fission products that may be introduced into the sodium, and from activation products of core structural materials. These radioactive isotopes impose many problems on plant design, operation, and maintenance. A report is being prepared that will define specific problems created by the radioactivity in the primary coolant system and cover gas, and that will assign priorities to R&D program dealing with these problems.

b. Data-analysis Methods for Determining Fuel Failures (W. E. Miller and N. Chellew)

Last Reported: ANL-7669, p. 50 (Feb 1970).

Fuel failures in sodium-cooled reactors can be classified into several failure types. Innocuous failures allow fission gases to escape from fuel pins. A much more serious condition arises, however, when a failure results in penetration of sodium coolant into the interior of the cladding. Contact of the oxide fuel with sodium causes swelling, and this enlarges the original defect. Failures in which sodium has ready access to the oxide matrix can eventually result in fuel washout.

Recent work in the area of oxide fuel-sodium compatibility indicates that failures in which sodium contacts oxide fuel are likely to lead to serious fuel swelling and failure propagation. The responses of fission-gas monitors or delayed-neutron detectors (existing failed-fuel detection equipment) do not appear to be sensitive to this condition of failure. Therefore, methods for detecting failures that allow sodium to contact fuel oxide are needed.

A method being considered for characterizing this type of failure is the detection of cesium, rubidium, iodine, and/or tellurium in the sodium coolant. Examination of irradiated oxide fuel has shown that these fission products have a strong tendency to migrate toward the cladding and should therefore be readily available for sodium leaching when liquid sodium contacts the oxide. The properties of cesium, rubidium, iodine, and tellurium isotopes (volatility, half-lives, precursor half-lives) are being examined to assess the feasibility of the method.

c. Development of Radioisotope-monitoring Method (W. E. Miller, N. Chellew, and P. Vilinskas)

Not previously reported.

A knowledge of the concentration of cesium, rubidium, iodine, or tellurium isotopes in primary sodium promises to yield much information regarding the condition of failed fuel in a reactor. Direct sodium assay by gamma spectroscopy is complicated by the presence of the overwhelming background created by activated sodium. Therefore, means are being sought which will give a high degree of separation ($\sim 10^6$) of these elements from sodium and which are adaptable to on-line automated instrumentation. Analysis of the problem reveals that a small, multistage, vacuum-distillation apparatus will give the degree of separation of cesium from sodium that is required. One concept uses a single-loop continuous on-line distillation apparatus. The feed rate to the unit would be about

0.5-1 liter of sodium per minute, of which about 1% would be vaporized. Apparatus is being procured for investigating multistage distillation separations of cesium and rubidium from sodium. A mockup of the apparatus, which uses water as the motive and evaporating fluid, has been built and operated in preliminary tests.

d. Sampling of Radioactive Sodium (W. E. Miller and P. Vilinskas)

Last Reported: ANL-7669, pp. 49-50 (Feb 1970).

The designs of the LASL and EBR-II Project distillation samplers are under review. Alternative means of removing the distillation cup, new ways of producing the vacuum and collecting the distillate, and means of dealing with high sodium pressures at the sampler location will be examined. Equipment for these distillation-sampler studies is being procured.

e. Nature and Control of Sodium Aerosol Formation (W. E. Miller and R. Kessie)

Last Reported: ANL-7661, pp. 32-33 (Jan 1970).

Currently operating sodium-cooled reactors with a temperature of 400°C or less at the interface between the sodium and the cover gas have not encountered serious problems due to sodium aerosol formation. Results of preliminary qualitative experiments indicate that a much more serious problem will exist when the interface temperature is raised to 500-600°C. A slight drop in temperature as the sodium vapor leaves the interface will result in aerosol formation. The most practical method of controlling the aerosol appears to be by filtration and recirculation of clean cover gas to those regions containing equipment that would be adversely affected by the presence of sodium aerosol.

Techniques for measuring sodium aerosol concentration and particle size are to be tested. When this work is completed, filtration methods for controlling sodium aerosol will be investigated.

4. Materials-Coolant Compatibility

a. Studies on Carbon Transport in Sodium-Steel Systems (T. F. Kassner, K. Natesan, and J. Y. N. Wang)

Last Reported: ANL-7661, pp. 25-27 (Jan 1970).

The objectives of this work are to elucidate the reactions involving carbon transfer in sodium-steel systems. Reactions included are the loss of carbon from ferritic steels, with an accompanying decrease in

strength; the carburization of stainless steels, with an accompanying loss in ductility; and the interrelated changes of carbon content and chromium-alloying content of stainless steel. Calculations (at 500-800°C) based upon thermodynamic data have been made to describe the variations in carbon activity of austenitic stainless steels and ferritic low-alloy steels with varying carbon concentration in sodium. The results of these calculations have made it possible to describe the circumstances under which transfer of carbon occurs from one material to another because of different compositions or temperatures. This study indicates that for a given concentration of carbon in austenitic stainless steels, carbon activity is strongly dependent upon chromium concentration. Hence, the loss of chromium by mass-transfer dissolution will cause the loss of carbon by increasing the local carbon activity.

To increase the reliability of the computed data, a wide range of carbon activities in Fe-Cr-8 wt % Ni alloys, with chromium contents ranging from 0 to 22 wt %, has been measured. Each experiment produces data that enable construction of a plot of total carbon content of alloys, as a function of chromium concentration, at constant carbon activity. The ratio of the carbon concentration at 18 wt % Cr to that at 0 wt % Cr (in an Fe-Cr-8 wt % Ni alloy) varies from about 6 to 11 at 900°C, depending upon the carbon activity in the alloy. Data are not yet available at lower temperatures (down to 600°C), primarily because of the longer equilibration times required.

A few measurements of the equilibrium distribution of carbon between sodium and austenitic stainless steels at 600 and 700°C have been made. Preliminary indications are that the equilibrium calculations will be confirmed.

Preparations are under way to measure the diffusion coefficient of carbon in Fe-Cr-Ni austenitic alloys and in Fe-Cr-Mo ferritic alloys. Such information can be used directly to evaluate rates of carbon transport and carburization-decarburization problems.

Preliminary measurements have been made of the carburizing potential of carbon-bearing species (dissolved in sodium) toward Fe-8 wt % Ni and Fe-Cr-8 wt % Ni alloys. The incomplete results suggest that the carburizing potential of the cyanide ion is considerably less than that of the species produced in the dissolution of graphite in sodium.

b. Candidacy of Vanadium Alloys for Cladding LMFBR Fuels
(T. F. Kassner and D. L. Smith)

Last Reported: ANL-7655, p. 53 (Dec 1969).

The objective of this program is to develop enough understanding and information so that a first assessment of the adequacy of vanadium alloys as cladding for LMFBR fuels can be made.

Rotating-disk corrosion studies have shown that at 500 and 600°C and at oxygen concentrations above that required to form a vanadium oxide, vanadium specimens lose weight at a constant rate. The linear corrosion rates vary with the square root of the velocity above a low threshold velocity, i.e., rotational speed. This result indicates that over a wide range of velocities, the rate of dissolution is controlled by diffusion in the liquid sodium. It is not evident from the present results whether the limiting process is the diffusion of oxygen toward the metal or the diffusion of corrosion-product species away from the surface. At a specified rotational velocity, the corrosion rate shows an approximately linear dependence on the concentration of oxygen in sodium. On the basis of the data available, the rate extrapolates to zero at the oxygen concentration below which vanadium oxide will not form. The practical significance of the results is that, for the oxygen concentrations used (viz., 5-20 ppm), the corrosion rates are too high to allow use of vanadium as fuel cladding.

An investigation of the effect of chromium addition on the activity and solubility of oxygen in vanadium has continued. The oxygen concentration in the alloys is significantly less than in unalloyed vanadium when equilibrium with given oxygen concentrations in sodium is established. The distribution coefficients are reduced by factors of 2, 5, and 8, respectively, by adding 10, 15, and 20 wt % chromium to vanadium. This result suggests that the V-Cr alloys have a higher tolerance for oxygen (in sodium) before the formation of an oxide and the loss of materials would occur. The corrosion of V-Cr alloys may still be excessive in sodium containing oxygen at the levels that, realistically, must be expected in LMFBR coolant.

The addition of 0.3-1.0 wt % Ti to a V-15 wt % Cr alloy resulted in the absorption of greater amounts of oxygen during exposure to sodium containing oxygen. The titanium in the alloy combines with any oxygen present until all the titanium is oxidized to Ti_3O_2. Any additional oxygen is dissolved in the V-15 wt % Cr matrix up to the saturation point. On this basis, titanium in the alloy would not have any beneficial effect for service under reactor conditions.

5. Purification of Sodium

a. Characterization of Cold-Trapped Sodium (J. T. Holmes, M. D. Adams, and J. E. Draley)

Not previously reported.

Work has been initiated using on-line impurity monitors and sampling and analysis techniques for characterizing cold-trapped sodium. Sampling and analytical techniques for hydrogen and oxygen are being worked out on the Sodium Analytical loop with the aid of a cold trap. A new

Apparatus for Monitoring and Purifying Sodium (AMPS) is in the conceptual stages of design. AMPS will rely heavily on the use of on-line impurity monitors for determining how cold-trap operating conditions affect the quality of the sodium. Construction of AMPS will be started in early FY 1971.

A plan is being developed to measure the total burden of impurities in a primary-system cold trap which was used at EBR-II between April 1963 and June 1968. Of special interest will be measurement of tritium to help establish a tritium material balance at EBR-II. The decision on whether to carry out the plan will be made after a cost estimate has been developed.

b. Identification and Removal of Particulate Matter in Sodium (J. E. Draley)

Last Reported: ANL-7669, pp. 47-48 (Feb 1970).

Filtration experiments aimed at establishing criteria for the control of particulate matter in LMFBR sodium are under way. Procedures are first being developed with the aid of a pumped-sodium loop (Type 347 stainless steel) before application at EBR-II. Two filtration experiments were completed following the use of the loop (in another program) for materials testing of vanadium alloys and stainless steels in sodium.

In the first experiment, a 1/4-in. layer of cobalt powder (3-4 μm) on a stainless steel filter disk (5-μm porosity) was used as a filter. The filter was located ahead of a cold trap operating at 130°C on a bypass line. During 27 hr of filtering sodium at 350°C, the flow rate decreased continuously. Spectroscopic analysis of material collected on the filter showed the presence of V, Cr, Ni, Cu, and Fe. Of these, only V and Cr were present in amounts greater than in the cobalt powder. The second experiment lasted for 7 days and used the same stainless steel filter, but without the cobalt powder. A fine, brown powder recovered from the filter yielded a complex, unidentified X-ray diffraction pattern similar to those of hydrated mixed sodium aluminum silicates. Spectroscopic analysis showed V, Fe, Si, Cu, and Ti (whose origins can be accounted for) and Al and Sn (whose origins are unknown).

c. Development of a Continuous Radioactive Contaminant Removal Process (H. M. Feder and C. Postmus)

Last Reported: ANL-7661, p. 32 (Jan 1970).

The concept that a semibatch solvent-extraction system, installed in a bypass loop and operated at ~150°C, might provide a method for the continuous purification of coolant sodium in a fast breeder reactor is

being evaluated. To find a suitable solvent, selected alkanes, alkylated aromatics, alkyl ethers, amines, phosphines, amides, and nitriles were tested for stability toward sodium at 150°C. Mineral oil, n-decane, and N,N-diethylaniline were stable after 100 hr in the presence of stainless steel. N,N-diethylaniline was chosen for further investigation. Preparations are being made for long-term testing of the carburization potential of flowing sodium that has been in contact with diethylaniline at 150°C.

Determination of the stabilities of certain covalent transition metal complexes, while dissolved, toward reduction by sodium at 150°C constitutes another phase of the work required for a logical development of the sought-after process. In this connection, ferrocene (biscyclopentadienyl iron) was selected for testing. The effect of solvent was found to be important; reduction of ferrocene to metallic iron proceeded readily when it was dissolved in mineral oil, but not at all when dissolved in N,N-diethylaniline.

6. Sodium Chemistry

a. Characterization of Carbon- and Nitrogen-bearing Compounds in Sodium

(i) Carbon Compounds: Na_2C_2 (F. A. Cafasso and J. Ackerman)

Last Reported: ANL-7632, pp. 37-38 (Oct 1969).

Disodium acetylide, Na_2C_2, a species that earlier work had demonstrated may be responsible for carbon transport, was shown by high-temperature X-ray studies to undergo a tetragonal-to-cubic transformation at 275°C and to persist in the cubic form at 500°C. Chemical tests substantiated its stability at 550°C; decomposition, however, was observed at ≥600°C. The findings suggest that the invariant decomposition temperature of disodium acetylide lies in the range 550-600°C.

(ii) Nitrogen Compounds (F. A. Cafasso and A. K. Fischer)

Last Reported: ANL-7661, p. 27 (Jan 1970).

A program on the chemistry of nitrogen in liquid sodium is under way, starting with a study of the roles of calcium and magnesium in transporting nitrogen through sodium and in enhancing nitridation. Experimental equipment for this study has been assembled, and measurements have begun.

b. Characterization of Oxygen- and Hydrogen-bearing Compounds in Sodium (F. A. Cafasso and K. M. Myles)

Last Reported: ANL-7640, pp. 33-34 (Nov 1969).

This program is directed toward developing a scientific basis for understanding the behavior of oxygen- and hydrogen-bearing species in liquid sodium. Accordingly, definition of the phases and phase interrelationships in the sodium-rich corner of the sodium-hydrogen-oxygen ternary system is being attempted. This will be done by simultaneously determining how the activities of oxygen and hydrogen in liquid sodium vary, and how the nature and concentration of species in the vapor phase vary, as NaOH, NaH, or Na_2O is added to sodium between 375 and 600°C. Apparatus for this study has been designed, and the parts are being fabricated.

c. Determination of the Solubility of Gases in Liquid Sodium (F. A. Cafasso and E. Veleckis)

Last Reported: ANL-7655, p. 49 (Dec 1969).

(i) Xenon Solubility in Sodium. The solubility of xenon in liquid sodium is being measured as functions of temperature and pressure. The analytical and operational capability for these measurements is now in hand. The first set of results from four experiments at 500°C yielded an average solubility of 19 ± 2 ppb/atm of xenon pressure.

D. EBR-II--Research and Development

1. New Subassemblies and Experimental Support (E. Hutter)

a. Experimental Irradiation Subassemblies

(i) Mark-E37B Irradiation Subassembly (O. S. Seim and R. Olp)

Not previously reported.

The Mark-E series of irradiation subassemblies was developed to provide vehicles for irradiating unencapsulated fuel elements having known defects and for irradiating to burnups higher than usual. Previously, high-risk test elements were encapsulated to contain all debris or particles that could possibly result from a rupture or meltdown during irradiation. Encapsulation, however, did not always allow an experiment to be conducted under environmental conditions (e.g., fuel-pin and cladding temperatures or pitch-to-diameter ratios) for which the fuel was designed. The Mark-E design provides a vehicle for closer approximation of the desired environment. It also includes features to prevent failure propagation to adjacent subassemblies and to keep particles of significant size within the subassembly.

The Mark-E37B subassembly is designed for experimental studies of oxide fuel elements. It accommodates 37 test elements, 40 in. long and 0.250 in. in diameter. However, this subassembly offers an optional arrangement that will accommodate a 42-in.-long, 0.250-in.-OD unencapsulated test element at the center position of the element bundle while retaining the safety features of the Mark-E series.

To contain debris in the subassembly, upper and lower collectors are provided. The upper collector, made of perforated sheet, prevents particles larger than 0.045 in. in diameter from leaving the subassembly at the top. The lower collector, a cup form, collects particles that settle to the bottom of the subassembly.

To prevent failure propagation, a trisegmented inner hexagonal liner surrounds the test elements. This liner directs the coolant flow through the elements and protects the outer hexagonal tube. The segmented design allows maximum utilization of the subassembly because the interior hexagonal dimensions can be resized to accommodate oversize or swollen elements.

The subassembly is designed for the maximum number (37) of 0.250-in.-dia elements that will fit into a standard outer hexagonal tube with a protective liner. The element length will extend $7\frac{5}{8}$ in. below the reactor core so as to provide space for a reflector in the bottom of the test

element. This reflector serves as a radiation shield to protect the reactor grid structure. The space needed for the upper collector set the maximum length of the element cluster at 40 in.

Each subassembly contains an internal orifice whose size can be varied to achieve specific flow rates.

Provisions are made to allow the extra-long (42-in.) unencapsulated center element to extend into the base of the upper collector. An alternate upper-collector base can also be used. This base can hold two temperature sensors (sodium thermometers developed at ANL).

Calculations were made to investigate how molten UO_2-PuO_2 breaching the cladding of an element and coming in contact with the subassembly wall would affect the wall. Results show that the molten oxide fuel, which has a low viscosity, would distribute itself in a thin layer over the surface of the wall. Therefore, the possibility of melting through of the wall is reduced to a point where it is not considered likely. The oxide is a good thermal insulator; the thin layer of the solidified oxide on the wall would thermally shield the wall. Because any molten fuel would first strike the inner hexagonal liner, that liner provides added protection for the outer hexagonal tube.

Figure I.D.1 shows the features of the final design. The outer structure of the subassembly uses standard hardware. All hardware--external and internal--is made of Type 304 stainless steel.

The distance ($7\frac{5}{8}$ in.) that the test elements extend below the bottom of the reactor core will allow locating ceramic platforms or portions of adjacent reflectors below the test fuels, a condition desired by experimenters. The outside of the test element is wrapped with 0.040-in.-dia spacer wire on a 12- or a 2-in. helical pitch. The lower tip of the element is T-slotted to fit over the T-shaped grid bars when securing the element to the subassembly.

The element grid consists of seven T-bars welded to a 1.840-in. hexagonal tube. The grid is in turn welded to the top of the lower axial reflector.

The orifice plate, $1\frac{23}{32}$ in. in diameter and 1/4 in. thick, is welded to the bottom of the lower axial reflector. For maximum flow rates, the orifice may be omitted.

The lower shield (axial reflector), $14\frac{29}{32}$ in. long, is welded to the lower adapter. The lower collector, located within the lower axial reflector, is a $1\frac{3}{8}$-in.-dia cup extending about 3 in. below the six 0.594-in.-dia upper flow holes. The cup has three 1/16-in.-dia holes at the bottom

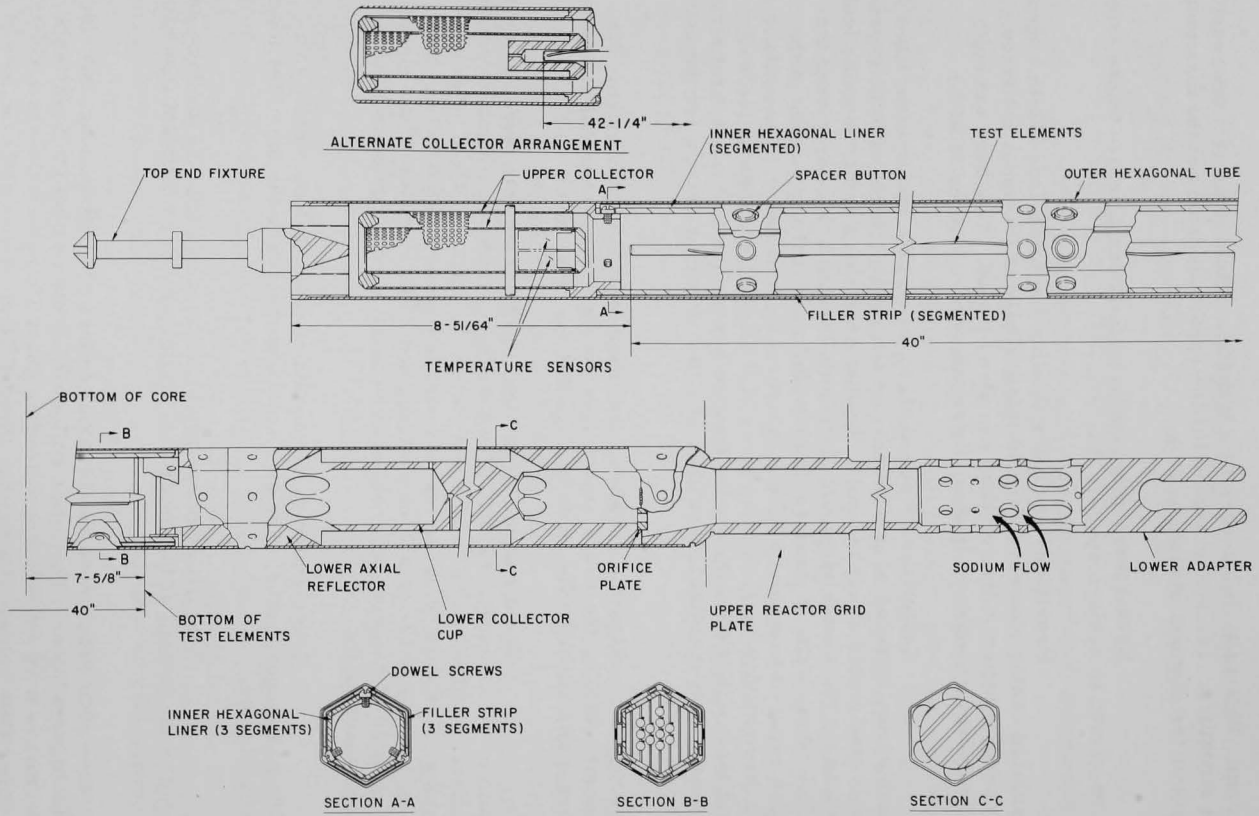

Fig. I.D.1. EBR-II Mark-E37B Irradiation Subassembly

for sodium drainage during fuel handling. The velocity of sodium through the six 0.594-in. upper flow holes should preclude any possibility of debris entering the flow annulus between the outer hexagonal wall and the collector. The volume inside the collector is sufficient to contain any debris that could possibly result from element failure.

The inner hexagonal liner, which totally surrounds the test elements, consists of three 0.120-in.-thick, $41\frac{5}{8}$-in.-long segments. The segments are separated from the outer hexagonal tube by 1/2-in.-dia spacer buttons located in groups of six at three elevations. With the segmented design, the hexagonal dimensions of the inner liner may be varied (before assembly) by varying the thickness of the spacer buttons.

Three 0.036-in.-thick filler strips in the space between the inner hexagonal liner and the outer hexagonal tube reduce the vertical flow of sodium in this space and provide additional protection for the outer hexagonal tube. The filler strips and the inner hexagonal liner are supported by the bottom group of spacer buttons, which are plug-welded to the outer hexagonal tube. A 3/16-in. hole at the top of the lower axial reflector drains sodium from the annulus between the hexagonal liner and the tube.

The upper collector is attached to the top end of the inner hexagonal liner with three dowel screws so as to allow radial movement of the liner sections. The collector is constructed of two concentric perforated cylinders and a cylinder base; the cylinders are closed at the top. The holes in each cylinder are 0.045 in. in diameter, and there are 233 holes per sq in. Calculations show that structural failure of the upper collector will not occur, even when the pressure drop across the collector exceeds the maximum pressure drop through the reactor (~40.8 psig).

The upper collector is designed to allow different types of bases to be installed on it. One collector base contains an 11/32-in.-dia, $1\frac{9}{16}$-in.-deep recess in the center to accept the top end of a single 42-in.-long, centrally located test element. A 3/64-in.-dia hole is provided to vent gas from the recess to the collector. Another base can contain two 1/2-in.-dia, $1\frac{1}{2}$-in.-long temperature sensors developed by ANL.

Flow and pressure-drop tests of the subassembly, for reactor Rows 1-6, were conducted in the pressurized-water test loop. The tests were made with a full-scale model of the complete subassembly, using two separate sections of dummy test elements having spacer wires wrapped on a 2- and a 12-in. pitch. Lower adapters were interchanged for the specific reactor rows. To determine maximum flow capability, no orifice plate was used in the first two tests. The water-flow data from these tests, converted to sodium conditions at 800°F, are plotted in Figs. I.D.2 and I.D.3.

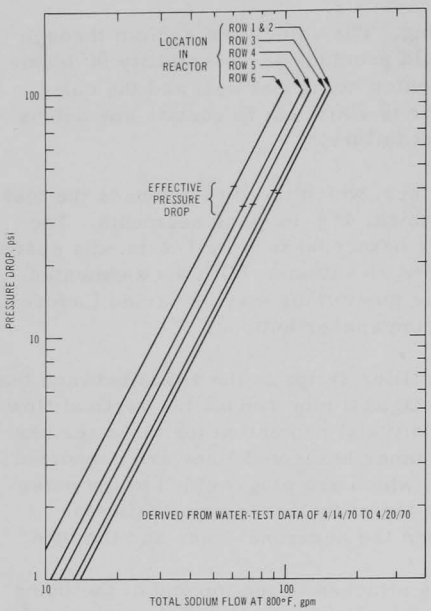

Fig. I.D.2. Relationship between Flow and Pressure Drop for Mark-E37B Irradiation Subassembly: No Orifice Plate; Spacer Wire Wrapped on 12 in. Pitch

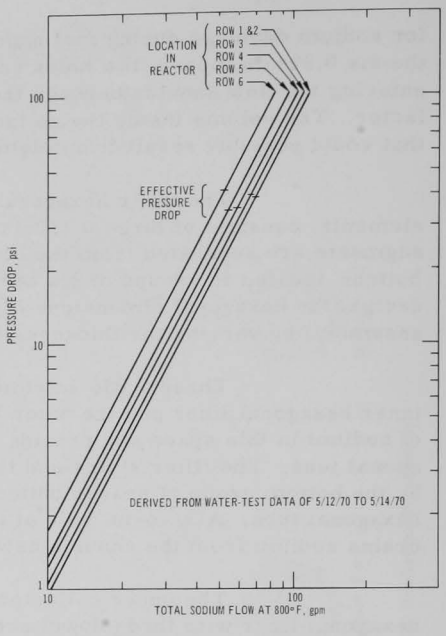

Fig. I.D.3. Relationship between Flow and Pressure Drop for Mark-E37B Irradiation Subassembly: No Orifice Plate; Spacer Wire Wrapped on 21in. Pitch

A third set of flow tests, using the 2-in. spacer-wire pitch and an orifice plate, was made to check the calculated orifice size for an experiment in reactor Row 4 with 50-MWt operation and in reactor Row 5 with 62.5-MWt operation. The results of these tests with the calculated 0.750-in. orifice hole were:

Reactor Row	Effective Pressure Drop, psi	Sodium Flow at 800°F, gpm
4	34.5	49
5	34.0	47

Diametral clearances can be varied over a 3% range by changing the thickness of the spacer buttons. The inside dimensions of the inner hexagonal liner are selected by predicting the size of the element at the end of the irradiation.

2. Instrumented Subassemblies (E. Hutter and A. Smaardyk)

a. Tests One and Two

(i) Testing of Quartz-fiber-insulated, High-temperature Cable (R. Dickman and A. E. Knox)

Not previously reported.

During development of the instrumented subassemblies, tests were made to determine the electrical resistance of the insulation on the commercial high-temperature, flexible cable to be used in the dry wells of the subassemblies. The insulation is made of fused-quartz fiber. The tests were made with the furnace facility described on pp. 58-60 of ANL-7161.* They were conducted under the following conditions:

(1) Tests were made at several temperatures up to 1175°F, with a uniform temperature field inside the furnace.

(2) The inside of the furnace was filled with ultrapure helium.

(3) The inside of the furnace and all clamps, trays, and mounting fixtures in the furnace were clean Type 304 stainless steel; electrical insulators used at the penetrations into the furnace were high-purity alumina.

(4) The megohmmeter used to measure insulation resistance was reliable. Fifty volts dc was applied in making the insulation-resistance measurements (except at 1175°F, when 10 V dc was used for most measurements).

At room temperature, the insulation resistance of the samples was 10^6 megohms/ft. The samples were heated to 700°F and held at that temperature for six days. During this period, the insulation resistance remained constant near 8×10^3 megohms/ft. Next, the temperature of the samples was raised to 1000°F. At this temperature, the insulation resistance decreased to about 400 megohms/ft in one day and remained constant at that value for nine more days. After this 10-day test, the temperature was lowered to 700°F. At this temperature, the insulation resistance increased and again became constant near 8×10^3 megohms/ft. The room-temperature insulation resistance after these tests was 1.6×10^6 megohms/ft.

Further testing was done at 1175°F. The initial resistance at this temperature and with an applied 50 V dc was 100 megohms/ft.

*Popper, G. F., and Knox, A. E., FARET In-core Instrument Development, ANL-7161 (July 1966).

(Subsequent testing at this temperature was done with an applied 10 V dc.) The insulation resistance had decreased to 5 megohms/ft after five days at this temperature. The rate of drop in resistance decreased with time during these five days, but remained constant during a sixth day at temperature.

After the sample had been at 1175°F for six days, the temperature was reduced to 1000°F. The resistance at 1000°F this time was 10% of what it was during the first test at 1000°F. The temperature was then decreased to 700°F. At this temperature also, the resistance was 10% of what it was during the first test. The resistance at room temperature at the end of the tests was about 40% of what it was at the beginning.

The test data indicated that the cable would be suitable for use in the dry wells of the instrumented subassemblies. The performance of the cable in the Test-1 and -2 (XX01) subassemblies has appeared satisfactory.

b. Test Four

(i) Lead-cutting Tests (J. Poloncsik)

Last Reported: ANL-7679, p. 39 (March 1970).

Another test cutting in air was made on representative leads for instrumented subassembly XX03. This test was made because the lead arrangement was revised by adding a heater return lead. In this test, the large leads were separated to reduce the cutting torque, which had been 80 ft-lb in the previous test reported in ANL-7679. The cutting torque was monitored by a torque transducer in the drive shaft of the cutting tool.

Results of the test are shown in Fig. I.D.4. The maximum torque of approximately 70 ft-lb occurred in the first 60° rotation of the cutting tool and involved the cutting of the 0.188-in.-OD heater lead (No. 22). The lead numbers on the plot of Fig. I.D.4 relate the cutting torque to the lead or leads being cut at the time. The lead arrangement during the actual lead-cutting operation in EBR-II is expected to be the same as that shown in the figure.

A final archive cut will also be made on this lead arrangement in 600°F sodium.

3. Experimental Irradiation and Testing (R. Neidner)

a. Experimental Irradiations

Last Reported: ANL-7688, pp. 94-96 (April-May 1970).

Table I.D.1 shows the status of the experimental subassemblies in EBR-II on June 16, 1970.

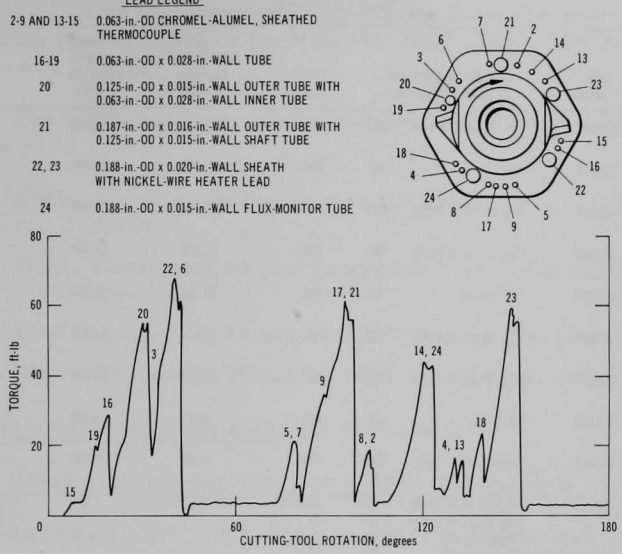

Fig. I.D.4. Results of Test Cutting, in Air, of XX03 Leads

TABLE I.D.1. Status of EBR-II Experimental Irradiations as of June 16, 1970 (Run 43 in progress)

Subassembly No. and (Position)	Date Charged	Capsule Content and (Number of Capsules)		Experimenter	Accumulated Exposure, MWd	Estimated Goal Exposure, MWd	Burnup[a]
XG03 (7D1)	7/16/65	UO_2-20 wt % PuO_2	(2)	GE	31,110	37,000	7.5
XG04 (7B1)	7/16/65	UO_2-20 wt % PuO_2	(2)	GE	32,306	45,000	7.8
X018B (4E2)	10/2/69	Structural	(3)	GE	6,800	10,000	2.5 + 5.8[b] = 8.3
		Structural	(2)	ANL			2.5 + 5.8[b] = 8.3
		Structural	(1)	ANL			2.5
		Structural	(1)	PNL			2.5
X021C (2D1)	4/17/70	Structural	(7)	PNL	2,344	3,200	0.9
X034A (2F1)	9/30/69	Structural	(4)	ORNL	6,800	7,500	2.8 + 4.8[b] = 7.6
		Structural	(3)	ORNL			2.8
X035 (7B3)	4/13/68	Structural	(7)	ORNL	19,384	44,800	4.3
X036 (7E1)	7/25/68	UO_2-25 wt % PuO_2	(19)	GE	16,990	43,300	4.5
X041 (7A3)	7/24/68	Structural	(7)	PNL	17,426	16,700	3.7
X042B (7D5)	3/4/70	Structural	(5)	PNL	3,462	6,400	0.7 + 2.1[b] = 2.8
		Structural	(2)	PNL			0.7
X051 (3A2)	12/16/68	UO_2-25 wt % PuO_2	(37)	PNL	13,251	18,200	2.6
X055 (7A4)	2/23/69	$(U_{0.85}\text{-}Pu_{0.15})C$	(19)	UNC	13,476	20,000	4.2

TABLE I.D.1 (Contd.)

Subassembly No. and (Position)	Date Charged	Capsule Content and (Number of Capsules)		Experimenter	Accumulated Exposure, MWd	Estimated Goal Exposure, MWd	Burnup[a]
X056 (5C2)	4/2/69	UO_2-25 wt % PuO_2	(37)	GE	12,106	13,000	5.8
X057 (2B1)	2/23/69	Structural	(7)	PNL	13,476	15,000	5.5
X058 (6F1)	4/24/69	UO_2-25 wt % PuO_2	(37)	GE	11,530	16,000	4.2
X059 (4A1)	4/23/69	UO_2-25 wt % PuO_2	(37)	PNL	11,530	17,500	3.8
X061 (7A5)	4/23/69	Structural	(7)	INC	12,300	18,000	2.6
X062 (6F3)	5/23/69	UO_2-25 wt % PuO_2	(37)	GE	9,627	13,400	4.2
X064 (4F2)	5/28/69	UO_2-25 wt % PuO_2	(19)	GE	10,398	10,700	5.6
X068 (4A3)	1/30/70	Mark IA	(61)	ANL	4,829	9,700	1.5
X069 (4F1)	10/1/69	UO_2-25 wt % PuO_2	(37)	PNL	6,800	20,700	2.3
X070 (3E1)	1/10/70	UO_2-20 wt % PuO_2 UO_2-20 wt % PuO_2 $(U_{0.8}\text{-}Pu_{0.2})C$ $(U_{0.8}\text{-}Pu_{0.2})C$ $(U_{0.8}\text{-}Pu_{0.2})C$ $(U_{0.8}\text{-}Pu_{0.2})N$	(8) (7) (1) (1) (1) (1)	NUMEC GE LASL LASL W BMI	5,429	6,000	3.0 + 6.2[b] = 9.2 3.1 + 4.9[b] = 8.0 2.9 + 1.4[b] = 4.3 2.9 2.9 2.9
X071 (4C3)	1/30/70	Mark II Mark II	(28) (9)	ANL ANL	4,829	5,200	2.5 + 4.1[b] = 6.6 1.8
X072 (6B2)	12/12/69	UO_2-20 wt % PuO_2 Structural	(18) (1)	ANL ANL	6,200	9,200	2.5 1.6
X073 (6C3)	12/12/69	UO_2-25 wt % PuO_2	(37)	PNL	6,200	29,600	1.5
X074 (5A2)	1/10/70	UO_2-25 wt % PuO_2	(37)	PNL	5,429	14,500	2.6
X075 (5E4)	1/30/70	$(U_{0.8}\text{-}Pu_{0.2})C$	(18)	UNC	4,829	5,100	2.3 + 5.9[b] = 8.2
X076 (7D3)	3/27/70	UO_2-25 wt % PuO_2	(19)	W	2,501	15,000	0.9
X077 (8C4)	3/26/70	Structural Structural	(2) (1)	ORNL PNL	2,501	8,100	0.3 0.3
X078 (4E3)	4/17/70	Mark IA	(1)	ANL	2,344	5,800	0.7 + 2.7[b] = 3.4
X079 (4B2)	4/17/70	$(U_{0.85}\text{-}Pu_{0.15})C$	(19)	UNC	2,344	6,300	1.2
X081 (7C5)	5/24/70	UO_2-25 wt % PuO_2	(9)	GE	1,000	16,000	0.3 + 6.7[b] = 7.0
X082 (5E2)	5/24/70	Mark IA	(61)	ANL	1,000	5,400	0.3 + 1.8[b] = 2.1
X087 (5B4)	5/24/70	UO_2-25 wt % PuO_2	(61)	PNL	1,000	2,700	0.3
X088 (6F4)	5/24/70	UO_2-25 wt % PuO_2	(19)	W	1,000	12,500	0.3
XX02 (5F3)	4/13/70	UO_2-25 wt % PuO_2	(36)	PNL	2,344	8,000	0.9

[a]Estimated accumulated center burnup on peak rod, based on unperturbed flux, but considering depletion effects (fuels, at. %; nonfuels, nvt x 10^{-22}).
[b]Previous exposure from another subassembly.

The following experimental subassemblies were removed from the grid during loading changes for Run 43: X027, X038, X040A, X043, X050, X054, and X065C.

The following experimental subassemblies were loaded for the start of Run 43:

X081: A reconstitution of nine GE oxide-fuel capsules from X020.

X082: Containing 61 previously irradiated Mark-IA fuel elements.

X087: Containing 61 series PNL-9 oxide-fuel elements.

X088: Containing 19 series WSA-1 oxide-fuel capsules.

4. Materials-Coolant Compatibility (D. W. Cissel)

a. Evaluation and Surveillance of EBR-II Materials

Last Reported: ANL-7688, pp. 96-101 (April-May 1970).

(i) Substitution of Other Stainless Steels for Type 304 Stainless Steel in EBR-II (W. E. Ruther and S. Greenberg)

The extensive penetration of the "free-machining" grades of stainless steel (Types 303, 303 CMC, and 203 EZ) by sodium has resulted in the decision to terminate this experiment on or about the end of June.

The high-temperature sodium dissolved the stringers of sulfur and selenium second-phase material responsible for the free-machining characteristics of the alloys. Where the stringers were interconnected, penetration completely through a 0.065-in. specimen was noted. Extensive use of such an alloy in EBR-II would be undesirable because of the potential loss of mechanical properties of the alloy and the contamination of the sodium with sulfur and selenium.

(ii) Postirradiation Examination of Subassembly A-837S--Nickel Surveillance Subassembly No. 2 (R. V. Strain)

Subassembly A-837S was irradiated in EBR-II to obtain data concerning the rate at which nickel corrodes in the reactor's primary-system sodium. The subassembly contained 20 thin-walled (0.060-in.) nickel rings positioned on a solid nickel spindle. It was irradiated in reactor position 7E3 from March 2, 1969, to March 17, 1970, to a maximum total fluence of ~2 x 10^{22} nvt (10,532 MWd).

Some difficulty was encountered in handling the subassembly in the reactor core and storage basket. Postirradiation measurements indicated that the subassembly had bowed and swollen during its residence in the reactor. Examination of the nickel rings and the spindle indicate that the deformation of the subassembly was caused by swelling and bowing of the nickel components.

Visual examination of the subassembly revealed longitudinal scratches or gouges about 30 in. long near the midlength of the two flats of the hexagonal tubing adjacent to the corner of the tube oriented closest to the center of the reactor core. Longitudinal marks were also observed at the top and bottom of the two flats oriented away from the center of the core. The hexagonal portion of the subassembly exhibited a maximum TIR (total indicated runout) of 0.229 in. oriented toward the core center at an axial location approximately 40 in. above the lower end of the hexagonal tube. The subassembly exhibited a TIR of 0.094 in. in the opposite direction approximately 12 in. above the lower end of the hexagonal tubing. The maximum increase in the distance across the flats of the hexagonal tubing was approximately 0.017 in., at a distance of 2 in. above the spacer buttons.

The straightness of the nickel spindle has not yet been measured accurately. The spindle is estimated to be bowed a maximum of about 1/4 in. from a straight line. Diameter measurements of the irradiated nickel rings showed a maximum OD of 2.174 in. The nominal, as-fabricated diameters (as per drawing) of the rings were between 2.156 and 2.166 in. On the basis of these values, swelling ($\Delta V/V$) of 1.1-2.5% has occurred in the rings. Swelling of the nickel is being determined by density measurements of samples cut from the rings. Samples from the side nearest the center of the reactor core and from the side away from the center of the core will be measured to determine if variations in the amount of swelling of the nickel spindle caused the spindle to bow.

b. Examination of Materials from EBR-II Surveillance Subassemblies

(i) Graphite-containing Cans from SURV-2 (S. Greenberg)

Last Reported: ANL-7679, pp. 51-52 (March 1970).

The effect of SURV-2 exposure on the room-temperature properties of the Type 304 stainless steel graphite-containing cans has been discussed in ANL-7679 and the Progress Report for December 1969 (ANL-7655, pp. 64-65). These discussions have been handicapped by the lack of data for unirradiated material, and conclusions covering the effect of the SURV-2 exposure were based to an undesirable degree on speculation.

Unirradiated cans have now become available. Tensile samples (duplicates of the irradiated samples) cut from unwelded faces of these cans were tested on the same machine and in an identical manner as used for the irradiated material. Table I.D.2 compares the room-temperature tensile properties of the irradiated and unirradiated material. The SURV-2 exposure affected the properties only slightly. The data for reduction in area and for elongation show that the material is still very ductile after exposure in SURV-2.

TABLE I.D.2. Tensile Properties of Type 304 Stainless Steel Graphite-containing Cans of SURV-2

Property[a]	Unirradiated		Irradiated in SURV-2	
	Average	Range	Average	Range
Yield strength, psi	39,400	38,300-40,400	42,500	40,950-44,100
Ultimate strength, psi	93,500	92,500-94,700	90,200	87,900-92,400
Ideal Elongation, %	44	42-45	41	32-44
Reduction in area, %	57	56-59	50	45-56

[a]Obtained at strain rate of 0.012 min^{-1} and room temperature.

c. Effect of Interstitial Elements in EBR-II Sodium

Last Reported: ANL-7669, pp. 64-65 (Feb 1970).

(i) Carbon-equilibration Experiment (T. D. Claar)

Although EBR-II components have been examined by metallography and by microprobe and chemical analyses to determine the effects of carburization and decarburization, no attempt has been made to determine the actual carburization potential of EBR-II primary sodium.

As a first step in evaluating this potential, a series of 10-mil Type 304 stainless steel foils with carbon concentrations of 0.009 to 0.070 wt % was exposed to EBR-II outlet sodium in an experimental subassembly. The foils were located at the upper end of Subassembly B-307AS, which was in reactor position 6C4. The exposure began with the startup of Run 37 and was terminated at the end of Run 41B. Run 37 began August 2, 1969, and Run 41B ended near the end of March 1970; so the foils were exposed to reactor sodium for about eight months. The time-at-temperature exposure data are still forthcoming, but the average measured sodium-outlet temperature during reactor operation was approximately 885°F at 50 MWt. A temperature of 921°F was measured during the 62.5-MWt operation of Run 38A.

The foils were removed from the subassembly in the Fuel Cycle Facility (FCF) after undergoing the normal FCF cleaning procedures.

The foils were individually cleaned and weighed, and each foil was cut into several pieces. One sample from each foil will be used for carbon analysis. Comparing the changes in the carbon concentration of the foils should indicate the carbon concentration at which stainless steel is in equilibrium with EBR-II primary sodium. The remaining samples from each foil will be used for metallographic and microprobe analyses of the material exposed to sodium.

In addition, small control tabs that were encapsulated in a stainless steel cup and exposed to the same thermal and radiation conditions as the sodium-exposed foils will be evaluated by metallography.

Table I.D.3 shows the original carbon concentration and the weight-change data for each foil.

TABLE I.D.3. Original Carbon Concentration and Change in Weight of Foils of Carbon-equilibration Experiment

Foil Identification	Carbon, wt %	Initial Weight, g	Final Weight, g	Weight Change per Unit Area, mg/cm^2
TC02	0.010	1.1294	1.1287	-0.05
TC03	0.018	1.1404	1.1396	-0.05
TC05	0.032	1.2222	1.2217	-0.03
TC06	0.041	0.9882	0.9878	-0.03
TC07	0.048	1.0395	1.0390	-0.04
TC08	0.070	1.3375	1.3371	-0.02

The results of this experiment will be evaluated in relation to ex-reactor carburization data to gain a better understanding of the carbon-transport behavior in EBR-II primary sodium.

5. Leak Detection and Location--Xenon Method (R. E. Rice)

Last Reported: ANL-7640, pp. 53-57 (Nov 1969).

a. Xenon-tag Prooftest (P. B. Henault)

An in-core prooftest to demonstrate the feasibility of the xenon-tag technique for identifying and locating defective, gas-bonded, ceramic fuel elements in EBR-II has been successfully completed. Two capsules were tagged with a unique xenon mixture and installed in the upper triflute reflector of an EBR-II driver subassembly. The tag volume in each was typical of the minimum volume that could be expected to be released from a defective fuel element. When the reactor was brought to power for the start of Run 42, at least one (and possibly both) capsules

released the xenon, which circulated through the primary system along the same path as would be followed by escaped gas from a defective fuel element. Part of the xenon tag was recovered from a sample of reactor cover gas and successfully identified, thereby demonstrating the feasibility of this method for immediately locating a defective subassembly.

The objective of the prooftest was threefold. The test was made to demonstrate that (1) the xenon-tag technique will work in EBR-II; (2) the recently installed xenon-tag sampling system (described in the Progress Report for September 1969, ANL-7618, pp. 40-41) is operational and capable of recovering the necessary amounts of tag; and (3) the mass spectrometer is operational and capable of analyzing tag ratios with the necessary sensitivity.

Some of the parameters involved in the xenon-tag technique can be controlled easily, but some are either difficult to control or cannot be controlled. Those parameters that can be controlled include (1) the volume of tag added to an element (now set at one standard cc); (2) the volume of the sample of cover gas necessary for recovery of a sufficient amount of tag for ratio analysis (set before the test at 10 cu ft at ambient conditions); and (3) the increment between tag ratios (values for tag ratios differ by a factor of approximately 1.2).

Parameters not controlled easily include (1) the amount of tag released from a defective element; (2) the solubility and entrapment of gaseous xenon in the primary sodium; (3) the maximum efficiency of the charcoal cold trap; and (4) the ultimate sensitivity of the mass spectrometer. Values for these "uncontrolled parameters," which have been used in calculations, are, respectively: (1) 10% release of tag to the sodium; (2) negligible solubility and entrapment in the sodium and complete diffusion in the cover gas; (3) approximately 100% efficiency for the charcoal cold trap; and (4) the vendor specification for the sensitivity of the mass spectrometer, i.e., the ability to analyze a tag containing only 10^{-12} g of an identifying isotope. By satisfactorily demonstrating achievement of the three objectives stated above, the test would establish that the correct values had been set for those parameters that could easily be controlled.

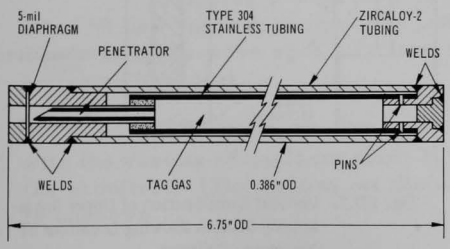

Fig. I.D.5. Xenon-tag Release Capsule

Each of the two release capsules (shown in Fig. I.D.5 and described under item b of this section) were tagged with 1.0-1.2 cc of tag gas having the composition shown in Table I.D.4. The volumes of the capsules were measured as 5.75 and 5.83 cc; therefore, each capsule contained 17-20% tag and

the remainder helium. The tagged capsules were installed in two holes drilled in the upper triflute reflector of a standard EBR-II driver subassembly (see Figs. I.D.6 and I.D.7). One capsule was designed to release its tag at 775°F, and the other at 825°F.

TABLE I.D.4. Nominal Composition of Tag Gas in Xenon-tag Release Capsules for Prooftest

Xenon Isotope	Content, vol %	Xenon Isotope	Content, vol %
124	11.52	131	2.98
126	4.58	132	1.62
128	15.91	134	0.28
129	60.74	136	0.24
130	2.14		

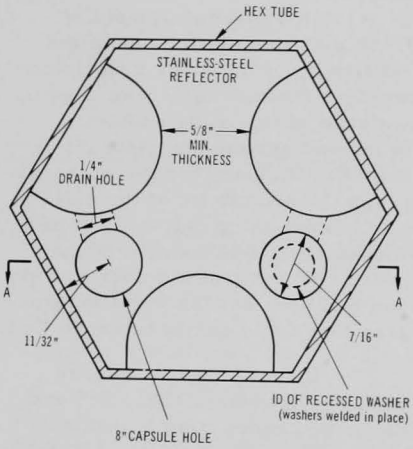

Fig. I.D.6. Cross Section above Upper Triflute Reflector Showing Location of Holes for Xenon-tag Release Capsule (Sect. A-A is shown in Fig. I.D.7)

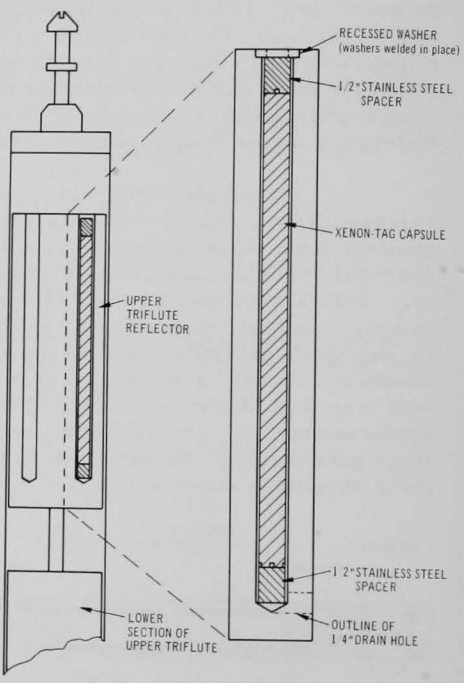

Fig. I.D.7. Vertical Cross Section of Upper Subassembly Section Showing Locations of Xenon-tag Capsules

Before the start of Run 42, two background samples of the cover gas were taken and analyzed for xenon isotopic composition. The test capsules were in the 700°F bulk sodium when the second sample was taken. Neither sample showed any evidence of ^{124}Xe, the main identifying tag constituent.

Run 42 started on April 19; but, after achieving 20 MWt, the reactor was shut down. This power level is equivalent to a test-capsule temperature of approximately 780°F. One of the two capsules, therefore, should have released its tag during this initial operation. A 5-cu-ft sample of the cover gas was taken, and the xenon was separated from the argon and krypton and analyzed for its isotopic composition by mass spectrometry. The results, shown in Table I.D.5 along with later results, indicated that at least one capsule had, in fact, successfully released its tag.

TABLE I.D.5. Results of Sample Analyses for Xenon-tag Prooftest

Sample No.[a]	126/124 Isotopic Ratio	128/124 Isotopic Ratio	129/124 Isotopic Ratio	Total Volume of Xenon Recovered in Sample, ml
Library	0.398	1.38	5.27	6.0×10^{-5}
1	0.398	1.37	5.27	4.4×10^{-4}
2	0.389	1.34	5.05	1.6×10^{-3}
3	0.399	1.38	5.24	1.9×10^{-3}
4	0.398	1.39	5.24	1.1×10^{-3}

[a]Sample 1 taken following 20-MWt operation; Samples 2-4 after 50-MWt operation.

The reactor was returned to power on April 20, this time achieving 50-MWt operation. In the several days following, a number of samples of cover gas were taken and analyzed. Sample size varied from 1 to 5 cu ft. Various trapping agents, such as charcoal, glass wool, chromium granules, and a molecular sieve, were used. Factors such as trap efficiencies at different temperatures, total capacity, and cryogenic-pumping efficiency were evaluated. (These factors will be reported later.)

Samples 2-4 (see Table I.D.5) were "routine" samples taken after 50-MWt operation to verify proper identification of the test tag. These samples were each 5 cu ft in volume and were trapped on cooled activated charcoal.

All results except those for Sample No. 2 agree satisfactorily with the results of analysis made of the "library" sample of the tag before the prooftest. (The reason for the anomalous results for the No. 2 sample is unknown.)

The amount of tag released to the primary coolant must depend on the temperature and dynamic pressure of the primary sodium in the

vicinity of the upper triflute. Since the test subassembly was located in a 6B4 position, the operating temperature of the capsule is known to have been approximately 910°F. The pressure of the primary sodium at the exit of the capsule should have been 24 psia. From these numbers, then, it was calculated that about 0.55 cc of tag gas should have been released from each capsule following penetration. Therefore the volume of tag in a 5-cu-ft sample of the cover gas should be approximately 3×10^{-3} cc. This volume is in fair agreement with the observed results. Whether both capsules actually released their tag cannot be determined until the test subassembly is removed for postirradiation examination.

b. Design and Testing of Xenon-tag Release Capsules (D. E. Walker and P. B. Henault)

The design of the release capsules takes advantage of the difference between the thermal coefficients of expansion of zirconium and steel. The gap between the penetrator and 5-mil diaphragm (see Fig. I.D.5) can be set so that the diaphragm will be penetrated at a predetermined temperature.

The penetrator is made of Type 304 stainless steel tubing, and the capsule wall of Zircaloy-2. The difference between the thermal coefficients of expansion of these materials (approximately 6×10^{-6} in./in.-°F) allows the penetrator to expand about 6 mils more than the capsule wall when going from the bulk sodium temperature of 700°F to an operating temperature of 850°F. This difference in expansion is sufficient to cause penetration of the 5-mil diaphragm and release of the gas. Because zirconium does not weld easily to stainless steel, the penetrator is fastened to the base of the capsule with a pin.

To provide the desired degree of confidence that a tag would be released while the reactor is operating (see Sect. a above), two capsules were installed in the test subassembly, one set to release at approximately 775°F, and one at approximately 825°F. Two capsules were used rather than one, because testing of the capsules showed that the release temperature could not be controlled precisely. Setting a single capsule for release at too low a temperature might lead to release of tag before reactor start-up. On the other hand, setting for release at too high a temperature might result in no significant release at the exit coolant temperature.

A series of tests with prototypal capsules was made to determine the depth of penetration of the diaphragm needed to release the tag gas. Calculated values for penetrations at different temperatures and starting gaps* are shown in Table I.D.6.

*The gap between the penetrator point and the diaphragm at room temperature (70°F).

TABLE I.D.6. Calculated Effect of Starting Gap and Sodium Temperature on Penetration of Diaphragm in Capsule for Controlled Release of Xenon

Reactor Sodium Temp, °F	Penetrator Gap, mils		Remarks
	Starting Gap	Gap at Temp[a]	
700	18	-4.7	
	19	-3.7	
	20	-2.7	
	21	-1.7	
	22[b]	-0.7	Needle in contact with diaphragm
800	18	-8.3	
	19	-7.3	
	20	-6.3	
	21	-5.3	
	22[b]	-4.3	Needle about 80% through diaphragm
850	18	-10.1	
	19	-9.1	
	20	-8.1	
	21	-7.1	
	22[b]	-6.1	Diaphragm penetrated
900	18	-11.9	
	19	-10.9	
	20	-9.9	
	21	-8.9	
	22	-7.9	

[a]Negative sign indicates that the needle has entered the diaphragm by the amount indicated at the given temperature.
[b]Calculated optimum condition.

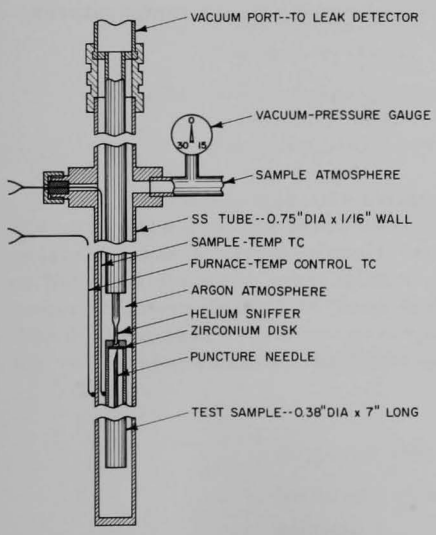

Fig. I.D.8. Rig for Testing Xenon-tag Release Capsules

The last two tests of the series were made by heating helium-filled capsules in the test rig shown in Fig. I.D.8 and noting the temperature at which the helium escaped. In these tests, the capsules were allowed to stand overnight at 700°F to simulate a reasonable residence time in the bulk sodium. In the final test, a pressure of 10 psig was maintained on the outside of the capsule to simulate a pressure differential across the diaphragm more typical of the real reactor environment. Since the conditions of this test came the closest to the conditions that could be expected in the reactor, the test and its results are described here.

The gap was adjusted to 23 mil, and the capsule was filled with helium and seal-welded. The capsule was

placed in a furnace about 4:00 p.m., gradually heated, and allowed to remain at 700°F overnight. After about 18 hr, the temperature was increased over about a 1-hr period to 851°F and held at that temperature for about 30 min. The reading from the helium leak detector remained constant, indicating background level. The temperature was then increased over about a 30-min period to 905°F, at which temperature the reading from the leak detector jumped to about five times background. The temperature was held at 905°F for several minutes with no change in the reading of the leak detector. This indicated the presence of a very small leak. The capsule was then slowly heated to 932°F, at which temperature a complete release of helium was indicated when the reading of the leak detector increased suddenly to 40 times background, the maximum signal.

The results indicated that when the needle first penetrates the diaphragm, a fairly tight seal remains between the two metals, and only minor leakage occurs. It was concluded that tag release actually occurs when the diaphragm has been penetrated by about 8 mils.

A study of the results of the three tests led to the decision to set the gaps on the two capsules at 18 and 20 mils. The capsule with the 18-mil gap would then have an 8.3-mil penetration and, therefore, complete release, at 800°F. The capsule with the 20-mil gap would have an 8.1-mil penetration at 850°F. The first capsule, therefore, should release its tag in the range of 775-800°F, and the second in the range of 825-850°F. With this arrangement, at least one of the capsules would release its tag while the reactor was in operation, even if the estimated release temperatures were in error by 50°F.

6. Reactor Analysis, Testing and Methods Development

Last Reported: ANL-7688, pp. 103-122 (April-May 1970).

a. Coefficients of Axial Fuel Expansion in EBR-II (B. R. Sehgal and R. Rempert)

A set of calculations was made to ascertain the coefficients of axial fuel expansion $[(\Delta k/k)/(\Delta L/L)]$ of an EBR-II core with different reflectors. In these calculations, only the fuel ($^{235}U + ^{238}U + ^{239}Pu$) in each row of the core was considered to have expanded axially and the atom densities of the elements to have been correspondingly reduced. Therefore, the results will not apply to a uniform increase in temperature when not only the fuel but also the structure and the coolant expand. The results may, however, apply to a fast transient. Radial expansion of the core was not considered in the calculations.

The calculations were made with the DOT code* in two-dimensional RZ geometry and with the S_2 approximation. The 26-group cross-section set BENDF derived from the ENDF/B data file was used.

The following cases for the EBR-II 62.5-MWt core for extended operations (see Fig. I.D.9) were considered:

(1) Axial and radial depleted-uranium reflectors.

(2) Axial stainless steel plus sodium reflectors and a radial depleted-uranium reflector.

(3) Axial stainless steel plus sodium reflectors and a radial reflector of four rows of nickel and depleted uranium in the remaining rows.

In each case, the compositions of the axial gaps above and below the core were kept the same as before expansion and contained the appropriate volume fractions of stainless steel and sodium. The compositions of the axial stainless steel sodium reflectors and of the depleted-uranium reflector corresponded to those in the present loading of EBR-II. Composition of the nickel reflector corresponded to that in the proposed design of the reflector. Composition of the axial depleted-uranium reflector was:

	Vol %
Depleted uranium	30.3
Stainless steel	18.5
Sodium	51.2

*Mynatt, F. R., DOT, A Two-dimensional Discrete-ordinate Code, Report K-1694, Radiation Shielding Information Center, ORNL. Also see Progress Report for October 1968, ANL-7513, p. 50.

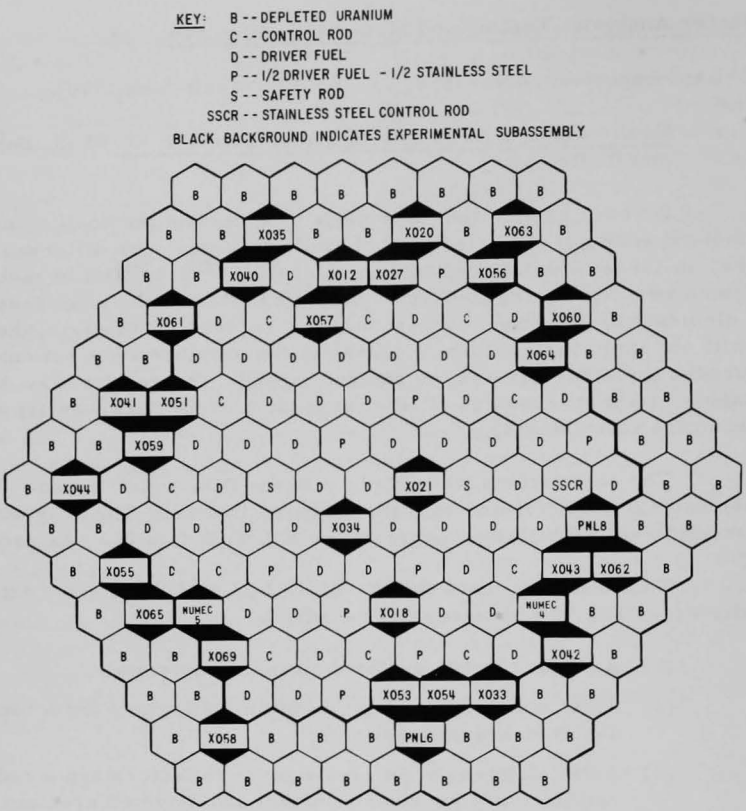

Fig. I.D.9. Typical Core Loading for Extended Operation of EBR-II at 62.5 MWt

The base and expanded core heights in each case were taken as 34.49 and 35.5 cm, respectively. The row number densities of ^{235}U, ^{238}U, ^{239}Pu, and fission products in the six reactor rows were reduced by the ratio 34.49/35.5. The core was expanded into the upper axial gap.

Table I.D.7 shows the results for k_{eff}, Δk, and $(\Delta k/k)/(\Delta L/L)$. The value of $(\Delta k/k)/(\Delta L/L)$ for axial fuel expansion is ~0.2 and hardly changes with changes in the axial and radial reflectors. If a temperature-expansion coefficient of ~2×10^{-5} $(\Delta L/L)/°C$* for the 5-wt % fissium alloy is used, the temperature-expansion coefficient would be ~4×10^{-6} $(\Delta k/k)/°C$.

*Zegler, S. T., and Nevitt, M. V., Structures and Properties of Uranium-Fissium Alloys, ANL-6116 (July 1961).

TABLE I.D.7. Values of k_{eff}, Δk, and $(\Delta k/k)/(\Delta L/L)$ for the EBR-II 62.5-MWt Extended-operation Core with Various Reflectors

Reflectors				
Axial	Radial	k_{eff}	Δk due to Expansion	$(\Delta k/k)/(\Delta L/L)$
Depleted U	Depleted U	1.01409	-0.00630	-0.21215
SS + Na	Depleted U	1.02008	-0.00631	-0.21124
SS + Na	Four rows Ni, rest depleted U	1.06045	-0.00627	-0.20191

b. Powers Generated in Individual Subassemblies of an EBR-II Core (B. R. Sehgal)

The results of two-dimensional DOT* XY calculations for the EBR-II core for extended operation at 62.5 MWt with a depleted-uranium blanket and with a nickel reflector were reported in the Progress Report for March 1970, ANL-7679, pp. 53-58. We have tried to calculate the power generated in the individual subassemblies of the core with the two cases when the total power generated in the reactor is 62.5 MWt. The normalization procedure is discussed in detail, and the total power and ^{235}U, ^{238}U, and ^{239}Pu fission power for some subassemblies are reported.

The power generated by fission of an isotope j in a subassembly i of volume V_i is given as

$$P_{ij} = (N_j A_j \nu_j)_i (Q_j/\nu_j) V_i \times 1.603 \times 10^{-19} \text{ MWt},$$

where N_j, A_j, ν_j, and Q_j are, respectively, the number density, the activity per atom, the mean number of secondary neutrons, and the energy generated in the fission of isotope j. Normalizing to a total power of P MWt generated in the reactor and to a unit source neutron in the DOT calculation gives

$$P_{ij} = (1/k_{eff})(N_j A_j \nu_j)_i V_i P[(Q_j/\nu_j)(\overline{\nu/Q})] \text{ MWt},$$

where $\overline{\nu/Q}$ is an average over the whole reactor.

The DOT XY problems represent a reactor of 1-cm height. The calculations in ANL-7679 and in this report are based on a 13-row representation. In this representation, fissions are not counted in the blanket regions above and below the core height in Rows 7-13 for the depleted-uranium blanket and in Rows 11-13 for the nickel reflector. The fraction

*Ibid, see p. 79.

of power generated in the regions for these two cases can be estimated from the DOT RZ runs, as can the power generated in Rows 14 and 15 (represented in RZ runs, but not in XY runs). Information about the axial peak/average power ratio in each row obtained from the DOT RZ run can also be used. Finally, we obtain

$$(P_{ij})_m = (1/k_{eff})(N_j A_j \nu_j)_{im} V_i [(Q_j/\nu_j)(\overline{\nu/Q})]$$

$$\times [(\text{Peak P/Avg P})_m / \overline{(\text{Peak P/Avg P})}] \times P(1 - f_1)(1 - f_2) \text{ MWt}$$

and

$$(P_i)_m = \sum_j (P_{ij})_m,$$

where f_1 and f_2 are, respectively, the fractions of the total power generated in the blanket regions beyond the core height and in Rows 14 and 15. The subscript m denotes the row m, and $\overline{\text{Peak P/Avg P}}$ is an average of these axial power ratios in each row for the whole reactor.

Table I.D.8 shows the values of Q_j (as reported by M. F. James of Winfrith), including an (n,γ) contribution of ~11 MeV, and values of ν_j obtained from the MACH* run of an EBR-II core. Table I.D.9 shows, respectively, the fractions f_1 and f_2 of the power generated in blanket regions above and below the core and in Rows 14 and 15 of the blanket. Table I.D.10 shows the values of (Peak P/Avg P) power density in Rows 1-7 for the two cases (blanket and reflector). Table I.D.11 shows the reactor average values of $\overline{\nu/Q}$, calculated by weighting the values of ν/Q for each isotope and the power generated by that isotope in the reactor, along with the values of the product $(Q/\nu)_j(\overline{\nu/Q})$ for the two cases.

TABLE I.D.8. Calculated Energy Yield (Q_j) and Average Neutron Yield/Fission (Q_j/ν) in EBR-II Core at 62.5 MWt

Isotope (j)	Energy Yield (Q_j), MeV	ν_j	Q_j/ν_j
^{235}U	204.0	2.510	81.2749
^{238}U	205.0	2.813	72.8759
^{239}Pu	209.6	2.995	69.9833

*Meneley, D. A., et al., MACH I: A One-dimensional Diffusion Theory Package, ANL-7223 (June 1966).

TABLE I.D.9. Calculated Fractions of Power (f) Generated in EBR-II Core at 62.5 MWt[a]

Reflector	f_1, %	f_2, %
Depleted uranium	2.85	0.035
Nickel and depleted uranium	0.785	0.082

[a] f_1 is the fraction of the power generated in the blanket regions above and below the reactor height; f_2 is the fraction of the power generated in Rows 14 and 15 of the blanket.

TABLE I.D.10. Calculated Row $(\text{Peak P/Avg P})_m$ Values for 62.5-MWt EBR-II Core

	$(\text{Peak P/Avg P})_m$	
Row No.	Depleted-uranium Blanket	Nickel Reflector
1	1.117	1.105
2	1.115	1.101
3	1.115	1.101
4	1.110	1.098
5	1.102	1.075
6	1.090	1.054
7	1.090	1.054

Note: $\overline{(\text{Peak P/Avg P})}$ = 1.1035 for depleted-uranium blanket
= 1.0786 for nickel reflector.

TABLE I.D.11. Calculated Values of $\overline{\nu/Q}$ and $(Q/\nu)_j\overline{(\nu/Q)}$ for 62.5-MWt EBR-II Core

	$\overline{\nu/Q}$
Depleted-uranium blanket	0.012528
Nickel reflector	0.0124024

	$(Q/\nu)_j\overline{(\nu/Q)}$	
Isotope (j)	Depleted-uranium Blanket	Nickel Reflector
^{235}U	1.01820	1.00800
^{238}U	0.91298	0.90384
^{239}Pu	0.87674	0.86796

Table I.D.12 shows the ^{235}U, ^{238}U, ^{239}Pu, and total power generated in an effective driver at an average subassembly position (i.e., 3N1 being the average position of effective driver subassemblies at positions 3A1, 3B1, 3C1, 3D1, 3E1, and 3F1) for the two cases. An effective driver subassembly is defined on a physical basis (i.e., a safety rod with 61 fuel pins is taken as equivalent to 0.67 of a driver subassembly).

TABLE I.D.12. Calculated Powers Generated in Effective Driver Subassemblies at Average Subassembly Positions in 62.5-MWt EBR-II Core

Number of Effective Drivers	Average S/A Position	Power with Depleted-uranium Blanket, MWt				Power with Nickel Reflector, MWt				
		P_{235}	P_{238}	P_{239}	P_{total}	P_{235}	P_{238}	P_{239}	P_{total}	Power Ratio[a]
1	1A1	0.9457	0.0555	0.00179	1.00294	0.9754	0.0589	0.00184	1.0362	1.0331
3.505	2N1	0.9249	0.0550	0.00086	0.98082	0.9558	0.0569	0.00088	1.0128	1.0326
4.352	3N1	0.8704	0.0518	0.00090	0.92313	0.8998	0.0531	0.00094	0.9539	1.0333
6	3N2	0.8897	0.0530	0.00120	0.9439	0.9197	0.0542	0.00124	0.9752	1.0332
6	4N1	0.7824	0.0461	0.00111	0.8297	0.8154	0.0477	0.00116	0.8642	1.0416
4.505	4N2	0.8311	0.0496	0.00116	0.8819	0.8621	0.0511	0.00120	0.9143	1.0368
3.352	5N1	0.6582	0.0359	0.00039	0.6945	0.6960	0.0373	0.00051	0.7339	1.0567
4.505	5N2	0.6964	0.0401	0.00115	0.7376	0.7266	0.0416	0.00123	0.7694	1.0431
4.022	5N3	0.7444	0.0405	0.00077	0.7857	0.7770	0.0419	0.00081	0.8197	1.0433
3	6N1	0.5151	0.0243	0.00070	0.5401	0.5925	0.0265	0.00079	0.6198	1.1478
2	6N2	0.5852	0.0274	0.00060	0.6132	0.6450	0.0295	0.00184	0.6763	1.1029
3.305	6N4	0.5978	0.0309	0.00126	0.6300	0.6470	0.0327	0.00135	0.6811	1.0811
5.011	6N5	0.5827	0.0285	0.00056	0.6118	0.6405	0.0305	0.00061	0.6716	1.0978

[a](P_{total} for nickel reflector)/(P_{total} for depleted-uranium blanket).

Table I.D.12 also shows the ratios of the total power generated per effective driver subassembly in the average positions for the nickel reflector to that for the depleted-uranium blanket. The powers per effective driver in Row-6 average positions for the nickel reflector are higher by ~8-15% than for the depleted-uranium blanket. In other rows, the difference in powers between the two cases is ~3-6%.

Table I.D.13 shows the isotopic and total fission powers for the fueled experimental subassemblies in Rows 6 and 7. The procedures for calculating these values were as described in ANL-7679. However, for the nickel reflector, the ^{235}U and ^{239}Pu fission powers in the Row-7 experimental subassemblies have been multiplied by an extra factor of 1.06. This

TABLE I.D.13. Calculated Powers Generated in Experimental Fuel Subassemblies in 62.5-MWt EBR-II Core

Experimental Subassembly	Position	Power with Depleted-uranium Blanket, MWt				Power with Nickel Reflector, MWt				
		P_{235}	P_{238}	P_{239}	P_{total}	P_{235}	P_{238}	P_{239}	P_{total}	Power Ratio[a]
X059	6A2	0.18439	0.01250	0.13669	0.33358	0.20501	0.01321	0.14963	0.36785	1.10274
X051	6A3	0.25164	0.000411	0.07413	0.326181	0.27804	0.00043	0.08075	0.35922	1.10129
X040	6B1	0.37719	0.001654	0.12744	0.506284	0.44160	0.001822	0.146228	0.58965	1.16466
X012	6B3	0.27566	0.000959	0.06348	0.340099	0.33957	0.001056	0.08448	0.425106	1.24995
X027	6B4	0.45120	0.000669	0.10210	0.553969	0.51992	0.000725	0.14449	0.665135	1.20067
X056	6C1	0.34083	0.001907	0.12404	0.466777	0.37331	0.002067	0.13565	0.513027	1.09908
PNL-8	6D2	0.36848	0.02424	0.13953	0.53225	0.39557	0.02594	0.14950	0.57101	1.07282
X043	6D3	0.39100	0.002569	0.14922	0.542789	0.41565	0.00272	0.15844	0.57681	1.06268
NUMEC-4	6D4	0.55492	0.001070	0.22240	0.77839	0.59529	0.001130	0.23770	0.83412	1.071597
X033	6E1	0.30236	0.00247	0.01919	0.32402	0.36391	0.00278	0.02988	0.39657	1.2239
X054	6E2	0.34219	0.002119	0.12266	0.46697	0.38719	0.00229	0.1383	0.52778	1.1302
X053	6E3	0.30844	0.00239	0.000088	0.31092	0.34890	0.00256	0.000093	0.351558	1.13071
X069	6F2	0.37229	0.00237	0.14072	0.51538	0.39221	0.00254	0.15286	0.54758	1.06248
NUMEC-5	6F3	0.58161	0.001167	0.23458	0.81735	0.61382	0.00123	0.24740	0.86245	1.05517
X020	7B5	0.16156	0.000280	0.044767	0.206607	0.27094	0.000353	0.07338	0.34467	1.66825
X060	7C3	0.34170	0.000437	0.12984	0.471977	0.44002	0.000502	0.16288	0.603402	1.2785
X062	7D3	0.30923	0.001677	0.113674	0.42458	0.39845	0.001889	0.14224	0.54258	1.2779
X042	7D5	0.00389	0.05712	0.001464	0.062474	0.00579	0.06341	0.00250	0.071700	1.14768
X065	7F4	0.33538	0.001809	0.11573	0.452119	0.42289	0.002007	0.15787	0.582767	1.28669

[a](P_{total} for nickel reflector)/(P_{total} for depleted-uranium blanket).

augmentation is necessary since we have seen earlier (see ANL-7679) that the ^{235}U cross sections averaged over the nickel-reflector spectrum give higher activation per atom than those averaged over the core spectrum (which we are using).

Experimental subassembly X020 will generate ~67% more power when a nickel reflector is substituted for the depleted-uranium blanket; some of the other experimental subassemblies will generate ~20-30% more power. Many experimental subassemblies in Row 6, however, will generate ~10% more power.

The results for subassembly power presented here are based on the assumption that the total power follows the spatial distributions of isotopic fissions in the reactor. However, a sizable fraction of the total power is accounted for by the γ power [both fission and (n,γ)], which may not have the same spatial distribution as the isotopic fission power. This is particularly true in the nickel reflector and the structural subassemblies, where all the power (or heat) is generated by absorption of γ rays. In addition, the fraction of power generated by γ rays in the blanket regions is higher than that in the core regions.

c. MELT-II Calculations on Run-37A Configurations of EBR-II
(R. H. Shum and G. H. Golden)

MELT-II calculations of the effects of reactivity transients on an all-metal-fuel and a hypothetical all-oxide-fuel configuration of EBR-II were reported in the Progress Report for April-May 1970, ANL-7688, pp. 106-109. The oxide fuel behaved quite differently than the metal fuel with regard to reactivity effects in a given transient. This suggested the desirability of a MELT-II analysis of a configuration containing both types of fuel. At present, however, the code can treat only one fuel. It was thus necessary to resort to an iterative approach to approximate the reactivity feedback due to each type of fuel at a given point in time. This approach was used to analyze a hypothetical EBR-II configuration similar to that of Run 37A. This configuration contains one experimental oxide subassembly in the third row, seven in the fourth row, two in the fifth row, and five in the sixth row. The cases studied were for unbounded ramp inputs of reactivity of 5 and 20 \$/sec. Values for power distribution, β_{eff}, and ℓ_p were obtained from a MACH-I calculation.

The iterative approach was as follows:

(1) A MELT-II problem was run for the totality of driver fuel subassemblies with an input reactivity rate of 5 \$/sec. For the wet critical configuration, the temperature coefficient of the fuel was -3.9×10^{-6} $(\Delta k/k)/°K$. The Run-37A core contained less driver fuel, but to compensate for the feedback due to fuel in the safety, control, and oxide subassemblies, the full value given above for the temperature coefficient was used in this first iteration.

(2) A special option of MELT-II that uses input power rather than reactivity as a function of time was used to run a second problem for the safety and control subassemblies. Under this option, a table of the ratio of power at time t to that at time zero is input; a 50-point table was prepared from the results of the first iteration on the driver fuel. The temperature coefficient of the fuel in the safety and control subassemblies was estimated from information on fuel worth and loading.

(3) The method described above in item 2 was used to run a problem on the oxide subassemblies.

(4) A second iteration was then made on the driver fuel subassemblies, but with two modifications of the input. First, instead of the 5$/sec input ramp, a 50-point table of reactivity as a function of time was the input. Each point was computed by modifying the input reactivity to account for effects due to expansion and collapse of fuel in the safety, control, and oxide subassemblies, as determined from the problems described in items 2 and 3 above. Second, the temperature coefficient of the fuel was reduced from -3.9×10^{-6} to -3.4×10^{-6} $(\Delta k/k)/°K$ to account for the smaller amount of driver fuel in Run 37A.

Results of the calculations for the 5$/sec case are summarized in Table I.D.14, and for the 20$/sec case in Table I.D.15. In both cases, there is close agreement between the results of the first and second iterations on the Run-37A driver fuel. Table I.D.14 also shows the corresponding results for the all-metal and hypothetical all-oxide configurations, described in ANL-7688, and Table I.D.15 also shows the corresponding results for the all-metal configuration. These calculations suggest that the 5$/sec and 20$/sec unbounded transients would have less serious consequences for the EBR-II Run-37A configuration containing a substantial amount of oxide fuel than for the wet critical (all-metal-fuel) configuration analyzed in ANL-5719.*

TABLE I.D.14. MELT-II Results for 5$/sec Ramp Insertion of Reactivity in Wet Critical, All-oxide, and Run-37A Configurations of EBR-II: 1% Power and 5.5% Flow

Core Configuration	Time after Start of Transient, sec	Total Power in Driver Subassemblies, MW	Total Energy Release in Driver Subassemblies, MW-sec	Peak Fuel Temperature, °K	Net Reactivity, ¢	Collapse Reactivity, ¢	Total Reactivity Rate,[b] $/sec	Peak Net Reactivity in Transient, ¢
Run 37A, First Iteration	0.3124	504	111	3,034[a]	89.9	2.0	-9.5	100.87
Run 37A, Second Iteration	0.3257	505	112	3,032[a]	89.9	1.8	-9.8	100.51
All-metal Configuration (wet critical)	0.3075	714	149	3,249[a]	90.3	4.4	-10.6	100.78
All-oxide Configuration[c]	0.3015	1.55×10^4	360	3,968[d]	98.9	3.7	2.9	102.49

[a]Peak temperature attained in transient; rapid disassembly does not occur.
[b]Input rate plus collapse rate.
[c]Temperature coefficient of reactivity of oxide fuel taken as 1/3 that of metal fuel in wet critical configuration.
[d]Assumed near threshold for rapid disassembly.

*Koch, L. J., et al., Hazard Summary Report, Experimental Breeder Reactor II (EBR-II) (May 1957).

TABLE I.D.15. MELT-II Results for 20$/sec Ramp Insertion of Reactivity in Wet Critical and Run-37A Configurations of EBR-II: 1% Power and 5.5% Flow

Core Configuration	Time after Start of Transient, sec	Total Power in Driver Subassemblies, MW	Total Energy Release in Driver Subassemblies, MW-sec	Peak Fuel Temperature, °K	Net Reactivity, ¢	Collapse Reactivity, ¢	Total Reactivity Rate,[b] $/sec	Peak Net Reactivity in Transient, ¢
Run 37A, First Iteration	0.1092	849.01	141.64	4,144[a]	92.086	-26.387	-22.5283	103.688
Run 37A, Second Iteration	0.1100	809.26	140.58	4,118[a]	91.732	-24.392	-21.66	103.720
All-metal Configuration (wet critical)	0.1035	1,114	180	4,275	92.2	-21.7	-24.2	103.384

[a]Peak temperature attained in transient; rapid disassembly does not occur.
[b]Input rate plus collapse rate.

Figure I.D.10 shows the feedback-reactivity components due to control-, safety-, and oxide-fuel expansion and to control- and safety-fuel collapse for the 5$/sec case. Collapse at oxide fuel did not occur in the given time scale.

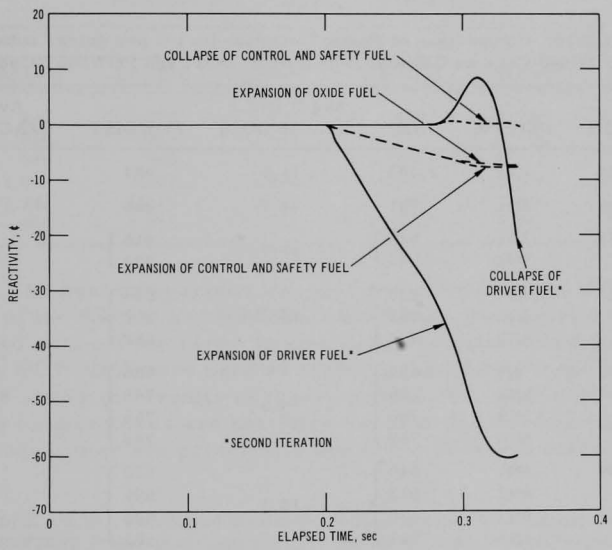

Fig. I.D.10. Feedback Reactivities from MELT-II Calculations on Run-37A Configuration of EBR-II: 5$/sec Input Reactivity Ramp; 1% Power; 5.5% Flow

d. Comparison of Results of Analyses of a Mixed Core (J. L. Gillette)

The method of analysis (with MACH) used in the studies of the mixed core reported previously--in the Progress Reports for February 1970, ANL-7669, pp. 78-81; March 1970, ANL-7679, pp. 71-72; and April-May 1970, ANL-7688, pp. 103-105--has been used to analyze the EBR-II

core for extended operation at 62.5 MWt.* The results obtained were compared with those obtained by Sehgal (Sect. I.D.6.b, above) and by Cushman (Progress Report for March 1970, ANL-7679, pp. 59-65), who have analyzed this core with the DOT and POWDIST codes, respectively.

Table I.D.16 records the power densities in kilowatts per driver subassembly as determined by each of three analyses. Because of the row-wise smearing of atom densities in one-dimensional cylindrical geometry, the power densities of all the driver subassemblies in a particular row are the same in the MACH analysis. The codes DOT and POWDIST determine the power density as a function of position in the row. The power densities agree well, except for Row 6. The values of the MACH results for this row are perhaps 2 or 3% too low because no information for determining the power split between the metallic drivers and the experimental oxide subassemblies was available. The agreement in Row 6 would be within 7 or 8% if this information were available.

TABLE I.D.16. Comparison of Power Densities (in kW per driver subassembly) in Mixed Core as Calculated by MACH, DOT, and POWDIST Codes

Row	MACH	Position	DOT	Avg % Diff.[a] (MACH-DOT)	POWDIST	Avg % Diff.[a] (MACH-POWDIST)
1	1,028	1N1	1,003	+2.5	984	+4.5
2	998	2N1	981	+1.7	966	+3.3
3	951	3N1	923	+1.7	916	+2.7
		3N2	944		933	
4	860	4N1	830	+6.2	824	+1.4
		4N2	882		862	
		4N3	730		862	
5	791	5N1	694	+4.5	686	+7.0
		5N2	738		746	
		5N3	786		766	
		5N4	787		746	
6	539	6N1	540	-10.3	520	-8.4
		6N2	613		591	
		6N4	630		628	
		6N5	612		591	

[a]Averaged over the row.

The MACH results are higher than the DOT and POWDIST results for the first five rows, but are lower for Row 6. Furthermore, the total power generated in the first six rows is approximately the same in all cases. The discrepancies in the power densities thus appear to be almost entirely due to the difference between one-dimensional diffusion theory and the two-dimensional transport theory used in the DOT and the POWDIST codes.

*Cushman, R. A., et al., Proposal for Operating EBR-II at 62.5 MWt, ANL/EBR-012 (to be published).

Table I.D.17 compares the maximum temperatures obtained when the power densities from the MACH calculation were put into the thermal-hydraulics code SNAFU, and those from the POWDIST calculation were put into the HECTIC code. The temperatures agree within a few percent in all cases. The greatest difference is again in Row 6, where the rise in coolant temperature calculated by SNAFU is 14.9% below that calculated by HECTIC.* This somewhat large discrepancy, however, is easily explained by the fact that the power density calculated for Row 6 by MACH is 8.4% lower than the average power density for Row 6 calculated by POWDIST. Furthermore, the MACH power density is 14.2% lower than the maximum power density in Row 6 (in the 6N4 position). Because Table I.D.17 shows maximum temperatures, the 14.9% difference in rise in coolant temperature is undoubtedly a reflection of the 14.2% difference in power density.

TABLE I.D.17. Calculated Maximum Temperatures (°F) in Mixed Core: MACH Power Densities Used for SNAFU Input, POWDIST Power Densities for HECTIC

	Coolant		Cladding		Fuel	
Row	SNAFU	HECTIC	SNAFU	HECTIC	SNAFU	HECTIC
1	943	919	994	976	1,138	1,113
2	936	907	985	961	1,126	1,090
3	955	940	1,003	996	1,133	1,123
4	1,015	1,007	1,058	1,061	1,169	1,172
5	1,042	1,019	1,082	1,068	1,184	1,165
6	968	1,015	996	1,057	1,065	1,140

The next comparison was made to determine the difference in the results of the SNAFU and HECTIC codes when the same power distribution was used as input for each. In this case, the power densities as determined by POWDIST were used as input for both SNAFU and HECTIC. Table I.D.18 shows the results of these calculations. Although the differences in the temperatures are partially due to different physical properties within the codes, they are principally due to the different calculational methods.

TABLE I.D.18. Calculated Maximum Temperatures (°F) in Mixed Core: POWDIST Power Distributions Used for SNAFU and HECTIC Inputs

	Coolant		Cladding		Fuel	
Row	SNAFU	HECTIC	SNAFU	HECTIC	SNAFU	HECTIC
1	932	919	981	976	1,120	1,113
2	928	907	976	961	1,112	1,090
3	950	940	997	996	1,124	1,123
4	1,015	1,007	1,058	1,061	1,170	1,172
5	1,031	1,019	1,070	1,068	1,169	1,165
6	1,004	1,015	1,035	1,057	1,115	1,140

*All temperature rises calculated on basis of 700°F inlet coolant temperature.

The temperatures in Table I.D.18 show good agreement between the two codes. The coolant temperatures as determined by SNAFU are higher than those determined by HECTIC in Rows 1-5, but are lower in Row 6. This situation is believed to result because HECTIC takes into account the rather steep decrease in radial power across Row 6, while the SNAFU value is based on the average power in the drivers of Row 6.

The final comparison was made between the power densities for an EBR-II core as determined by MACH and by the DIF2D two-dimensional, diffusion-theory code.* The DIF2D problem was done in RZ geometry with nine axial and eight radial regions.

The value of k_{eff} decreases from 0.9997 to 0.9782 as one goes from one- to two-dimensional diffusion theory. If the two-dimensional problem is assumed to be the most accurate of the two, the higher k_{eff} from the one-dimensional code will give higher, more conservative temperature estimates in the subassemblies. This conservation exists because one would have to add driver subassemblies to bring k_{eff} from 0.9782 to 1.000. Since the total reactor power is kept constant at 62.5 MWt, the addition of more driver subassemblies would decrease the power per subassembly and thus the temperatures in the subassemblies.

Table I.D.19 shows the average power density per subassembly, as calculated with the two diffusion-theory codes. Also shown is the percent difference between the results of the two calculations.

TABLE I.D.19. Average Power Densities (kW/subassembly) in Mixed Core, as Calculated by MACH and DIF2D Codes

Row	Subassembly Type	MACH	DIF2D	% Diff. (MACH-DIF2D)
1	Driver	1,120	1,089	2.8
2	Driver	1,101	1,069	2.9
3	Driver	1,057	1,026	2.9
3	Safety	709	688	3.0
4	Driver	961	937	2.5
5	Oxide	782	769	1.7
5	Control	473	465	1.7
6	Oxide	630	616	2.2
6	Blanket	130	127	2.3

The agreement between the results from the two codes is very good. The MACH results are higher in all rows of the core because the

*Toppel, B. J., Ed., The Argonne Reactor Computation (ARC) System, ANL-7332 (November 1967).

code must compact all of 62.5 MWt into a height of 13.5 in. while the DIF2D code allows some power to be generated in the other sections of the radial blanket.

The analysis tools (e.g., the MACH neutronics code and the SNAFU thermal-hydraulics code) used in studies of the mixed core yield results that are quite comparable with those obtained with more-sophisticated codes such as DOT, DIF2D, POWDIST, and HECTIC. Although the detail of the last four codes is lacking, MACH and SNAFU are believed to be adequate for scoping calculations such as those in the studies.

e. Temperature Distribution in Blanket Elements in Subassemblies in EBR-II Rows 7, 8, and 9 under Postulated Flow Blockage (R. K. Lo and J. E. Sullivan)

Calculations were made to determine the temperature distribution in blanket elements in the 19-element subassemblies in EBR-II Rows 7-9 under postulated conditions of flow blockage by deposits of stainless steel and depleted uranium. The elements have a wall that is 0.493 in. OD x 0.457 in. ID and contain a 0.012-in.-thick sodium bond. At 62.5-MWt operation, the heat-generation rates of the blanket elements of depleted uranium in Rows 7-9 were taken to be 7.8, 2.77, and 1.27 kW/ft, respectively. The calculated rate of sodium flow through the subassemblies in Row 7 was 20 gpm, and that through the subassemblies in Rows 8 and 9 was 5.9 gpm. The average velocity of the sodium flow at an inlet temperature of 700°F was calculated to be 11.6 fps for Row 7 and 4.3 fps for Rows 8 and 9.

The general heat-transfer code THTB (Transient Heat Transfer B) was used to calculate the temperature distributions for different angular coverages with the depleted-uranium and stainless-steel deposits. The first six lines of Table I.D.20 show the results for the conditions when the maximum cladding temperature would be equal to or above the cladding-fuel eutectic temperature of ~1260°F.

TABLE I.D.20. Maximum Cladding Temperatures in Blanket Subassemblies with Flow Blockage

Row	Heat Generation, kW/ft	Coverage		Maximum Cladding Temperature, °F
		Angle, deg	Blocking Material	
7	7.80	240	Depleted Uranium	1,279
7	7.80	240	Stainless Steel	1,260
8	2.77	340	Depleted Uranium	1,296
8	2.77	340	Stainless Steel	1,272
9	1.27	358	Depleted Uranium	1,374
9	1.27	358	Stainless Steel	1,364
9	2.54	340	Depleted Uranium	1,241
9	2.54	340	Stainless Steel	1,233

Calculations also were made to determine the maximum cladding temperature in Row 9 when the heat-generation rate of its elements is doubled to 2.54 kW/ft and the flow rate is kept the same. (This heat-generation rate is still lower than that in Row 8--2.77 kW/ft.) The last two lines of Table I.D.20 show the results of these calculations. The maximum cladding temperature in Row 9 would be lower than that in Row 8 under the same angular coverage. However, it is very close to the cladding-fuel eutectic temperature.

f. Program EBRFLOW--An Approach to Predicting Flow Rates in Subassemblies (A. Gopalakrishnan)

In a typical loading of the EBR-II core, subassemblies differ from each other in flow and pressure-drop characteristics. Characteristics of the driver subassemblies depend on the row position, and characteristics of safety rods, control rods, and experiments usually differ from those of driver subassemblies. For a known rate of total flow to the high-pressure plenum, an analytical tool to predict flow rates in individual subassemblies for any specified loading is desirable. An analysis and a computer program were developed for this purpose.

(i) Analysis. For a channel of effective length L and equivalent diameter D, the pressure drop through the subassembly can be written as

$$\Delta p = \frac{4fLV^2\rho}{2gD}. \tag{1}$$

The friction factor, f, is given by

$$f = C_1 Re^n = C_1(VD\rho/\mu)^n, \tag{2}$$

where C_1 and n are constants. If A_f is the effective flow area, the mass flow rate can be expressed as

$$W = A_f \rho V. \tag{3}$$

Combining Eqs. 1-3 gives

$$\Delta p = (4C_1/2g)(W^{2+n}D^{n-1}L/A_f^{2+n}\mu^n\rho). \tag{4}$$

For any subassembly, L, D, and A_f are constants; therefore, Eq. 4 becomes

$$\Delta p = C_2 W^{2+n}\rho^{-1}\mu^{-n} = C_2 W^{2+n}(\rho/\rho_0)^{-1}(\mu/\mu_0)^{-n}\rho_0^{-1}\mu_0^{-n}, \tag{5}$$

where ρ_0 and μ_0 are properties evaluated at the reference temperature, T_0, and C_2 is a constant. Equation 5 can be expressed finally as

$$W = \left[\frac{\Delta p\left(\frac{\mu}{\mu_0}\right)^n \frac{\rho}{\rho_0}}{K}\right]^{1/(2+n)}, \tag{6}$$

where K is a constant for any particular subassembly.

Let W_{ij} be the mass flow rate through subassembly j in row i. The effective pressure drop in row i is related to the pressure drop between the plenum in Rows 6 and 7 as follows:

$$\Delta p_i = F_i \Delta p_{6-7}, \tag{7}$$

where F_i, for i = 1, ..., 7 are given in ANL-5719 (Addendum).* If μ_{ij} and ρ_{ij} correspond to values for the viscosity and density at the average sodium temperature, T_{ij}, in the subassembly, use of Eq. 6 gives

$$W_{ij} = \left[\frac{F_i \Delta p_{6-7}\left(\frac{\mu_{ij}}{\mu_0}\right)^{N_{ij}} \frac{\rho_{ij}}{\rho_0}}{K_{ij}}\right]^{1/(2+N_{ij})}, \tag{8}$$

where

$$\Delta p = K_{ij} W^{2+N_{ij}} \tag{9}$$

gives the relation of pressure drop to mass flow rate for subassembly ij. Usually, this calibration information is available in the form

$$\Delta p = K'_{ij} Q^{2+N_{ij}}, \tag{10}$$

where Δp is in psi and Q is in gpm (at 800°F).

(ii) Program EBRFLOW. EBRFLOW is an IBM/360 program written in FORTRAN IV. The present version considers only the flow distribution in Rows 1-7. Future extensions will include the low-pressure, outer-blanket region and will incorporate pump characteristics.

If W_T is the total flow rate through the high-pressure plenum,

$$W_T = \sum_i \sum_j W_{ij}. \tag{11}$$

The calibration constants K'_{ij} and N_{ij}, and the subassembly power P_{ij}, are part of the input data. In addition, the values for F_i are input from ANL-5719 (Addendum).

*Koch, L. J., Loewenstein, W. B., and Monson, H. O., Addendum to Hazard Summary Report, Experimental Breeder Reactor II (EBR-II) (June 1962).

The program uses initial guess values (input) for T_{ij} and Δp_{6-7} and calculates values for W_{ij} through Eq. 8. By use of these values of W_{ij} and the input values of P_{ij}, the average temperatures T_{ij} are correctly evaluated, and on this basis the values for W_{ij} are recomputed. A check is then made to determine whether Eq. 11 is satisfied. If it is not, the value of Δp_{6-7} is readjusted, and the above procedure is repeated until Eq. 11 is satisfied within a specified error band.

(iii) Results from EBRFLOW. Three types of problems have been investigated with the aid of EBRFLOW. The first problem was on the distribution of flow in the "nominal" 67-subassembly core described in ANL-5719 (Addendum). The second was the determination of the changes in Δp_{6-7} associated with replacing one or more drivers in various rows with a low-flow experimental subassembly. These calculations were repeated for a high-flow experimental subassembly. The last problem was a study of the changes in relative flow rates in subassemblies when the total flow rate is decreased to different fractions of its nominal value.

(a) Flow Distribution in "Nominal" Core Loading. The "nominal" core described in ANL-5719 (Addendum) consists of 53 driver subassemblies, two safety rods, 12 control rods, and 60 inner-blanket subassemblies in the high-pressure flow region. The values of K'_{ij} and N_{ij} used in this calculation were obtained from the out-of-core calibration data. The total high-pressure flow rate was taken as 7,620 gpm at 800°F.

Table I.D.21 compares the flow rates from EBRFLOW with the flow rates reported in ANL-5719 (Addendum). The K'_{ij} and N_{ij} coefficients used were recent values, and some were different from those used in ANL-5719 (Addendum).

TABLE I.D.21. Comparison of Flow Rates from EBRFLOW with Those Reported in ANL-5719 (Addendum)

Type of Subassembly	Reactor Row	Flow Rate, gpm: Calculated by EBRFLOW	Flow Rate, gpm: Reported in ANL-5719 (Addendum)
Driver	1	140.9	140.0
Driver	2	140.9	138.0
Driver	3	124.3	124.0
Driver	4	95.1	94.0
Driver	5	78.9	78.0
Driver	6	70.8	72.5
Inner blanket	6	28.7	31.0
Inner blanket	7	20.5	20.0
Control	5	57.6	60.0
Safety	3	94.2	84.5

(b) Changes in Effective Pressure Drop Associated with Minor Loading Changes. The effect of minor loading changes on the flow distribution has been studied by selecting a series of hypothetical core loadings, all of which were small perturbations of the "nominal" core used in the previous section. The total flow was maintained at 7,620 gpm, and the calculations were done for a uniform T_{ij} of 800°F.

The first set of these loadings involved the replacement of one or two drivers in different rows with one or two low-flow experimental subassemblies. The low-flow subassembly selected for this purpose had a K'_{ij} of 0.0145 and an N_{ij} of -0.08, and when installed in Row 5, would have a flow rate identical with that of a control subassembly. The results show that replacing a driver with a subassembly of lower flow (and maintaining the same total flow) would cause all other subassemblies to take in a slightly higher flow rate, at a correspondingly larger pressure drop. Also, the results showed that replacing a driver subassembly in Row 1 or 2 with a low-flow subassembly had almost the same effects as replacing two driver subassemblies in Row 4 with two similar experimental subassemblies.

The second set of loadings was similar to the above, except that the hypothetical replacement subassembly was chosen to permit a flow rate 50% in excess of that of a driver subassembly in the same row. As expected, the trends were in the direction opposite to those for the previous set of loadings. In general, flow for all subassemblies decreased, and pressure drop decreased correspondingly. The maximum reductions in flow occurred when two driver subassemblies in Row 2 were replaced with high-flow subassemblies. These reductions are (a) 1.9% for a driver subassembly in Row 5, (b) 1.95% for an inner-blanket subassembly in Row 7, (c) 1.74% for a control subassembly in Row 5, and (d) 1.81% for a safety subassembly in Row 3.

(c) Variation of Subassembly Flow Rates with Changes in the Total Flow Rate to the High-pressure Plenum. It is usually assumed that when the total flow rate drops to a percentage of its nominal value, flow rates for all subassemblies also decrease to the same percentage of their nominal values. This assumption is not strictly correct, because the flow rate in a subassembly as a fraction of its nominal value depends on the value of N_{ij}; these values differ slightly for different subassemblies. To determine the effect of these differences, subassembly flow rates were calculated for the "nominal" core at different total flow rates ranging from 7,620 gpm (100% flow) to 228.6 gpm (3% flow). The flow rates for the individual subassemblies, both in gpm and as a percentage of their values at nominal full flow, are shown in Table I.D.22 as a function of the total high-pressure flow rate. These calculations also indicate that the subassemblies with the lowest value of N_{ij} have a percentage flow lower than that for the total, while those with larger N_{ij} values have a higher percentage flow. Also, these differences increase for lower values of the total flow rate. These calculations were all based on a uniform T_{ij} value of 800°F.

TABLE I.D.22. Flow Distribution for Subassemblies as a Function of Total High-pressure-plenum Flow

Total High-pressure Flow	Driver, Row 1	Driver, Row 2	Driver, Row 3	Driver, Row 4	Driver, Row 5	Driver, Row 6	Inner Blanket, Row 6	Inner Blanket, Row 7	Control S/A, Row 5	Safety S/A, Row 3
7620 (100.0)[a]	140.9 (100)	140.9 (100)	124.4 (100)	95.1 (100)	79.0 (100)	70.8 (100)	28.6 (100)	20.5 (100)	57.6 (100)	94.2 (100)
6096 (80)	112.4 (79.76)	112.4 (79.76)	99.2 (79.76)	75.9 (79.76)	63.0 (79.76)	56.5 (79.76)	23.2 (81.51)	16.5 (80.51)	46.3 (80.33)	75.2 (79.86)
4572 (60)	84.0 (59.59)	84.0 (59.59)	74.1 (59.59)	56.7 (59.59)	47.1 (59.59)	42.2 (59.59)	17.7 (61.79)	12.5 (60.88)	34.9 (60.56)	56.3 (59.76)
3048 (40)	55.7 (39.51)	55.7 (39.51)	49.1 (39.51)	37.6 (39.51)	31.2 (39.51)	28.0 (39.51)	12.08 (42.16)	8.41 (41.05)	23.44 (40.67)	37.4 (39.70)
1524 (20)	27.6 (19.56)	27.6 (19.56)	24.3 (19.56)	18.6 (19.56)	15.5 (19.56)	13.9 (19.56)	6.28 (21.93)	4.29 (20.93)	11.86 (20.59)	18.59 (19.74)
762 (10)	13.6 (9.69)	13.6 (9.69)	12.05 (9.69)	9.21 (9.69)	7.65 (9.69)	6.86 (9.69)	3.27 (11.40)	2.19 (10.67)	6.00 (10.42)	9.24 (9.81)
381 (5)	6.75 (4.79)	6.75 (4.79)	5.96 (4.79)	4.56 (4.79)	3.78 (4.79)	3.39 (4.79)	1.70 (5.92)	1.11 (5.43)	3.04 (5.27)	4.59 (4.87)
228.6 (3)	4.02 (2.85)	4.02 (2.85)	3.55 (2.85)	2.71 (2.85)	2.25 (2.85)	2.02 (2.85)	1.05 (3.66)	0.68 (3.30)	1.84 (3.19)	2.74 (2.91)

[a]The numbers within parentheses are the percentages of full flow. The other numbers indicate the actual flow in gpm.

g. Displacement and Bending Stress of a Subassembly with Parallel Flow (L. K. Chang)

The parallel-flow-induced vibration of an EBR-II subassembly has been studied. The system used in the study was a clamped-free (clamped on one end, free on the other) cylindrical tube subject to turbulent boundary pressure due to the sodium flowing parallel to its surface.

Paidousis' equation* of motion of a cylindrical rod was used, and the equation was solved by an eigenfunction series and a separation-of-variable technique. The mathematical model used in the analysis was similar to that of Chen's for a simply supported rod;** in Chen's model, the equations of motion are decoupled by neglecting the off-diagonal terms of the matrix. The pressure loading was considered to be random with time, and the power spectral density of pressure was assumed independent of rod position.

The power spectral density of displacement can be written as†

$$\Phi_{\eta\eta}(\xi,\omega) = \Phi_{pp}(\omega) \sum_m \sum_n \frac{\alpha_n(\xi)\alpha_m(\xi)}{|Y_n(\omega)||Y_m(\omega)|} \int_0^1 \int_0^1 \alpha_n(\xi)$$

$$\times\, \alpha_m(\xi_1) R_{pp}(\xi,\xi_1,\omega)^{-(\theta_n-\theta_m)i}\, d\xi d\xi_1, \qquad (1)$$

*Paidousis, M. P., Dynamics of Flexible Slender Cylinders in Axial Flow, J. Fluid Mech. 26, Part 4, p. 717 (1966).

**Chen, S. S., Response of a Flexible Rod to Turbulent-Boundary-Layer Pressure (to be published).

†Powell, A., "On the Response of Structures to Random Pressures and to Jet Noise in Particular," Chapter 8 in Random Vibration, S. H. Crandall, Ed., The MIT Press, Cambridge, Mass., Vol. 1 (1958).

where $Y(\omega)$ and θ are defined in the listed reference; $\Phi_{pp}(\omega)$ is the power spectral density of pressure; ω is the nondimensional frequency; ξ and ξ_1 are coordinate parameters in the axial direction of the cylinder; $\alpha_n(\xi)\alpha_m(\xi)$ are the displacement configurations of the system vibrating in modes n and m; and $R_{pp}(\xi, \xi_1, \omega)$ is the longitudinal spatial cross-correlation function in the frequency domain. The pressure correlation in Eq. 1 is assumed to be homogenous in space, and since the modes are widely separated and the damping is small, the equation can be simplified by neglecting cross-coupling terms. The expression $R(\xi, \xi_1, \omega)$ has been theoretically and experimentally determined in several references,† and the experimental data for $\Phi_{pp}(\omega)$ have been reported for bodies in water flow†† and in air flow.‡

Figure I.D.11 plots the log of power spectra of pressure against the Stronhal number, in which Ω, δ^*, and U denote the dimensional frequency, turbulent-displacement thickness, and fluid velocity, respectively. The rms displacement is given by

$$\overline{\eta}(\xi) = \left[\lim_{\omega \to \infty} \int_0^{\omega} \Phi_{\eta\eta}(\omega, \xi)\, d\omega \right]^{1/2} \tag{2}$$

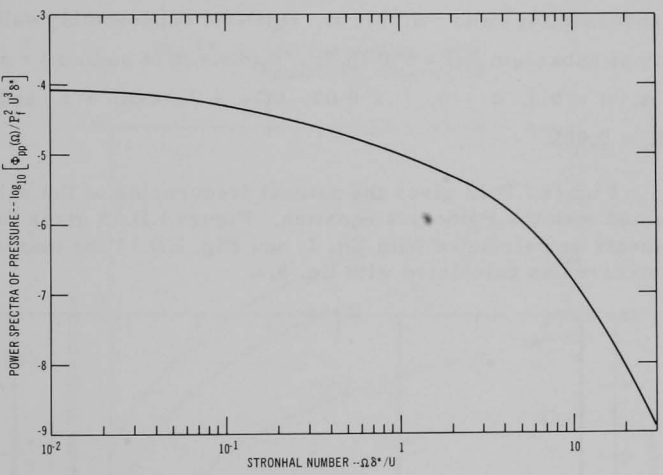

Fig. I.D.11. Density of Power Spectra of Pressure on Surface of Subassembly with Parallel Flow

---

†Chen, S. S. op. cit.; Croco, G. M., Resolution of Pressure in Turbulence, J. Acoust. Soc. Am. 35, p. 192 (1963); Bakewell, H. P., Jr., Turbulent Wall-pressure Fluctuation on a Body of Revolution, J. Acoust. Soc. Am. 43, p. 1358 (1968); Willmarth, W. W., and Wooldridge, C. E., Measurements of the Fluctuating Pressure at the Wall Beneath a Thick Turbulent Boundary Layer, J. Fluid Mech 14, Part 2, p. 187 (1962).

††Bakewell, H. P., Jr., op. cit.; Cluich, J. M., Measurements of Wall Pressure Field at the Surface of a Smooth-Walled Pipe Containing Turbulent Water Flow, J. Sound Vibration 9, p. 398 (1969).

‡Willmarth, W. W., and Wooldridge, C. E., op. cit.

If the subassembly is assumed to be axisymmetric under random loading, the dimensional rms moment can be expressed by

$$\overline{M(x)} = \frac{Eh^3}{12(1-\nu^2)} \frac{d^2\overline{y}}{dx^2}, \tag{3}$$

where E is Young's modulus, h is the thickness of the cylinder, ν is Poisson's ratio, and

$$x = \xi L \text{ and } \overline{y}(x) = \overline{\eta}(\xi)L, \tag{4}$$

where L is the length of cylinder. The maximum rms bending stress can be written as

$$\overline{\sigma}(x) = \frac{6\overline{M}(x)}{h^2}. \tag{5}$$

In calculating the natural frequencies, displacement, and bending stress, we used the following values (terms not defined above or in the cited Paidousis or Chen papers are defined here):

D_i(ID of subassembly wall) = 0.1975 ft, D_0(OD of subassembly wall) = 0.204 ft, ρ_s(density of subassembly) = 500 lb/ft^3, ρ_f(density of sodium) = 53.88 lb/ft^3, L = 5.4 ft, ν = 0.3, α = 0, δ = 0.07, ϵC_T = 1, ϵC_N = 1, and $\overline{\delta} = \delta^*/L = 0.005$.

Figure I.D.12 gives the natural frequencies of the subassembly as calculated with the Paidousis equation. Figure I.D.13 gives the rms displacements as calculated with Eq. 2, and Fig. I.D.14 the maximum rms bending stresses as calculated with Eq. 5.

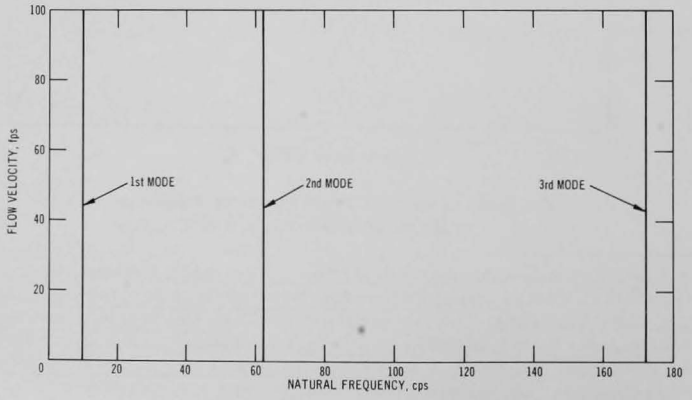

Fig. I.D.12. Natural Frequencies of Subassembly with Parallel Flow

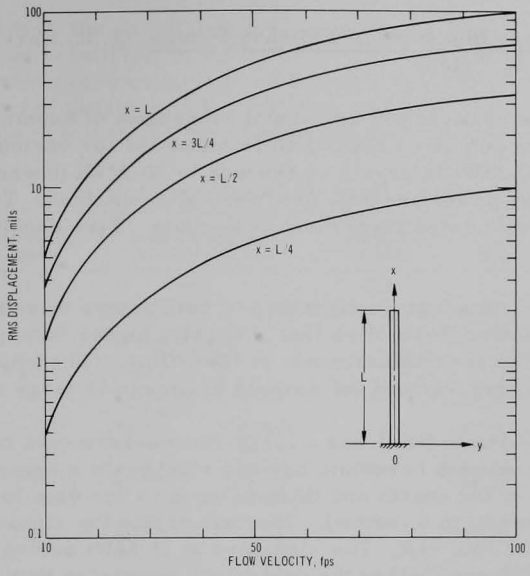

Fig. I.D.13. RMS Displacements of Subassembly with Parallel Flow

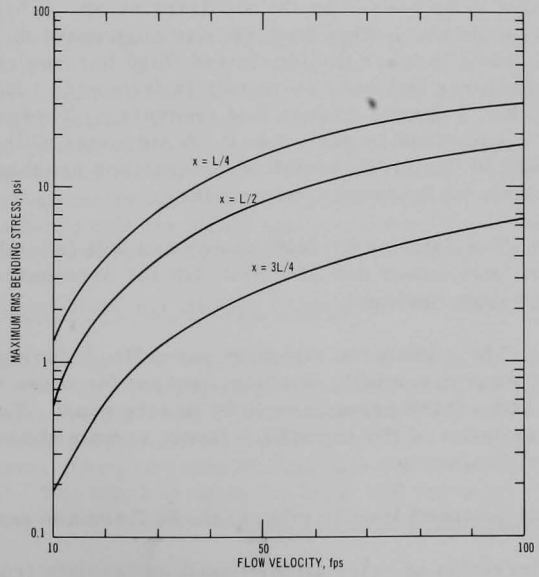

Fig. I.D.14. Maximum RMS Bending Stresses of Subassembly with Parallel Flow

h. Noise Signature of Primary Pumps (J. R. Karvinen and C. C. Price)

The vertical and horizontal vibrations of housings of both primary sodium pumps on EBR-II were recorded for various flows at zero power and at 10-MWt intervals on the way to 50-MWt power during Run 43; data for 25-MWt power and 55% flow were also obtained. Table I.D.23 shows results calculated from most of the data. Five conclusions have been reached:

(1) An accurate signature of both pumps was attained. However, data for lower flows show that a slightly higher band pass should be used to obtain the seventh harmonic at 100% flow. (The impeller has seven blades, and the frequency of the seventh harmonic is large at lower flows.)

(2) Pump No. 1 has a large second-harmonic content. At lower flows, only the seventh harmonic has any significant magnitude, except for the peculiarity of the fourth and third harmonics for data for 30 and 55% flow, respectively (see item 3, below). The data verify the signature obtained at zero power after Run 42A. The signature at 50 MWt during the end of Run 42A was different before the pump-induced scram that ended that run.

(3) At 100% flow, pump No. 2 has only a fifth harmonic of appreciable magnitude. The data for this pump at zero flow show a 29.6-Hz vibration, thought to be caused by the auxiliary pump. (This will be checked during the next shutdown.) This frequency is augmented on both pumps for the 30 and 55% flows because the fourth and third harmonics, respectively, of the pump signatures fall very close to this frequency. However, signatures for pump No. 2 always contain this frequency. This pump is closer to the auxiliary pump than is pump No. 1. A signature of the auxiliary pump will be attempted to verify the tentative conclusions reached here. If they are correct, a natural flowmeter may evolve.

(4) The data for 25-MWt power and 55% (actually 51%) flow verify those for zero power and 55% flow, but the harmonics indicate some dead band in the flow readings.

(5) The signatures taken for pump No. 1 during the 10-MWt steps to power were essentially identical, except for those for 40 MWt, which show the first and second harmonics to be nearly equal. For the other power levels, the magnitudes of the second harmonic remained about twice that of the fundamental frequency.

i. Self-powered Ion Chambers (J. R. Karvinen and C. C. Price)

Correction of calculations based on the data from the self-powered ion chamber of the instrumented subassembly (reported in the Progress Report for February 1970, ANL-7669, p. 74) gives better

agreement between the calculated and measured current. The manufacturer's reported sensitivity of 1.2×10^{-21} A/nv, which was used in calculating the current previously, is for a thermal flux. Results of a calculation for a self-powered detector in the fast flux of EBR-II agree well with the measured value of 6×10^{-8} A for the chamber current.

TABLE I.D.23. Noise Signatures of Primary Sodium Pumps of EBR-II

Power	Flow, %	Amplitude of 29.6-Hz-frequency Component	Harmonics of Pump No. 1 (Normalized Amplitudes)		Amplitude of 29.6-Hz-frequency Component	Harmonics of Pump No. 2 (Normalized Amplitudes)		Record Number
0	0	0	0		0.0048	0		2
0	31.7	5.44	1st --5.44	6th--2.45	1.4	4th --That for 29.6 Hz		6
			4th --Near that for 29.6 Hz	7th--7.5		5th --0.021		
			5th --2.66					
500 kW	54.4	1.09	3rd --Near that for 29.6 Hz	9th--0.48	1.66	2nd--0.0192	6th--0.17	11
			7th --0.72	11th--0.016		3rd --Near that for 29.6 Hz		
500 kW	74.6	-	2nd--1.84	5th--0.84	0.8	1st --0.06	3rd--0.38	10
			3rd--0.52	6th--0.76		2nd--0.02	5th--0.04	
				7th--1.92			7th--0.24	
500 kW	98.5	-	1st --4.25	6th--0.56	0.72	1st --0.04	3rd--0.2	7
			2nd--3.2			2nd--0.03	5th--1.06	
			4th --0.68					
50 MW	100	-	1st --2.67	4th--0.105	0.82	1st --0.093	3rd--0.14	23
			2nd--5.35			2nd--0.062	5th--1.33	
25 MW	55[a]	0.76	3rd--2.85		0.275	7th --0.0347		14
			4th --1.05					

[a]Harmonic frequencies indicate this flow to be actually 51%, not 55%.

Three self-powered rhodium detectors (one with active material 10 cm long and 0.04 cm in diameter, and two with active material 20 cm long and 0.04 cm in diameter) were calibrated in the Argonne Fast Source Reactor (AFSR). With the reactor power at 10 W, a minimal current signal of 2×10^{13} A was generated by the longer detectors. The detector current increased proportionately with an increase in reactor power, and at 500 W, statistical fluctuations in the current signal became negligible. The results of this work indicate that the AFSR can be used as a relative calibration standard for self-powered ion chambers to be inserted into EBR-II.

j. Digital Data-acquisition System (R. W. Hyndman)

The digital data-acquisition system (DAS) has been delivered and installed. The digital input-output channels and the high-level multiplexors have met specification. Some difficulty discovered in the high-level, sample-and-hold amplifier within the MD-51 has been traced to a faulty component. The low-level multiplexor does not meet the specification at present. The noise level is too high, and the input circuit must be changed to bring the noise rejection within specification.

7. Driver Fuel Development (C. M. Walter)

a. High Burnup Encapsulated Irradiations

Last Reported: ANL-7688, pp. 123-128 (April-May 1970).

(i) Incipient Cracking of Type 304L Stainless Steel Cladding of Mark-II Encapsulated Element during Storage in Air Cell (W. N. Beck and J. E. Sanecki)

An isolated instance of incipient cracking of a fuel-element cladding during prolonged storage in an air cell was reported last month. The cracks first became apparent after the Mark-II element (No. 279) had been in storage for seven weeks. During the following six weeks, the existing cracks widened, and new cracks developed. A complete metallographic examination had been performed and was reported; however, the scanning-electron microscopy (SEM) examination had not been completed in time to be reported. This examination was performed on a fractured surface of the cladding. To obtain a suitable section of cladding, a 1/32-in. wafer was cut out of the element through one of the largest cracks. The fuel was removed, and the cladding was decontaminated. A second radial cut was made 0.040 in. to one side of the fracture surface. This segment was cemented to a conducting mount.

Figure I.D.15 is a 500X SEM photograph of the fracture surface. Intergranular separation is evident, as is a secondary crack normal to the surface plane of the initial crack. Small pores are visible on grains; these may or may not have been present before fracture of the cladding section.

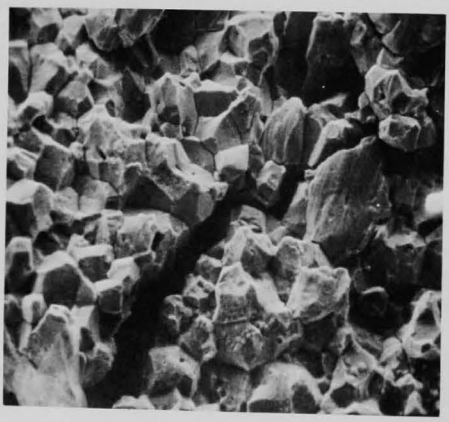

Fig. I.D.15
SEM Photograph of Fracture Surface of Cladding of Mark-II Element No. 279 (500X)

b. Fuel and Cladding Surveillance

Last Reported: ANL-7688, pp. 128-132 (April-May 1970).

(i) Destructive Examination of Mark-II Elements from Subassembly C-2201S (R. V. Strain)

The results of the destructive examination of Elements 46 and 73 from Subassembly C-2201S support the results obtained during the nondestructive examination, which were reported last month. Some of the more important results were:

(1) The maximum burnup of the elements was verified as being ~2.2 at. % by chemical analysis.

(2) Fission-gas releases of 37 and 43% were calculated for Elements 46 and 73, respectively, based on pressure and volume determinations made for the gas plenum.

(3) Metallography revealed that the fuel had swollen out and contacted the cladding over a region near the midlength of the fuel pins. The annulus still existed at the upper and lower ends of the fuel.

(4) No fuel-cladding interactions were observed in the areas of fuel-cladding contact.

(5) The cladding was sensitized in the region above the midlength of the fuel pin. The degree of sensitization was no more severe than that observed in Mark-IA fuel elements at 1.8 at. % burnup. No unusual features were observed in the microstructure of the cladding.

The destructive examination of the two elements consisted of: (1) determination of pressure and volume of the gas in the plenum; (2) chemical analysis for technetium in samples from five axial positions (for determining burnup); and (3) optical metallography of samples from five axial positions.

Element 46 had a plenum volume of 1.76 cc, and the pressure of the gas in the plenum was 95 psia at 37°C. At STP, therefore, the gas volume would be 10.0 cc. Element 73 had a plenum volume of 1.52 cc, and the pressure of the gas in the plenum was 124 psia at 37°C. At STP, therefore, the gas volume would be 11.3 cc. The plenum was assumed to have contained 2.9 cc of helium at STP before irradiation, and the volume of fission gas generated in the pins at 2.2 at. % burnup was calculated to be ~19.6 cc at STP. On the basis of these data, Element 46 had a 37% release of fission gas and Element 73 had a 43% release.

The amount of fuel-pin swelling determined from the sodium levels observed in the bond-test traces was 26 and 29% $\Delta V/V$ for Elements 46 and 73, respectively.

Figure I.D.16 plots the burnup data for these elements. A value of 5.84% was used for the technetium yield. The measured burnup values agree well with the calculated values.

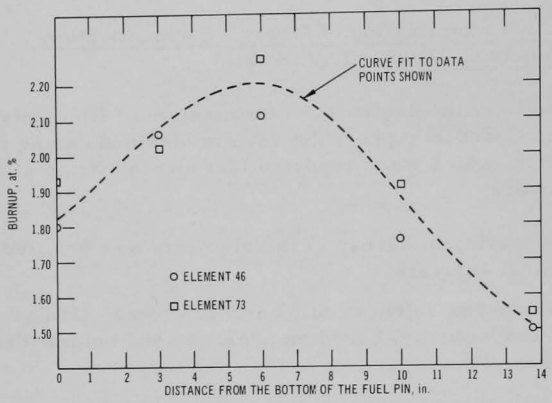

Fig. I.D.16
Burnup Profile for Mark-II Elements 46 and 73 from Subassembly C-2201S

Figure I.D.17 shows cross sections of samples of Element 46 taken at the bottom and at various distances from the bottom of the fuel pin. These cross sections show fuel-cladding contact near the midlength of the fuel pin, but not at the bottom. A longitudinal section taken at the top of the fuel pin also exhibited an annulus around the pin. The large void seen in two of the sections is a casting defect. Examination of cross sections of Element 73 also indicated fuel-cladding contact only in a region near the midlength of the fuel pin.

The microphotos in Fig. I.D.18 show the fuel-cladding interfaces in Element 46 where there has been contact between the fuel and the cladding. The microphotos of the same areas in Element 73 were similar. There is no evidence of interaction between the fuel and the cladding in either element. The microstructure of the fuel near the centerline of the elements is also shown in the figure. The fuel shows two and possibly three phases, but there is no evidence of an acicular phase. The acicular phase would indicate that the fuel had exceeded the gamma-phase transformation temperature (~640°C). Both the acicular phase and some large, well-defined voids were observed in one of the 93%-enriched Mark-II encapsulated elements (Element 25) in Subassembly X053 at about 2.2 at. % burnup. The microstructures of Elements 46 and 73 seem to indicate that these elements ran cooler than the highly enriched encapsulated elements. However, the differences between the microstructures of the encapsulated and the unencapsulated elements may be due, in some part, to the lower rate of swelling of the higher-silicon fuel in the unencapsulated elements.

Figure I.D.19 shows the microstructure of the cladding samples taken from the bottom and at various distances from the bottom of

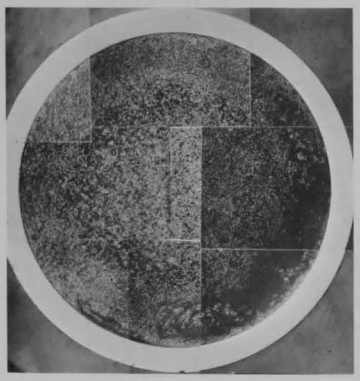

~15X

10 in. from Bottom

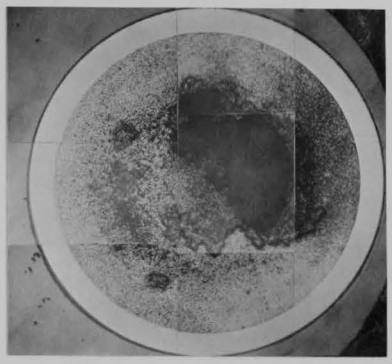

~15X

6 in. from Bottom

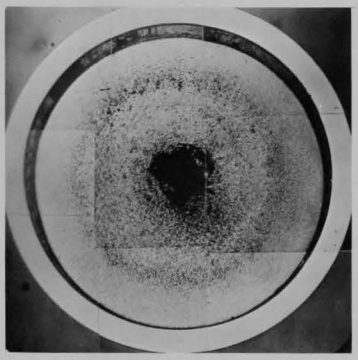

~15X

3 in. from Bottom

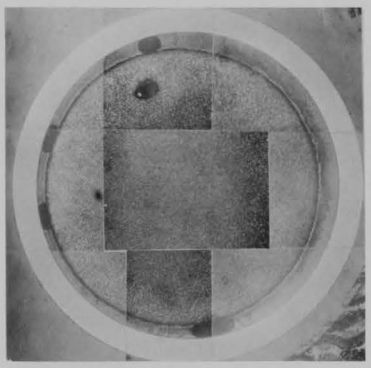

~15X

Bottom

Fig. I.D.17. Cross Sections of Mark-II Fuel Element 46 from Subassembly C-2201S (as-polished)

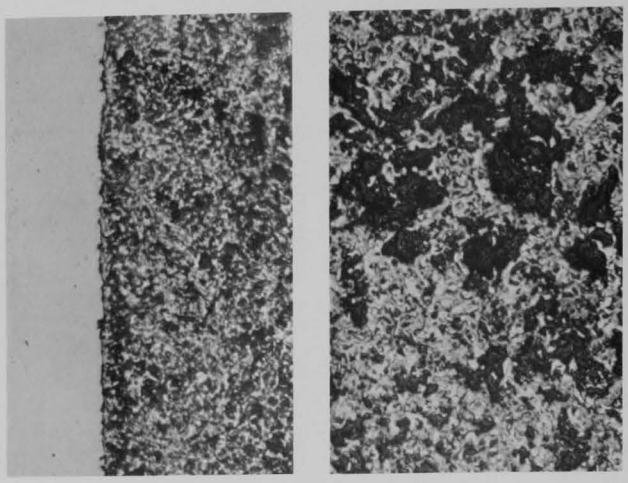

500X 500X

10 in. from Bottom

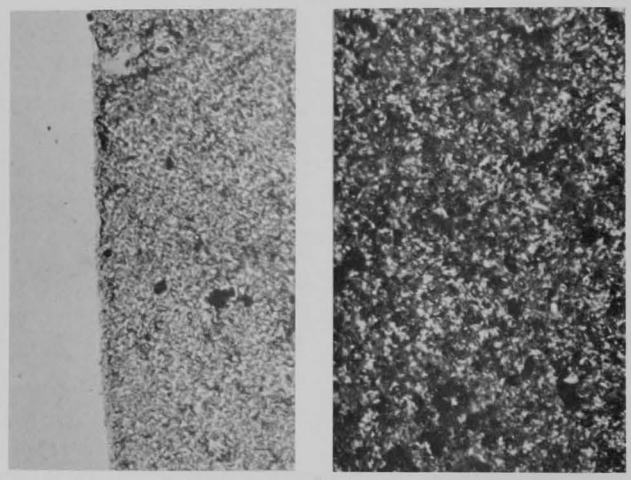

500X 500X

6 in. from Bottom

Fig. I.D.18. Photomicrographs of Typical Areas at the Fuel-Cladding Interface (left) and of the Fuel (right) near the Centerline of Element 46 from Subassembly C-2201S (as-polished)

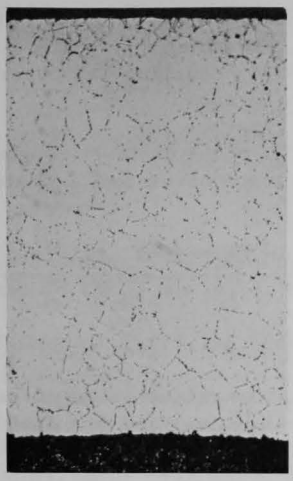

250X

10 in. from Bottom

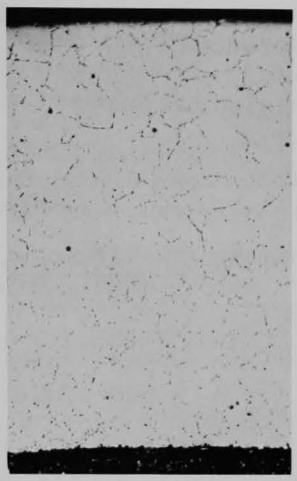

250X

6 in. from Bottom

250X

3 in. from Bottom

250X

Bottom

Fig. I.D.19. Photomicrographs of Cladding Samples from Element 46 of Subassembly C-2201S (electroetched with 665 cc lactic acid, 45 cc phosphoric acid, 30 cc water, and 10 cc dioxane)

the fuel pin in Element 46. These samples exhibited the normal degree of sensitization (similar to that observed in irradiated Mark-IA elements). No evidence of corrosion or grain-boundary cracking was observed. Again, the microstructures of Element 73 were similar.

In conclusion, the results of the destructive examination verify the results of the nondestructive examination and indicate that the elements are performing as predicted.

(ii) In-reactor Creep Experiments on Stainless Steel Tubing
(L. C. Walters, M. A. Pugacz, and C. M. Walter)

Last Reported: ANL-7688, pp. 129-131 (April-May 1970).

The results of three studies related to the in-pile creep experiments are reported here: (a) strain values and flux profiles for the capsules in the creep-test subassembly (X065) after the fourth irradiation; (b) temperature profiles of the capsules in the X065 subassembly, as obtained by a heat-transfer analysis; and (c) the relationship of hoop strain to temperature at constant hoop stress, as determined by out-of-pile experimentation.

(a) Strain Values and Flux Profiles. After the fourth irradiation, the capsules in Subassembly X065 had accumulated a maximum fast fluence (>0.1 MeV) of 7.6 x 10^{21} n/cm^2. The neutron-flux-enhanced creep is now readily apparent in the core region of the higher stressed capsules. Figure I.D.20 shows the outer diameters of Capsule 29 (hoop stress = 24.7 kpsi) in the preirradiated condition (lower plot) and after the fourth irradiation (upper plot).* The enhanced creep, indicated by the larger diameters in the core region, is readily apparent.

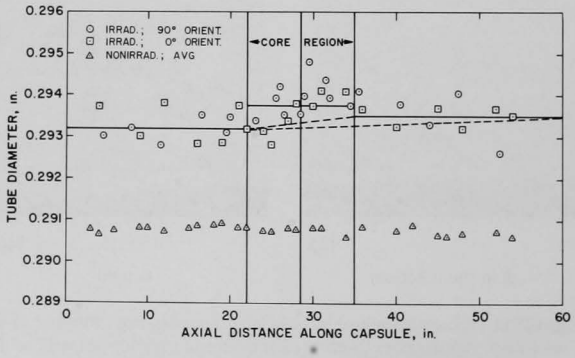

Fig. I.D.20. Pre- and Postirradiation Outer Diameters of Capsule 29 from Subassembly X065

*The significance of the solid and broken lines in Fig. I.D.20 is explained in the Progress Report for March 1970 (ANL-7679), pp. 78-79, where the method of analysis used for determining enhanced hoop strain is described.

Figure I.D.21 shows the enhanced hoop strain as a function of fluence for the capsules with the largest hoop stress. Also shown are the results of the strain analysis for a capsule with zero hoop stress. The results for this unstressed capsule show that neutron-induced swelling has not yet become an important factor.

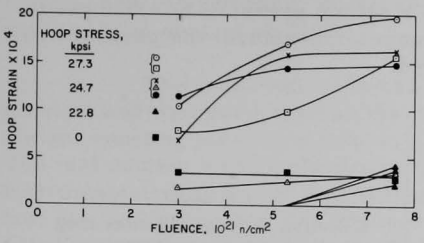

Fig. I.D.21. Hoop Strain vs Fluence for Capsules in Subassembly X065 (two capsules shown for 27.3 kpsi, three for 24.7 kpsi)

Figure I.D.22 shows the gamma scans along the lengths of five of the capsules. The number next to each curve indicates the relative position of the capsule in the subassembly. For example, 44 means that the capsule is located 44% of the distance across the subassembly, measured from the edge of the subassembly nearest the core center. The flux varies by about a factor of three across the subassembly.

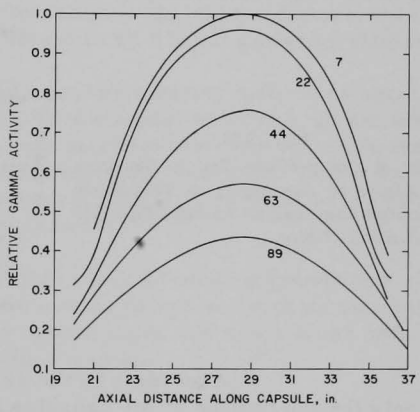

Fig. I.D.22
Results of Gamma Scans Taken along Five Capsules from Subassembly X065

(b) Temperature Profiles. The HECTIC computer code was used to determine the in-reactor temperature profiles along the creep capsules. The calculation made with that code takes into account the heat generation of adjacent subassemblies. Figure I.D.23 plots two examples of the results. The upper curve is representative of the temperature profile along the capsules near the outer edge of the subassembly; the lower curve is representative of the temperature profile along the capsules toward the center of the subassembly.

(c) Temperature Dependence of Hoop Strain. A test was made on the BRATT (biaxial rupture-anticipating tubing tester) to determine the hoop strain as a function of temperature at constant hoop stress.

A hoop stress of 27 kpsi was chosen as being representative of stresses on the irradiated capsules. The test consisted of bringing a 12-in. length of Type 304L stainless steel tubing (the same material used for the irradiated capsules) to temperature and imposing a helium pressure of 4,000 psi for 4 hr. The sample was then cooled to room temperature, the pressure released, and the outer diameter measured.

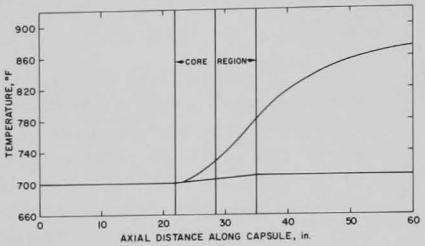

Fig. I.D.23

Calculated Temperature Profiles along Capsules in Subassembly X065

Figure I.D.24 shows the results of this test over the temperature range of 650-900°F. The temperature dependence is small below 850°F, but rises sharply above 850°F.

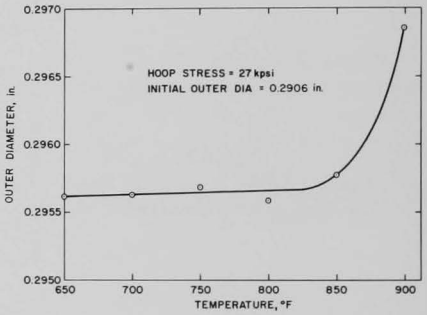

Fig. I.D.24

Results of Out-of-reactor Test to Determine Dependence of Hoop Strain on Temperature at Constant Hoop Stress for Annealed Type 304L Stainless Steel Tubing

According to the results from the heat-transfer analysis, only the top portion of the capsules near the outer edge of the subassembly reached 850°F or above. Therefore, the assumption made in the analysis of the in-reactor creep data (i.e., that a linear temperature gradient exists along the capsules and that the hoop strain is linearly dependent on temperature) appears to be justified.

8. Operation with Failed Fuel (R. R. Smith)

a. Studies of Transient Performance of Driver Fuel with Fuel-motion Monitor (A. A. Madson and R. M. Fryer)

Last Reported: ANL-7688, p. 133 (April-May 1970).

The first two of a series of TREAT transients have been performed with an axial-fuel-motion monitor installed in a Mark-I TREAT loop.

These two transients were designed to test the response of the motion transducer in the TREAT nuclear environment. The transients covered the expected energy range of future tests in this series and were initiated with the loop sodium at 700°F.

The fuel-motion fixture contained a stainless steel dummy fuel element and was positioned as the central pin of a seven-pin cluster. The six surrounding pins were hollow, argon-filled EBR-II Mark-IA jackets. The test section was shielded by a 0.030-in. dysprosium metal wrap. Instrumentation included four thermocouples (inlet and outlet sodium, central pin, and probe head) in addition to the motion transducer. The loop was filled with sodium coolant, heated to 700°F for the transients. This is the expected configuration that will be used with an actual EBR-II driver-fuel element installed in the motion fixture.

The first transient was of low power with a relatively slow reactor period of 2.6 sec. The peak power reached during this transient was 5 MWt. The second transient was of higher power with a reactor period of 0.62 sec. The peak power reached during this transient was 31 MWt. With a 52%-enriched fuel element installed in the motion fixture, this transient would be approximately equivalent to an EBR-II power level of 100 MWt.

The motion detector was operable during both transients; however, since a stainless steel dummy fuel element was used, no net motion was observed or expected. There was no observable difference in the transducer signal before, during, or after each transient. There was also no detectable difference in the transducer signal in relation to the difference in reactor power level of the two transients.

In its present configuration, the fuel-motion transducer should be able to measure a total axial fuel motion of 1/8-in. with an estimated accuracy of 20 to 25%. The next transient tests will use a fresh 52%-enriched, EBR-II Mark-IA driver-fuel element.

9. Hot Fuel Examination Facilities

a. Fuel Cycle Facility Improvements (M. J. Feldman)

(i) Filtration of Atmosphere of Argon Cell

Not previously reported.

The system for cooling and circulating the atmosphere of the argon cell consists of two independent subsystems (north and south). The cooling box, cooling coils, and circulating fan of each subsystem were installed in the subcell area of the Fuel Cycle Facility so that direct maintenance could be performed on the equipment. A bypass filter system using

AEC filters was installed as part of the south circulating system to reduce contamination of the subcell equipment by the radioactive particulates from the fuel-reprocessing operations. About 15% of the total atmosphere circulated was passed through the bypass filter. Nevertheless, with the amount of high-burnup fuel handled during hot-line operations, the radiation levels in the subcells rose to a point where contact maintenance work on the circulation fans is difficult to accomplish.

It was decided, therefore, to filter all the circulating atmosphere to prevent further particulate contamination of the subcell equipment. (The contamination already present would be reduced by a cleanup of the equipment.) Filters would first be installed on the north circulating subsystem. Of various filter media tested, "Dri Pak 100" filter cartridges (glass-fiber media) fabricated by the American Air Filter Company, Inc. were the most efficient (97.5%) for removing radioactive particulate. (Filter efficiencies were based on the removal of cerium-141-144 and zirconium-niobium-95, which are two of the major isotopes found in argon-cell contamination and are likely to exist as solid matter.) Mockup tests showed that a filter area of approximately 20 sq ft could be used without adversely affecting the horsepower requirements of the existing circulation fan or the performance of the cooling system.

The filter frame (with filters) was remotely installed in the argon cell and tied in with the inlet duct to the north circulating subsystem. The filter frame was attached to the cell liner with toggle clamps, which had been bolted to the liner; studs for the toggle clamps were remotely welded to the liner. The joint between the filter frame and the cell liner was sealed with felt (animal hair) gaskets. (Irradiation of felt samples to approximately 10^9 rad caused no apparent damage and to 2×10^{10} rad slightly reduced the ability of the felt to resist bending.)

The north circulating subsystem has operated satisfactorily with the filter installed.

Plans are being made to install a similar filtration system on the south circulating subsystem; this will eliminate the bypass filter. With the two filter systems installed, all recirculating argon will then be filtered.

(ii) Leaks in Atmosphere-circulating System of Argon Cell

Not previously reported.

Some small leaks developed in the atmosphere-circulating system of the argon cell while fuel-processing equipment was being removed from the cell. Attempts to locate and isolate the leaks by routine methods failed to isolate all the leaks. Therefore, isolating of individual pieces of

equipment and feedthroughs and covering of all penetrations with plastic were initiated. However, the concurrent disassembly of one piece of equipment unknowingly opened a major line to the cell, which caused a large leak of approximately 650 cfh. While the large leak was being searched for, sealing of all small penetrations and checking of all large penetrations were completed. Four small leaks and the large leak were located and isolated. A negative pressure was maintained in the cell during the two days of the large leak by pumping gas from the cell and discharging the gas through the HEPA filters to the 200-ft site stack. Operation of the atmosphere-control system has been acceptable since the leaks were isolated; apparently, all leaks have been located. The air content of the cell atmosphere increased gradually to approximately 20% during the period of small leaks. It increased rapidly to 80% during the period of the large leak.

No experiments being performed in the argon cell were affected by the change in atmosphere.

Preliminary procedures have been initiated that would lead to a replenishment of argon in the cell atmosphere beginning in July and a return to a normal atmosphere by early August.

10. Physics Mock-up Studies (D. Meneghetti)

Last Reported: ANL-7688, pp. 136-139 (April-May 1970).

(Experimental results for the ZPR-3 assemblies discussed here are reported in Sect. I.A.4.)

a. Calculated Effect of Modification of Upper Reflector on Reactivity in ZPR-3 Assembly 60 (D. Meneghetti and K. E. Phillips)

The worth of replacing the central nine matrix elements of the 18-in.-thick upper axial reflector with the composition of the 6-in.-thick upper axial gap was calculated using the 29-group cross-section set based on ENDF/B (Version I). Analysis was made by S_4 transport in two-dimensional, RZ geometry, using the DOT code. The area being replaced will have the composition of the gap (~25.5 vol % stainless steel, ~63 vol % sodium) instead of the composition of the reflector (~45 vol % stainless steel, ~42 vol % sodium).

The calculated worth of this substitution is -0.030% $\Delta k/k$. The experimental value reported in the Progress Report for March 1970 (ANL-7679, p. 18) is -0.024% $\Delta k/k$.

b. Calculated Change in Axial Reaction-rate Traverses Caused by Modification of Upper Reflector in ZPR-3 Assembly 60 (D. Meneghetti, D. G. Stenstrom, and K. E. Phillips)

The ratios of ^{238}U fission, ^{235}U fission, and ^{10}B capture axial reaction-rate traverses with the modified upper reflector relative to the corresponding traverses through the normal reference system have been calculated. Figure I.D.25 shows these calculated ratios together with experimental ratios deduced from the data for the modified and the reference reflector reported in ANL-7679 (pp. 21 and 23).

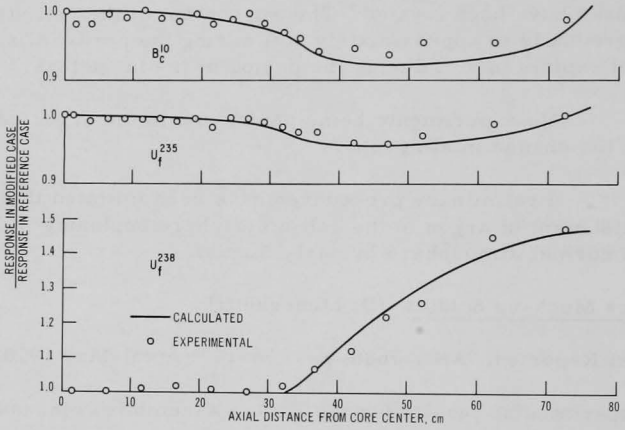

Fig. I.D.25. Calculated Effect of Modified Axial-reflector Composition on Reaction-rate Traverses in ZPR-3 Assembly 60

The introduction of the gap composition through the central nine drawers of the upper reflector augments the relative ^{238}U fission response toward the top because of the increased leakage of high-energy neutrons. The ^{235}U fission response in the modified case is slightly decreased, relative to the reference case, at the locale of normally large response near the interface of the gap and reflector. This relative decrease of response in the interval region is more evident in the ^{10}B capture rate.

Calculations show that the modification of the reflector region increases the leakage out of the total top of the system by about 4%. If the increase of leakage is assumed to occur through the central nine-drawer area of the 100-drawer area comprising the axial surface of the core, the increase in leakage density through the top surface of the central modified region is about 40-50%. The increase in leakage density of high-energy (>1.35 MeV) neutrons, however, is of the order of 300%.

E. EBR-II--Fuel Fabrication

1. Cold Line Operations (D. L. Mitchell)

Last Reported: ANL-7688, pp. 140-141 (April-May 1970).

Sixteen Mark-IA subassemblies containing vendor-fabricated elements were assembled in the cold line during this reporting period. As of June 15, 22,643 vendor-fabricated elements were available after verification inspection. (This figure does not include the vendor elements impact bonded by ANL.) Table I.E.1 summarizes the production activities for May 9 through June 15, 1970, and for fiscal year 1970.

TABLE I.E.1. Production Summary for FCF Cold Line

	5/9/70 through 6/15/70 Mark-IA Fuel		Totals for FY 1970 Mark-IA Fuel
Subassemblies Fabricated			
With cold-line elements	0		46
With vendor elements	16		53
Preirradiation Treatment of Vendor Fuel			
Impact bonding of unbonded elements (11,853[a])			
Impact-bonded, inspected, and accepted[b]	0		11,109
Impact-bonded, inspected, and rejected	0		734
Total Elements Available for Subassembly Fabrication as of 6/15/70			
Cold-line fuel: Mark IA		323	
Mark II		223	
Vendor fuel (Mark IA)		22,643[c]	

[a]This is the total number of unbonded vendor fuel elements scheduled for impact bonding by ANL. Ten unbonded elements were set aside as historical samples; all the rest have been impact-bonded.

[b]Thirty "accept" impact-bonded elements were set aside for historical samples, and 10 additional accepts were decanned for metallographic examination.

[c]Accepted by FCF verification inspection, but not yet approved for general use in the reactor. This figure does not include vendor elements that were impact-bonded by ANL.

Testing of a heat-treating procedure for reclaiming centrifugally bonded vendor fuel elements continued. For tests recently completed, the procedure reported last month was modified as to time at temperature and cooling procedure. The elements were heat-treated in two steps. First, they were held at 660 ± 10°C for 1 hr, argon-quenched (at 20-cfm flow) to 350°C, and then air-cooled slowly to room temperature. Next, they were heated again at 510 ± 10°C for 1 hr and then air-cooled slowly to room temperature. (The argon and air cooling in both steps was done in a vented, insulated chamber.) Of 97 vendor elements heat treated with the modified procedure, 94 were "accept" elements and three were "reject" elements.

(Of the three "reject" elements, two were rejected for size of bubbles and one for size of voids* in their sodium bond.) The reject elements may be reclaimed by impact bonding; or they may prove to be acceptable on the basis of the approved Revision 7 of Specification FCF-1. Heat treating of additional vendor elements with the modified procedure is planned.

F. EBR-II--Operations

1. Reactor Plant (G. E. Deegan)

Last Reported: ANL-7688, pp. 141-143 (April-May 1970).

Run 42, which was completed on May 18, was the longest period of operation for EBR-II without interruption. During the 22 days and 21.5 hr of operation for the run, 1139 MWd were accumulated. Operation (in Runs 42 and 43) during the present reporting period totaled 1077 MWd. The accumulated total of EBR-II operation is 36,213 MWd.

When the power level was at 35 MWt during the shutdown after Run 42, electrical power to the No. 1 primary-sodium pump began to increase while flow parameters remained unchanged. Because the conditions indicated possible binding of the pump or motor, the reactor was manually scrammed and the primary pumps were tripped. The pumps were then restarted, but there was no evidence of binding or loading of the motor. During an 8-hr test period with the pumps at 100% flow, all indications remained normal. The pumps were shut down after that period, and cleaning of the seal trough of the large plug was begun.

After the seal trough had been cleaned, the reactor was loaded for Run 43. An approach to critical was made, but the reactor was shut down because of insufficient excess reactivity. After a loading adjustment was made, the reactor was restarted. Noise-analysis tests were made as part of the instrumented-subassembly experiment. Routine zero-power physics tests also were made, after which the reactor power was raised to 50 MWt.

Soon after steady-power operation had been achieved, the turbine generator was purposely separated from the 138-kV loop because thunderstorms were expected to cause voltage disturbances. The generator breaker subsequently opened on underfrequency, and the reactor scrammed. The underfrequency condition apparently was caused by an additional load being applied to the system while the turbine-load limit was set at approximately the existing site load.

---

*Rejection for void size was based on the definition in Revision 6 of Specification FCF-1, Product Specification for the EBR-II Elements. Revision 7 of this specification, which allows acceptance of larger void sizes (radial widths of 125 mils) than does Revision 6, has been approved, but the present sodium-bond testers can measure voids with radial widths of up to only about 80 mils. New sodium-bond testers are being procured to measure the larger voids acceptable under Revision 7.

Operation at 50 MWt resumed and, except for brief reductions in power for an experiment and for maintenance of a condenser-cooling-water pump, continued until June 13. At that time, a thunderstorm caused automatic separation of the turbine generator from the 138-kV loop. The nuclear continuous power supply dropped out of parallel at the time of separation; when an attempt was made to reparallel, the reactor scrammed. A voltage perturbation during the reparalleling apparently caused the scram. The reactor was restarted, and Run 43 is continuing.

Fuel handling during this period consisted of the loading changes for Run 43. These changes involved experimental subassemblies, as reported under Sect. I.D.3.a above, and also included the following. Removed from grid: one controlled-flow, driver-fuel surveillance subassembly; two Mark-II-fuel surveillance subassemblies; four vendor-fuel surveillance subassemblies; and two depleted-uranium, inner-blanket surveillance subassemblies. Installed: two centrifugally bonded and one impact-bonded vendor-fuel surveillance subassemblies.

2. Fuel Cycle Facility (M. J. Feldman)

a. Surveillance (M. J. Feldman, J. P. Bacca, and E. R. Ebersole)

Last Reported: ANL-7688, pp. 143-148 (April-May 1970).

(i) Postirradiation Analysis of EBR-II Fuel (J. P. Bacca)

(a) Surveillance of Vendor-produced Fuel (A. K. Chakraborty and G. C. McClellan)

(1) Fuel-characterization Studies

(A) Subassembly C-2263. This subassembly is the third of eight qualification subassemblies containing fuel cast by the vendor and impact-bonded by ANL to be examined following irradiation in the reactor. The other two subassemblies were C-2261 (0.85 at. % burnup) and C-2260 (1.50 at. % burnup). Subassembly C-2263 attained a peak burnup of 1.70 at. % at the end of Run 42. It contained 85 fuel elements (from five different casting batches) that had been cast by the vendor and impact-bonded by ANL, as well as six elements produced in the cold line of the Fuel Cycle Facility.

Postirradiation eddy-current bond testing of 29 of the vendor-cast elements revealed no axial shortening of the fuel from its original as-fabricated length of 13.5 in. Fuel swelling for these 29 elements averaged 9.3% and ranged from 5.2 to 13.4%. This amount of swelling is similar to that observed in the past for ANL-produced fuel elements after comparable burnup. Table I.F.1 summarizes the swelling data.

TABLE I.F.1. Summary of Postirradiation Examinations of Fuel Elements from Subassembly C-2263[a]

(Calculated Burnup: 1.70 at. % max)

Injection-casting Batch No.	Number of Elements Examined	Silicon Content of Fuel, ppm	Burnup Range, at. %	Total Volume Fuel Swelling (ΔV/V), %		Cladding-diameter Changes		
						Number of Elements Diameter Measured	Maximum Cladding-diameter Change (ΔD/D), %	
				Average	Range		Average	Range
				Vendor Fuel				
AG 585	10	430	1.61-1.67	11.30	6.8-13.4	4	0.46	0.37-0.56
AG 586	3	450	1.59-1.65	10.97	9.3-13.4			
AG 587	5	490	1.57-1.66	8.20	6.5-9.8	1	0.40	-
AG 589	6	510	1.59-1.68	6.26	5.2-6.8	1	0.43	-
AG 590	5	500	1.59-1.68	8.10	6.7-8.8			
				ANL Cold-line Fuel				
145 I	2	480	1.66-1.69	6.70	6.6-6.7			

[a]Contained 85 fuel elements cast by vendor and impact-bonded by ANL as well as six elements produced in the cold line. This subassembly is the third of eight qualification subassemblies containing vendor fuel that had been impact-bonded by ANL.

Diameter surveys of the vendor elements indicated peak diameter increases ($\Delta D/D$) ranging from 0.37 to 0.56%. These increases, summarized also in Table I.F.1, are somewhat higher than those observed in the past for ANL-produced fuel elements after similar burnup. This trend was also observed earlier for impact-bonded vendor fuel elements after they had been irradiated to 1.5 at. % burnup in qualification subassembly C-2260. The increases in diameter of the six elements from C-2263 are greater than those that can be attributed to irradiation swelling of the stainless steel cladding only. Additional measurements and tests of elements from C-2263 are being initiated to provide more information on the causes of the larger diameter increases.

(2) Study of the Transformation Kinetics for Vendor-produced Fuel (A. K. Chakraborty)

A study has been made to provide data on the transformation kinetics of U-5 wt % driver fuel produced by the vendor--Aerojet-General Corporation (AGC). These data were used in developing a corrective heat-treating program (see Sect. I.E.1) to reclaim some 23,000 centrifugally bonded, AGC-produced elements now at ANL before they are used in EBR-II. Samples from the top and bottom regions of selected nonirradiated AGC fuel pins were subjected to hardness, density, and electrical resistivity measurements, metallographic examinations, and X-ray diffraction analysis. The results of this study are summarized under (A), (B), and (C) below.

(A) Transformation of the As-cast Alloy Structure to $\alpha + \delta + U_2Ru$ Phases at 500°C. Changes with time in Vickers Hardness Number, electrical resistivity, and density were determined for samples

from as-cast AGC pin 302 while the samples were subjected to isothermal annealing at 500°C. Figure I.F.1 shows the results of these measurements. These data, sustantiated by X-ray diffraction patterns, indicate that transformation of the as-cast $\gamma + U_2$ Ru phases to the $\alpha + \delta + U_2$ Ru phases is essentially complete after 20 min.

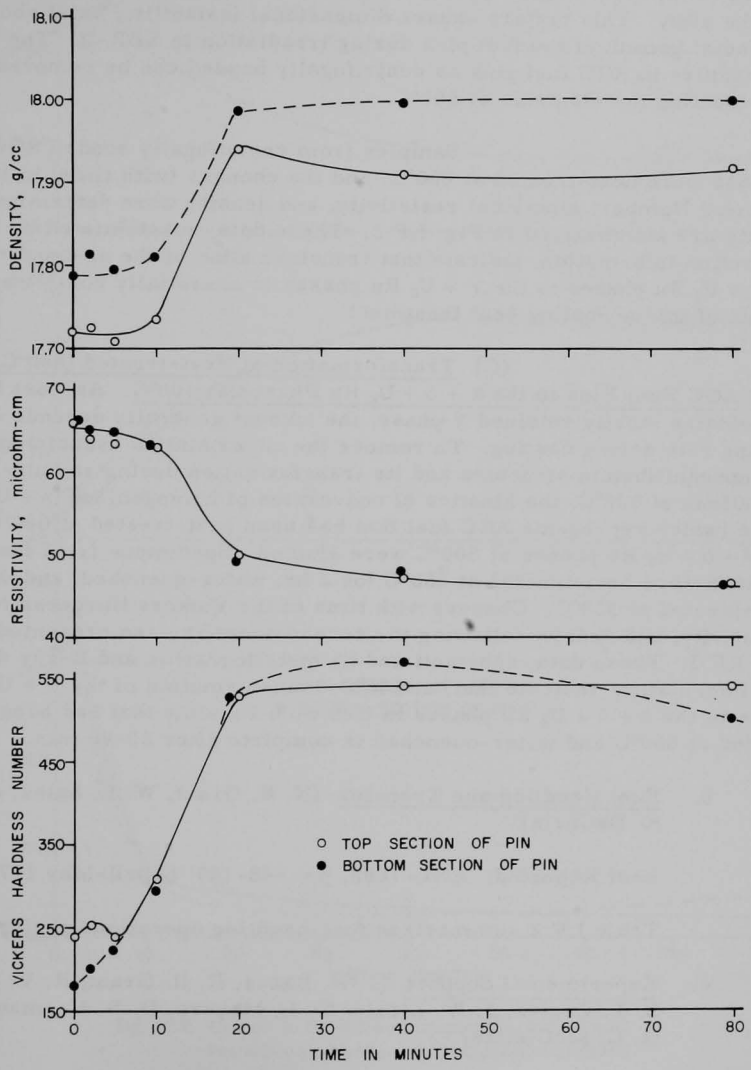

Fig. I.F.1. Changes in Properties of As-cast AGC Pin 302 during Isothermal Transformation at 500°C

(B) Transformation Kinetics of As-bonded Fuel Pins at 660°C. During centrifugal bonding at 480 to 500°C, the as-cast U-5 wt % Fs alloy transforms to the $\alpha + \delta + U_2$ Ru phases. This transformation, which takes place while significant compressive stresses are being applied in the centrifugal bonder, introduces a texture (preferred orientation) into the alloy. This texture causes dimensional instability, axial shortening, and radial growth of the fuel pins during irradiation in EBR-II. The undesirable texture in AGC fuel pins as centrifugally bonded can be removed by heat-treating the elements at 660°C.

Samples from centrifugally bonded AGC pin 4618 were heat-treated at 660°C, and the changes (with time) in Vickers Hardness Number, electrical resistivity, and density were determined. The results are summarized in Fig. I.F.2. These data, substantiated by X-ray diffraction information, indicate that transformation of the as-bonded $\alpha + \delta + U_2$ Ru phases to the $\gamma + U_2$ Ru phases is essentially complete after 40 min of this annealing heat treatment.

(C) Transformation of Heat-treated (660°C for 2 hr) AGC Fuel Pins to the $\alpha + \delta + U_2$ Ru Phases at 500°C. As-cast U-5 wt % Fs contains mostly retained γ phase; the amount generally depends upon the cooling rate during casting. To remove the uncertainties associated with this nonequilibrium structure and its transformation during sodium-bonding operations at 500°C, the kinetics of conversion of homogenized $\gamma + U_2$ Ru phase (which represents AGC fuel that has been heat-treated at 660°C) to the $\alpha + \delta + U_2$ Ru phases at 500°C were studied. Specimens from fuel pin 4618 were heat-treated at 660°C for 2 hr, water-quenched, and then heat-treated at 500°C. Changes with time of the Vickers Hardness Number, resistivity, and density following the second annealing are presented in Fig. I.F.3. These data, substantiated by metallographic and X-ray diffraction information, indicate that, at 500°C, transformation of the $\gamma + U_2$ Ru phase to the $\alpha + \delta + U_2$ Ru phases in U-5 wt % Fs alloy that had been heat-treated at 660°C and water-quenched is complete after 20-40 min.

b. Fuel Handling and Transfer (N. R. Grant, W. L. Sales, and K. DeCoria)

Last Reported: ANL-7688, pp. 148-149 (April-May 1970).

Table I.F.2 summarizes fuel-handling operations performed.

c. Experimental Support (J. P. Bacca, N. R. Grant, R. V. Strain, S. T. Zegler, J. W. Rizzie, C. L. Meyers, D. B. Hagmann, and G. C. McClellan)

Last Reported: ANL-7688, pp. 148-152 (April-May 1970).

Subassemblies X027, X038, X040A, X050, and X065C were received from the reactor and dismantled.

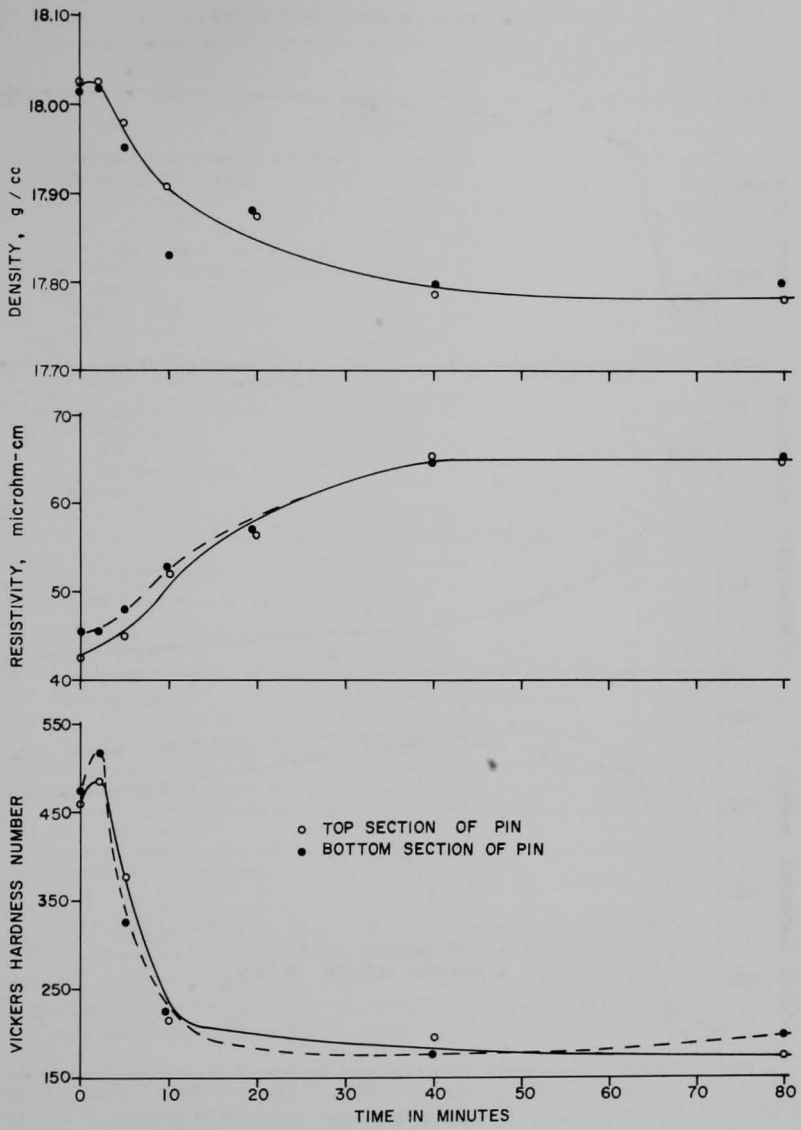

Fig. I.F.2. Changes in Properties of Centrifugally Bonded AGC Pin 4618 during Isothermal Transformation at 660°C

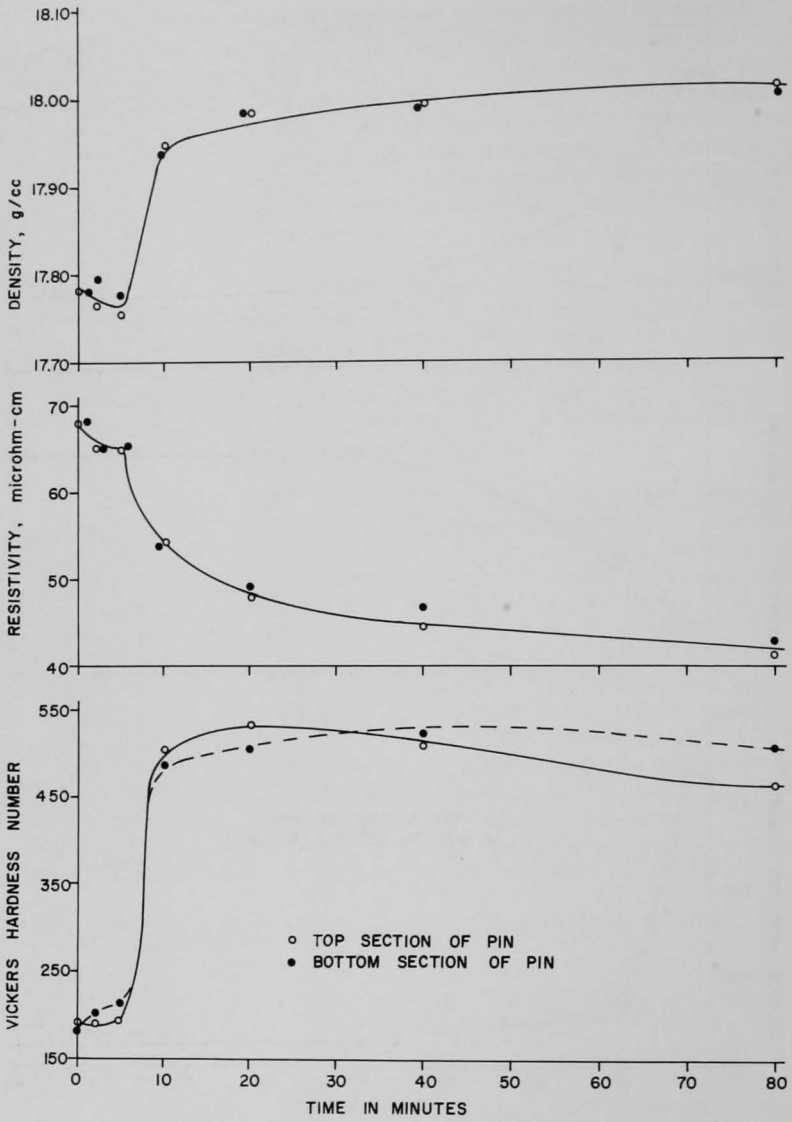

Fig. I.F.3. Changes in Properties of AGC Fuel Pin 4618 during Isothermal Transformation at 500°C. Specimens had been initially heat-treated at 660°C for 2 hr and then water-quenched.

TABLE I.F.2. Summary of FCF Fuel Handling

	5/9/70 through 6/15/70	Totals For FY 1970
Subassembly Handling		
Subassemblies received from reactor		
Driver fuel (all types)	18	141
Experimental	5	24
Other (blanket)	3	10
Subassemblies dismantled for surveillance, examination, or shipment to experimenter		
Driver fuel	5	69
Experimental	5	24
Other (blanket)	1	5
Driver-fuel elements to surveillance	188	3,398
Number from subassemblies	4	68
Subassemblies transferred to reactor		
Driver fuel		
From air cell	0	21
From cold line[a]	13	105
Experimental	4	16
Fuel-alloy and Waste Shipments		
Cans to burial ground	0	19
Skull oxide and glass scrap to ICPP	0	5
Recoverable fuel alloy to ICPP		
Fuel elements	2 (32.94 kg of alloy)[b]	24 (416.35 kg of alloy)
Subassemblies	5 (21.50 kg of alloy)	52 (268.40 kg of alloy)
Nonspecification material	0	0

[a]Cold-line subassemblies, following fabrication and final tests, are transferred either to the reactor or to the special-materials vaults for interim storage until needed for use in the reactor.

[b]Figure outside parentheses is number of shipments made. Figure inside parentheses is weight of alloy shipped.

Interim examination for Subassembly X027, which contained 18 GE encapsulated mixed-oxide elements (8.5 at. % burnup) and one PNL structural element, has been started. The examination will include neutron radiography; measurements of diameter, weight, bowing, and length; gamma scans; and stereomacroscopic examinations.

Subassembly X038 contained only structural samples in its Mark-B7 capsules and had been irradiated to a calculated total fluence of 3.8×10^{22} nvt. The capsules will be given a short terminal examination and returned to the experimenter.

For Subassembly X040A, interim examination of 18 ANL (peak burnup to 6.1 at. %) and 16 GE (peak burnup to 5.8 at. %) mixed-oxide elements was started.

In the examination of Subassembly X050, eight GE capsules containing mixed-oxide elements (average burnup for lead element, 11.3 at. %) will be neutron-radiographed, weighed, and shipped to the experimenter along with four GE structural elements (calculated total fluence of 9.6×10^{22} nvt). The subassembly also contained two Westinghouse encapsulated mixed-carbide elements (5.4 at. % average burnup) and five ORNL encapsulated mixed-oxide elements (5.4 at. % average burnup). These capsules will be examined and stored.

The changes in diameter of the 21 helium-pressurized structural elements in Subassembly X065C were measured in their fourth interim examination (cumulative calculated total fluence of 7.6×10^{21} nvt). Gamma scans were made of six of the 21 elements. Five other elements from this subassembly contained temperature monitors based on sodium expansion; these elements were opened to recover the monitors, which are being stored until they are shipped to the experimenter.

An attempt was made to assemble Subassembly X080 in the air cell. This subassembly was scheduled to contain 15 Mark-A capsules of NUMEC mixed-oxide fuel (average burnup, 10 at. %) from Subassembly X012A and for Mark-A capsules of GE structural elements (calculated total fluence, 1.0×10^{22} nvt) from X039. The diametral distance between the dimples in the shroud tubes in the upper preassemblies had been increased from 0.380 to 0.392 in. for the first 20 in. of shroud length to accommodate the increased diameter of the fueled capsules. Some bowing was noticeable in three of the capsules from Subassembly X012A, but the amount of bowing was not measured. After the capsules had been loaded on the grid, the upper preassembly was lowered until the bottom of the hexagonal tube was just above the grid. At this time, the hexagonal tube was observed to be offset from the grid, and the bottoms of many of the capsules were shifted to one side of the grid rather than being evenly spaced. Efforts to align the hexagonal tube with the grid were not successful, so the upper preassembly was removed from the capsules. Examination showed that the lower ends of the shroud tubes had been damaged. A few of the shroud tubes were elongated. The damage probably was caused by the misalignment of the capsules because of their bow. The capsules will be reexamined soon; bowing will be measured. A maximum capsule bow possibly will have to be specified for acceptance for reassembly.

Subassembly X081 was loaded with nine GE capsules containing mixed-oxide fuel elements previously irradiated in Subassembly X020 (average burnup, 6.0 at. %) and two dummy elements. For the other eight positions in the subassembly, the shroud tubes were replaced with solid stainless steel rods; therefore, the coolant in the subassembly will flow only through 11 shroud tubes. Because of the increased diameter of the capsules, the diametral distance between the dimples in the bottom 20 in. of the shroud tubes was increased to 0.392 in. The subassembly has been transferred to the reactor.

Subassembly X082 (Mark-E61 type) was assembled with driver-fuel elements previously irradiated in three other subassemblies: 20 elements from C-2186S (maximum of 1.23 at. % burnup), 20 elements from C-2187S (maximum of 1.50 at. % burnup), and 21 elements from C-2188S (maximum of 1.76 at. % burnup). The diameters of all 61 elements were measured. This subassembly was transferred to the reactor.

Subassembly X087 was loaded with 61 unirradiated PNL mixed-oxide elements, flow-tested, and transferred to the reactor. This was the first Mark-B61A irradiation subassembly to be assembled.

Subassembly X088 was loaded with 19 unirradiated Westinghouse capsules containing mixed-oxide fuel elements and transferred to the reactor.

d. Reactor Support (N. R. Grant and J. P. Bacca)

Last Reported: ANL-7688, p. 152 (April-May 1970).

A program has been initiated to examine each safety rod removed from position 3A1 of the reactor to detect any sign of mechanical interference between the safety rod and its guide thimble. This guide thimble is the original unit and has been subjected to a very high neutron fluence ($>1 \times 10^{23}$ n/cm^2 total). The first safety rod (Subassembly S-620) examined in this program was removed from position 3A1 after Run 41. Visual examination revealed nothing that would indicate mechanical interference between the subassembly and its guide thimble. Straightness measurement of the safety rod was well within specification. Flat-to-flat measurements of the hexagonal tube at four axial locations, however, ranged from 1.905 to 1.922 in. (Specification maximum is 1.912 in.)

PUBLICATIONS

Pilot-lot Fabrication of ZPPR Oxide-rod Elements
J. E. Ayer, A. G. Hins, and F. D. McCuaig
ANL-7649 (Jan 1970)

Loading Diagrams for Experimental Subassemblies Irradiated in EBR-II Runs 5 through 42
J. C. Case, Comp.
ANL/EBR-015 (May 1970)

Symptoms and Detection of a Fission-Product Release from an EBR-II Fuel Element. Case 1. Defect above Fuel Elevation
R. M. Fryer, E. R. Ebersole, P. B. Henault, and R. R. Smith
ANL-7605 (Jan 1970)

BOW-V: A CDC-3600 Program to Calculate the Equilibrium Conditions of a Thermally Bowed Reactor Core
D. A. Kucera and D. Mohr
ANL/EBR-014 (Jan 1970)

Evaluation of Materials-Compatibility Problems in the EBR-II Reactor
W. E. Ruther, T. D. Claar, and R. V. Strain
Corrosion by Liquid Metals. Plenum Press, New York, 1970, pp. 81-96

Irradiations Work at EBR-II
P. G. Shewmon
Fast Reactor Irradiation Testing, Proc. Int. Conf., Thurso, Caithness, Scotland, April 14-17, 1969. UKAEA Report TRG-1911(R), pp. 220-224

Application of Thermodynamic and Kinetic Parameters of the V-O-Na System to the Sodium Corrosion of Vanadium-Base Alloys
D. L. Smith and T. F. Kassner
Corrosion by Liquid Metals. Plenum Press, New York, 1970, pp. 137-149

The following appeared as abstracts in Trans. Am. Nucl. Soc. 13(1) (June 1970):

Measured Fission Yields of ^{99}Mo and ^{140}Ba in Fast-Neutron-Induced Fission of ^{239}Pu
R. J. Armani, R. Gold, R. P. Larsen, and J. H. Roberts*
p. 90

Low-Energy Limitations on Proton-Recoil Spectroscopy through the Energy Dependence of W
E. F. Bennett
p. 269

Plant Performance of EBR-II at 62.5 MW(th)
H. W. Buschman, J. F. Koenig, and W. H. Perry
p. 360

Dynamic Simulation and Analysis of EBR-II Rod-Drop Experiments
A. V. Campise
p. 353

βeff Measurements in Two Fast Reactor Critical Assemblies
S. G. Carpenter, J. M. Gasidlo, and J. M. Stevenson
p. 92

*Macalester College.

Comparison of Measured and Calculated Capture-to-Fission Ratios in a Soft Spectrum Fast Critical Assembly
M. M. Bretscher, J. M. Gasidlo, and W. C. Redman
p. 89

Speed Tests on Some Control Computers
C. E. Cohn
p. 177

Level Distribution of Count Rate Meters for Various Circuit Parameters Not Giving Gaussian Distributions
W. C. Corwin, K. G. Porges, and R. T. Daly
p. 241

Performance of the EBR-II Reactor at 62.5 MW(th)
R. A. Cushman, R. W. Hyndman, J. K. Long, and L. B. Miller
p. 359

Compton Recoil Measurement of Continuous Gamma-Ray Spectra
R. Gold
p. 421

A Postanalytical Study of Eight ZPR-3 Benchmark Criticals Using ENDF/B Data
A. L. Hess, R. G. Palmer, and J. M. Stevenson
p. 288

Analysis of Sodium-Void Coefficients
R. A. Karam and J. E. Marshall
p. 254

An Integral Measurement of ^{239}Pu Alpha
W. Y. Kato, R. J. Armani, R. P. Larsen, P. E. Moreland,
L. A. Mountford,* J. M. Gasidlo, R. J. Popek, and C. D. Swanson
p. 88

The Intermediate Structure of the Fission Width of ^{239}Pu
Y. Kikuchi
p. 312

Application of the BEMOD Fuel-Element Modeling Code to EBR-II Blanket Elements
J. F. Koenig, V. G. Eschen, and C. M. Walter
p. 126

BOW-V, Program to Calculate Subassembly Configurations of a Thermally-Bowed Reactor Core
D. A. Kucera and D. Mohr
p. 348

*Atomics International.

The Effects of S/N Ratio on the Results of Polarity Correlation Experiments
W. K. Lehto and R. W. Goin
p. 271

Comparison of Measured and Calculated Null Compositions, Central Reaction Ratios, and Reactivity Worths in ZPR-9 Assemblies 24 and 25 and ZPR-3 Assembly 55
L. G. LeSage, C. E. Till, and G. S. Stanford
p. 93

Heat Transfer in Heterogeneous UO_2-PuO_2 and UC-PuC Fuels in EBR-II
R. K. Lo and N. A. McNeal
p. 342

Structural-Subassembly Spectra Using Spatially Dependent and Spatially Independent Cross-Section Averagings
D. Meneghetti and K. E. Phillips
p. 256

Detailed Analysis of Space-Dependent Phenomena
L. B. Miller and R. E. Jarka
p. 307

Testing of Heterogeniety Methods Used in Fast Reactor Critical Analyses by Comparison with Theoretical (GEDANKEN) Experiments
R. G. Palmer, J. P. Plummer, and R. B. Nicholson
p. 253

Environmental Neutron Measurements with Solid-State Track Recorders
J. H. Roberts,* F. J. Congel,* R. J. Armani, R. Gold, J. Kastner, and B. G. Oltman
p. 419

^{239}Pu Doppler Analysis for a Proposed ZPR-3 Assembly
V. C. Rogers
p. 320

Effects of Cross-Section Averaging Spectra on the Worth of Reflectors for Fast Reactors
B. R. Sehgal
p. 257

Neutronic and Thermal-Hydraulic Characteristics of a High-Worth Control Rod for EBR-II
B. R Sehgal and R. K. Lo
p. 343

*Macalester College.

Behavior of In-Core Structural Components--EBR-II
P. G. Shewmon
p. 114

Liquid Organic Fast-Neutron Detector Assembly
G. G. Simons and J. M. Larson
p. 429

The Instrumented Subassembly System in EBR-II
A. Smaardyk, C. J. Divona, and E. Hutter
p. 355

Postirradiation Examination of EBR-II Tantalum-Clad Antimony Neutron Sources
R. V. Strain, V. G. Eschen, and D. C. Cutforth
p. 99

The Demonstration Reactor Benchmark Critical Assemblies Program
C. E. Till and W. G. Cavey
p. 293

A Formulation of High-Order Perturbation Theory for Critical Systems
A. Travelli
p. 186

Analysis of Reactivity Changes Associated with Large Perturbations in ZPPR/FTR-2
A. Travelli, A. J. Ulrich, and J. C. Beitel
p. 321

A Hydrogen Monitor for Detecting Leaks in LMFBR Steam Generators
D. R. Vissers, J. T. Holmes, and P. A. Nelson
p. 96

Application of X-Ray Texture Studies to Explain the Anomalous Performance of Centrifugally Bonded EBR-II Driver Fuel
C. M. Walter, M. H. Mueller, and J. P. Bacca
p. 95

Comparison between BEMOD Modeling Code Predictions and Observed Performance of EBR-II Driver Fuel
C. M. Walter, J. P. Bacca, and W. N. Beck
p. 125

EBR-II In-Pile Creep Experiments on Stainless Steel Tubing
L. C. Walters, C. M. Walter, M. A. Pugacz, J. A. Tesk, R. Carlander, and C-Y. Li
p. 145

High-Energy Limitations in Neutron Spectrometry with Proton-Recoil Proportional Counters
T. J. Yule
p. 269

II. OTHER FAST REACTORS--OTHER FAST BREEDER REACTORS--FUEL DEVELOPMENT

A. Irradiation Effects, Mechanical Properties and Fabrication

1. Irradiation Effects on Creep of FFTF-specified Type 316 Stainless Steel (R. Carlander and J. A. Tesk)

Not previously reported.

Specimens of Type 316 stainless steel are being heat-treated to develop different microstructures in the material for use in ex-reactor, postirradiation, and in-pile pressurized tube creep experiments. An attempt will be made to develop the following microstructures: (1) fine grain size (ASTM 7-8), (2) coarse grain size (ASTM 3-4), (3) carbide precipitates in the grain boundaries, and (4) carbide precipitates in both the grain boundaries and the matrix.

Test specimens of 20% cold-worked Type 316 stainless steel were sealed in quartz tubes under a partial pressure of helium and treated under varying conditions of temperature, time, and rate of quench to develop the microstructures listed previously. An ASTM grain size of 7.2 was produced in the material by solution annealing at 1020°C for 20 min followed by a rapid water quench. A grain size of 3-4 was produced by solution annealing at 1250°C for 1 hr followed by a rapid water quench. Two of the Garofalo* heat treatments are being utilized to develop the carbide precipitation in the matrix. Both treatments result in variations in the size and distribution of carbides precipitated on dislocations within the matrix. One treatment consists of heating the 20% cold-worked stainless steel for 24 hr at 480°C. The second treatment follows the same procedure, except that the samples are heated for an additional 216 hr at 705°C. The heat treatments necessary to precipitate carbides in grain boundaries and in both the grain boundaries and the matrix of fine and coarse grain-size Type 316 stainless steel will be developed.

Fourteen samples of Type 316 stainless steel tubing (0.230-in. OD, 0.015-in. wall, and 37 in. long) were solution-annealed at 1020°C for 20 min and water-quenched to provide specimens for ex-reactor control and in-reactor creep experiments. Thirteen of the samples were successfully heat-treated in the previously described manner. One specimen oxidized because a leak developed in the quartz capsule during heat treatment.

---

*Garofalo, F., VonGemmingen, F., and Domis, W. F., The Creep Behavior of an Austenitic Stainless Steel as Effected by Carbides Precipitated on Dislocations, Trans. ASM 54, 430 (1961).

2. Mechanical Properties of Austenitic Stainless Steel (R. Carlander)

Last Reported: ANL-7661, p. 85 (Jan 1970).

Specimens of Type 304 stainless steel are being irradiated in the EBR-II experimental subassembly X034 at design temperatures of 480, 590, and 705°C. The effects of the different neutron spectrums of the ETR and the EBR-II on the postirradiation mechanical properties will be determined.

Three deadweight creep testers are being installed to test the irradiated specimens. Three additional machines to test unirradiated, aged specimens are scheduled for installation about July 15. The manufacture of a grinding fixture to produce additional test specimens for the ex-reactor control studies has been initiated.

The tentative test program is shown in Table II.A.1. The same test conditions will be used for unirradiated control specimens, unirradiated-and-aged control specimens, and irradiated specimens. The exact test conditions will be established by discussions between ANL and PNL. PNL is conducting a study of the effects of neutron spectrum on Type 316 stainless steel irradiated in the same experimental capsules as the Type 304 stainless steel specimens.

TABLE II.A.1. Tentative Test Program--Spectrum Effects on Type 304 Stainless Steel

Irradiation and Test Temperature	Type of Test	Strain Rate, min^{-1}	Time to Produce Rupture at a Given Stress, hr
480	Tensile	0.01	-
480	Tensile	0.001	-
480	Creep	-	100
590	Creep	-	10
590	Creep	-	100
590	Creep	-	1,000
705	Creep	-	10
705	Creep	-	100
705	Creep	-	1,000

PUBLICATION

The Effect of Fast Neutron Irradiation on the Tensile Properties of Type 304 Stainless Steel
R. Carlander and S. D. Harkness
Abstract Bull. IMD-AIME 4(1), 178 (May 1970)

III. GENERAL REACTOR TECHNOLOGY

A. Applied and Reactor Physics Development

1. Theoretical Reactor Physics--Research and Development

a. Theoretical Reactor Physics

(i) Cross Section Data Evaluation (E. M. Pennington and D. A. Meneley)

Last Reported: ANL-7661, p. 88 (Jan 1970).

A new version of ETOE, which can handle all the new formats involved in Version II ENDF/B cross-section data, has been made operable on the IBM System 360. The format changes pertain to inelastic scattering, unresolved resonance parameters, minimum ENDF/B File 2 data for materials without resonance parameters, and fission spectra.

For inelastic scattering, cross sections for scattering to various resolved levels and the continuum may now be given in File 3, with only the nuclear temperature for continuum scattering being given in File 5. Formerly, the total inelastic cross section was given in File 3, and probabilities for scattering to individual levels and the continuum were given in File 5. Also, new MT numbers for individual level and continuum scattering have recently been introduced. ETOE can now treat inelastic scattering data presented in either the new or the old formats.

Unresolved resonance parameters may now be given in a format in which all widths and level spacings are functions of energy. Originally, only the fission widths could be energy-dependent. Changes were made in ETOE to handle the new formats, and corresponding changes were made in MC^2. The MC^2 changes were required, since changes were necessitated in the format of the resonance file of the MC^2 library produced by ETOE.

For materials having no ENDF/B resolved or unresolved resonance parameters, a minimum amount of data, which allows the calculation of the potential scattering cross section, has been introduced into ENDF/B File 2. ETOE will now calculate σ_p from these data rather than using an input value.

The MC^2 code can use only ENDF/B fission spectra with laws LF = 6 or 8, in which nuclear temperatures are constant. New ENDF/B data contain spectra with laws LF = 7 and 9, which correspond to LF = 6 and 8, except that nuclear temperatures are energy-dependent. For such materials, ETOE treats the nuclear temperatures as being constant and having the value at the lowest energy of the tabulation.

As mentioned above, the new ENDF/B unresolved resonance formats forced changes in the resonance file of the MC^2 library. Thus the MERMC2 code, which merges MC^2 libraries, was changed to allow the new formats.

Version II ENDF/B tape 201 was received from Brookhaven. This tape contains data for ten fissionable materials. The tape was corrected using CRECT (according to a memo from Marvin Drake of BNL) to yield revision 1 of tape 201. Then the data were processed through DAMMET and ETOE to produce a 10-material MC^2 library. A test MC^2 problem was run using these data. The problem was the GODIVA assembly, which contains only ^{234}U, ^{235}U, and ^{238}U, and is one of the 10 assemblies chosen for ENDF/B data testing.

(ii) Reactor Computation and Code Development (B. J. Toppel)

Last Reported: ANL-7688, pp. 157-163 (April-May 1970).

(a) The Fuel Cycle Analysis System, REBUS. A calculational capability such as REBUS could be used with diverse objectives as various survey and parametric studies are done. Calculations with differing in-reactor and external cycle conditions would be done in seeking optimum conditions and in evaluating design alternatives. Efficient utilization of the REBUS system under these conditions necessitates reasonable estimation of the computation cost and selection of acceptable error limits. To assist the code user in meeting these objectives, timing studies were done to determine the sensitivity of the computation time to the convergence criteria and to obtain suggested values for the error limits. The results of these studies are presented below.

REBUS is programmed in the Argonne Reactor Computation (ARC) system using FORTRAN-IV on the IBM 360 Model 75. Under the MVT (Multitasking with Variable number of Tasks) environment operable on this machine, the computation time separates into two categories, a central processing unit time (CPU) and a wait time (WAIT) for required peripheral interaction. With an MVT environment, precise determination of the CPU and WAIT times are impossible. Thus, exact timing studies become impossible. However, as noted below, meaningful timing studies can still be done.

With REBUS, more than 90% of the computation time is used in doing the neutronics solutions, so that the computation time is directly proportional to the number of neutronics solutions. Therefore, timing studies were done using different convergence criteria and comparing the number of neutronics solutions. Because of the relation between the computation time and the number of neutronics solutions, these studies are also useful for computation time estimates with a non-MVT operating system.

In REBUS, the convergence criteria divide into two classes--physics criteria and numerical criteria. The physics criteria are concerned with the physics constraints of an equilibrium fuel-cycle problem. These are the obtaining of the desired unpoisoned multiplication constant and the specified fuel-discharge burnup. The unpoisoned multiplication constant is converged if

$$\frac{|k_{eff} - k_d|}{k_d} < \text{epsf},$$

where k_d is the desired unpoisoned multiplication constant, k_{eff} is the unpoisoned multiplication constant obtained, and epsf is a specified error limit. The fuel-discharge burnup b is converged if

$$\frac{|b - b_d|}{b_d} < \text{epsg},$$

where b_d is the desired fuel discharge burnup, and epsg is the specified tolerance.

The numerical criteria are concerned with the computational strategy chosen in REBUS to obtain the equilibrium solution. The numerical criteria are: the convergence of the region density vectors at each time node in the burn interval, the convergence of the cyclic mode iterations, and the convergence of the external cycle search. Following a neutronics calculation at a particular time node, the error for each region density vector is compared with the specified error limit. The neutronics solution is repeated with recalculation of the density vectors until convergence. The convergence criterion for each region density vector is

$$\underset{i}{\text{Max}} \left(\frac{\left| n_{r,i}^{(q)} - n_{r,i}^{(q-1)} \right|}{n_{r,i}^{(q-1)}} \right) < \text{epsn},$$

where $n_{r,i}^{(q)}$ is the density of isotope i in region r after q neutronics solutions, and epsn is a specified error limit.

The number of cyclic mode iterations is determined by the convergence of the material densities at the end of cycle condition. The convergence criterion for each material stage (ℓ,τ) is

$$\underset{i}{\text{Max}} \left(\frac{\left| n_{\ell,\tau,i}^{(p)} - n_{\ell,\tau,i}^{(p-1)} \right|}{n_{\ell,\tau,i}^{(p-1)}} \right) < \text{epsc},$$

where $n^{(p)}_{\ell,\tau,i}$ is the density of isotope i in stage τ of material type ℓ after p cyclic mode iterations, and epsc is a specified tolerance.

In the external cycle iterations, the discharge distribution is passed through the external cycle and the in-reactor cycle, thereby generating a new discharge distribution. These steps are repeated until a converged charge distribution (stage 1 of each material type) is obtained. The convergence criterion is

$$\max_i \left(\frac{\left| n^{(\nu)}_{\ell,1,i} - n^{(\nu-1)}_{\ell,1,i} \right|}{n^{(\nu-1)}_{\ell,1,i}} \right) < \text{epse},$$

where epse is a specified error limit.

Timing studies were done using various values for the above error limits. Some of the results are presented in Table III.A.1. These results should serve as a guide in estimating the computation time. If the time required for each neutronics solution is known, then the total computation time can be estimated by multiplying this by the number of neutronics solutions. The results in Table III.A.1 can be understood by studying the calculation strategy in REBUS. A search monitor line for a typical calculation is shown in Table III.A.2. The three search procedures

TABLE III.A.1. Results of Sensitivity Studies

Number of Neutronics Solution	epsf	epsc	epsn	epsg	epse
24	0.001	0.001	0.001	0.01	0.001
24	0.01	0.001	0.001	0.01	0.001
29	0.0002	0.001	0.001	0.01	0.001
34	0.0001	0.001	0.001	0.01	0.001
18	0.01	0.01	0.01	0.01	0.01
22	0.001	0.01	0.01	0.01	0.01
29	0.001	0.0005	0.0005	0.01	0.0005
31	0.001	0.0001	0.0001	0.01	0.0001
39	0.001	0.00001	0.00001	0.01	0.00001
25	0.001	0.01	0.001	0.01	0.001
24	0.001	0.001	0.01	0.01	0.001
28	0.001	0.00001	0.01	0.01	0.001
27	0.001	0.001	0.00001	0.01	0.001
25	0.001	0.001	0.001	0.01	0.01

TABLE III.A.2. Search Monitor Line

Outer Iterations in the Neutronics Solution	Time Node[a]	k_{eff}	Enrichment Search Parameter	Burn Time, days	External Cycle Iterations
		Preliminary Search			
17	BOL	1.0003	1.000	156	
15	BOC	0.9855			
14	EOC	0.9761			
9	BOC	0.9856			
2	EOC	0.9761			
10	BOC	1.0457	1.150		
10	BOC	1.0090	1.0595		
		Intermediate Search			
8	BOC	1.0084			
13	MOC	1.0017			
13	EOC	0.9948			
				162	6
5	αT	0.9934			
4	BOC	1.0157	1.0795		
9	MOC	1.0081			
8	EOC	1.0001			
					3
3	αT	1.0003			
		Final Search			
7	BOC	1.0159			
3	MOC	1.0082			
2	MOC	1.0081			
1	MOC	1.0081			
1	EOC	1.0003			
1	EOC	1.0003			
1	BOC	1.0159			
2	MOC	1.0082			
2	MOC	1.0081			
1	MOC	1.0081			
1	EOC	1.0003			
1	EOC	1.0003			
1	αT	1.0003			

[a]BOL: beginning of life.
BOC: beginning of cycle.
MOC: middle of cycle.
EOC: end of cycle.
αT: unpoisoned k_{eff} at EOC in this calculation.

(preliminary, intermediate, and final) are described in pp. 89 and 90 of the Reactor Development Program Progress Report, August 1969, ANL-7606. In the preliminary search, the user input burn time is used (the burnup constraint is not considered), no external cycle iterations are done, and the main emphasis is on estimating the enrichment required to obtain the desired multiplication constant. In the intermediate search, burn-time iterations are done to meet the burnup constraint, external cycle iterations are done to obtain a converged charge distribution, and an enrichment giving the desired multiplication constant is obtained. Iterations to obtain converged region-density vectors and cyclic mode iterations are not done. In the final search procedure, all of the convergence criteria are tested. In particular, iterations to obtain converged region-density vectors and cyclic mode iterations are now done. In Table III.A.3, an X indicates the search procedures in which each convergence criterion is evaluated.

TABLE III.A.3. Evaluation of Convergence Criteria

Convergence Criteria	Search Procedure		
	Preliminary	Intermediate	Final
epsf	X	X	X
epsg		X	X
epse		X	X
epsn			X
epsc			X

The external cycle iterations and the burnup convergence method use simple algorithms which require only a small amount of computation time in comparison to the neutronics solution. Thus the total computation time is rather insensitive to epse and epsg. From Tables III.A.2 and III.A.3, note that the iterations to meet these criteria are only done in the intermediate and final search procedures. The number of outer iterations in a neutronics solution decreases as the solution to the fuel-cycle problem proceeds (see Table III.A.2). This is a result of saving the mesh-point fluxes at each time node, which are used as initial estimates in the neutronics solution. In this manner, the computation time for a neutronics solution, which is proportional to the number of outer iterations, is reduced significantly. This information combined with the matrix in Table III.A.3 shows that the total computation time is relatively insensitive to the error limits epsc and epsn. The most significant parameter is the error limit for the convergence of the unpoisoned multiplication constant, epsf. Decreasing this error limit increases the number of neutronics solutions in the preliminary, intermediate, and final search procedures. The total computation time is most sensitive to this error limit. However, there is a trade-off between epsf and epsc. Increasing the error limit for the unpoisoned multiplication constant does not necessarily decrease the number of neutronics

solutions. Increasing this error limit does decrease the number of neutronics solutions in the preliminary and intermediate search procedures; however, this can result in more cyclic mode iterations in the final search procedure. This trade-off results from the fact that physically equilibrium is approached only after N operating cycles (where N is the highest stage number of any material). The calculation strategy chosen for REBUS eliminates explicit calculation of N operating intervals; however, convergence still requires repetitive calculation of a number of operating intervals.

Table III.A.4 lists the suggested values for the error limits. These values should give acceptable accuracy for equilibrium fuel-cycle calculations in the conceptual design analysis of Liquid Metal Fast Breeder Reactors. These error limits were chosen on the rather subjective basis of comparing the trade-off between accuracy and computation cost. To obtain the suggested values for the error limits, fuel-cycle parameters characterizing the reactor performance were analyzed for the various values of the error limits in Table III.A.1. The fuel-cycle parameters examined were feed enrichment, breeding ratio, burn time, and fissile mass discharge. For the convergence criteria in Table III.A.4, the resulting errors in the fuel-cycle parameters are shown in Table III.A.5. The fissile mass discharge error was calculated separately for each core zone, the axial blanket above each core zone, and the radial blanket. The error in Table III.A.5 refers to the maximum error in the above regions.

TABLE III.A.4. Suggested Values for Error Limits

Error Limit	Suggested Value
epsf	0.001
epsc	0.001
epsn	0.001
epsg	0.01
epse	0.0001

TABLE III.A.5. Errors in Fuel-cycle Parameters

Fuel Cycle Parameter	Error, %
Feed enrichment	0.4
Breeding ratio	0.4
Burn time	0.7
Fissile mass discharge	1.0

2. Nuclear Data--Research and Development

a. Cross-section Measurements (N. D. Dudey and C. E. Crouthamel)

(i) Yields of Low-mass Fission Products

Last Reported: ANL-7679, pp. 111-112 (March 1970).

The gas-handling system for separation of tritium from fast-neutron-irradiated fissile materials has been assembled and has undergone a Division safety review. Several modifications were recommended to provide additional safety features for the handling of plutonium samples. These modifications are currently being made, and the system is being reassembled in a plutonium glovebox.

The equipment for irradiating samples in the Dynamitron has been assembled and tested. The main equipment item is a wheel for mounting samples, which is capable of holding about 20 samples in three concentric rings. The three rings of samples will permit the simultaneous irradiation of samples at three different neutron energies; this is possible because the neutron energies from the Dynamitron depend upon the angle the samples intercept relative to the neutron source. The system incorporates features that provide accurate alignment of the wheel relative to the neutron beam, as well as a mechanism for rotating the wheel at 1 rpm.

Two samples each of ^{239}Pu, ^{235}U, and ^{233}U, as well as mica fission-track detectors containing these materials, have been prepared for irradiation in the Dynamitron. In the first experiment attempted, the irradiation could not be carried out because the neutron flux obtained was too low. Neutrons are produced in the Dynamitron by the $^{7}Li(p,n)$ reaction, and calculations had shown that proton-beam currents $>100\ \mu A$ would be required for a period of at least 30 hr to produce enough tritium for a quantitative determination of the fission yield. However, in the initial experiment, proton beam currents of only $\sim 30\ \mu A$ were obtained. Therefore, further irradiation experiments will not be attempted until adequate proton-beam currents can be obtained.

b. Burnup Analysis and Fission Yields for Fast Reactors (R. P. Larsen)

(i) Development of Analytical Procedures for Fission-product-burnup Monitors

Last Reported: ANL-7679, p. 112 (March 1970).

The manpower normally allotted to this work has, during this reporting period, been assigned to the work described in Sect. (ii), below.

(ii) Development of a New Method for the Determination of the Absolute Fast-fission Yields of Burnup Monitors for Fast Reactor Fuels

Last Reported: ANL-7679, pp. 112-114 (March 1970).

(a) Determination of Fission Yields. A new method has been developed for determining the number of fissions that occur in irradiated fast-reactor fuel materials, and this method is now being applied to the determination of fast-fission yields. Two irradiations are required: one at low reactor power (1-10 kW) for ~1 hr, and one at full reactor power for about 3 months. Included in the low-power irradiation are fission-track

detectors (mica disks alternately stacked with platinum disks on which are mounted nanograms of the fissile material) and fission foils (milligram amounts of the fissile material). These samples provide data for establishing a factor relating the number of fissions that occurred to the count rate of a particular fission product, e.g., ^{95}Zr (65 d). The fission tracks on the mica disks are counted under a microscope; the ^{95}Zr activity of the fission foils is determined by gamma spectrometry. Included in the long irradiation are gram amounts of fissile material, which are subsequently analyzed for the fission product whose yield is being determined and for ^{95}Zr activity. The number of fissions that occurred is established from the ^{95}Zr activity and the previously determined fissions-to-^{95}Zr factor.

The low-power irradiations are being conducted in the ZPR-3 mockup experiments of the EBR-II core. The first of these irradiations was carried out in Assembly 60 (the present EBR-II configuration) on February 26, 1970. The three irradiation packages each contained fission-track detectors and foils of ^{235}U, ^{238}U, and ^{239}Pu and were located at positions in ZPR-3 which correspond to the center of the core, the core-blanket interface, and the blanket of EBR-II. A detailed description of these packages and the techniques being used to analyze the irradiated materials was given in ANL-7679, pp. 113-114.

The gamma-spectrometric measurements of the sections of the ^{235}U, ^{238}U, and ^{239}Pu foils from the Assembly-60 irradiation packages are continuing. For each section of foil, the activities of ^{95}Zr (65 d), ^{97}Zr (17 hr), ^{99}Mo (67 hr), ^{103}Ru (42 d), ^{103}Te (77 hr), ^{131}I (8 d), ^{140}Ba (13 d), and ^{141}Ce (33 d) have each been measured a number of times since the irradiation. For each nuclide, a least-squares fit of a plot of log of activity versus decay time gives a straight line with the appropriate half-life slope (the decay times were greater than two half-lives for each nuclide), thus demonstrating that the gamma rays used in the measurements were free of interference.

Since the detector used for these measurements had been previously calibrated with respect to both geometry and gamma energy, the activities can, with the use of the appropriate decay constants (half-lives, branching ratios, and conversion coefficients), be used to calculate the number of atoms of each fission-product nuclide at time zero. The calculations of atoms of fission product per gram of fissile nuclide will be completed as soon as the individual foil samples are weighed.

A second irradiation of packages containing fission-track detectors and fission foils was carried out on June 4 in Assembly 61 of ZPR-3. The irradiation in Assembly 61, which contained a nickel reflector, provided an even softer neutron spectrum than that obtained in the blanket of Assembly 60. Included in the Assembly 61 irradiation, in addition to fission-track detectors and foils of ^{235}U, ^{238}U, and ^{239}Pu, were fission-track

detectors and foils of ^{237}Np and ^{242}Pu. As in the first irradiation, the foils were received and sectioned, and gamma-spectrometric measurements initiated within 24 hr of the termination of the irradiation.

(b) Determination of Burnup of EBR-II Driver Fuel. A portion of an EBR-II driver fuel pin has been analyzed for burnup and the results compared with those obtained on the same fuel by E. R. Ebersole (EBR-II) and B. F. Rider (General Electric Vallecitos Atomic Power Laboratory). This comparison was prompted by some discrepancies between predicted and observed burnups on certain General Electric test specimens that had been irradiated in EBR-II. The burnup monitors used and the values obtained by the three laboratories are summarized below:

Laboratory	Burnup Monitor	Burnup, %
EBR-II	^{137}Cs	0.931
	^{99}Tc	0.920
GE	^{137}Cs	0.941
	^{148}Nd	0.945
ANL-CEN	^{137}Cs	0.931

The analyses for ^{137}Cs (^{235}U fission yield, 6.20%) were performed by radiochemical techniques, with all laboratories using the Nuclear Chicago-A.S.T.M. Standard; the analysis for ^{99}Tc (fission yield, 5.80%), by spectrophotometry; and the analysis for ^{148}Nd (fission yield, 1.77%), by mass-spectrometric isotope dilution.

The excellent agreement among the burnup values for the driver fuel obtained by the several laboratories indicates that the burnup values previously determined on test specimens are reliable values.

c. Reactor Code Center (M. Butler)

Last Reported: ANL-7688, pp. 164-165 (April-May 1970).

In June, six program packages were assimilated into the Argonne Code Center computer program library.

Three of the programs were contributed by the Westinghouse PWR Systems Division. They include ETOM1 (ACC No. 436), which processes ENDF/B library tapes and produces library decks for use with the MUFT4 and MUFT5 programs; ETOG1 (ACC No. 437), which processes the ENDF/B tapes and produces library decks for use with the MUFT4, MUFT5, GAM1, GAM2, or ANISN programs; and the ETOG library data (ACC No. 447), which includes the MUFT4, MUFT5, GAM1, and GAM2 libraries produced by

ETOG1 processing of ENDF/B tapes 114, 115, 116, and 117. Both ETOM1 and ETOG1 use a straightforward group-averaging process using the input weight and ENDF/B data to produce the cross sections. The Breit-Wigner single-level formula is employed in calculating the resonance values. An attempt was made to produce, insofar as practicable, computer-independent FORTRAN programs.

A revised version of PIPE (ACC No. 329) was received from the Bettis Atomic Power Laboratory, replacing the existing library package. This CDC 6600 program performs an elastic stress analysis of a three-dimensional piping structure. All recipients of the original program were notified of the replacement by Code Center Note 70-31.

The Los Alamos Scientific Laboratory contributed an r-z geometry version of their TWOTRAN two-dimensional design code (ACC No. 358), written for the UNIVAC 1108, and Oak Ridge National Laboratory submitted the XSDRN discrete-ordinate program for the generation of multigroup constants in fast, resonance, and thermalization energy regions (ACC No. 393). XSDRN was written for the IBM 360.

Supplement 4 to ANL-7411, containing the abstracts for library programs 385-410, is now being printed and will be available shortly.

B. Reactor Fuels and Materials Development

1. Fuels and Claddings--Research and Development

a. Oxide Fuel Studies

(i) Fuel-swelling Studies (L. C. Michels and L. A. Neimark)

Last Reported: ANL-7688, pp. 178-179 (April-May 1970).

The behavior of fission-gas bubbles in UO_2-PuO_2 fuel elements irradiated in EBR-II is being studied to further the understanding of fuel swelling and fission-gas release. Optical and electron-microscopy techniques are being used to study the migration tendencies of the bubbles and their interaction with structural features such as high- and low-angle grain boundaries.

An analysis of "bubble trails" in etched metallographic specimens of oxide fuel has been initiated. Although initially these trails were found behind bubbles, hence the name "bubble trails," similar trails have now been found associated with solid fission-product inclusions. These trails are believed to be the result of the migration of fission-gas bubbles and solid fission-product inclusions up the temperature gradient. The submicroscopic constitution of the trails is not known, but a possible explanation

is that the trails do not etch in the same manner as the surrounding material because they contain line and/or planar defects. The formation of defects in the wake of the bubbles moving by a vapor-transport mechanism could be similar to the formation of defects in the deposition of thin films. The vapor-transport mechanism is consistent with the observation of transverse striations in some of the trails. Conceivably, line and planar defects also would be produced in the cases of surface or volume diffusion mechanisms of bubble or inclusion migration.

Since the trails are probably the result of bubble and inclusion migration, it should be possible, in certain cases, to measure the lengths of the trails and, with a knowledge of the time involved, to determine the velocities of the bubbles and inclusions during irradiation. A specimen from mixed-oxide fuel element HOV-15, which was irradiated in EBR-II, was chosen for the analysis. For most of the irradiation time, this element operated in a partially molten condition at a peak power rating of 21.4 kW/ft, but was operated at a peak power rating of only 14.2 kW/ft for 29.7 hr at the end of the irradiation. As a result of the low power operation, grain-boundary migration and fission-product (gas bubbles and solid inclusions) movement occurred across the large, once-molten grains. Any trails observed in the once-molten region of the fuel and in the nonmolten region near the melt radius would probably have been formed during the last low power cycle, for which the time interval is known accurately.

Trail lengths and diameters have been measured for a total of 30 gas bubbles and inclusions, and the average velocities calculated. The major sources of error occur in the determination of trail length and of bubble or inclusion diameters. The full lengths of the trails may not have etched, and part of the trails may have annealed out during migration. Since both these sources of error tend to reduce the observed trail length, the effect is to produce measured average velocities lower than the real velocities. The sizes of the bubbles and inclusions could be in error because the plane of polish intersects them at different diametral positions. (A correction to account for the error in measurement of bubble diameter will be factored in at a later date.) Also, an additional complication lies in the possibility of mistaking a void left by inclusion pullout for a gas bubble.

The radial positions in the fuel over which the measurements were made correspond to a temperature range of 1685-1845°C and an almost constant temperature gradient of 3280°C/cm. The calculated velocities for bubbles and inclusions fall into three somewhat overlapping groups. The highest velocity group, ranging from 3.6 to 12.9 Å/sec, corresponds to features observed only in what had been the molten region of the fuel. The middle velocity group, ranging from 0.93 to 4.7 Å/sec, corresponds to features observed mainly in the nonmolten columnar region of the fuel near the melt radius. The lower velocities in the middle range group are thought to be due to somewhat lower temperature or the retardation

of migration by defects such as subgrain boundaries. The third and lowest velocity group, ranging from 0.21 to 1.5 Å/sec, corresponds to features known to be solid fission-product inclusions. The low velocity of this group suggests that the mechanism of migration is different from that of the other groups. This last observation offers the possibility of being able to differentiate voids due to inclusion pullout from gas bubbles, on the basis of differing migration rates. There is, at this point, no clear-cut relationship between velocity and bubble or inclusion diameter.

Additional metallographic work is under way to provide a greater statistical sample to enlarge upon these preliminary results.

(ii) Fuel-element Performance (L. A. Neimark and W. F. Murphy)

(a) Irradiation of Group O-3 Fuel Elements

Last Reported: ANL-7688, p. 181 (April-May 1970).

Midway in Run 43, the 18 mixed-oxide fuel elements of Group O-3 have accumulated 6001 MWd exposure in Subassembly X072 in EBR-II. This exposure is 63% (~2.2 at. %) of the first target burnup of 3.5 at. %. Extrapolation of reactor operation at 50 MW indicates that this target would be attained about October 1, 1970, subject to the possible conversion of reactor power from 50 to 62.5 MW before that date.

2. Radiation Damage on Structural Materials--Research and Development

a. In-Reactor Creep Studies

(i) Simulation of In-pile Creep Behavior through Cyclotron Bombardment (S. D. Harkness and F. L. Yaggee)

Last Reported: ANL-7688, pp. 183-184 (April-May 1970).

A 50-hr creep test of Type 304 stainless steel has been completed. The sample was continuously bombarded by 22-MeV deuterons during the entire test period. Since difficulties were encountered in beam and temperature control, creep rates could be established for only two sets of conditions. The first set of conditions consisted of a stress of 47,800 psi, an average sample temperature of 450°C, and a deuteron current on the sample of 4.9 μA. The specimen temperature fluctuated within a band of ±5°C, except for occasional temperature spikes of -25°C, which were caused by momentary beam fluctuations. The measured creep rate for the 6.5-hr period was 6.47×10^{-5} in./in./hr. The correlation factor for the data was 0.8, reflecting some scatter in the results. This strain rate appears to reflect a steady-state creep rate, because the sample had been loaded at the

same stress and temperature for 72 hr, before the incidence of the deuteron flux, and for an additional 10 hr in the deuteron flux before the measurements were made.

The second set of stable conditions persisted for 13 hr and consisted of a stress of 50,500 psi, an average specimen temperature of 420°C, and a deuteron current on the sample of 4.2 μA. The measured creep rate for these conditions was 5.83×10^{-5} in./in./hr. The correlation factor for the strain-versus-time plot was 0.97, indicating little scatter in the data. Ten hours elapsed between the first and second set of operating conditions, again, sufficient time for the establishment of a steady-state creep rate. Upon completion of the deuteron bombardment, the sample was allowed to continue as a thermal creep test at a temperature of 420°C. No detectable strain was observed after 48 hr. Since the detection limit of the apparatus is 5×10^{-5} in., the strain rate must be less than 1×10^{-6} in./in./hr under these conditions; therefore, the deuteron bombardment enhances the creep rate at least 50 times.

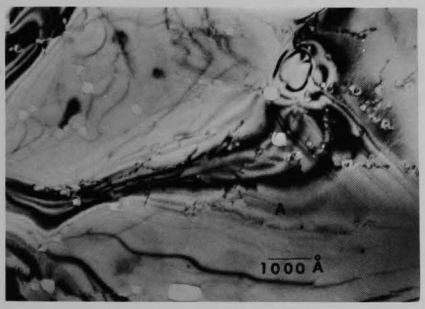

Fig. III.B.1. Cavities Formed in Type 304 Stainless Steel after a 50-hr Bombardment with 22-MeV Deuterium. Note dislocations pinned by cavities at A.

Transmission electron microscopy on the bombarded sample has revealed that cavities formed during the irradiation (see Fig. III.B.1). Stereomicrographic techniques have established that these cavities lie within the foil thickness. Whether these cavities are voids or deuterium bubbles has not been determined. The ability of cavities to act as barriers to dislocation motion is also reflected in Fig. III.B.1.

(ii) Void Growth under a Stress System in the Presence of Irradiation-enhanced Point Defects (D. G. Franklin)

Not previously reported.

Void nucleation and growth are expected to play a significant role in the swelling and fracture of Types 304 and 316 stainless steel cladding material.* Some stress systems will give enhanced flow of point defects in metals.** These stress systems can contribute a small bias to the flux of vacancies and interstitials to sinks. A computer program has

*Harkness, S. D., and Li, Che-Yu, Nucl. Appl. (to be published).
**Ham, Frank S., J. Appl. Phys. 30, 915 (1959).

been written that numerically solves the diffusion equation for interstitials to voids using the Ham equation

$$J = D(\nabla C + \frac{C}{kT}\bar{V}\nabla P),$$

where

D = the diffusion coefficient,

C = the concentration of point defects,

P = pressure,

and

$\bar{V}$ = the partial molar volume of a point defect.

The hydrostatic component of the stress field around a hole under uniaxial tension has been given by Goodier* as

$$\sigma = -\frac{5}{12}\frac{1+\nu}{8-10\nu}\frac{\tau R^3}{r^3}(2+6\cos 2\theta),$$

where

θ = the angle measured from the tension axis,

ν = Poisson's ratio,

r = the distance from the center of the void,

τ = the applied stress,

and

R = the radius of the void.

Our results show that for τ = 10 ksi, T = 700°K, and R = 100 Å the effective increase in the void radius due to the stress field is 0.3% of the radius.

3. Techniques of Fabrication and Testing--Research and Development

a. Nondestructive Testing Research and Development

(i) Neutron Radiography (H. Berger)

(a) Fast-neutron Techniques

Last Reported: ANL-7669, pp. 116-118 (Feb 1970).

Fast-neutron radiographic studies have been initiated with a nominal 2-mg source of ^{252}Cf fabricated at ORNL. The fission spectrum from this source (average neutron energy 2.3 MeV) contains a reasonable

*Goodier, J. N., Trans. Am. Soc. Mech. Eng. 1, 39 (1933).

percentage of neutrons with an energy <1 MeV. Therefore, as previously reported (see ANL-7669, p. 118), somewhat improved material discrimination capability may be anticipated compared with fast-neutron radiography in the 3- and 14-MeV range.*

Initial neutron image-detection investigations have been made by means of direct-exposure methods using film with hydrogenous conversion screens such as plastic and Bakelite to obtain knock-on proton response of the film, and with X-ray fluorescent screens as scintillators. The results tend to confirm the order of magnitude of the neutron-exposure requirements found for the higher-energy neutrons.* Differences are observed, however, that may be partially due to the gamma and X-radiation associated with the ^{252}Cf source. Lead filters (~3 mm thick) used at the source appear to reduce substantially the gamma and X-ray background, and some improvement in contrast of the plastic components results. However, initial results with the lead filters indicate that neutron scatter in the lead contributes to reduced image sharpness in the resultant radiographs. Differences in image sharpness also have been observed when the disk-shape source (source size ~0.25 cm) is used in a side orientation toward the radiographic object as opposed to when the source disk (source diameter ~0.5 cm) is used in the end-on radiographic orientation.

Initial tests with gamma radiation-insensitive detectors have been made. Track-etch images with total exposures on the order of 2 x 10^{10} n/cm^2 have been obtained, again confirming earlier results with MeV-energy neutrons.* Transfer images have been produced by activating screens of sulfur, phosphorus, rhodium, indium, or cadmium. The images produced by the sulfur and the phosphorus activation are primarily due to the higher-energy neutrons from the source, since the (n,p) reactions in these materials have neutron-energy thresholds of 1.7 and 1.8 MeV, respectively. In the latter three materials, however, much of the response is due to keV-energy neutrons by (n,n') reactions, as shown in Table III.B.1.

TABLE III.B.1. Some keV Neutron Energy-transfer Detectors for Fast-neutron Radiography

Reaction	Threshold Energy, MeV	Half-life	Reaction Cross Section, mb	
			1 MeV Neutron	3 MeV Neutrons
^{103}Rh(n,n')^{103m}Rh	<0.1	57 min	450	800
^{111}Cd(n,n')^{111m}Cd	0.3	48.7 min	130	300
^{115}In(n,n')^{115m}In	0.5	4.5 hr	55	340

*Berger, H., Mater. Eval. 27, 245-253 (1969).

In all the transfer-detector cases, the total neutron yield from the source (~4.5 x 10^9 n/sec) has not been adequate for activation of these screen materials when source-detector distances great enough to yield sharp radiographs were used. Although the planned tests with this source should yield information on the exposure requirements for transfer detectors, actual radiographic evaluation of such images is expected to be difficult, except for sulfur, where the 14.3-day, half-life activity could be sufficiently activated at greater source-detector distances.

(ii) Development of High-temperature Ultrasonic Transducer (K. J. Reimann)

Last Reported: ANL-7688, pp. 187-189 (April-May 1970).

The investigation of high-temperature ultrasonic transducers that can be used to obtain acoustic-emission measurements proceeded primarily in the area of dielectric and piezoelectric receivers.

The main problem encountered with most dielectric transducers operating at elevated temperatures is an increase of leakage current and a simultaneous deterioration of signal-to-noise ratio. The temperature range of such a device, with mica as the dielectric, does not exceed 300°C for a tolerable signal-to-noise ratio. To evaluate an alternative dielectric material, a piece of a 1-mil-thick, heat-resistant polyimide film (Kapton, E. I. du Pont de Nemours & Company) was exposed to steadily increasing temperatures up to 600°C. No change could be observed below 500°C. At higher temperatures, discoloration occurs and the material becomes progressively darker until it evaporates around 600°C. The material is, therefore, unsuitable for the intended application at 600°C, but conceivably could be used for operation below 500°C.

Other dielectrics such as air and sapphire are being considered. It is anticipated that the sensitivity of a transducer with air as the dielectric will be lower than that for a transducer with a solid dielectric, because of the smaller dielectric constant. However, a trade-off in sensitivity for greater stability over a wider temperature range may be desirable. The effects of humidity and impurity will have to be evaluated.

Low-temperature transducers are predominately based upon piezoelectricity. The maximum temperature of operation of this type of transducer depends upon the Curie point of the piezoelectric material. Thus, quartz is suitable for a temperature range up to 400°C, and lithium niobate can be used up to 1000°C. An experimental transducer, consisting of a round, single-crystal lithium-niobate disk (1 mm thick and 1 cm in diameter) sandwiched between the test specimen and a pressure plate, performed satisfactorily as a listening device for acoustic emission. To check its performance at elevated temperatures and under actual environmental conditions,

the transducer was subsequently mounted on a sodium loop. The output signal is generated by pump noise, flow noise, and mechanical vibrations of the sodium system. Figure III.B.2 shows an amplified, detected, and recorded change in output level caused by a change in the flow rate of the liquid sodium at 600°C. The transducer is still being monitored to determine its stability over an extended period of time. Although the initial results are promising, further investigations are necessary.

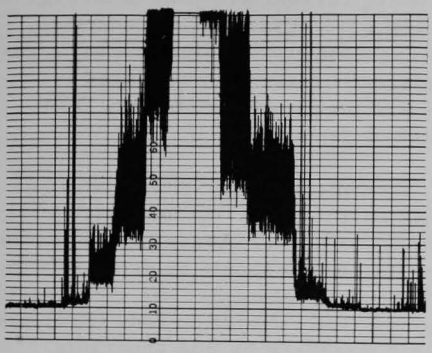

Fig. III.B.2. Recorded Output of a Lithium-Niobate Receiver, Mounted on a Sodium Loop at 600°C

To improve the high-frequency response, a solid bond between one side of the transducer and the test specimen is desirable, and a test lead has to be attached to the other side of the transducer. Brazing was considered the most favorable bonding method, with regard to the temperature requirement. The electrodes are attached by applying silver paint to both sides of the crystal and baking at 850°C. A shim of Nioro brazing metal subsequently is sandwiched between the crystal and the support or lead wire, and the entire assembly is mounted in a vacuum oven. To prevent the crystal from breaking, the heating rate does not exceed 100°C/hr. Brazing occurs at 850°C. The sample fabricated by this method showed very good bonding between the crystal and the support, as well as between the crystal and the lead wire. Additional samples will be brazed in a similar manner to investigate the reproducibility of this procedure. Brazing, however, is not the only bonding method, and other processes are being considered.

b. NDT Measurement of Effective Cold Work in Cladding Tubes (C. J. Renken)

Last Reported: ANL-7661, pp. 105-107 (Jan 1970).

Experiments were continued to check the feasibility of various methods of measuring the cold work in a series of seven 7.6-mm-dia Type 316 stainless steel rods. The rods had undergone various amounts of reduction by tensile elongation, and had been well-characterized by metallographic examination and microhardness measurements. The magnetic retentivity measurements of the rods had shown good correlation with percentage reduction. Electrical resistivity measurements of a sensitivity compatible with a practical nondestructive test had shown no correlation. The recent experimental emphasis has been on the development of methods to measure the amount of magnetic phase present in a specimen. Two coils

were constructed through which rod or tube specimens could be passed. A probe from a high-sensitivity flux-gate magnetometer was located near each coil so that when the same magnetizing current was passed through each coil the magnetometer probes, which were differentially connected, produced a null-field indication on the magnetometer. Using this arrangement, a specimen that contained ferromagnetic material was placed in one of the coils and a reading was produced on the magnetometer. The field in each coil measured approximately 2 gauss.

To calibrate the apparatus, specimens were constructed from a paper tubing coated with powdered martensite steel. Various thicknesses of coating were used to establish a calibration curve. Assuming a uniform field in the coil, percentages of martensite <0.07% should be detectable in a 7.6-mm-dia stainless steel rod. The amount of martensite that existed in even the most heavily reduced sections of the calibration rods (39%) was below the amount that could be accurately measured by this apparatus.

4. Engineering Properties of Reactor Materials--Research and Development

a. High Temperature Mechanical Properties of Ceramic Fuels

(i) High-temperature Stress Relaxation of UO_2 (J. T. A. Roberts)

Last Reported: ANL-7679, pp. 128-129 (March 1970).

The activation volume-stress dependence of stoichiometric UO_2 reported previously is consistent with the predictions of a recent analysis by Cheng.†

If the creep rate is expressed as

$$\dot{\epsilon} = \dot{\epsilon}_0 \exp(-\Delta F/RT), \tag{1}$$

where ΔF is the Helmholtz free energy of activation, $\dot{\epsilon}_0$ contains structure sensitive terms, and RT has the usual meaning, then the stress dependence of the creep rate is given by

$$\frac{\partial \ln \dot{\epsilon}}{\partial \sigma} = -\frac{1}{RT}\frac{\partial \Delta F}{\partial \sigma} = \frac{V'}{RT} . \tag{2}$$

Variations of Eq. 2 also can be used, where σ can be σ^*, the effective stress, and V' becomes V, the true activation volume (see ANL-7679). Alternatively, V' can be written (perhaps more correctly) as Ab, where A is the activation

† Cheng, C. Y., Scripta Met. 4(5), 375 (1970).

area, and b is Burgers vector.* For purposes of discussion, however, the applied stress σ and the apparent activation volume V' will be used.

Since the stress exponent of the steady-state creep rate can be written as $n \equiv (\partial \ln \dot{\epsilon} / \partial \ln \sigma)_T$, then

$$V' = \frac{RT}{\sigma} n. \tag{3}$$

(The assumption has been made that the dislocation density does not change with the instantaneous change of stress.) Hence, as is observed experimentally, the activation volume is inversely proportional to the applied stress.

The average of the calculated values of n, using the stress-relaxation data, is 4.7 ± 0.57 over the temperature range 1400-1800°C. In comparison, values of 4 to 5 were obtained from creep measurements,** and the value of 4.23 was obtained from plastic flow measurements. (See Progress Report for April-May 1970, ANL-7688, p. 192.)

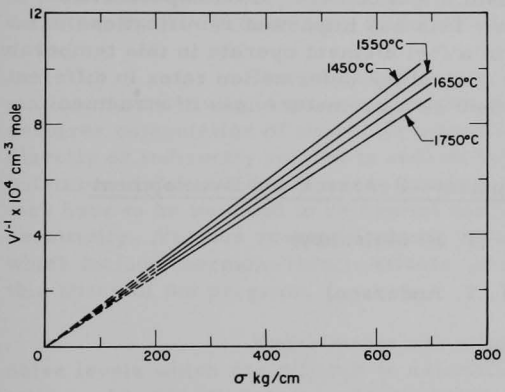

Fig. III.B.3. A Plot of V'^{-1} vs σ Using Data from Steady-state Creep Measurements

Conversely, Eq. 3 can be used to determine V' and its stress dependence from creep data. A generalized case will be presented to reveal some differences in behavior. A value of n equal to 4.5, a stress range of 200-700 kg/cm^2 (~3,000-10,000 psi), and a temperature range of 1450-1750°C have been used, since these incorporate most of the reported** compressive creep data on UO_2. The same trend is observed with the bend creep data, but the stresses are higher. Figure III.B.3 is a plot of V'^{-1} versus σ, for several temperatures, that illustrates the small temperature dependence of the activation work W (defined as $V'\sigma$). Values range from 15.5 kcal/mole at 1450°C to 18.3 kcal/mole at 1750°C; the average value of 17 ± 1 kcal/mole agrees very well with the value of 18 ± 1.8 kcal/mole calculated from

*Li, J. C. M., Dislocation Dynamics, McGraw-Hill Book Co., Inc., New York, p. 87 (1968).

**Poteat, L. E., and Yust, C. S., in Ceramic Microstructures, Fulrath, R. M., and Pask, J. A., eds., John Wiley & Sons, New York, p. 646 (1968); Bohaboy, P. E., Asamoto, R. R., and Conti, E. A., GEAP-10054 (May 1969); and Wolfe, R.A., and Kaufman, S. F., WAPD-TM-587 (Oct 1967).

stress-relaxation experiments. The point of interest, however, is to determine which term, n or V', is truly temperature-insensitive, since, in stress relaxation, V' was essentially temperature-independent. Certainly the results on UO_2 are not of sufficient accuracy to resolve the problem.

The correlation between high-temperature stress-relaxation parameters and creep parameters supports the contention that the same rate-controlling process controls both types of plastic flow. There are few mechanisms, however, that can explain the activation volume-stress dependence. One suggestion is a mechanism that involves jog-limited dislocation motion with a distribution of jog spacings.* Since the diffusion of jogs is the rate-limiting step, both the activation enthalpy and the activation volume should be similar to those for self-diffusion.

Stress relaxation in four-point bending has been restricted to temperatures above 1200°C, due to the inherent brittleness of UO_2 in tension. Measurements down to ~800°C will be made using compression tests. The opening of flaws, which leads to fracture, is suppressed under these conditions. Several reported experimental observations suggest that a different deformation mechanism might control "low-temperature" deformation under high stresses. This has important ramifications in fuel design, since the outer regions of a fuel element operate in this temperature range. If different mechanisms control the deformation rates in different regions of the fuel, the result might be a premature loss of structural integrity.

C. Engineering Development--Research and Development

1. Instrumentation and Control (T. P. Mulcahey)

a. Boiling Detector (T. T. Anderson)

(i) Acoustic Method

(a) Development of High-temperature Detector (A. P. Gavin and T. T. Anderson)

Last Reported: ANL-7688, pp. 198-200 (April-May 1970).

Exploratory tests of the stainless steel-encased sensor have shown that the electrical resistivity of lithium niobate depends upon both temperature and oxygen partial pressure. Briefly, the sensor was heated in 200°F increments to 1200°F and, at a given temperature, partial pressures of dry room temperature air were admitted to the sensor housing while controlling partial vacuum. Air pressures were varied from 50 to 700 mm Hg abs.

---

*Li, J. C. M., Trans. ASM 61, 699 (1968).

Increasing the pressure inside the housing caused an increase in resistance, and decreasing the partial vacuum caused a decrease in resistance. However, the magnitude of resistance at fixed partial pressure and temperature was not constant, but depended upon past history.

Sensitivity of the sensor was determined by the ball-dropping method described in ANL-7688. Voltage response was a factor of 10 below room-temperature values. However, initial values of electrical resistivity and voltage response were recovered when the sensor was cooled to room temperature.

(ii) Flux-noise Method (L. J. Habegger)

Last Reported: ANL-7595, p. 105 (July 1969).

(a) Plan of Feasibility Research. Previous plans for the theoretical and experimental research program are being reformulated in more detail, and revisions are being made to allow coordination with acoustic-boiling-detection research. The initial objective is demonstration of feasibility, and the final objective is development of a working boiling-detection system if feasibility is indicated.

The principal goal of the theoretical research is estimation of sensitivity of measured neutronic noise to sodium boiling. This requires computation of characteristics of neutron-density fluctuations directly or indirectly related to sodium boiling. In the final analysis, computations of fluctuations in space and in the neutron energy spectrum also may have to be included to determine methods of increasing measurement sensitivity. Various reactor dynamic codes, such as SASIA* and FREADM,** which include thermohydraulic effects, are being studied for possible use in this phase of the program.

Experiments are required to: (1) determine background noise levels which are difficult to estimate theoretically; (2) verify computations of boiling-induced fluctuations obtained from the theoretical analysis; and (3) determine the statistical nature of voids in liquid metal during boiling.

Background noise levels and boiling-induced fluctuations are to be measured on the EBR-II, and a survey of existing instrumentation on this system has been initiated. It is proposed that these experiments will be performed simultaneously with similar experiments relating to the acoustic-boiling-detection program. In addition to the advantages of avoiding

*Fischer, G. J., et al., Fast Reactor Accident Study Code, SASIA, CONF-690401 (1969), pp. 51-54.
**Freeman, D. D., Coupling of Dynamics Calculations in the FREADM Code, CONF-690401 (1969), pp. 30-50.

duplication of various experimental procedures, simultaneous data collection would introduce the possibility of cross-correlation between acoustic and neutronic noise signals.

b. Flow Monitor (T. T. Anderson)

(i) Two-thermocouple Method (A. E. Knox and C. W. Michels)

(a) Temperature Variation of Coolant Sodium at the Outlet of the EBR-II Instrumented Subassembly

Last Reported: ANL-7679, p. 132 (March 1970).

The 50-MW noise data obtained from four coolant thermocouples (OTC 5, OTC 14, SWTC 17, and ITC 4) in Test XX01 EBR-II Instrumented Subassembly have been spectrum-analyzed, using a Spectral Dynamics SD301 analyzer and a SD302 ensemble averager. Typically, 16 Fourier amplitude (in V rms) versus frequency ensembles were averaged to produce a final record. The amplitude spectrum was determined in the range of 0.01 to 100 Hz.

Each thermocouple featured Type 304 stainless steel sheaths, Chromel/Alumel thermoelements, and alumina insulation. Listed below are the respective sheath diameters at the hot junction, and the measured step-response times. The latter were measured by step-immersing the thermocouples in hot water and measuring the time for the output emf to achieve 63.2% of its final value.

Thermocouple Identification	Sheath Diameter at Hot Junction, in.	Measured Step-response Time, msec
Outlet TC 5 (OTC 5)	0.062	300
Outlet TC 14 (OTC 14)	0.040	120
Spacer Wire TC 17 (SWTC 17)	0.040	Not measured
Inlet TC 4 (ITC 4)	0.062	600

The spectrum analyses were performed on the thermocouple output signals from which the dc component had been removed. The following spectrum characteristics were obtained by averaging two 50-MW spectrum records (data obtained from the beginning of Runs 39A and 39B at full coolant flow):

Thermocouple Identification	V rms at 0.1 Hz, μV	V rms at 1.0 Hz, μV	-20 dB Frequency, Hz
OTC 5	4.8	1.0	1.2
OTC 14	5.0	1.1	2.2
SWTC 17	7.5	3.7	3.2
ITC 4	1.1	0.15	0.48

The amplitude of a typical spectrum record was nearly constant in the region of 0.01 Hz, and began to decrease at 0.1 Hz. The -20 dB frequency is the frequency at which the spectrum amplitude had decreased by a factor of 10 from the constant low-frequency value. The spectra below 4 Hz represent the nature of coolant-sodium temperature variations in an EBR-II Instrumented Subassembly when processed by the low-pass frequency characteristics of a thermocouple. The spectra above 4 Hz have significant amplitudes at a number of frequencies; these are probably due to electrical noise and direct heating of thermoelements by varying nuclear-radiation intensities.

The 50-MW spectra discussed here and spectra obtained at other power and flow levels are being further examined.

c. Vibration Sensor (T. P. Mulcahey)

(i) Out-of-pile Tests of Sodium-immersible Commercial Transducers (T. T. Anderson)

Last Reported: ANL-7688, pp. 200-201 (April-May 1970).

An accelerometer (No. 1), attached to the midpoint of a hexagonal panel of the FFTF Mark-II fuel subassembly, is being evaluated for sodium-immersion service, with eventual application for monitoring internal components of an LMFBR.

As reported in ANL-7688, the accelerometer was functional in 400°F sodium. However, as the temperature of the sodium was increased gradually to 850°F over a one-week period, both cable and sensor resistivity decreased exponentially with temperature. This is typical behavior of insulation resistance; however, both cable and sensor resistance were a factor of 200 below the sensor resistance alone during previous furnace tests. At 850°F sodium temperature, insulation resistance had dropped to 1 kΩ. Line-frequency pickup increased in direct proportion to increasing insulation conductivity. For 1 kΩ insulation resistance, this pickup amounted to 280 mV rms, measured at amplifier output.

On June 1, after $1\frac{1}{2}$ weeks of sodium-immersed operation, the accelerometer began transmitting an erratic signal. Resistance had decreased to 60 ohms at 800°F, indicating a faulted condition. Location of the fault, determined by a time-domain reflectometer, was at or near the sensor end of the cable. Upon suggestion of the accelerometer vendor, the cable external to the CCTL vessel was heated while simultaneously being evacuated (connector removed). The fault was not cleared, eliminating trapped moisture as a possible cause.

Before the failure, acoustic noise levels at 275 gpm sodium flow were comparable for two accelerometers: No. 1 on the FFTF subassembly inside the CCTL test vessel, and No. 3 on the external base support of the CCTL test vessel. Noise levels were 0.05 g rms wide-band (>1 Hz) and 0.01 g rms acoustic range (>100 Hz). Acoustic noise level from accelerometer No. 4 on the pump line was found to be 0.1 g rms for a modulating vibration frequency of 330 Hz associated with pump operation. This pump vibration was detected by the two accelerometers at the test vessel; however, the noise levels were lower by a factor of 10 for No. 1 and by a factor of 50 for No. 3.

As an independent check on response of accelerometer No. 1 prior to failure, a bolt at an upper flange of the CCTL test vessel was struck lightly with a hammer while simultaneously monitoring accelerometers No. 1 and 3. Relative vibration amplitudes remained constant between 400 and 850°F, 1 g rms at No. 3 and 0.1 g rms at No. 1.

Although failure of a single unit has occurred, feasibility of operation at 1000°F in sodium has not been disproved. Long-term immersion in high-temperature liquid sodium will check the integrity of sensor housing and cable sheath. Results of this test emphasize the desirability of long-term furnace and sodium-immersion tests to evaluate future accelerometers with long integral-sheathed cables.

2. Heat Transfer and Fluid Flow (M. Petrick)

a. LMFBR Burnout Limitations (R. J. Schiltz and R. Rohde)

(i) Preparation of Apparatus

Last Reported: ANL-7688, p. 201 (April-May 1970).

The total electrical installation effort is about 50% complete. Fabrication of the argon gas pressurizing system is about 75% complete. The oscillating plugging meter has been designed, and final detailing of components has started.

b. Nonboiling Transient Heat Transfer (R. P. Stein)

(i) Analysis of Heat-flux Transients

Last Reported: ANL-7669, p. 126 (Feb 1970).

As described in ANL-7669, a computer program which models a fluid flowing between parallel plates subjected to transient heat fluxes equal at both channel walls is available for general use. The accuracy of this program was tested satisfactorily by comparing its results for plug

flow and various flux transient with those of exact analytical solutions. The program was then used to compare its results with those given by the proposed engineering prediction relationship (see Progress Report for August 1969, ANL-7606, p. 106) for various flux transients with turbulent flow. Since exact analytical solutions are not available for turbulent-flow cases, the results of the computer program were considered "exact" for comparison purposes.

Figure III.C.1 shows a typical comparison of results for turbulent flow in which the wall heat flux is rising linearly in time, but is uniform axially. For this case, the engineering relationship reduces to

$$\Delta = \frac{\theta}{Nu} + \frac{R_1 + S_1}{2\beta}, \tag{1}$$

where

Δ = dimensionless temperature difference, $(t_w - t_B)k/q_r D$,

Nu = Nusselt number, hD/k,

θ = dimensionless time, $\tau\alpha/a^2$,

q_r = reference heat flux, $r\alpha/a^2$,

r = linear rate of heat flux, $Btu/(ft^2)(hr^2)$,

τ = time, hr,

a = channel width, ft,

α = fluid thermal diffusivity, $k/\rho C_p$,

D = channel equivalent diameter, $2a$,

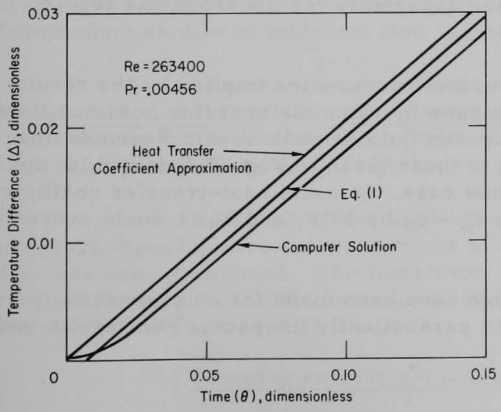

Fig. III.C.1

Comparison of Solutions for Linear Transient Heat Flux in a Parallel-plate Channel

h = fully developed heat-transfer coefficient for the case where the heat flux is uniform, constant, and equal at both walls, Btu/(ft^2)(hr),

and

R_1, S_1, β = dimensionless coefficients. (See ANL-7606, p. 107, for a tabulation of these coefficients.)

(Note that the above definition of θ is different than that given in ANL-7606, p. 106. All other notation has the customary meaning.)

This dimensionless formulation was chosen so that the graphs of the results (e.g., Fig. III.C.1) would be independent of the actual rate of change of heat flux. If the second term on the right-hand side of Eq. 1 is neglected, then the relationship becomes equivalent to the conventional engineering usage of steady-state heat-transfer coefficients for transients.

Figure III.C.1 shows the improvement obtained over the use of the usual heat-transfer coefficient relationship by the proposed engineering relationship. As noted in previous progress reports, the proposed engineering relationship (e.g., Eq. 1) is based on two main assumptions. These assumptions introduce potential inaccuracies, and this is probably why the results of the engineering prediction method do not agree more closely with the results of the computer program. The first assumption neglects the thermal entrance region, defined both with respect to axial distance and time; its effect can be noted on the graph for small values of θ. The second assumption neglects nonuniformities of turbulent velocity profiles during transients. For large values of θ, the difference between the engineering relationship and the exact solution apparently results from this second assumption.

As an example of the inaccuracies implied by the results shown in Fig. III.C.1, consider a case in which the heat flux is rising linearly at 10^4 Btu/(ft^2)(hr) per msec. Let the fluid be sodium with Reynolds and Prandtl numbers corresponding to those given in Fig. III.C.1, and let the channel spacing be 0.06 in. In this case, the usual heat-transfer coefficient relationship would overestimate $t_w - t_B$ by 50°F, and Eq. 1 would overestimate it by 25°F.

Comparisons also have been made for an exponentially increasing heat flux which varies parabolically in space. The results were similar to those cited above.

3. Engineering Mechanics (G. S. Rosenberg)

a. Structural Dynamics Studies--Structure-Fluid Dynamics (M. W. Wambsganss, Jr.)

(i) Preparation of Two Structural-dynamics Test Loops (H. Halle)

Last Reported: ANL-7688, p. 206 (April-May 1970).

The defective control unit of a valve in the large structural dynamics test loop has been replaced. Upon testing, the control unit and the valve have been found to function properly.

(ii) Near-field and Far-field Flow Noise (M. W. Wambsganss, Jr., and P. L. Zaleski)

Last Reported: ANL-7679, pp. 136-137 (March 1970).

Normalization of the mean-square spectra of the near-field flow noise was studied. A Strouhal-number representation of frequency was shown to satisfactorily normalize the spectra with respect to frequency. The magnitude of the spectra was effectively normalized by nondimensionalizing, or scaling, with the square of the mean flow velocity; the conventional method of normalizing by scaling with the cube of the flow velocity tended to "over-correct" the spectra associated with the lower flow velocities.

Convection velocity ratios, average eddy lifetimes, and longitudinal correlation lengths were obtained from broad-band, space-time correlation measurements. In general, these results, which aid in characterizing the near-field flow noise, are in agreement with results from independent studies of turbulent flow in pipes.

The above study is discussed in detail in a paper entitled Measurement, Interpretation and Characterization of Near-field Flow Noise, which will be included in the Flow-induced Vibrations Conference Proceedings to be published as ANL-7685.

A second series of flowtests involving the measurement of pressure-time histories on the surface of a test element in annular water flow has been performed. The tests were run with the acoustic filter systems in the loop. The data have been recorded on magnetic tape and are currently being analyzed.

(iii) Damping and Virtual Mass (S. S. Chen)

Last Reported: ANL-7618, p. 110 (Sept 1969).

To understand the mechanism of damping, the modal damping ratio of a cantilevered rod in parallel flow is being studied analytically.

The analysis is based on the equation derived by Paidoussis.* Since the eigenvalue problem is nonself-adjoint, the adjoint eigenfunctions** associated with this system are utilized. The damping ratio of the system was obtained as

$$\zeta = \zeta_0 + \zeta_d + \zeta_c, \tag{1}$$

where

$$\zeta_d = \zeta_d(\epsilon C_N, \epsilon C_T, \epsilon C_T', \beta, u)$$

and

$$\zeta_c = \zeta_c(\epsilon C_T, \epsilon C_T', \beta, u). \tag{2}$$

Here ϵ is the ratio of rod length ℓ to rod diameter; β is the square root of the ratio of added mass M to virtual mass; u is the dimensionless flow velocity; C_N and C_T are the drag coefficients in normal and axial directions, respectively; and C_T' is the drag coefficient characterizing the free end.

Note that ζ_0 is the damping for zero flow velocity, ζ_d is the damping induced by drag forces, and ζ_c is associated with the Coriolis force. A numerical example is shown in Fig. III.C.2, where $\beta = 0.707$, $\epsilon C_N = \epsilon C_T = 1$, and $\epsilon C_T' = 0.5$. It is seen that the damping for a cantilevered rod is much larger than that of a simply-supported rod. The physical reason is easily understood. The energy dissipated by the Coriolis force from time t_0 to time t_1 is

$$\Delta W = -\int_{t_0}^{t_1} MU\left[\frac{\partial y(0,t)}{\partial t}\right]^2 dt + \int_{t_0}^{t_1} MU\left[\frac{\partial y(\ell,t)}{\partial t}\right]^2 dt, \tag{3}$$

where U is the flow velocity, and y(x,t) is the rod displacement. From Eq. 3 it is realized that so long as there is no displacement at both ends, the Coriolis force is pure gyroscopic and the system is conservative. However, for a cantilevered rod, $W \neq 0$, and the Coriolis force acts as a strong damping mechanism.

The foregoing analysis is in agreement with independent experiments.†

*Paidoussis, M. P., Dynamics of Flexible Slender Cylinders in Axial Flow; Part I, Theory, J. Fluid Mech. 26(4), 717-736 (1966).

**Chen, S. S., Forced Vibration of a Cantilevered Tube Conveying Fluid (to be published).

†Knudsen, S. A., and Smith, G. M., "Dynamic Response of Slender Tubes in Parallel Flow when Subjected to Time Varying Boundary Conditions" (to be published in ANL-7685). Also see Paidoussis, M. P., Dynamics of Tubular Cantilevers Conveying Fluid, J. Mech. Eng. Science 12, 85-103 (1970).

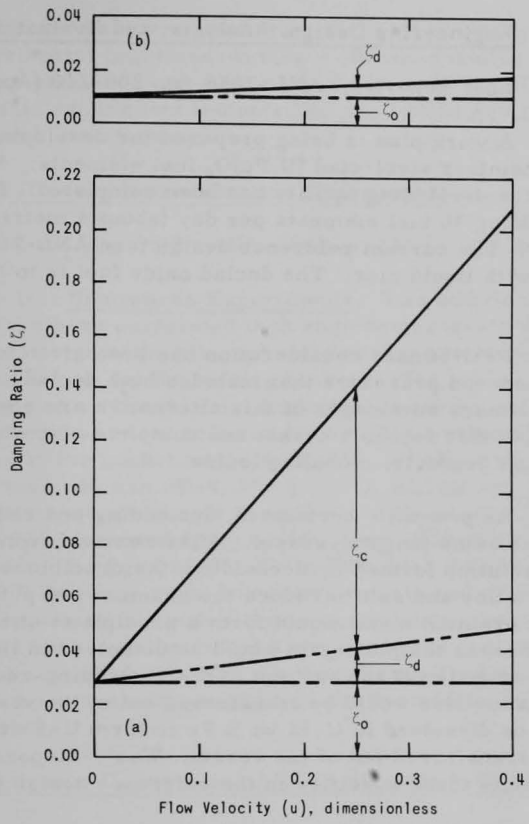

Fig. III.C.2. Damping Ratio as a Function of Flow Velocity for (a) Cantilevered and (b) Simply-supported Rods

D. Chemistry and Chemical Separations

1. Fuel Cycle Technology--Research and Development

a. Molten Metal Decladding (R. D. Pierce)

Last Reported: ANL-7688, pp. 208-212 (April-May 1970).

Laboratory and engineering work is being done on the development of a molten-metal decladding technique to be used as a head-end procedure for aqueous processing of LMFBR fuels. Although molten-metal decladding is being studied in relation to mixed uranium-plutonium oxide fuel clad with stainless steel, this technique can also be used to remove Zircaloy from light-water-reactor fuels.

(i) Engineering Design, Analysis, and Evaluation

Last Reported: ANL-7688, pp. 209-210 (April-May 1970).

A work plan is being prepared for developing liquid-metal decladding of stainless steel-clad $(U,Pu)O_2$ fuel elements. A conceptual design for a large decladding facility has been completed. The design is based on decladding 36 fuel elements per day (about 4 metric tons of uranium plus plutonium). The current reference design (see ANL-7688, p. 209) is for decladding with liquid zinc. The declad oxide fuel is to be fed to a voloxidizer.

Preliminary consideration has been given to an alternative liquid-metal head-end procedure that includes both decladding and fuel reduction. The primary advantages of this alternative are elimination of the handling of solid oxide fuel in a basket and complete removal from the fuel of volatile fission products, including iodine.

As presently envisioned, decladding and reduction would be performed in the same tungsten vessel. After removal from the vessel of the zinc-steel solution formed by decladding, the crucible would be charged with Mg-Cu-Ca alloy and salt to reduce the uranium and plutonium oxides to metals. The uranium metal would form a precipitate at the bottom of the crucible, whereas the plutonium would be dissolved in liquid Mg-Cu. After pressure-transfer of the salt out of the decladding-reduction vessel, the Mg-Cu-Pu alloy also would be transferred out of the vessel. The uranium would be dissolved in U-12 wt % Fe to form U-5 wt % Fe solution, which could be transferred out of the vessel. Waste-disposal procedures would be similar to those specified in the reference design (see ANL-7688).

(ii) Engineering Development

Last Reported: ANL-7688, p. 210 (April-May 1970).

(a) Basket-Draining Experiments. A series of experiments is under way to develop a satisfactory basket design and reliable operational techniques for small-scale decladding tests with irradiated fuel. Additional holes were made in the 18-in.-dia, $4\frac{3}{4}$-in.-long tapered basket described in ANL-7688. The modified basket had a total of 57 holes of 1/32-in. diameter. The fabricated basket was placed in an oven for 20 hr at 300°C to form a thin oxide layer, which layer is thought to improve draining efficiency. In the first test, an empty basket was held in liquid zinc-salt for 5 min and drained for 7 min; ~13 g of salt and metal was held up within the basket at the end of the test. In a second test, the basket (loaded with four stainless steel tubes filled with UO_2 pellets) was held in the melt 55 min and drained 15 min. A holdup of about 16 g of zinc and salt was observed after draining. The third run used the same loaded basket as the second run. After 30 min of

immersion, the basket was removed from the melt and intermittently jarred to produce a horizontal movement during a 10-min draining period. Excellent draining was obtained, with only ~3 g of salt and ~3 g of zinc retained. The results of this experiment indicate that the basket design and draining procedure are both satisfactory.

(iii) Process Demonstration Experiments

Last Reported: ANL-7688, p. 211 (April-May 1970).

(a) Semiworks Experiments. Two additional experiments (SD-4 and -5) have been performed with engineering-scale decladding equipment in a high-purity helium-atmosphere glovebox to develop decladding techniques and a design for decladding baskets. The basket used in SD-4 and -5, consisting of a 30-mil, 6-in.-high liftable tantalum shroud (with 1/16-in.-dia holes) that rests on a solid base, is described in ANL-7688, p. 211. Charged in the basket was a 4-in.-OD, 1/8-in.-wall, 5-in.-high stainless steel tube. In Run SD-4, 250 g of UO_2 pellets and 110 g of crushed UO_2 pellets were charged in addition to the steel tube. The charge for Run SD-5 included 200 g of UO_2 fines. The melt for each run was 65 kg of zinc and 3 kg of $MgCl_2$-NaCl-KCl salt. The basket was immersed for 2.5 hr in the melt, which was maintained at 800°C and mixed at 300 rpm. Samples of the basket contents, the zinc-iron solution, and acid used to leach the basket at the end of a run are being analyzed for uranium and iron. Results will indicate how much iron remained with the UO_2 in the basket and how much uranium passed into the decladding solution through holes in the basket.

b. Continuous Conversion of U/Pu Nitrates to Oxides (N. Levitz)

Last Reported: ANL-7688, pp. 212-213 (April-May 1970).

In the preparation of LMFBR fuel, uranium-plutonium nitrate solutions produced in reprocessing plants must be converted to powdered fuel oxides suitable for the fabrication of fuel shapes. The high rates of plutonium throughput needed for LMFBR fuel recycle require equipment of large capacity. The problems of nuclear criticality and self-radiation from plutonium provide an incentive to develop continuous equipment and processes so that large capacity can be achieved with a relatively low plutonium holdup.

A continuous denitration process for Pu/U nitrate solution is under development. The major objective is a capability for producing (1) either combined U-Pu oxide or plutonium oxide that could be mechanically mixed with uranium oxide and fabricated into fast reactor fuel and (2) plutonium in powder form (i.e., oxide) which could be shipped more safely and in smaller volumes than the nitrate solutions currently being shipped.

Recent work reported below has included (1) laboratory-scale testing of a dissolution procedure in which the bulk of the uranium is separated from the plutonium in dilute nitric acid solutions before the plutonium is dissolved in concentrated acid solutions, (2) study of the reduction of hexavalent plutonium to tetravalent plutonium in a nitrate solution, and (3) progress in the construction of the pilot plant.

(i) Dissolution of UO_3-PuO_2 Powder. In the proposed operation of the engineering-scale fluid-bed denitrator, it is planned to minimize the inventory of fissile material by redissolving the oxide product in nitric acid to provide fresh feed solution. Earlier experiments (see ANL-7688) indicated that plutonium in UO_3-20 wt % PuO_2 dissolves more rapdily than pure plutonium oxide in 16M HNO_3 at 120°C.

A method for redissolving denitrated oxide product has been tested. Initially, a 2.95-g sample of UO_3-PuO_2 (prepared at 450°C) was stirred in approximately 8 ml of 3M HNO_3 at room temperature for 1 hr. The supernatant solution was removed from the residue by decanting. Then approximately 8 ml of 16M HNO_3 was added to the residue, and dissolution was continued at 95°C with stirring. After 5 hr of dissolution, this supernatant was decanted from the residue. For material balance, the residue was then completely dissolved at 95°C in about 8 ml of 16M nitric acid containing 0.05M HF. Analysis for plutonium was by a liquid-scintillation technique. In the initial dissolution, 14% of the plutonium charged was dissolved. During the 5-hr dissolution, three samples were taken. Analyses showed that 31% of the plutonium was dissolved during the first 1/2 hr of this period, 29% during the following $1\frac{1}{2}$ hr, and 1% during the following 3 hr. The residue contained 11% of the plutonium.

Samples were also submitted for X-ray fluorescence analysis to establish the disposition of the uranium. These results indicated that about 70% of the uranium had dissolved in the dilute nitric acid and about 30% had dissolved in the concentrated nitric acid. Greater uranium dissolution can probably be achieved in the first acid strike by applying heat. These data indicate that the procedure as contemplated appears promising. The uranium-rich and plutonium-rich solutions can be mixed to obtain a relatively dilute HNO_3 solution that is suitable as feed for the denitrator.

(ii) Stability of Plutonium Ions in Solution. The change in valence distribution of plutonium ions in nitrate solutions with time has been measured by spectrophotometric examination of a 3M HNO_3 solution containing 1.35M plutonium. This solution was sampled periodically, and the amounts of Pu(VI) and Pu(IV) were calculated from the optical spectra.

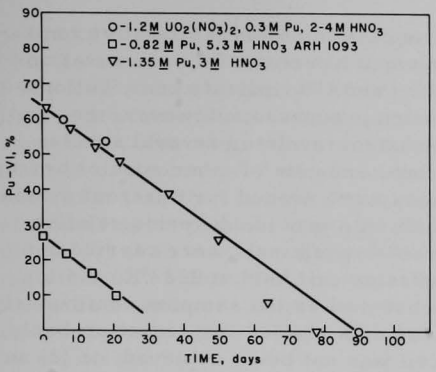

Fig. III.D.1. Reduction of Pu(VI) in HNO_3.

Figure III.D.1, which presents our results along with data from Atlantic-Richfield Hanford* for 0.82M Pu, 5.3M HNO_3 solution, shows a straight line for the concentration of Pu(VI) as a function of time for the early part of the reaction, indicating a zero-order reaction with respect to the Pu(VI) concentration. The slopes for the two plutonium solutions are similar, indicating that the rate of valence change is independent of the initial plutonium concentration in this range. After about 50 days, the rate of reaction in the ANL solution increased. For comparison, three data points obtained in earlier ANL work for a 2-4M HNO_3 solution containing 1.2M $UO_2(NO_3)_2$ and 0.3M Pu are included in Fig. III.D.1.

No trivalent or pentavalent spectra were observed in the spectra for the 3M HNO_3 solutions containing 1.35M plutonium.

(iii) Pilot-plant Program. Equipment for the pilot plant for the continuous denitration of U/Pu solutions has been tested for leaks. The thermocouples have been installed and tested for accuracy. The Allen-Bradley Sonic Sifter, which will be used to obtain particle-size distribution of powder samples, was assembled and tested satisfactorily with a mixture of alumina.

2. General Chemistry and Chemical Engineering--Research and Development

a. Thermophysical Properties

(i) Total Effusion of Pu-O and U-Pu-O System (P. E. Blackburn and R. K. Edwards)

Last Reported: ANL-7679, p. 145 (March 1970).

The partial pressures of fuel and fission-product gases are required to aid in establishing chemical control of cladding corrosion, fuel swelling, and/or fuel-coolant interactions. The partial pressures will be calculated from mass-spectrometric ion intensities measured as a function of temperature and composition. Relative ionization cross sections (or the calibration factors that include these terms) are necessary to make the calculation.

---

*Crawley, D. T., Pressure Buildup of Plutonium Nitrate Solutions in Sealed Shipping Containers, ARH-1093 (July 15, 1969).

Experiments are in progress to obtain the relative ionization cross sections of uranium-oxygen vapor species. Sets of ionization-efficiency data measured for U, UO, UO_2, and UO_3 indicate contributions to U^+ and UO^+ from at least two ionization processes. However, the analysis of the data is not simple in a system involving several species (some of which might contribute additional amounts of other species by fragmentation). To separate the effects, data were needed for different urania compositions; the various compositions would provide differing relative amounts of the species. Some "traverse" experiments were carried out with samples of $UO_{2.09}$ in an iridium effusion cell held at 2323°K, and ion currents of the several species were observed as the samples continuously changed compositions. Analysis of these data showed that, most probably, either (1) full equilibrium within the cell was not being achieved, or (2) an important contribution to the ion current of the UO_2 species is arising from fragmentation (possibly 90-95%) of the UO_3 species. An additional traverse experiment in which conditions have been altered to achieve a closer approach to equilibrium (smaller effusion orifice, same sample area, smaller sample of urania) is in progress to permit evaluation of the relevance of the first possibility. If the second explanation is found to prevail, then the partial pressure of the UO_3 species would be significantly higher than generally assumed. Thus, to calculate accurate pressures from UO_3 ion intensities, one needs both relative ion cross-section data and fragmentation data. Work is continuing to obtain this information.

(ii) Phase Diagram of the U-Pu-O System Containing Fission Products (Nonradioactive) (C. E. Crouthamel and I. Johnson)

Last Reported: ANL-7679, pp. 146-147 (March 1970).

The objective of these studies is to develop a chemical basis for the understanding of the interactions between UO_2-PuO_2, fission products, and cladding that determine the lifetime of fuel elements under conditions of reactor irradiation.

As an aid to the definition of conditions of reactor irradiation, theoretical computations have been made of the dependence on burnup of the overall oxygen potential of a UO_2-20% PuO_2 fuel. In studies of the ternary U-Pu-O system, Markin and McIver* developed a general relationship for the dependence of the partial molar free energy of oxygen, $\overline{G}_{O_2}$, on temperature, T, and mean plutonium and uranium valences, Z_{Pu} and Z_U, respectively. Our computations are based on the assumption that this relationship is also valid for mixed uranium-plutonium oxide that contains fission

*Markin, T. L., and McIver, E. J., "Thermodynamic and Phase Studies for Plutonium and Uranium Oxides with Application to Compatibility Calculations," Plutonium 1965, Chapman and Hall, London (1967), pp. 845-857.

products in solid solution in the fluorite lattice. This assumption implies that the atoms of uranium and plutonium that are removed from the UO_2-PuO_2 fuel matrix by fission are replaced insofar as possible by atoms of fission products (such as zirconium, strontium, barium, yttrium, and the rare-earth elements) that are soluble in the fluorite lattice. Since the number of fission-product atoms that are soluble in the fluorite lattice is somewhat less than the number of atoms fissioned and the average valence of these fission product elements is less than that of the atoms fissioned, electrical neutrality is maintained by an increase in the valence of either the uranium or plutonium atoms remaining in the fuel matrix. This gradual increase in valence, as burnup proceeds, causes an overall increase of oxygen potential in the fuel. The condition of electrical neutrality may be expressed by

$$n_U Z_U + n_{Pu} Z_{Pu} + \Sigma n_i Z_i = 2(2+x), \tag{1}$$

where, for UO_2-20% PuO_2 fuel,

$n_U = 0.8 - f_U b$,

$n_{Pu} = 0.2 - f_{Pu} b$,

f_U, f_{Pu} = fraction of fissions in uranium and plutonium, respectively, and $f_U + f_{Pu} = 1$,

b = at. % burnup/100,

$n_i = b\, y_i$; i = fission product soluble in UO_2-PuO_2 matrix,

y_i = yield of fission product i, gram-atoms of fission element i per gram-atom of uranium and plutonium fissioned,

and

Z_U, Z_{Pu}, Z_i = valence of uranium, plutonium, and fission product.

For hypostoichiometric fuels ($x < 0$) $Z_U = 4$, $Z_{Pu} \leq 4$; and for hyperstoichiometric fuels ($x > 0$) $Z_U \geq 4$, $Z_{Pu} = 4$.

Numerical computations were made for the change in the average valence of plutonium and uranium with burnup for UO_2-20% PuO_2 fuel having two different isotopic compositions of uranium. In the first, the uranium was fully enriched in ^{235}U; in the second, it was natural uranium. The first composition simulates the fuel used in many EBR-II test irradiations; the second simulates the fuel proposed for large fast breeder reactors. The yields of zirconium, strontium, barium, yttrium, and the rare-earth fission elements required to evaluate $\Sigma n_i Z_i$ were computed with the

Radio Isotope Buildup and Decay (RIBD) computer code.* For the enriched uranium fuel, it was assumed that 75% of the fissions occur in ^{235}U and 25% in ^{239}Pu; for the natural uranium fuel, it was assumed that 90% of the fissions occur in ^{239}Pu and 10% in ^{238}U. A neutron flux of 3×10^{15} neutrons cm^{-2} sec^{-1} was assumed. The computed value of $\Sigma n_i Z_i$ for 1 at. % burnup was 2.8594 for fuel with natural uranium and 3.3956 for fuel with enriched uranium. The principal cause of the larger value for enriched uranium is the higher zirconium yield from the fission of ^{235}U compared with the yield of ^{238}U or ^{239}Pu.

Figure III.D.2 shows the variation of the oxygen potential (at 1000°K) with burnup, for fuels having initial oxygen-to-metal (O/M) values of 1.95 and 1.97. The oxygen potential in an actual fuel probably varies with both radial and longitudinal positions in the fuel rod, and temperatures would be higher than 1000°K. The curves of Fig. III.D.2, however, indicate in a general manner how the oxygen potential, at any given position in the fuel, would vary with burnup, initial O/M ratio, and fuel composition. The oxygen potential of fuel in future large fast reactors, where natural uranium will be used, will increase more rapidly with burnup than do the typical test fuels used in current EBR-II irradiations. Since the chemistry of reactions in the oxide is dependent on the oxygen potential, this difference should be kept in mind when the operation of fuels in large reactors is projected from data obtained in EBR-II tests with enriched uranium.

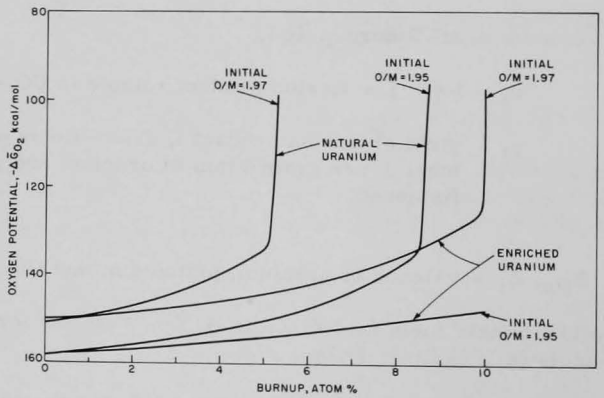

Fig. III.D.2. Variation of Oxygen Potential with Burnup for $U_{0.8}Pu_{0.2}O_{2-x}$ (1000°K)

*Grumprecht, R. O., Mathematical Basis of Computer Code RIBD, DUN-4136, Douglas United Nuclear, Inc., June 17, 1968.

PUBLICATIONS

Use of Changes in Laser Speckle for Vibration Analysis
N. Fernelius and C. Tome
J. Appl. Phys. 41(5), 2252-2253 (April 1970) Letter

An Analysis of Fast Neutron Effects on Void Formation and Creep in Metals
S. D. Harkness, J. A. Tesk, and C-Y. Li
Nucl. Appl. Technol. 9, 24-30 (July 1970)

Statistical Models for Surface Renewal in Heat and Mass Transfer. Part III. Residence Times and Age Distributions at Wall Surface of a Fluidized Bed, Application of Spectral Density. Part IV. Wall to Fluidized Bed Heat Transfer Coefficients
L. B. Koppel, R. D. Patel, and J. T. Holmes
A.I.Ch.E. Journal 16(3), 456-471 (May 1970)

Engineering Development of Fluid-bed Fluoride Volatility Processes. Part 14. Processing Experience in Fluorinating Plutonium Materials and Thermally Decomposing Plutonium Hexafluoride in the Engineering-scale Alpha Facility
N. M. Levitz, G. J. Vogel, E. L. Carls, I. E. Knudsen, D. E. Grosvenor, R. W. Lambert,* E. L. Youngblood,** W. A. Murphy, B. J. Kullen, R. V. Kinzler, and J. E. Kincinas
ANL-7473 (Nov 1969)

Interaction between Gas Bubbles and Migrating Grain Boundaries in Copper
S. R. Pati and P. S. Maiya
Abstract Bull. IMD-AIME 4(1), 35 (May 1970)

Method for Detailed Calculation of Bubble Size Distribution in an Oxide Fuel
R. B. Poeppel and C-Y. Li
Abstract Bull. IMD-AIME 4(1), 177 (May 1970)

An Approximate Solution to the Asymptotic Slowing Down Equations of Fast Neutrons
M. Segev
Nucl. Sci, Eng. 40, 424-437 (1970)

Fast-Neutron Total and Scattering Cross Sections of Bismuth
A. B. Smith, J. F. Whalen, E. Barnard,† J. A. M. DeVilliers,† and D. Reitman†
Nucl. Sci. Eng. 41, 63-69 (July 1970)

In-Reactor Creep Behavior of Austenitic Stainless Steels
J. A. Tesk, S. D. Harkness, and C-Y. Li
Abstract Bull. IMD-AIME 4(1), 178 (May 1970)

---

*General Electric Co.
**Oak Ridge National Laboratory.
†South African Atomic Energy Board.

Bubble-Defect Interactions in Nuclear Fuels
R. W. Weeks, R. O. Scattergood, and S. R. Pati
Abstract Bull. IMD-AIME 4(1), 177 (May 1970)

The following appeared as abstracts in Trans. Am. Nucl. Soc. 13(1) (June 1970):

An Improved LMFBR Fuel Element
T. R. Bump, D. H. Lennox, and H. Greenspan
p. 128

An LMFBR Design to Accommodate Steel Swelling
T. R. Bump and W. W. Marr
p. 129

Vibration and Stability of Tube Exposed to Pulsating Parallel Flow
S. S. Chen and G. S. Rosenberg
p. 335

Survey of Design Considerations for LMFBR Steam Generators and Intermediate Heat Exchangers
S. A. Davis and K. D. Kuczen
p. 110

On the Evaluation of Functionals with Discontinuous Trial Functions
P. P. Lambropoulos and V. Luco
p. 178

Single-Level Inelastic Scattering in a Simple Approximate Way
M. Segev
p. 295

A New Definition of Composite Moderating Parameters for the Goertzel-Greuling Continuous Slowing Down Theory
W. M. Stacey
p. 199

Resolved Resonance Reaction Rates in Fast Reactors
W. M. Stacey
p. 295

Exact Analysis of Local, Non-Plane, Elastic Stresses in Fuel Element Geometries
R. A. Valentin and J. J. Carey
p. 348

IV. NUCLEAR SAFETY RESEARCH AND DEVELOPMENT

A. LMFBR Safety--Research and Development

1. Accident Analysis and Safety Evaluation (G. J. Fischer)

a. Initiating-accident Code Development (G. J. Fischer)

Last Reported: ANL-7606, pp. 123-124 (Aug 1969).

(i) Development of SAS1A Code. A multiple-channel version of the SAS1A accident-analysis code has been written; the initial debugging of this new version has begun. A multiple-channel capability is needed to account for the incoherent behavior of accident phenomena due to variations in power level across the core and variations in the material properties in different subassemblies. Differences in power level are caused by the radial gradient in the neutron flux. Differences in power level and in material properties will also occur if a batch refueling scheme is used involving replacement of only part of the fuel in the core at each refueling period.

The new multiple-channel version of SAS1A is based on the existing single-channel version, so relatively little additional effort was required to produce the multiple-channel version. The single-channel modules for heat transfer, coolant dynamics, fuel and cladding deformation, and neutron kinetics required little modification to handle the multiple-channel case.

b. Single-subassembly-accident and Core-slumping-accident Analysis, and Related Computer-code Development (G. J. Fischer)

Not previously reported.

The DEFORM module of the SAS1A code is being revised. In the current version of SAS1A,* the mechanical behavior of the fuel is calculated by the DEFORM module. The current model in DEFORM is reasonably accurate for fresh, unirradiated fuel pins. However, it is inappropriate for highly irradiated fuel pins near the ends of the their lives. Therefore, it is necessary to revise the model to extend its applicability.

In the present model, the fuel is assumed to behave always elastically and the cladding first elastically and then plastically. The fuel and the cladding are assumed to be free of stress or strain, and the fuel is either a solid cylinder or a straight annulus. The major revisions in the new model are: (1) Distinct metallurgical regions in the fuel are treated, each with its own material properties; in particular, the plastic stress-strain

*MacFarlane, D. R., ed., SAS1A, A Computer Code for the Analysis of Fast Reactor Power and Flow Transients, ANL-7607 (to be published).

relations in both the fuel and the cladding are assumed to be given by general work-hardening laws that also account for the temperature dependence of the yield surface; (2) the behavior of fission-product gases in the fuel matrix, the central cavity, and the plenum is considered; (3) the transient may be initiated after a certain irradiation when the stresses and strains have developed, the central cavity has been formed, and fission-product gases have been accumulated; (4) an option is provided to treat the columnar and the equiaxed, if desired, region as a strengthless material; such a treatment may lead to a different stress distribution; and (5) several different cladding failure criteria are to be provided, which can be checked against experiments and used as appropriate.

The major assumptions used in the model are: (1) Plane strain approximation is used; the stress-strain equations are treated quasi-statically; (2) the long-term effects, such as swelling or creep, are assumed to be negligible during the short transient; (3) each fuel and cladding region is treated as isotropic and homogeneous; in particular, the presence of cracks is ignored (crack effects must be included in a later stage of the work); (4) the fuel and the cladding, once they are in contact, are assumed to slip freely over each other; this restriction will be removed as soon as acceptable numerical convergence is obtained, and (5) melting of the fuel is assumed to start either from the inner cavity wall or from the centerline of the fuel.

The work has been mathematically formulated, and the programming is nearing completion. The code will be tested before it is incorporated as a module in SAS.

c. Sensitivity Studies and Basic Fast Breeder Reactor Safety Studies for Full Range of Accident Events, and Including Parametric-change-type Studies (G. J. Fischer)

Last Reported: ANL-7688, pp. 220-222 (April-May 1970).

(i) Safety Studies. Pretransient SAS1A calculations for the H2 experiment were repeated for a slightly more powerful transient than reported earlier (see Progress Report for April-May 1970, ANL-7688) using SNARG-2D estimated values for the calibration factor and the radial and axial power profiles in the test pin. The power transient used in present calculations is assumed to produce peak TREAT power of 1640 MW and the integrated TREAT power of 463 MW-sec. With the inlet coolant at 400°C and a calibration factor of 3.30 J/MW-sec per gram of oxide, SAS1A predicted coolant boilings with about 85% of the transient energy and cladding melting at the hot spot with 90% of the transient energy (or, 1375 J/g of oxide). It was, therefore, concluded that the cladding would fail at this time due to melting of the cladding, because the estimated plastic strain was only 2%.

The actual power transient, which was close to the assumed power transient, indicated pin failure with 85% of energy deposition (i.e., with 1282 J/g of oxide). Since the inlet coolant temperature was 27°C higher than the value used in pretransient calculations, SAS1A prediction agrees rather well with the experiment. Posttransient analysis of this experiment will be reported.

2. Reactor Control and Stability (W. C. Lipinski)

a. Reactor Stability and Stability Design Criteria for Spatially Dependent Systems (C. Hsu)

Last Reported: ANL-7640, p. 128 (Nov 1969).

A terminal report is being prepared to summarize the progress made to date and the current state of research and development.

b. Transfer-function Techniques to Measure Large Fast Reactor Stability (L. J. Habegger)

Last Reported: ANL-7688, pp. 222-223 (April-May 1970).

A terminal report is being prepared to summarize the progress made to date and the current state of research and development.

3. Coolant Dynamics (H. K. Fauske)

a. Liquid-vapor Dynamics (H. K. Fauske and M. A. Grolmes)

(i) Pressure Drop in Sodium Liquid-vapor Flows

Last Reported: ANL-7679, pp. 151-152 (March 1970).

Two-phase sodium pressure-drop data obtained in the Sodium Flashing Facility included subcritical flow as well as flow in which two-phase choking occurred at the test-section exit. The detailed axial pressure and temperature profiles for the subcritical runs have also been analyzed. For steady flashing flow, the assumption of thermodynamic equilibrium was supported by simultaneous measurements of pressure and temperature along the test section, as was reported earlier for critical-flow runs. It was also reported (see Progress Report for January 1969, ANL-7548, p. 117) that measured void fractions were in good agreement with the well-known Lockhart-Martinelli correlation.

Two-phase frictional pressure-drop data were reduced from the total pressure-drop measurements using the Lockhart-Martinelli void correlation to evaluate momentum-pressure change. This procedure

was necessary because the pressure-drop data at these subatmospheric pressures are for flows in which both momentum and friction losses must be considered. However, only subcritical runs were used in this procedure, because the frictional pressure drop constitutes a greater fraction of the total pressure drop in these runs as compared to critical-flow runs. Any error involved in estimating the momentum pressure-drop contribution will have less effect on the residual frictional pressure drop. Friction-factor data reduced from experimental pressure profiles for subsonic flow conditions are illustrated in Fig. IV.A.1. Data are shown for the square root of the ratio of two-phase to all-liquid pressure drop, ϕ_L, as a function of the Lockhart-Martinelli flow modulus, χ_{tt}. The residual friction multipliers, ϕ_L, are based on the local gradient between pressure-tap locations. Figure IV.A.2 also includes potassium data.* Both sets of data, which together cover a large range of χ_{tt}, illustrate good agreement with the

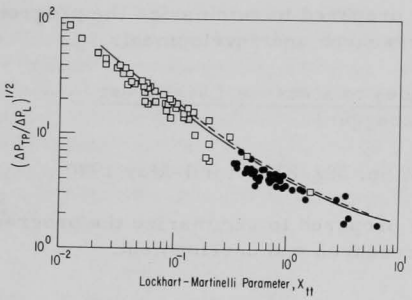

Fig. IV.A.1

Experimental Sodium and Potassium Two-phase Friction Pressure-drop Data. Blocks are potassium data by Alad'yev et al.; solid circles are our sodium data; broken line is simplified annular-flow model $1/(1 - \alpha)$; solid line is the Lockhart-Martinelli frictional-multiplier correlation; and $\chi_{tt} = [(1 - x)/x]^{0.9}(\rho_g/\rho_f)^{0.5}(\mu_f/\mu_g)^{0.1}$.

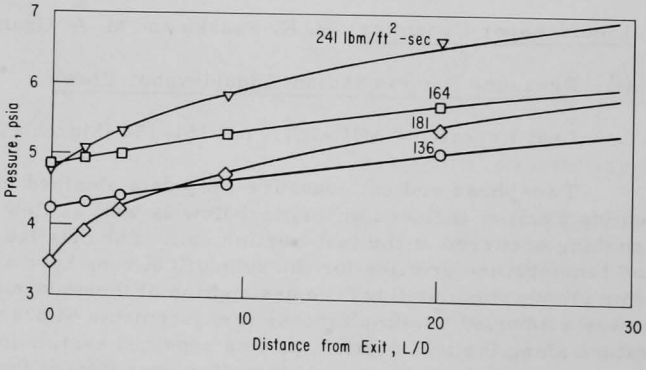

Fig. IV.A.2. Calculated Pressure Profiles per Sodium Two-phase Subcritical Flow. Typical sodium two-phase subcritical-flow data (points) with calculated (lines). Subcritical-pressure profiles based on assumed or required 90% of experimental flow rates to match the experimental pressure profile. Sodium flashing flow $T_0 = 1500^oF$.

*Alad'yev, I. T., et al., ASME, Heat Transfer, Soviet Research, Vol. 1, No. 4, p. 1 (July 1969).

Lockhart-Martinelli frictional-multiplier correlation as well as the simplified annular-flow model $1/(1 - \alpha)$ employed earlier (see Progress Report for October 1969, ANL-7632, p. 131).

Two-phase pressure-drop calculations for subcritical runs can be carried out according to the same procedure outlined for critical flow runs (ANL-7632). However, a flow rate must be assumed if the total pressure drop is known. Typical subcritical-flow runs are shown in Fig. IV.A.2 with calculated pressure profiles based on the assumed or required flow to match the experimental pressure profile. In all cases, the required flow rate is within 10% of the measured experimental flow rate.

In summary, (a) measured two-phase sodium critical flow rates can be predicted by a slip-equilibrium model that also is in good agreement with nonmetallic critical-flow data (see Progress Report for October 1968, ANL-7513, p. 131), (b) measured sodium liquid volume fractions are in good agreement with the Lockhart-Martinelli void correlation (ANL-7548), (c) although significant liquid superheat can be sustained before onset of steady two-phase flashing flow, once steady flashing is established, thermodynamic equilibrium conditions apparently are substantiated by simultaneous temperature and pressure measurements along the flow channel (ANL-7679), and (d) with the above considerations, a simple procedure can be used to predict sodium two-phase pressure drop for subsonic as well as sonic flow at low pressures where the annular flow regime is most likely (ANL-7632).

This concludes progress reporting on sodium two-phase liquid volume fractions, pressure drop, and critical flow data from the Sodium Flashing Facility. A topical report is being prepared to present the detailed results.

(ii) Liquid-Film Breakup

Last Reported: ANL-7669, p. 139 (Feb 1970).

The stability of a liquid film flowing down a vertical heated wall was investigated from two aspects. First, the classical Yih-Benjamin analysis of the stability of a uniform film to small surface perturbations was extended to take into account surface evaporation or condensation. As expected, evaporation destabilizes the film, and for vertical walls it is unstable at every Reynolds number. For a heated wall at a given Reynolds number, the angle of inclination with the horizontal for neutral stability is less than for an unheated wall at the same Reynolds number. However, the effect of heating on the rate of growth is very small until a critical heat flux is reached, after which the most dangerous wavelength grows as the fourth power of the heat flux. The estimated length for both Freon-113 and sodium to form a thin spot at the critical heat flux is very short (<0.1 cm) for both

Freon and sodium, and 5.9 cm for water in a 0.01-cm-thick film. Although this critical heat flux is quite large (28 cal/cm^2-sec for Freon, 254 for sodium, and 47 for water), it indicates that in loss-of-flow accidents thin spots will form in the film quite rapidly.

Second, an energy criterion, adapting the work of Handley and Murgatroyd to take into account the effect of surface wettability, was developed to predict the minimum stable film thickness of a uniform draining film. At the initial thickness, it is assumed that the film breaks up into rivulets whose cross section is a segment of a circle, and whose aspect ratio is determined by the liquid-solid contact angle; it also is assumed that the sums of the kinetic and surface energies per unit volume of the film and of the rivulets are equal. The results in Fig. IV.A.3 show that sodium and Freon-113 are surprisingly close in behavior, and for well-wetted walls (θ_0 = 15°) the critical film thickness for sodium is less than 0.003 mm. For zero contact angle the film is stable at all thicknesses. Because the maximum evaporation rate of the sodium film in a typical loss-of-flow reactor accident is about 0.1 cm/sec of liquid, resulting in a time period of the order of 0.1 sec, it apparently is possible that the film

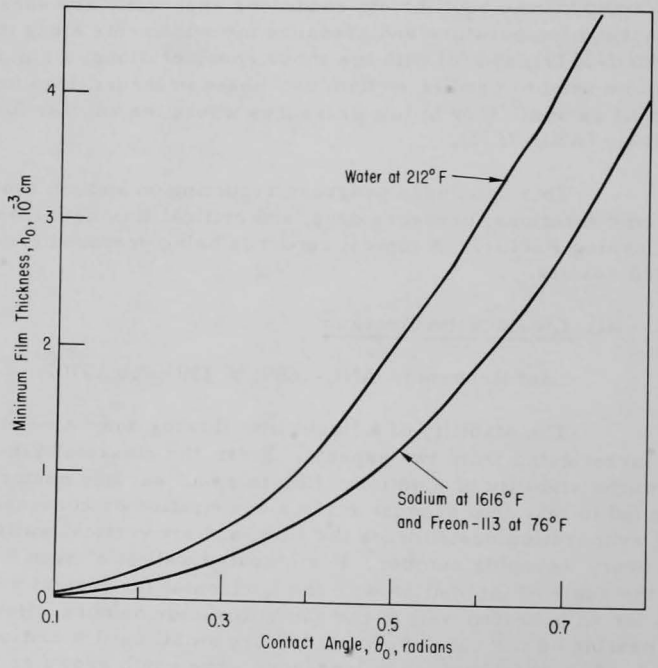

Fig. IV.A.3. Film Thickness vs Liquid-Solid Contact Angle for Water, Sodium, and Freon-113

will remain unbroken during the first expulsion phase. However, the formation of thin spots proceeds rapidly, as noted above, which might modify these conclusions. Experiments are being planned to verify these analytical predictions.

4. Fuel Element Failure Propagation (J. F. Schumar)

a. In-pile Studies (W. K. Barney and R. J. Dunworth)

Not previously reported.

(i) Planning, Design, and Evaluation of Experiments. To evaluate the potential propagation of fuel-element failures within a subassembly requires a test bed in which reactor operating conditions can be simulated.

Studies have been conducted to determine the feasibility of using a thermal reactor with a filter surrounding the test section to remove the thermal neutrons. Figure IV.A.4 shows the relation between the high-energy neutron spectra to be expected in such a filtered volume in a thermal reactor, in FFTF, and in a 1000-MWe LMFBR. The spectrum is satisfactory. A further test of feasibility was the capability to achieve the specific power postulated for reactor operating conditions. Based on transport-theory neutronics and experiments performed in the Argonne Thermal Source Reactor* (ATSR), the results shown in Figs. IV.A.5-IV.A.7 were determined.

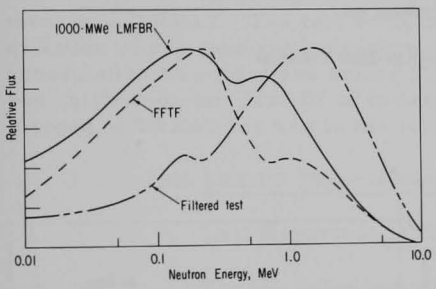

Fig. IV.A.4. High-energy-neutron Spectra in the FFTF, in a 1000-MWe LMFBR, and in a Filtered Test Section in a Thermal Reactor

The 2-in.-dia central hole in the ATSR restricted the experiments to a 19-element test assembly of near-representative LMFBR fuel. The experiments were designed to measure the average and spatial power distributions in the fuel and were used to estimate the uncertainty associated with the calculated power generation. The uncertainty is represented by the bands shown in Fig. IV.A.6. The calculations are based on a model with 10^{14} thermal neutrons/cm^2-sec incident on the filter, so the associated fast-neutron flux is representative of an LMFBR.

From these results, we conclude that it is feasible to develop a test bed composed of a self-contained sodium loop having a filtered

* A water-moderated plate-type reactor using fully enriched fuel. The neutron-energy spectrum is representative of that in high-flux thermal reactors.

test section. Thus, fuel-element failures of all types could be investigated in a high-flux ($>10^{14}$ n/cm^2-sec) thermal reactor; the results would meet the requirements of the LMFBR safety program.

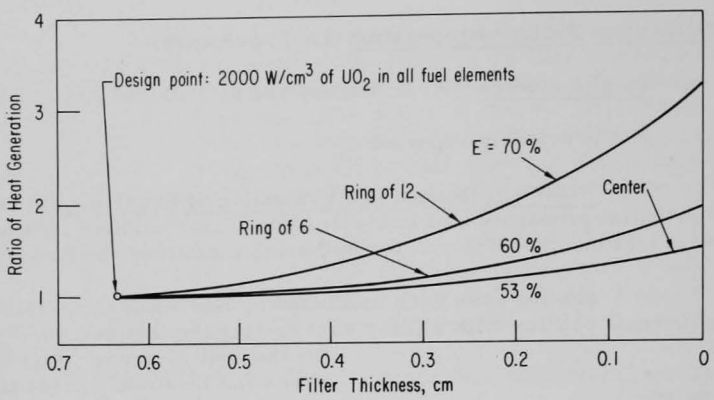

Fig. IV.A.5. Effect of Neutron-filter Thickness

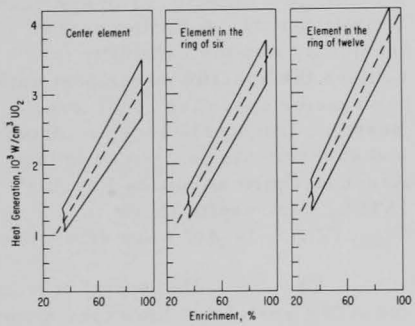

Fig. IV.A.6. Heat Generation vs Enrichment for 19-pin Fuel Assembly

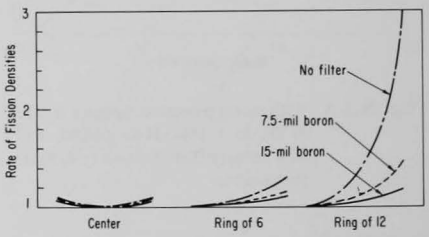

Fig. IV.A.7. Fission Distribution inside Fuel Elements

5. Fuel Meltdown Studies with TREAT

a. Transient In-Pile Tests with Ceramic Fuel (C. E. Dickerman)

(i) EBR-II Irradiation of 18 Mixed-oxide Pins, Unencapsulated, to 5 at. % Burnup

Last Reported: ANL-7632, pp. 134-137 (Oct 1969).

EBR-II unencapsulated mixed-oxide subassembly X040A has been removed from the reactor at attainment of its scheduled irradiation

to 50,000 MWd/T burnup. Eighteen of the pins are fully enriched UO_2-20 wt % PuO_2 mixed-oxide samples irradiated to provide a stock of 5 at. % burnup pins for use in TREAT fast-reactor safety experiments. Maximum midplane burnup of the ANL pins is 6.3 at. %, subject to verification by burnup analysis on a control specimen. Eight of the pins are planned to be used in the EBR-II run-to-failure tests, in which lead pins previously irradiated in the reactor are reinserted for continuing irradiation to failure in a special E-type subassembly. Use of these pins will not interfere with the FFTF-support TREAT experiments on fuel dynamics, because of the planned availability of pins from the PNL-17 instrumented EBR-II subassembly irradiation. Plans are being made to ship the X040A pins to a hot laboratory for examination.

(ii) Loop Meltdown Experiment on Preirradiated UO_2 Pins (E3)

Last Reported: ANL-7688, pp. 225-226 (April-May 1970).

All equipment necessary for performance of the E3 experiment is at TREAT. The test section has been loaded into the B1 loop. Acquisition of pretransient hodoscope data and the experiment itself are scheduled to be performed before July 1, 1970. The TREAT core and control-rod calibration for Test E3 is in progress. The prototype loop has been shipped to TREAT for use in the control-rod calibrations.

(iii) TREAT Experiments with Unirradiated Mixed-oxide Pins

Last Reported: ANL-7688, pp. 226-227 (April-May 1970).

The H2 failure-threshold test with a PNL prototype pin was performed. The preliminary data on the test conditions for the checkout transient were: 1.36% Δk_0, 405 MW peak TREAT power, and 175 MW-sec integrated TREAT power. Test conditions for the failure-threshold transient were: 1.99% Δk_0, 1560 MW peak power, and 450 MW-sec integrated power. With a sample power equivalence of 3.3 J/g-oxide-MW-sec, this represented an integrated sample power of 1485 J/g.

Pretest SAS1A calculations for a comparable transient, with a sample integrated power of 1528 J/g, predicted coolant boiling in the test section at 85% of the transient energy input with the sample failing by melting of the cladding at 90% of the energy input. The experimental results verified the reliability of that analysis. Failure, which was indicated by flow, pressure, and temperature anomalies, occurred at approximately 85% of the transient energy input. After the test, flow through the test section could be reestablished.

b. Experimental Support (C. E. Dickerman)

Last Reported: ANL-7688, pp. 227-228 (April-May 1970).

(i) Shipping Cask. Work is proceeding on the procurement package to be submitted to the AEC for approval. The revised design and analysis are complete, including revisions made to satisfy RDT comments. The cask design and revised specification are ready for final review and approval. The quality-assurance program and the quality-control plan are being reviewed. After completion of the ANL reviews and approvals, the package will be assembled for submission to RDT.

The cask design revisions are being incorporated into shop drawings.

c. Postirradiation Examination (L. A. Neimark and W. F. Murphy)

Last Reported: ANL-7679, pp. 156-158 (March 1970).

(i) Examination of Unirradiated PFR Fuel Elements. A prototype mixed-oxide PFR fuel element (No. 726) is being examined after a transient test in TREAT (experiment H1). The nondestructive phase of the examination that has been completed includes neutron radiography, visual examination, macrophotography, profilometry, gamma scanning, and weight, volume, balance-point, and length determinations. Eddy-current inspection will complete this phase of the examination, and further nondestructive examination will follow. The results of the examinations are being compared with predictions made by the SAS1A code.

d. TREAT Operations (J. F. Boland)

Last Reported: ANL-7688, pp. 232-233 (April-May 1970).

(i) Reactor Operations (J. F. Boland)

Neutron radiographs were made of EBR-II blanket rods, melt-wire temperature indicators, and experimental capsules from Subassemblies X040A, X027, and X050. Neutron radiographs were also made of TREAT experiments ANL-H-2, ANL-S-5, and ANL-E-3, and of a PBF fuel rod after irradiation in SPERT.

A prototype FTR-type fuel pin (experiment H-2) was subjected to two transients in a Mark-II sodium loop to determine failure threshold and fuel-motion characteristics with the pin in a flowing-sodium environment. A three-pin cluster of preirradiated UO_2 fuel pins (experiment E-3) was irradiated in a Mark-II sodium loop to investigate failure characteristics and fuel movement of irradiated oxide fuel in flowing

sodium. Pressure, flow, and neutron-radiograph data showed that extensive failure of both the FTR and preirradiated pins occurred during these tests.

A cluster of five UO_2 fuel rods (experiment S-5) contained in stainless steel tubing that had been evacuated and sealed was tested in the piston autoclave. The purpose was to investigate the influence of plenum-gas pressure on the magnitude of the pressure pulses observed when oxide-fuel pins failed in stagnant sodium. Evaluation of data from experiments S-3 and S-4 had indicated that the maximum pressure pulses might be due to release of plenum-gas pressure rather than sodium vaporization. (See Progress Reports for February 1969, ANL-7553, p. 113, and September 1969, ANL-7618, p. 133.) Although the energy release for experiment S-5 was comparable to that from experiment S-3, the maximum pressure pulse was about twice as large. Detailed analysis of data from this experiment is in progress.

(ii) Automatic Power Level Control System (J. F. Boland)

Data supplied by the contractor has shown that the acceleration characteristics of the hydraulic-control-rod drives are not within specifications and that the transfer time of the selector valve, which transfers high-rate oil flow from one drive to the other, is slower than specified. However, computer simulation of automatic reactor control using a control system with the slightly degraded acceleration and selector-valve characteristics has shown that adequate reactor control can be obtained with the as-built system. An ANL representative is scheduled to witness system testing at the contractor's plant the week of July 6; if overall system performance is in accordance with that reported by the contractor, terms for acceptance of the system will be negotiated.

6. Materials Behavior and Energy Transfer (M. G. Chasanov)

a. High-temperature Physical-property Studies (M. G. Chasanov)

Last Reported: ANL-7679, pp. 159-160 (March 1970).

(i) Total Pressure over Liquid UO_2. An important input parameter for equation-of-state calculations for reactor fuels is vapor pressure of the fuel. Presently available data must be extrapolated over many orders of magnitude to obtain vapor-pressure values at the temperatures of interest in reactor-safety calculations. Consequently, a program was initiated (see Progress Report for June 1969, ANL-7581, p. 127) to measure vapor pressures over liquid reactor fuels by means of transpiration techniques, so as to reduce the extent of the extrapolation. The data to be obtained will allow the calculations to be made with greater confidence.

Preliminary vapor-pressure measurements on liquid urania have been carried out up to approximately 3400°K. These preliminary measurements, made with an inert carrier gas for the transport of urania vapor, serve to establish guidelines for experimental procedure and yield approximate values for the total pressure at the temperature measured. For temperatures above the melting point of urania, and below the melting point of tungsten, the total urania pressure approaches 1 atm.

During a typical measurement, an appreciable fraction of the sample is converted to vapor with attendant changes in the unvaporized material. In measurements where the starting material was of composition O/U = 2.00, the composition of the charged urania varied as vaporization proceeded, moving toward lower O/U ratios. For two measurements at 3390°K, where the O/U ratio at the start of the run was 2.00 and the final composition was 1.94, the vapor pressure was 0.18 atm. Measurements at the same temperature with a starting O/U ratio of 1.94 showed no apparent further reduction in O/U ratio and gave a somewhat lower total pressure of 0.15 atm. However, this apparent trend of decreasing pressure with lowering of O/U ratio may be the result of scatter in the data.

Presently, work is under way to extend the preliminary measurements to approximately 3500°K, to examine further the effect of composition, and to start final measurements over the range 2600-3500°K.

7. Fast Reactor Safety Test Facility Study (L. Baker, Jr.)

a. Programmatic Definition and Justification

Last Reported: ANL-7679, pp. 160-161 (March 1970).

The effort to delineate LMFBR accidents is continuing in order to provide the basis for in-pile experiment priorities and schedules. Potential sources of LMFBR accidents have been reviewed. To treat the potential sources of single-assembly accidents, five general accident categories were defined: (1) partial assembly blockage, (2) fuel-pin-failure gas release, (3) loading error of single pin or pellet in otherwise normal assembly, (4) full-fuel-assembly blockage, and (5) loading error of fuel assembly in wrong location.

The most likely sequence of each accident was developed, including an identification of each point in the sequence where accident detection and protective system action might be achieved. Also, an approach to accommodate each accident was developed and, from this, key uncertainties were identified. The accident sequences and the key uncertainties for single-assembly accidents are outlined in Fig. IV.A.8.

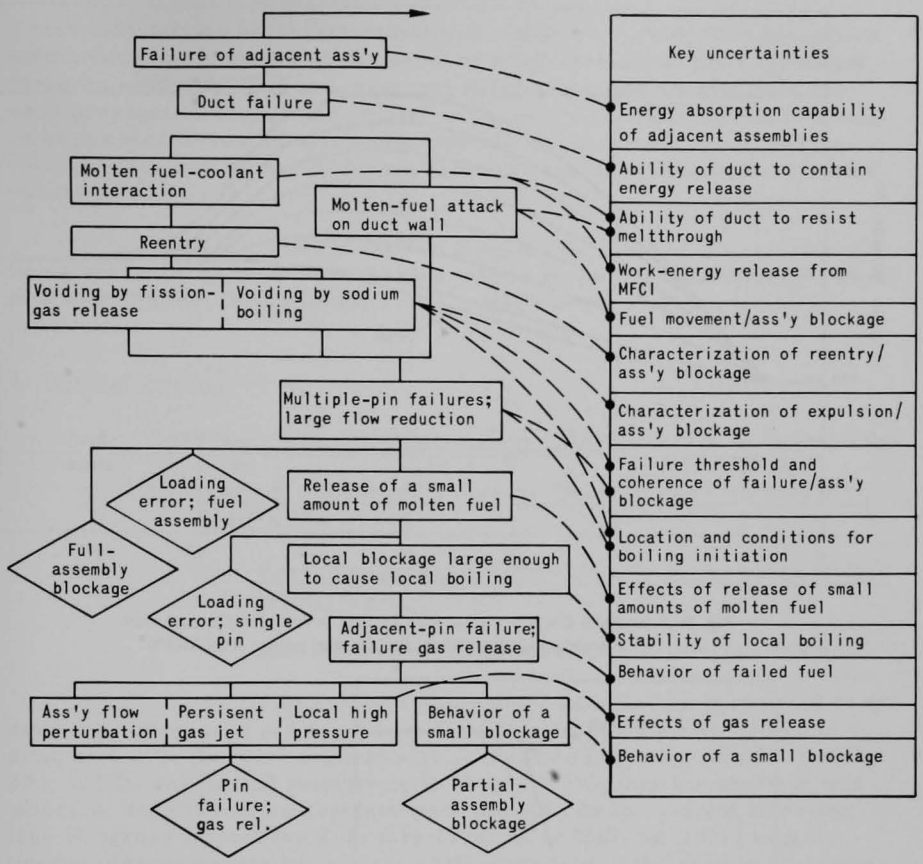

Fig. IV.A.8. Accident Sequences and Key Uncertainties for Single-assembly Accidents

Calculations using the ANL SAS1A code are being performed to substantiate considerations of accident sequences. Figure IV.A.9 shows calculated axial coolant temperature profiles after a sudden flow reduction to one assembly for FFTF conditions. The results indicate that a minimum of 0.7 sec is available before coolant boiling could begin. After boiling initiation, there would probably be a general expulsion of coolant from the assembly; however, a residual film of sodium will remain and provide cooling for an additional period of time.

After film dryout, it is assumed that there is complete vapor blanketing of the fuel elements. After blanketing, it requires about 3.7 sec to melt 50% of the fuel-pin cross-sectional area at the hottest point and about 5 sec to melt 50% of the fuel in a single element, as shown in Fig. IV.A.10.

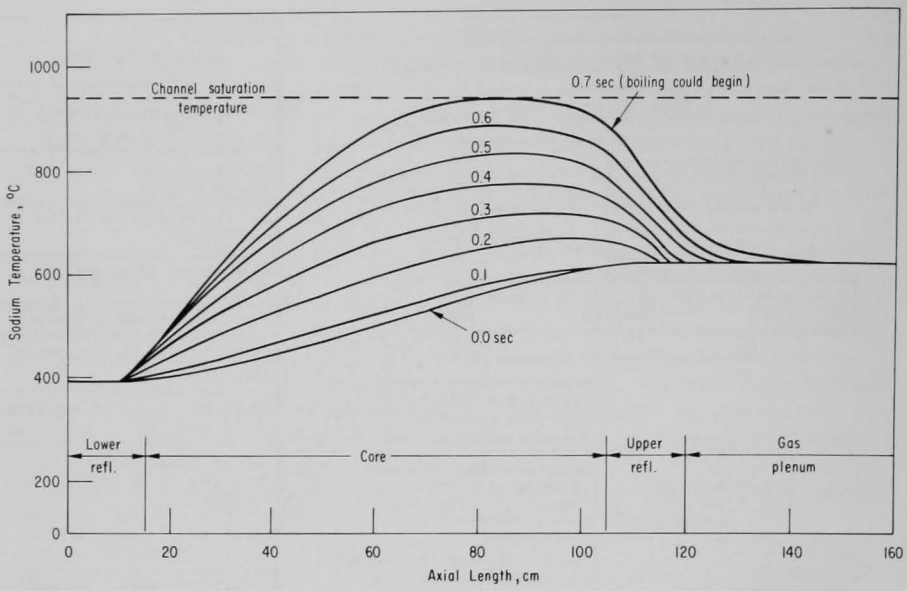

Fig. IV.A.9. Axial Coolant Temperature Profiles in FFTF Hot Channel after Flow Blockage (maximum fuel thermal rating: 14.0 kW/ft)

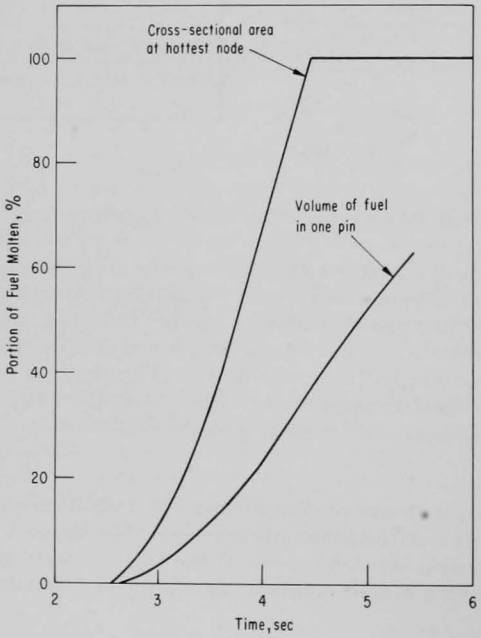

Fig. IV.A.10

Percentage of Fuel Molten vs Time after Complete Vapor Blanketing of FFTF Hot-channel Fuel Pin

These calculations show that considerable time is available for protective action even in the very unlikely event of a full-fuel-assembly blockage. More important is the conclusion that these times may be available for each propagation step in the partial-assembly-blockage accident, if it can be shown that blockage, blanketing, and fuel melting must occur sequentially in each row of fuel elements before a general fuel-assembly failure occurs.

Each uncertainty derived from the delineation of accidents is being examined to determine the best way to resolve the uncertainty. From this examination, the optimum in-pile experimental program is being developed.

8. Violent Boiling (R. O. Ivins)

a. Violent Boiling with Molten Fuel and Sodium (D. R. Armstrong)

(i) Violent Boiling and Pressure Generation upon Contact of Molten Materials

(a) Pressure-generation Experiments by Dropping Molten Material into Coolant

Last Reported: ANL-7688, pp. 238-240 (April-May 1970).

Two experiments (Runs 3 and 4) were performed to examine the pressures and forces generated by dropping molten UO_2 into sodium at 400°C. In these experiments, a tungsten crucible containing about 25 g of UO_2 was heated inductively to about 2900°C; then the crucible was inverted, and the molten contents were poured into the sodium container (see Progress Report for February 1970, ANL-7669, pp. 140-141). Continuous measurements were made of the pressure in the sodium container, the force exerted on the sodium container, and the overpressure in the gas space above the sodium. The entire event was photographed with high-speed motion-picture film at 1000 frames/sec. After the event, data were obtained on the UO_2-particle-size distribution and the spatial distribution of sodium within the glovebox.

Although the third and fourth experiments were performed under conditions nearly identical to the earlier experiments, the results were markedly different. The film record for Run 3 showed that the UO_2 fell as a number of discrete drops, several of which caused minor explosions, while others quenched without any noticeable disturbance of the sodium. There was a variable time delay of 2-60 msec between the entry of the drop into the sodium and the explosion. Only one of the drops produced an explosion of sufficient magnitude to be detected by the pressure transducer in the sodium tank. The measured pressure pulse from this

event had a peak pressure of 200 psi with a width at half-maximum of 1 msec. A relatively small amount (<3 g) of sodium and essentially no UO_2 were expelled from the tank. The mass of UO_2 that dropped from the crucible was 10.2 g.

The high-speed motion-picture record of Run 4 showed that the molten UO_2 (12.9 g) fell from the crucible into the sodium as either a continuous stream or as a series of closely spaced drops. (Details of the falling UO_2 were obscured by UO_2 vapor.) An explosion in the sodium tank occurred 49 msec after the first contact of UO_2 with the sodium surface. This explosion ejected sodium from the tank, whereupon it contacted the UO_2 falling from the crucible inducing a second, aerial explosion 3 msec after the initial explosion in the sodium tank. This explosion caused a rapid dispersal of UO_2 and sodium droplets with initial velocities of about 30 msec. After the experiment, 86 g of sodium and 4 g of UO_2 were found outside the sodium tank.

The pressure record corresponding to the explosion in the tank showed a peak pressure pulse of 655 psi with a width at half-maximum of 0.1 msec. The calculated impulse delivered by the pressure pulse to the force transducer supporting the sodium tank was within 20% of the measured impulse (350 lb, half-width 0.7 msec).

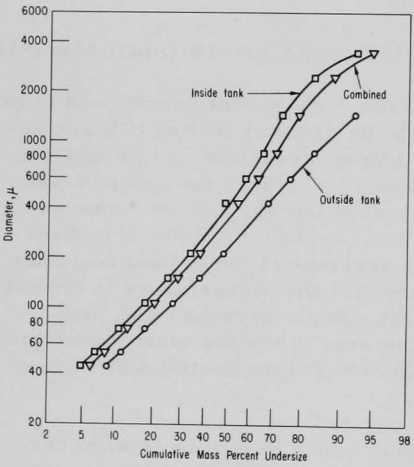

Fig. IV.A.11. UO_2 Particle-size Distribution after Run 4

The UO_2 found outside the tank was treated separately from that remaining in the tank for the particle-size analysis. These separate residues had markedly different size distributions (see Fig. IV.A.11) and appearance. The mean diameter of the expelled particles was 225 μ, whereas those remaining in the tank had a mean diameter of 400 μ. The residue from the sodium tank was angular and rough surfaced, indicating that much of the fragmentation occurred in the solid state. The particles found outside the tank had smooth, rounded surfaces, indicating liquid-state fragmentation.

The UO_2 was separated from the sodium by dissolving the sodium in ethyl alcohol. During dissolution, the UO_2 particles in the residue remaining in the tank tend to disintegrate into smaller particles as the supporting sodium is removed. Therefore, the measured particle-size distribution of the residue found in the tank is

biased toward smaller diameters. (This behavior was not observed for UO_2 particles that had been ejected from the sodium container in Run 4. These particles retained their size and shape during dissolution of accompanying sodium.) The measured mean diameter of the residue from Run 3, which all came from inside the tank, was 370 μ.

The experimental apparatus is being modified for a set of two experiments at a sodium temperature of 600°C.

(b) Pressure-generation Experiments with New Methods of Contact

Last Reported: ANL-7595, pp. 121-122 (July 1969).

The impact-column experiment was designed to measure the pressures and work energies generated by the impact of coolant upon molten fuel. This experiment is similar conceptually to the TRW-STL water-molten aluminum laboratory shock-tube experiment.* A major difference is that this experiment is performed in the TREAT reactor with the UO_2 fuel material melted by a TREAT transient. After fuel melting, a diaphragm is ruptured allowing the coolant to impact upon the molten UO_2 contained in a graphite crucible.

The impact autoclave was designed originally to use water for the initial tests of the equipment, and sodium for the later tests to investigate UO_2-sodium interactions. (The autoclave and its components for use with water coolant are described in ANL-7595.) A complete hazards report for use of the autoclave with water coolant in TREAT was prepared and approved. An energy-calibration test, I1, was also run in TREAT without coolant.

The initial water tests have been eliminated from the program. The autoclave has been modified for use with sodium in preparation for test I2. The hazards report has been revised for use of the autoclave in TREAT with sodium coolant. The major modifications to the autoclave were the addition of electrical heaters for the sodium column, additional thermocouples, and the attendant electrical fittings. The revisions have been completed, and test I2, the initial experimental run, is planned for July 1970.

*Kinetic Studies of Heterogeneous Water Reactors, 1965 Annual Summary Report, STL-372-30 (1966); Kinetic Studies of Heterogeneous Water Reactors, 1966 Annual Summary Report, STL-372-50 (1967).

b. Simulations of Fuel Dispersal (J. J. Barghusen)

Last Reported: ANL-7688, p. 240 (April-May 1970).

(i) In-pile Experiments on Material Interactions during Nuclear Transients

(a) In-pile Experiments with UO_2 in Piston Autoclave. TREAT meltdown experiment S-5 has been performed in the sodium-filled piston autoclave. This experiment used an array of five stainless steel-clad UO_2 fuel rods and four dummy rods. All rods were evacuated to 1×10^{-5} Torr before being sealed, so they contained essentially no gas. The objective of this experiment was to determine the effect of the absence of helium bond gas on the pressures and the work-energy produced by fuel-coolant interaction. The experimental conditions for experiment S-5 were nearly identical to those employed in the comparable experiment S-3. (See Progress Report for February 1969, ANL-7553, pp. 113-116.) Experiment S-3 used an array of five helium-bonded (15-psia) fuel pins and four dummy pins containing helium at 15 psia and a total fission-energy input to the fuel of 460 cal/g UO_2. Experiment S-5 was performed with evacuated fuel and dummy pins in the same array at a total fission-energy input of 509 cal/g UO_2.

Preliminary data indicate that the amplitudes of the pressure pulses occurring upon pin failure were greater with the evacuated pins than in the previous tests with helium-bonded fuel pins.

c. Mathematical Models of Fuel-coolant Dynamics (R. W. Wright)

Last Reported: ANL-7655, pp. 135-136 (Dec 1969).

(i) Fuel-sodium Interaction and Heat Transfer Leading to Pressure Generation

(a) Fuel-failure Model. The effects of (a) fuel porosity and central-void formation and (b) thermal contributions to cladding stress and strength are important in determining the thresholds of cladding failure and cladding-failure mechanisms.

At present, it apparently is necessary to divide the oxide fuel into up to five concentric zones of varying porosities depending on the temperature distribution in the fuel:

Zone	Temp Range, °C	Density Range, % T.D.	Nature of Structure
I	Surface-1400	Initial (<96-96)	Initial porosity
E	1400-1900	96-98	Equiaxed grain
C	1900-melting	98-100	Columnar grain
M	Melting-maximum	100	Molten fuel
V	Maximum	-	Void (central)

The cladding thermal stress ordinarily decreases, while the pressure stress increases, during the temperature transient in a loss-of-coolant incident. During the transient, the temperature in the fuel pin increases and increases the pressure stress, while the temperature gradient in the cladding wall decreases and decreases the thermal stress. Consider, for example, a fresh FFTF mixed-oxide fuel-pin section operating at an average power density of 304 cal/cm^3-sec and surrounded with sodium coolant at 400°C. At steady state and at the threshold of failure (due to loss of coolant), the stresses on the inner and outer walls of the 304 SS cladding are estimated to be:

	Steady State	Failure Threshold
Time into incident, sec	0	1.24
Helium pressure, psig	49.6	51.3
Cladding ΔT, °C	28	10
Inner-surface stresses,* lb/in.^{2}		
Pressure stress	+343	+355
Thermal stress	-9,253	-2,695
Total	-8,910	-2,340
Outer-surface stresses,* lb/in.^{2}		
Pressure stress	+294	+304
Thermal stress	+8,428	+2,455
Total	+8,722	+2,759
Cladding yield strength, lb/in.^{2}	+1,400	+2,800

9. Post-accident Heat Removal (R. O. Ivins)

a. Engineering Analysis (J. C. Hesson)

Last Reported: ANL-7688, pp. 244-249 (April-May 1970).

(i) Assessment of Possible Core Damage due to Accidents

Not previously reported.

Heating in a blocked subassembly due to fission-product decay has been analyzed. For an accident-damaged subassembly, a number of fuel-structure configurations would be possible: The fuel might be present as a porous bed of fragments that would be cooled by forced sodium coolant flow or by natural convection as previously discussed (ANL-7661, pp. 134-136, January 1970), or the subassembly might be blocked partially so that the sodium flow through the assembly is insufficient for adequate cooling. This latter case is analyzed here.

*The plus sign indicates tension and the minus sign indicates compression. In determining the threshold of failure, the effect of thermal stress should be considered along with the pressure stress.

Although the reactor has been shut down, the question arises as to the conditions under which fission-product-decay heating might be sufficient to cause a meltthrough of the blocked subassembly can and a possible meltthrough of the can of an adjacent subassembly. It is assumed that the subassemblies are hexagonal and that the six adjacent subassemblies have flow of sodium. The criteria for meltthrough of the blocked and possibly adjacent subassembly is that the can of the subassembly would need to reach the melting temperature of stainless steel (1400-1500°C). In general, the fuel in a completely blocked subassembly would melt and possibly boil, particularly soon after shutdown when the decay heat is great. The paths for the heat transfer would be (1) from the molten fuel in the blocked subassembly through the frozen layer next to the can wall, through the can wall, through the thin stagnant sodium layer between subassembly cans, through the wall of the unblocked subassembly into the flowing sodium; and (2) from condensing fuel vapors above boiling fuel, through condensed fuel (liquid and solid) to the blocked subassembly can, and then, as above, to the sodium in the adjacent subassembly. The magnitude of heat flux due to condensing vapors could be greater than that due to conduction from the boiling liquid. For short times, sodium could be prevented from entering the top of the subassembly and cooling the top of the pool due to vapor-locking or fuel blockages in the upper part of the subassembly. This would result in fuel vapor condensation on the can wall.

The heat flux due to conduction from the molten fuel through the can walls, assuming no convection in the molten fuel, would be

$$Q = [2k_\ell(T_b - T_m)q + 2k_s(T_m - T_s)q]^{1/2}, \text{ cal/sec-cm}^2,$$

where T_b and T_m are the boiling and melting temperatures of the fuel material in °C, T_s is the can temperature in °C, k_ℓ and k_s are the liquid and solid fuel material thermal conductivities in cal/sec-cm-°C, and q is the decay-heat generation rate in cal/sec-cm^3.

If T_b = 3200°C, T_m = 2800°C, $k_\ell = k_s = 0.005$, q = 24 (~6% decay heating), and T_s = 1450°C (m.p. of stainless steel), then Q = 20.5 cal/sec-cm^3. Circulation in the liquid due to boiling could reduce the boundary-layer thickness and thus increase somewhat the heat-transfer rate.

As an example, the FFTF subassembly is in the form of a hexagonal can 4.335 in. across flats inside (38.14-cm periphery) and contains about 39,000 g of oxide fuel having a volume of about 3,900 cm^3 in a normal 36-in. length. At a decay-heat value of q = 24 (6%), the average heat flux Q required to remove all the heat through the can walls to adjacent subassemblies would be about 26.8 cal/sec-cm^2 for the 36-in. unslumped length or 42 cal/sec-cm^2 for a slumped length of about 23 in.

If the heat flux from the molten fuel to the can walls were only 20.5, the extra heat would go into the production of fuel vapor at 48,000 cal/sec, or 1,258 cal/sec-cm of periphery. The vapors would condense on the surface of the liquid condensate layer at a temperature near the boiling point of the fuel, T_b, and heat would be conducted to the surface of the frozen layer, which would be at the melting temperature T_m of the fuel. The thickness of the frozen fuel layer on the can depends on the heat flux from the liquid layer and the can wall temperature.

For vapor with no noncondensable gas, the heat-transfer rate* from the liquid film to the frozen fuel at distance x cm from the upper condensing limit (see Fig. IV.A.12) is

$$Q = [h\rho^2 g k^3 (T_b - T_m)^3 / 4\mu x]^{1/4}, \text{ cal/sec-cm}^2,$$

and the total heat transferred per centimeter of width in the distance x = L (from upper condensing limit to boiling liquid surface) is $H_t = 4xQ/3$ in cal/sec-cm. We obtain $Q = 307/x^{1/4}$ and $H_t = 409L^{3/4}$, using the following values for molten fuel: H = latent heat = 600 cal/g, ρ = density = 8.7 g/cm^3, k = thermal conductivity = 0.005 cal/sec-cm-°C, μ = viscosity = 0.01 poise, T_b = fuel boiling temperature = 3200°C, T_m = fuel melting temperature = 2800°C, and g = acceleration due to gravity = 980 cm/sec^2.

The formula for heat flux gives a very large local value as x approaches 0. A more meaningful value is the average flux over the total length x = L (see Fig. IV.A.12). For condensing vapors equivalent to 1,258 cal/sec-cm of periphery, H_t would be $409L^{3/4} = 1258$ and L = 4.473, so that the average heat flux = 1258/4.473 = 281 cal/sec-cm^2.

Because of the presence of noncondensable gases, sodium vapor, and liquid sodium, such a high heat flux would probably not result from condensation of fuel vapor. It is estimated that the maximum average flux would be about one-third of this value, or 90 cal/sec-cm^2 at 6% decay heat.

The burnout flux for heat transfer to a boiling sodium pool would be about 38-75 cal/sec-cm^2 or 5×10^5 to 10^6 Btu/hr-ft^2.** Higher values to subcooled sodium under forced convection might be attained. From the above values of heat fluxes, there is danger of meltthrough from a blocked to an adjacent subassembly, particularly early in an accident situation when the heat generation is high. Figure IV.A.12 shows the heat fluxes as a function of decay heat.

---

*Jakob, Max, Heat Transfer, Vol. 1, John Wiley, p. 665 (1949); Perry, J. H., Chemical Engineers Handbook, 3rd Ed., McGraw-Hill, p. 476 (1950).

**From Fig. 21 in Collier, J. G., and Kosky, P. G., Natural Convective Boiling of the Alkali Metals: A Critical Review, AERE-R5436 (Sept 1967).

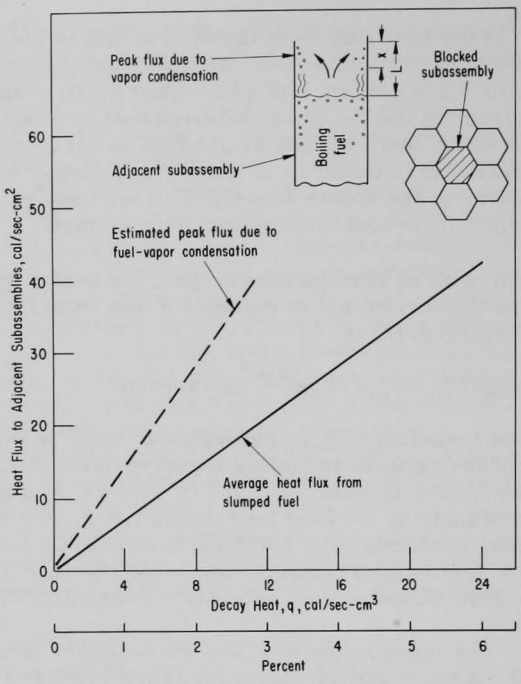

Fig. IV.A.12. Heat Transfer from Blocked Subassembly to Adjacent Subassemblies (for 4.335-in. subassembly). The approximate burnout-flux region for heat transfer to boiling sodium is 38-75 cal/sec-cm^2.

The can of the blocked subassembly would melt through at a lower heat flux than would the can of the adjacent subassembly, since the can of the blocked subassembly would melt through when the stagnant sodium layer between cans boiled or became vapor-locked. Further analytical studies are being made.

B. Effluent Control--Environmental Studies--Research and Development

1. Mass-Energy Balance (J. G. Asbury)

Last Reported: ANL-7679, pp. 169-170 (March 1970).

The method developed to determine average lake-wide effects of thermal discharges on Lake Michigan (ANL-7679, March 1970, p. 169), has been applied to the other Great Lakes. The data used in evaluating month average values of the exchange coefficients included: (1) the temperature

data of Richards and Irbe,* and (2) wind-speed data acquired by H. G. Acres Lts.** and by the Illinois State Water Survey.

Table IV.B.1 shows the lake-wide response to a 1-GW advective input of each of the five Great Lakes; $\overline{K}$ and $\overline{K}_e$ are annual average values for the total and the evaporative portion of the exchange coefficient, respectively; $\overline{q}$ equals 1 GW divided by the lake surface area; and ΔT_s the increase in water surface temperature, and Q_e the increase in evaporative water loss are calculated from

$$\Delta T_s = \overline{q}/\overline{K}$$

and

$$Q_e = \frac{\overline{K}_e}{\overline{K}} \frac{1\ GW}{L},$$

where L is the latent heat of evaporation.

TABLE IV.B.1. Lake-wide Response to a 1-GW Advective Input

	Exchange Coefficients		Lake Response/1-GW Input		
Lake	$\overline{K}$, Btu/(ft^2-day-°F)	$\overline{K}_e$, Btu/(ft^2-day-°F)	$\overline{q}$, Btu/(ft^2-day)	ΔT_s, °F	Q_e, cfs
Superior	80	38	0.092	1.1×10^{-3}	8
Michigan	92	49	0.130	1.4×10^{-3}	9
Huron	88	46	0.126	1.4×10^{-3}	8.5
Erie	95	52	0.296	3.1×10^{-3}	9
Ontario	92	49	0.385	4.2×10^{-3}	8.5

*Richards, T. L., and Irbe, J. G., "Estimates of Monthly Evaporation Losses from the Great Lakes 1950-1968--Based on Mass Transfer Technique," Proc. Twelfth Conf. Great Lakes Research (1969).

**H. G. Acres Ltd., Effects of Thermal Inputs to Lake Ontario 1968-2000 (Feb 1970).

PUBLICATIONS

Serial Solution of Nonlinear Partial Differential Equations of a Counterflow Heat Exchanger Using S/360-CSMP
J. F. L. M. Brukx* and J. H. Tessier
Proc. 1970 Summer Computer Simulation Conference, Denver, June 10-12, 1970. Assoc. Computing Mach., New York, 1970, Vol. I, pp. 360-371

Studies of Fast Reactor Core Behavior under Accident Conditions
C. E. Dickerman
Nucl. Safety 11(3), 195-205 (May-June 1970)

Discussion of "On Some Aspects of Steam Bubble Collapse"
H. K. Fauske, T. T. Theofanus,** and H. S. Isbin**
J. Heat Transfer 92(1), 211 (Feb 1970)

Two-Phase Critical Flow at Low Qualities. Part I. Experimental. Part II. Analysis
R. E. Henry, H. K. Fauske, and S. T. McComas†
Nucl. Sci. Eng. 41, 79-91 and 92-98 (July 1970)

Measurements of Superheating and Expulsion in Static Sodium
R. M. Singer
Proc. European Liquid Metal Boiling Working Group, Second Mtg., Casaccia di Roma, Italy, April 9-10, 1970. EURATOM, Brussels, 1970

The following appeared as abstracts in Trans. Am. Nucl. Soc. 13(1) (June 1970):

Size Distribution of Bubbles Emitted from Simulated Cladding Breaks
R. P. Anderson, L. Bova, and C. J. Roop
p. 328

Simplified Coolant Expulsion Model
R. P. Anderson and P. L. Zaleski
P. 388

The Performance of Small Assemblies of Fast Reactor Fuel Elements in a Thermal Core
J. C. Carter, E. W. Barts, M. V. Davis,†† and R. A. Morris
p. 94

Molten Material-Coolant Interactions
D. H. Cho, D. R. Armstrong, and W. H. Gunther
p. 385

---

*Technological University, Delft.
**University of Minnesota.
†University of Notre Dame.
††The University of Arizona.

Suppression of Sodium Slug Impacts in the TREAT Mark-II Loop
L. W. Deitrich
p. 341

Radiation Effects on Superheating of Liquid Sodium
L. W. Deitrich
p. 368

First TREAT Experiment on High-Energy Fuel Failure of an Unirradiated Oxide Fast Reactor Fuel Pin in Flowing Sodium
C. E. Dickerman, L. E. Robinson, J. F. Boland, R. T. Purviance, and K. J. Schmidt
p. 370

Incipient Liquid Superheat, Hysteresis Effect and Equilibration in Forced Convection Flashing Sodium Flow
H. K. Fauske and M. A. Grolmes
p. 331

On the Measurement of Throat Pressure in Flashing Sodium Critical Flow
H. K. Fauske and R. E. Henry
p. 330

Analysis of a Slug Expulsion for a Nonmetallic Fluid
W. D. Ford, H. K. Fauske, and S. G. Bankoff*
p. 372

Transient and Steady-State Natural Convection of Mercury in a Closed Vertical Rectangular Channel
R. P. Heinish, R. Viskanta,** and R. M. Singer
p. 344

Calculation of the Thermodynamic Efficiency of Molten-Fuel-Coolant Interactions
A. M. Judd
p. 369

High Integrity Trace Heating for Sodium Process Piping
E. L. Kimont, L. H. Bohne, and F. A. Smith
p. 97

Structural Analysis of Subassembly Fuel Ducts
D. Krajcinovic
p. 374

System for Computer Control of Prompt-Critical Transients in TREAT
G. R. Larsen and J. F. Boland
p. 238

---

*Northwestern University.
**Purdue University.

The Mark-II Integral Sodium TREAT Loop
L. E. Robinson, R. T. Purviance, and K. J. Schmidt
p. 354

Determination of Temperature Coefficients in a Nonlinear Space-Dependent Reactor System
W. S. Roman, C. Hsu, and L. J. Habegger
p. 284

Neutron Filter for TREAT Safety Studies on Fast Reactor Fuel
A. B. Rothman, C. E. Dickerman, G. G. Dewey, and E. W. Barts
p. 356

Coupled Neutronic-Hydrodynamic Fast Reactor Disassembly Analysis
W. T. Sha and T. H. Hughes
p. 365

An Apparent Effect of Heat Flux upon the Incipient Pool Boiling of Sodium
R. M. Singer
p. 367

Nonuniform Sodium Slug Ejection from an Asymmetrically Heated Channel
R. M. Singer, R. E. Holtz, H. R. Niemoth, and R. J. Moses
p. 373

Protection against LMFBR Local Core Accidents
J. B. Van Erp, D. R. MacFarlane, and H. K. Fauske
p. 363

A New Computational System for Fast Reactor Accident Investigation
A. E. Waltar* and W. T. Sha
p. 371

Correlation of Plastic Response of Tubes to General Pressure Pulses
C. K. Youngdahl and G. S. Rosenberg
p. 374

PUBLICATION--General

Reactor Physics Division Annual Report, July 1, 1968 to June 30, 1969
ANL-7610

---

*Pacific Northwest Laboratory.

ARGONNE NATIONAL LAB WEST
3 4444 00011470 2